

# Cosmological and astrophysical observables from field theory in curved backgrounds

by

**José Tomás Gálvez Gherzi**

M.Sc., Imperial College London, 2013

B.Sc., Universidad Nacional de Ingeniería, 2011

Thesis Submitted in Partial Fulfillment of the  
Requirements for the Degree of  
Doctor of Philosophy

in the  
Department of Physics  
Faculty of Science

© José Tomás Gálvez Gherzi 2019  
**SIMON FRASER UNIVERSITY**  
Summer 2019

Copyright in this work rests with the author. Please ensure that any reproduction or re-use is done in accordance with the relevant national copyright legislation.

# Approval

**Name:** José Tomás Gálvez Gheri

**Degree:** Doctor of Philosophy (Physics)

**Title:** Cosmological and astrophysical observables from field theory in curved backgrounds

**Examining Committee:** **Chair:** John Bechhoefer  
Professor

**Andrei Frolov**  
Senior Supervisor  
Associate Professor

**Levon Pogosian**  
Supervisor  
Professor

**Malcolm Kennett**  
Supervisor  
Associate Professor

**David Sivak**  
Internal Examiner  
Assistant Professor

**Robert Brandenberger**  
External Examiner  
Professor  
Department of Physics  
McGill University

**Date Defended:** May 3, 2019

# Abstract

The framework of effective field theory has provided valuable insights needed to understand the evolution of physical systems at different energy scales. In particular, when comparing the near-equilibrium phenomena at astrophysical scales with effects at cosmological distances. The objective of this thesis is to introduce useful tools for the evaluation of (a) the observational consistency of an effective field theory of gravity, and (b) the potential modifications of theories, equipped with diffeomorphism invariance. We calculate the evolution of gravitational observables relevant in early universe field configurations, and also in effective theories modified by contributions from higher curvature terms or semiclassical effects testable at astrophysical scales. To do so, we develop efficient numerical routines to resolve the dynamic two-point correlation functions of primordial fluctuations in inflationary and bouncing cosmologies, the accretion of scalar fields and spacetime curvature in modified gravity, and the evolution of scattering processes involving scalar and gravitational radiation. Additionally, we investigate the viability of defining gauge-invariant quantities in theories of gravity, where the canonical coordinates are deformed to incorporate extra degrees of freedom.

**Keywords:** Effective field theory (EFT); Single and multifield models of Inflation; IS-Bounce; Constraint Algebra and deformations; Scalar accretion; Modified Gravity; Wormholes; Gravitational Waves; coalescence of exotic compact objects (ECOs).

# Acknowledgements

I would like to thank Alex Zucca, Alexander Vikman, Sabir Ramazanov, Mason Protter, Levon Pogosian, Justine Munich, Claire Maulit, Malcolm Kennett, Jun-Qi Guo, Ghazal Geshnizjani, David Dobre, Aditya Dhumuntarao, Michael Desrochers, Andrew DeBenedictis, David Broun and Niayesh Afshordi for their time and their valuable advice, comments and discussions. In particular, I have a large debt of gratitude with my supervisor, Andrei Frolov, for his guidance and patience throughout the completion of my PhD. My work was partly funded by the Discovery Grants program of the Natural Sciences and Engineering Research Council of Canada and the Billy Jones Graduate Scholarship, granted by the Physics Department at SFU. Part of my research was done at the Perimeter Institute for Theoretical Physics. Research at the Perimeter Institute is supported by the Government of Canada through the Department of Innovation, Science and Economic Development Canada. This research was enabled in part by support provided by WestGrid ([www.westgrid.ca](http://www.westgrid.ca)) and Compute Canada Calcul Canada ([www.computecanada.ca](http://www.computecanada.ca)).

# Table of Contents

Approval	ii
Abstract	iii
Acknowledgements	iv
Table of Contents	v
List of Tables	viii
List of Figures	ix
<b>1 Introduction</b>	<b>1</b>
<b>I Early Universe Cosmology: Inflationary and bouncing scenarios</b>	<b>9</b>
<b>2 Single-field Inflation: observational constraints on Constant-Roll Inflation</b>	<b>10</b>
2.1 Model and background dynamics . . . . .	12
2.2 Perturbations . . . . .	14
2.3 Planck constraints . . . . .	18
2.4 Discussion . . . . .	20
<b>3 Two-point correlators revisited: fast and slow scales in multifield models of inflation</b>	<b>22</b>
3.1 Perturbation theory: a lightning review . . . . .	23
3.2 Two-point correlators revisited . . . . .	24
3.3 Initial conditions and spectral evolution scheme . . . . .	28
3.4 Results . . . . .	32
3.5 Discussion . . . . .	37
<b>4 Unbraiding the bounce: superluminality around the corner</b>	<b>39</b>
4.1 Model and main equations . . . . .	43
4.2 Conformal transformations, gauges and acoustic geometry . . . . .	49

4.3	Inverse method: reconstructing the theory from its solutions . . . . .	51
4.4	Phase space . . . . .	54
4.5	Discussion . . . . .	55
<b>II Modifying GR via variable deformations, action corrections and semiclassical effects</b>		<b>58</b>
<b>5</b>	<b>Hamiltonian consistency of the gravitational constraint algebra under deformations</b>	<b>59</b>
5.1	Transforming the action from its canonical variables . . . . .	62
5.1.1	Transformations into theories with second-order equations of motion	62
5.1.2	Transformations into higher-order theories . . . . .	64
5.2	Review of Hamiltonian general relativity and the gauge algebra . . . . .	67
5.3	Deforming canonical general relativity . . . . .	74
5.3.1	Lovelock's theorem . . . . .	74
5.3.2	Deforming GR by introducing extra degrees of freedom . . . . .	76
5.3.3	Further constraints in the deformations . . . . .	83
5.4	Deforming general relativity in tetrad theory and Ashtekar variables . . . .	84
5.5	Discussion . . . . .	92
<b>6</b>	<b>Unscreening scalarons with a black hole</b>	<b>94</b>
6.1	Matter distribution for spherically symmetric black holes . . . . .	95
6.2	Scalar accretion in $f(R)$ theories . . . . .	97
6.2.1	Chameleons in Starobinsky and Hu-Sawicki model . . . . .	98
6.2.2	Accreting chameleons in Hu-Sawicki and Starobinsky models . . . .	100
6.3	Resolving curvature singularities in $f(R)$ theories . . . . .	107
6.4	Scalar accretion for the symmetron model . . . . .	109
6.4.1	Action and equations of motion . . . . .	109
6.4.2	Accreting symmetrons . . . . .	111
6.5	Accretion of the Ratra-Peebles chameleons . . . . .	112
6.5.1	Equations of motion and setup . . . . .	112
6.5.2	Accreting chameleons . . . . .	115
6.6	Discussion . . . . .	118
<b>7</b>	<b>Echoes from the scattering of wavepackets on wormholes</b>	<b>119</b>
7.1	Scattering of scalar wavepackets . . . . .	121
7.1.1	Scattering by a Schwarzschild black hole . . . . .	121
7.1.2	Scattering by a traversable wormhole . . . . .	125
7.2	Scattering of tensor wavepackets . . . . .	131

7.3	Echoes and gravitational wave polarimetry . . . . .	138
7.4	Discussion . . . . .	139
<b>8</b>	<b>Concluding remarks</b>	<b>140</b>
	<b>Bibliography</b>	<b>145</b>
	<b>Appendix A Deviations of <math>n_s</math> and <math>r</math> from the slow-roll expressions</b>	<b>160</b>
	<b>Appendix B Decomposition scheme in a curved field space</b>	<b>162</b>
	<b>Appendix C Plotting two-point correlation functions</b>	<b>164</b>
	<b>Appendix D Power spectra in the Ijjas-Steinhardt bounce</b>	<b>166</b>
	D.1 Setting up the equations of motion and initial conditions . . . . .	166
	D.2 Evolution of the mode amplitudes and length scales . . . . .	169
	<b>Appendix E Numerical setup for scalar accretion and scattering</b>	<b>174</b>
	E.1 Scalar field equations of motion . . . . .	174
	E.2 Absorbing boundary conditions . . . . .	175
	E.3 Spectral basis . . . . .	176
	E.4 Gauss-Legendre integrator . . . . .	177
	E.5 Static solver . . . . .	178
	E.6 Inverting tortoise coordinate . . . . .	178

# List of Tables

Table 5.1	The various ways to decompose the tensorial structure of the new degree of freedom $J_{ab}$ . . . . .	81
-----------	---	----



# List of Figures

Figure 1.1	Cosmic Microwave Background (CMB) obtained by the Planck Mission. . . . .	3
Figure 1.2	Features of the gravitational wave profile . . . . .	7
Figure 2.1	Constant-Roll potential and phase space for the background. . . . .	12
Figure 2.2	Evolution of scalar and tensor fluctuations in Constant-Roll Inflation	13
Figure 2.3	Power spectrum of scalar curvature and tensor fluctuations in Constant-Roll Inflation. . . . .	15
Figure 2.4	Injection scheme for the scalar and tensor modes for Constant-Roll Inflation. . . . .	17
Figure 2.5	Scanning the model parameters in the potential at $N_* = 0, 30, 60, 80$ .	18
Figure 2.6	Different projections of the joint probability distribution from Planck 2015 posterior for Constant-Roll Inflation . . . . .	19
Figure 2.7	Constraints for the Constant-Roll model parameters from joint Planck 2015/BKP likelihood on $n_s$ and $r$ . . . . .	21
Figure 3.1	Schematic representation of the Cholesky gauge separation. . . . .	27
Figure 3.2	Phase space projections for the double $\lambda\phi^4$ model. . . . .	29
Figure 3.3	Projected surface of initial conditions. . . . .	30
Figure 3.4	Mode injection scheme for the double $\lambda\phi^4$ model. . . . .	32
Figure 3.5	Gauge condition $\langle \hat{\chi}_A, \hat{\chi}_B \rangle = \delta_{AB}$ at all times. . . . .	33
Figure 3.6	Verifying the final gauge condition in (3.14). . . . .	33
Figure 3.7	Suppressed oscillation scale in a mode injected at $k_1 = e^{10} k_{\text{phys}}$ . . .	34
Figure 3.8	$\langle \Phi_1, \Phi_1 \rangle$ correlator obtained after injecting modes from two different physical length scales. . . . .	35
Figure 3.9	Components of Cholesky modes inserted at $N = 10$ and $N = 50$ . . .	36
Figure 3.10	Evolution of $\langle \zeta_{\mathbf{k}}^2 \rangle$ . . . . .	37
Figure 4.1	Evolution of the first coefficients in the quadratic action (4.21) for the scalar perturbations. . . . .	47
Figure 4.2	Evolution of the second coefficients in the quadratic action (4.21) for scalar perturbations. . . . .	48

Figure 4.3	Different side views of the phase space hypersurface given by the first Friedmann equation. . . . .	54
Figure 4.4	Phase space for the system defined by (4.1) and (4.48), (4.49). . . . .	57
Figure 5.1	Canonical mapping between $S_1$ and $S_2$ in its Lagrangian and Hamiltonian versions. . . . .	63
Figure 5.2	Mapping between $S_1$ and the higher-derivative theory in $S_2$ , in its Lagrangian and Hamiltonian versions. . . . .	65
Figure 5.3	Gauge fixing by the intersection with the surface $\Sigma$ as the scalar and vector constraint evolve. . . . .	73
Figure 5.4	Depiction of deformation of variables . . . . .	77
Figure 6.1	Scalaron potentials of the Hu-Sawicki and Starobinsky models. . . . .	100
Figure 6.2	Accretion of the field in the Starobinsky and Hu-Sawicki models in tortoise coordinates. . . . .	101
Figure 6.3	Static profiles of the scalar field in the Starobinsky model for varying $\lambda$ and $n$ . . . . .	103
Figure 6.4	Static profiles of the scalar field in the Starobinsky model for $n = 1$ and varying density contrast $\sigma$ . . . . .	104
Figure 6.5	Static profiles of the scalar field in the Hu-Sawicki model for varying $\alpha$ and varying $n$ . . . . .	105
Figure 6.6	Static profiles of the scalar field in the Hu-Sawicki model for $n = 1$ and varying density contrast $\sigma$ . . . . .	105
Figure 6.7	Scalar field flux accreting towards horizon in the Starobinsky and in the Hu-Sawicki models. . . . .	106
Figure 6.8	Consistency check for local scalaron equilibrium in fully screened configuration with $\sigma = 0.5$ in the Hu-Sawicki model. . . . .	106
Figure 6.9	Formation of a naked singularities in the Starobinsky and Hu-Sawicki models. . . . .	107
Figure 6.10	Dynamical resolution of curvature singularities. . . . .	108
Figure 6.11	Effective potential of the symmetron model. . . . .	110
Figure 6.12	Evolution of the symmetron field for two sets of model parameters in tortoise coordinates. . . . .	111
Figure 6.13	Scalar field flux in the symmetron field evolution. . . . .	113
Figure 6.14	Static solutions of the symmetron for different values of $\mu$ and $\lambda$ . . . . .	113
Figure 6.15	Static field profiles for different values of $\sigma$ in the symmetron model. . . . .	114
Figure 6.16	Evolution of the Ratra-Peebles chameleon for $n = 1$ and its flux. . . . .	115
Figure 6.17	Effective potential for the Ratra-Peebles chameleon. . . . .	116
Figure 6.18	Static solutions of the chameleon field for different values of $\gamma$ and $n$ . . . . .	117
Figure 6.19	Field profiles for different values of $\sigma$ in the chameleon model. . . . .	117

Figure 7.1	Effective potential for the spherical modes $\mathcal{U}_{20}^{\text{bh}}(x, t)$ scattered by a Schwarzschild black hole. . . . .	121
Figure 7.2	Dispersion of the incident Gaussian wavepacket $\mathcal{U}_{20}^{\text{bh}}$ . . . . .	123
Figure 7.3	Asymptotic solution for the quadrupole mode $\mathcal{U}_{20}^{\text{bh}}(x, t)$ . . . . .	124
Figure 7.4	Reflection and transmission coefficients of the cavity as functions of frequency. . . . .	124
Figure 7.5	Schematic depiction of a Misner-Thorne wormhole . . . . .	125
Figure 7.6	Effective potential cavity for the wormhole. . . . .	125
Figure 7.7	Schematic reconstruction of the outgoing solution by the geometrical optics approximation. . . . .	126
Figure 7.8	Evolution of the quadrupole mode $\mathcal{U}_{20}$ and the scalar flux. . . . .	127
Figure 7.9	Asymptotic evolution of the quadrupole mode $\mathcal{U}_{20}$ for different values of $\sigma$ . . . . .	129
Figure 7.10	Comparing the geometrical optics approximation with the Fourier transform of the full asymptotic solution. . . . .	130
Figure 7.11	Amplitudes of the first four echoes as a function of $\sigma$ for $\ell = 2$ . . . . .	131
Figure 7.12	Regge-Wheeler and Zerilli potentials. . . . .	132
Figure 7.13	Asymptotic solution of $\Psi_{20}^{\text{odd}}$ considering an incident wavepacket with $\sigma = 0.9185r_g$ and $\sigma = 5.196r_g$ . . . . .	134
Figure 7.14	Evolution of $\Psi^{\text{odd}}$ for an ingoing Gaussian pulse with $\sigma = 0.9185r_g$ . . . . .	135
Figure 7.15	Reflection and transmission coefficients for the Regge-Wheeler cavity and the geometrical optics approximation. . . . .	136
Figure 7.16	Amplitudes and relative ratios of the first four echoes of $\Psi_{20}^{\text{odd}}$ as a function of $\sigma$ . . . . .	137
Figure 7.17	Dispersion of a Gaussian wavepacket by a Morris-Thorne wormhole with a longer throat. . . . .	137
Figure 7.18	Polarimetry of gravitational waves. . . . .	138
Figure A.1	Testing the consistency relations in (A.2) and (A.1). . . . .	161
Figure C.1	Two-point correlators for different model parameters. . . . .	165
Figure D.1	Evolution of three different scalar and tensor wavelengths and the sound/light horizons. . . . .	167
Figure D.2	Evolution of the effective scalar and tensor mode frequencies at different physical wavenumbers. . . . .	169
Figure D.3	Evolution of scalar and tensor mode amplitudes . . . . .	170
Figure D.4	Scalar and tensor power spectrum at various instants. . . . .	171
Figure D.5	Evolution of the occupation numbers $n_{\mathbf{k}}(t)$ of the scalar mode at various times. . . . .	172

# Chapter 1

## Introduction

*“Effective field theories can be loved or hated, but should always be used”*

*Clifford Burgess, at Testing Gravity 2017*

The need of the notion of effective field theory (EFT) emerges from a simple fact: a scale-invariant theory can not solely model our understanding of physical reality in the current energy regime. It is, therefore, necessary to evaluate the ways in which all magnitudes in a given action vary with respect to the energy scales of a dynamical system. The study of EFTs in both astrophysical and cosmological scales is motivated by the behavior of matter and gravity in both regimes: from the absence of a healthy ultraviolet completion leading to a final quantum theory of gravity to the intriguing existence of Dark Energy and Dark Matter at large scales. Although each of the chapters of this thesis corresponds is devoted to a specific EFT, with different content of degrees of freedom and dynamical features; we must investigate the viability of each of these realizations as a different limit of a grand unification theory (GUT), finally canvassing all the fundamental interactions of nature in a single scheme.

In order to understand the change of a set of physical parameters, let us start with an entirely classical toy model: suppose that the one-dimensional action of a mechanical system is given by

$$S = \int dt \left[ \frac{\dot{q}^2}{2} - V(q) \right], \quad (1.1)$$

where  $V(q)$  is a potential function of the generalized coordinate  $q$ , such that there exists  $q_{\text{eq}}$  in which the system has an equilibrium point given by  $V^{(1)} \equiv \partial_q V|_{q=q_{\text{eq}}} = 0$  and an effective spring constant  $k \equiv \partial_q^2 V|_{q=q_{\text{eq}}} > 0$ . Furthermore, investigating the dynamics of small deviations  $q - q_{\text{eq}} \equiv \Delta q$  around equilibrium has a similar objective than the well-known methods of mean field theory. For these fluctuations around the equilibrium position, the system can be sufficiently described by

$$S^1 = \frac{1}{2} \int dt \left[ (\Delta \dot{q})^2 - k(\Delta q)^2 \right]. \quad (1.2)$$

It is curious to notice that the form of the harmonic oscillator in this truncated action reflects the state of our current attempts in perturbation theory. Now we introduce a small interaction term  $V_I$ , which modifies the latter action by

$$S_{\text{int}}^1 = \frac{1}{2} \int dt \left\{ [(\Delta\dot{q})^2 - k(\Delta q)^2] - V_I \right\}, \quad (1.3)$$

such that the effective spring constant  $k_* \approx k + V_I^{(2)}$  and the equilibrium position  $q_{\text{eq}}^* \approx q_{\text{eq}} - V_I^{(1)}/k$  have small corrections. The superscript  $(n)$  denotes the  $n$ -th derivative with respect to the canonical coordinate  $q$ . What happens if after increasing the overall energy scale in the system, the amplitude of oscillations also increases? In that case, the second order expansion will not be sufficient to describe oscillations around an equilibrium point (in general, the equilibrium position calculated from (1.3) will not coincide with  $q_{\text{eq}}$ ). Assuming we can truncate the action to the next order, the action for the 1D system now will be given by

$$S_I^{\text{new}} = \int dt \left\{ \frac{1}{2} [(\Delta\dot{q})^2 - k(\Delta q)^2] - \frac{V^{(3)}}{6} (\Delta q)^3 - V_I \right\}. \quad (1.4)$$

The new truncated effective potential  $V_{\text{new}}$  is given by

$$V_{\text{new}} = \frac{k}{2} (\Delta q)^2 + \frac{V^{(3)}}{6} (\Delta q)^3 + V_I, \quad (1.5)$$

There is not a unique solution yielding the equilibrium position in this case. Thus, after choosing an adequate branch, the equilibrium position can be found after finding  $q_{\text{eq}}^{**}$  such that  $\partial_q V_{\text{new}} = 0$  and the new effective spring constant from  $k_{**} \equiv \partial_q^2 V_{\text{new}}|_{q_{\text{eq}}^{**}}$ . We observe that both quantities will be shifted again

$$q_{\text{eq}}^{**} \approx q_{\text{eq}} - \frac{k}{V^{(3)}} + \sqrt{\left(\frac{k}{V^{(3)}}\right)^2 - \frac{2V_I^{(1)}}{k}}, \quad (1.6)$$

$$k_{**} \approx k \sqrt{1 - \frac{2V_I^{(1)}}{k} (V^{(3)})^2} + V_I^{(2)}. \quad (1.7)$$

The relative strength of the interaction compared to last two terms in the potential shown in (1.4), plays a fundamental role to determine how significant the corrections are to both quantities. With respect to the new variables and all the corrections reabsorbed, it is viable to rewrite the action in (1.4) as

$$S_I^{\text{new}} = \frac{1}{2} \int dt \left[ (\Delta\dot{q}^{\text{new}})^2 - k_{**} (\Delta q^{\text{new}})^2 \right], \quad (1.8)$$

where  $\Delta q^{\text{new}} \equiv q - q_{\text{new}}^{**}$ . The latter expression in (1.8) is a valid truncation of the effective action, useful to represent the dynamics of small perturbations around the new equilibrium point and a new effective spring constant. We learn a few lessons from this exercise:

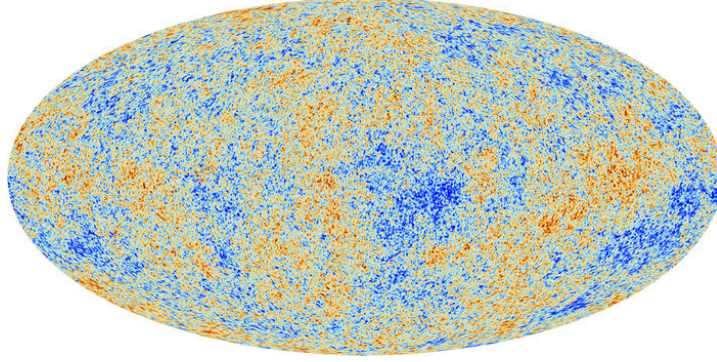


Figure 1.1: Cosmic Microwave Background (CMB) obtained by the Planck Mission [6, 10, 9]. Initial conditions are given by the spectrum of scalar curvature and tensor fluctuations after solving for the background and perturbations of (1.10). The spectrum is clear evidence of the early homogeneity in the early universe since each red/blue spot represents a deviation of one part in  $10^5$  from a blackbody background of  $3K$ .

- It is possible to describe the dynamics of the system by the standard methods of Classical Mechanics (i.e., finding equations of motion and their symmetries) after considering that all the coupling parameters depend on both the strength of external interactions and the relevant terms of the effective potential. In the case we study, the expression in (1.8) is a valid truncation of the effective action for (1.4).
- From all the terms inside the square roots in (1.7), we notice that the extension of this treatment (a simplified version of the bottom-up formalism) to consider potential extra terms is only valid when the interaction terms are small: i.e., in the perturbative regime, where the new spring constant and the equilibrium positions are required to be real numbers.
- Different energy scales will truncate the expansion of the potential up to different powers, the notion of an energy cutoff is crucial to evaluate the range of validity of each distinct realization of an EFT.

In the first part of this thesis, we use a prototypical example of an effective action incorporating gravitational degrees of freedom, the Einstein-Hilbert action

$$\int d^4x \sqrt{-g} \left[ \frac{M_{\text{Pl}}^2}{2} R + \mathcal{L}_{\mathbf{m}}(\phi) \right] \quad (1.9)$$

where  $g \equiv \det(g_{\mu\nu})$ ,  $R$  is the Ricci scalar curvature and  $\mathcal{L}_{\mathbf{m}}(\phi)$  is the matter Lagrangian density. In the same way as in (1.4), perturbations of the geometrical degree of freedom – i.e., the spacetime geometry  $g_{\mu\nu}$  – will only be large enough to alter this action at energy scales above  $M_{\text{Pl}} \equiv 1/\sqrt{8\pi G}$ . In the subsequent sections of this thesis, we use  $c = \hbar = 1$  as our unit convention.

In general, it is natural to think that equilibrium configurations are not restricted to be spacetime-independent solutions as we discussed in the toy model shown in equations (1.3) - (1.8). In part I of this thesis, we study the cosmological observables generated by two specific realizations of a field theory in the context of the early universe such as the inflationary paradigm, in Chapters 2 and 3 and the Ijjas-Steinhardt (IS) bouncing scenario in Chapter 4. We follow the usual perturbative approach in order to describe different regimes of the matter sector. In the inflationary scenarios we describe in this thesis, the effective action for a model with  $\mathcal{N}$  scalar degrees of freedom is given by

$$S = \int d^4x \sqrt{-g} \left( \frac{M_{\text{Pl}}^2}{2} R - \frac{1}{2} \partial_\mu \phi_A \partial^\mu \phi_A - V(\phi_A) \right), \quad (1.10)$$

where  $A \in [1; \mathcal{N}]$ . Each one of the fields is decomposed by  $\phi^A(\mathbf{x}, t) = \phi^A(t) + \delta\phi^A(\mathbf{x}, t)$ , similar to the generalized coordinate separation leading to (1.3) and (1.8). As we will briefly see, this decomposition is motivated by the dynamical properties of the inflationary phase, resulting in the small power of anisotropies, sourced by spacetime dependent quantum fluctuations  $\delta\phi^A(\mathbf{x}, t)$ , and Boltzmann transported to the Cosmic Microwave Background (CMB), as depicted in Figure 1.1<sup>1</sup>. Here the evolution of the background is used to find a nearly scale-invariant power spectrum of scalar and tensor fluctuations, which serve as initial conditions for the CMB spectrum. In Chapters 2 and 3, we solve both the background and fluctuations for single-field models like Constant-Roll Inflation, and multifield models such as double  $\lambda\phi^4$  and  $(m_1\phi^2 + m_2\sigma^2)$ . After noticing that the rapidly and slowly oscillating scales can be separated [116], our results are implemented to create efficient evolution routines and provide constraints on the model parameters for many inflationary models [113].

In Chapter 4, we explore another form of the effective Lagrangian

$$S = \frac{1}{2} \int d^4x \sqrt{-g} \left[ M_{\text{Pl}}^2 R + \left( 2k(\phi) (\partial\phi)^2 + q(\phi) (\partial\phi)^4 + (\partial\phi)^2 \square\phi \right) \right], \quad (1.11)$$

where  $\square \equiv g^{\alpha\beta} \nabla_\alpha \nabla_\beta$  is the four-dimensional d'Alembertian in a curved geometry. The perturbations of the field act on the field derivatives instead of creating extra terms in the potential. Both the background and fluctuations still follow second-order equations of motion, even when the Lagrangian depends on second derivatives. Our results in this section put serious constraints on the ultraviolet (UV) completion of the theory: the setup of the model yields superluminal propagation of scalar curvature perturbations results in negative cross sections for diverse processes at tree level, i.e., at the first-order in diagrammatic expansion [7]. Moreover, we find that the stable expansion history suggested by Ijjas

<sup>1</sup><https://www.cosmos.esa.int/web/planck/picture-gallery>

and Steinhardt [139] is a separatrix in phase space [85]. In appendix D, we show that the spectrum of scalar and tensor fluctuations is not scale-invariant, as required to provide a consistent CMB spectrum. The latter calculations were performed using the same separation techniques explained in detail in sections 2 and 3, proving that the range of validity of our method goes beyond the inflationary setup.

In the second part of this thesis, we study modifications of the effective action in the gravitational degrees of freedom. In Chapter 5, we modify two forms of the gravitational effective action: the Einstein-Hilbert action shown in (1.9), now choosing the 3D geometry  $h_{ab}$  as the canonical coordinate and its Lie derivative  $\mathcal{L}_t h_{ab}$  to span the whole configuration space, and the tetrad-Palatini action

$$S_{\text{tp}} = \frac{1}{2} \int d^4x \epsilon_{IJKL} \epsilon^{\mu\nu\rho\sigma} e^I{}_\mu e^J{}_\nu F^KL{}_{\rho\sigma}. \quad (1.12)$$

Here  $e$  is a tetrad with greek indices from Lorentz symmetry, and the capital indices label the generators of the  $so(1,3)$  algebra.  $F^KL{}_{\rho\sigma}$  is the field-strength tensor (which is very similar to the Yang-Mills field-strength tensor) of the potential  $\omega^{JK}{}_\nu$ , so for this action the corresponding pair of variables is  $(e^I{}_\mu, \omega^{JK}{}_\nu)$ . In both cases, the action is modified by deforming the canonical gravitational variables via the introduction of field fluctuations in a similar way to the toy model. Nonetheless, the ‘‘oscillations’’ around the time-dependent equilibrium variables now are explicitly dependent on the canonical coordinates and their derivatives. The resulting deformed action might thus represent a higher-derivative theory of gravity. In addition to this, holonomy corrections provide a physical motivation to deform the canonical variables of the tetrad-Palatini action in order to find the first semi-classical corrections from Loop Quantum Gravity. The objective of this chapter is to show that the deformed theories can retain diffeomorphism invariance by introducing new gravitational degrees of freedom, and therefore, bypass Lovelock’s theorem [69], implying that the definition of gauge-invariant quantities is still attainable. Closure of the *algebra* of Hamiltonian constraints provides the analog of the well-known Ward identities, now for the case of diffeomorphic transformations when corrections are introduced at perturbative order [118]. In the language of symplectic manifolds, the punchline of Chapter 5 can be rephrased as follows: given a  $D$ -dimensional symplectic manifold representing a dynamical system, it is possible to construct at least one other  $(D + 2N)$ -dimensional symplectic manifold, where  $2N < D$ , such that the original manifold is a projection of the one with higher dimensions. The role of the higher derivative terms, corresponding to new degrees of freedom, is to provide the projection map between the two manifolds.

One of the lessons learned after deforming the gravitational action is that the higher derivative actions we obtained can be recast as systems with extra degrees of freedom.



Consequently, in Chapter 6, we explore the dynamics of the extra fields emerging from higher-curvature terms directly introduced in the gravitational action (i.e., not via field deformations)

$$S_{\text{R}} = \int d^4x \sqrt{-g} \left[ \frac{f(R)}{16\pi G} + \mathcal{L}_{\mathbf{m}}(\psi) \right], \quad (1.13)$$

here we introduce a modification of the theory by considering  $f(R)$  to be a function of the Ricci scalar (different than  $R$ ), whose role is similar to the free energy function in thermodynamics considering the curvature as an “order parameter”. In the metric formalism, it can be shown that these theories have an extra scalar degree of freedom living in the trace of the Einstein’s equations, just as written in the Jordan frame (where matter is minimally coupled to the geometry). We study the dynamics of scalar accretion in a spherically symmetric black hole surrounded by a dust-like radial distribution of matter, finding that the time-dependent solution of the scalar converges to a non-trivial static hair configuration. The field is not screened in the region between the event horizon and the innermost stable circular orbit (ISCO), where matter density drops due to relativistic effects [111]. We select two realizations of  $f(R)$  gravity: the Hu-Sawicki [136] and the Starobinsky [229] models with a vanishing bare cosmological constant. For particular choices of the model parameters, we show the formation of naked singularities outside the event horizon in both of these models. Moreover, we still observe the formation of non-divergent curvature cusps after adding corrections to these in the higher curvature regime [21]. In this chapter, we also explore other scalar-tensor theories of gravity, such as the Ratra-Peebles chameleon [206] and the  $\mathbb{Z}_2$  symmetron [132]. In the latter scenario, the convergence to non-trivial scalar hair solutions only occurs for particular choices of the symmetron parameters.

Semiclassical corrections from matter fields can also generate modifications to gravity, it has been argued [181] that those effects might severely alter the structure of cosmological and event horizons. The distortion appears when solving the semiclassical field equations

$$G_{\mu\nu} = 8\pi G \langle \hat{T}_{\mu\nu} \rangle_{\psi}. \quad (1.14)$$

Where  $G_{\mu\nu}$  is the Einstein tensor  $G_{\mu\nu} \equiv R_{\mu\nu} - 1/2 R g_{\mu\nu}$  and  $\langle \hat{T}_{\mu\nu} \rangle_{\psi}$  is the expectation value of the energy-momentum operator at the quantum state  $\psi$ . Recently, there is growing interest in testing the limit in which the corrections to the gravitational field are strong by searching for exotic compact objects (ECOs) at astrophysical scales, looking for configurations such as wormholes, gravastars and firewalls. Due to the recent discovery of gravitational waves (GWs) [2], it has been recently suggested that the detection of a peculiar feature in the gravitational wave signal, showing a series of wavelets after the merger transient (colloquially known as echoes [64], and depicted in Figure 1.2) could be attainable within the next few years. In Chapter 7, we study the scattering dynamics of Gaussian wavepackets of scalar and GW radiation colliding against the most straightforward configuration of an

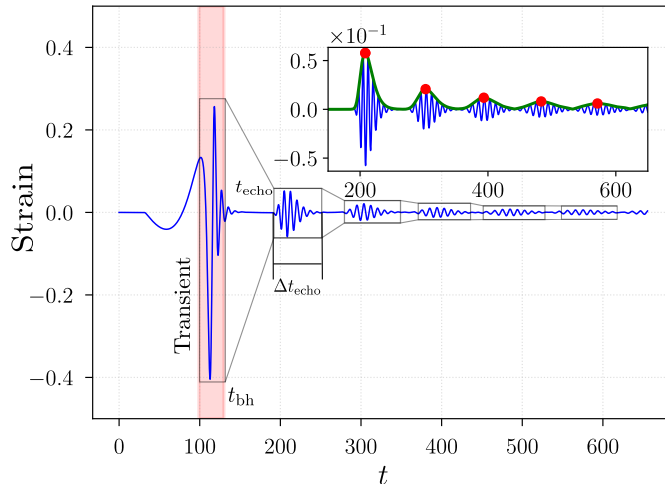


Figure 1.2: Features of the gravitational wave profile from the scattering of gravitational waves by ECOs. The transient is not significantly different from the original black hole signal before  $t_{\text{bh}}$ , at  $t > t_{\text{echo}} + t_{\text{bh}}$  a train of wavelets with decaying amplitude appears as a consequence of successive reflections between the walls of an effective potential cavity. The gray lines roughly represent the envelope of the outgoing pulse,  $A$  is the amplitude of the transient. The exact transient is plotted in green.

ECO, which happens to be a Morris-Thorne wormhole. The outgoing signal for the scattering problem shares many of the features with the full asymptotic signal obtained after the coalescence of ECOs, including the generation of post-transient echoes. We evaluated the evolution of many Gaussian wavelets with different widths and extracted the frequency dependence of the reflectivity and transmissivity coefficients of a fixed effective potential cavity [117]. After evaluating the dynamics of the scattering problem, we found:

- The formation of echoes with significant amplitude in the signal (shown as the red dots in the figure) is not generic: it will be conditioned by the contribution of specific frequencies of the ingoing signal. Such a “sweet spot” in the frequency range corresponds to a particular interval of variances from the ingoing Gaussian pulse.
- The geometrical optics approximation is only sufficient in order to provide the envelope shape of the spectrum for the outgoing signal. Quasinormal mode (QNM) peaks cannot be resolved with this approximation.
- Given an unpolarized ingoing wavepacket, the corresponding reflected signal has a piecewise net polarization.

The range of frequency space where the amplitude of echoes is maximum is determined by the frequency at which reflectivity and transmissivity curves overlap; this overlap frequency corresponds to the characteristic length of the potential cavity. Successive internal collisions with the potential walls provide energy to the QNMs (with frequencies squeezed around the

“sweet spot”) while these modes propagate across the shell  $r = 3M$  and leak energy through the echoes each time an internal reflection occurs. Even when the spectral content of the two polarizations is the same, the effective potentials for even and odd modes are slightly different. Thus, this difference will induce a small net polarization.

The plan of this thesis is as follows: in chapter 2, we present a novel technique to calculate the evolution of scalar and tensor perturbations during the inflationary regime. In particular, we study constant roll inflation in order to parametrize deviations from the slow-roll behavior of inflation. It is interesting to consider that the deviation parameter of this model also determines the scale of symmetry breaking for natural inflation, which is closely related to constant-roll inflation. In chapter 3, we extend the technique developed in the previous section to the case of inflationary models with more than one field. Multifield models of inflation are useful to investigate the delegation of the roles of (a) sourcing accelerated expansion and (b) generating tensor/curvature fluctuations to different fields; in addition to the characterization of the moduli space geometry in theories with higher-symmetry. In chapter 4, we study the viability of an alternative to the inflationary scenario, called the Ijjas-Steinhardt bouncing scenario driven by a cubic galileon, which models an imperfect fluid. In chapter 5, we test the consistency of the constraint algebra under deformations of canonical variables. Our objective is to show that the imposition of the constraint algebra will constrain the space of possible semiclassical corrections of the field variables in a background-independent way. In chapter 6, we investigate the behavior of extra scalar degrees of freedom – dubbed as scalarons – in scalar-tensor theories. In presence of a non-trivial matter profile, observing the formation of scalar “hair” by accreting spherical waves around a black hole. In chapter 7, we study the generation of echoes by the scattering of Gaussian waveforms by a wormhole. We solve the scalar and tensor scattering, showing (i) the dispersive solutions inside and outside the effective potential cavity and (ii) the production of wavelets isolated from the main radiation transient, known as echoes. Our aim is to show that the amplitude of the outgoing echoes is not generically large. To conclude, we present our results and final remarks in chapter 8.

## Part I

# Early Universe Cosmology: Inflationary and bouncing scenarios

## Chapter 2

# Single-field Inflation: observational constraints on Constant-Roll Inflation

The EFT of inflation has been one of the most successful developments since its very first appearance in [228, 220, 126, 167, 16], as its characteristic accelerated expansion solves most of the caveats of standard big bang cosmology. In its most common form, inflation is driven by a scalar degree of freedom rolling slowly down a not very steep potential. Primordial inhomogeneities, from which the actual large-scale structure of the Universe emerges, are generated by quantum fluctuations of the inflaton field.

Throughout the years, a multitude of inflationary models were proposed where the dynamics of the background field is highly overdamped, and the production of scalar and tensor fluctuations can be completely characterized by the so-called slow-roll parameters. Slow roll by itself is not a necessary condition for an inflationary model to be viable, and it is interesting to also explore models which break away from the slow-roll restrictions. Motohashi *et. al.* recently introduced a constant-roll inflation [180, 178] which replaces the usual slow-roll condition with an ansatz that the field rolls at a constant rate, be it slow or not. The model is rather neat as it characterizes the deviation from a slow roll by a single parameter and allows analytic integration of the expansion history and the full scalar field potential reconstruction. The potential driving constant-roll inflation only differs from the one in natural inflation [106] by the addition of a negative cosmological constant (with specially chosen value). The constant-roll rate can be tuned by the period of the potential, which corresponds to the global symmetry breaking scale in natural inflation. In this chapter, we investigate constraints on constant-roll inflation from cosmic microwave background anisotropy data [6, 9, 10, 8].

In previous efforts [178], the confrontation of this model with observational data used the well-known consistency relations between slow-roll and fluctuation spectra parameters [166, 122]. The progress was achieved under the assumption that it is sufficient to know the

exact background solutions to describe the primary features of the perturbation spectra. Even though this assumption is not inconsistent with the data, we find that there are small but noticeable differences if one computes the fluctuation spectra exactly. In our approach we do not impose any slow-roll assumptions and instead just directly evaluate the scalar and tensor power spectra of primordial fluctuations in a sufficiently large sector of the parameter space by numerical integration. This procedure allows us to evaluate deviations from the standard slow-roll approximation of the spectral index  $n_s$  (the slope of the scalar spectrum) and the tensor-to-scalar ratio  $r$  (which is the ratio relating the amplitude of tensor and scalar fluctuations). Achieving this with adequate parameter sampling and high precision throughout the mode evolution can be computationally expensive. We use a single-field version of our general method [116] which separates the fast and slow scales in the mode evolution to exponentially increase efficiency of sub-horizon integration. Our computational method allows us to scan a significant portion of the parameter space quickly and extremely accurately on a personal computer with minimal specifications.

Constant-roll inflation has an uncertainty on the field value where inflation ends, as the potential needs to be cut at some value  $\phi_0$  to exit from inflation. This introduces a third parameter to the model in addition to the mass scale and the roll rate, this parameter and the mass scale turn out to be entirely degenerate as far as fluctuation spectra are concerned. This allows us to set tight constraints on two combinations of the model parameters for constant-roll inflation: one that determines the amplitude of scalar and tensor perturbations (along with the characteristic energy scale where inflation occurs), and the second one which sets the roll rate (and quantifies the deviations from the slow-roll approximation). We also compare constant-roll inflation with other models via estimation of the allowed region on the  $r$  versus  $n_s$  diagram, where each point can be identified with (at least) one choice of the model parameters after the spectrum is evaluated at the pivot scale, which is (approximately) to the wavenumber assigned to the Hubble parameter.

The layout of this chapter is as follows: In section 2.1, we present the model and scan a representative subset of the background phase space in order to determine the expansion history due to each choice of initial conditions. Our exploration of the phase space also includes the attractor formed by converging field trajectories. We describe the dynamics of the scalar and tensor fluctuations in section 2.2, where we discuss the separation technique of scalar and tensor modes into fast and slow components. Additionally, we show our mode injection scheme to calculate the spectra numerically, and compute the representative spectra given a set of arbitrary model parameters. We show that both the scalar and tensor spectra are featureless, and, as a consistency check, we also explicitly show that none of the modes evolve on super-horizon scales. In section 2.3, we use the joint likelihood data from

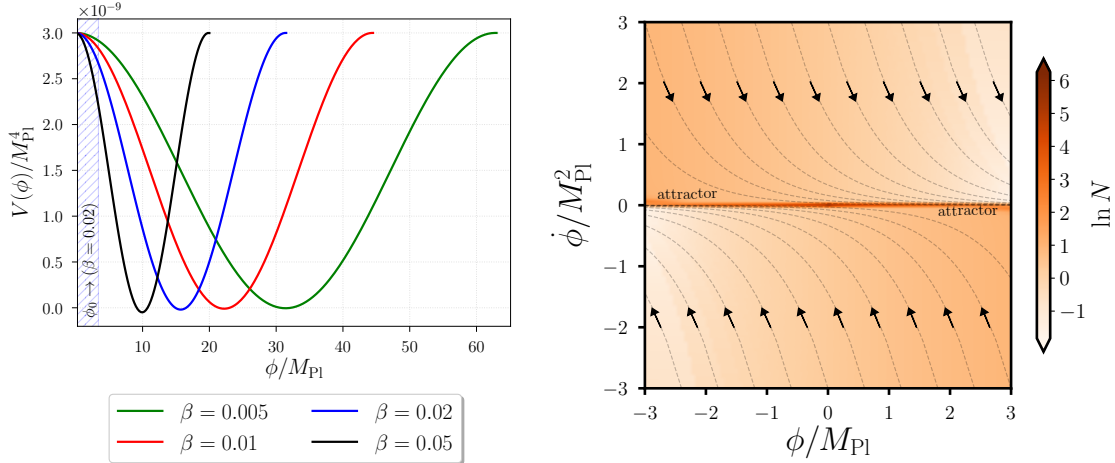


Figure 2.1: Left panel: constant-roll inflation potential (2.4) for the model parameters  $M^2 = 2.0 \times 10^{-9} M_{\text{Pl}}^2$  and different values of  $\beta$ . The region of interest is in the range  $\phi \in (0; \phi_0]$ , shown for the specific value of  $\beta = 0.02$ . Right panel: Map of initial conditions in the phase space for  $M^2 = 2.0 \times 10^{-9} M_{\text{Pl}}^2$ ,  $N_* = 55$  and  $\beta = 0.02$ . The color map represents the number of e-folds before reaching  $\pm\phi_0$ . Phase space trajectories converge as a power-law towards the attractor (instead of exponentially, as is usually the case in slow-roll inflation) as in the case of power-law inflation, which is a particular scenario of the constant-roll model.

Planck 2015 [6, 9, 10] and BICEP2/Keck Array [8] to constrain the constant-roll inflation model parameters<sup>1</sup>. Finally, in section 2.4, we discuss the results and conclude.

## 2.1 Model and background dynamics

In this section, we recite the results in [178] using one of the forms of the potential reconstructed in [180]. These are necessary to provide a full description of the background evolution of this model. The dynamics of the inflaton field minimally coupled to gravity is governed by the single-field version of the action shown in (1.10)

$$S = \int d^4x \sqrt{-g} \left[ \frac{M_{\text{Pl}}^2}{2} R - \frac{1}{2} g^{\mu\nu} \partial_\mu \phi \partial_\nu \phi - V(\phi) \right], \quad (2.1)$$

which has a canonical kinetic term for the scalar field. We will use the signature  $(-, +, +, +)$  throughout the first two chapters of this thesis, and will assume the spatially flat Friedmann-Lemaître-Robertson-Walker metric for background of this first part. The constant-roll inflation potential we use throughout this chapter was derived in [171, 178] after reducing the

<sup>1</sup>We are profoundly aware of the Planck 2018 release [14, 12, 15], however the joint likelihood with BICEP/Keck is not available yet at the time of this writing.

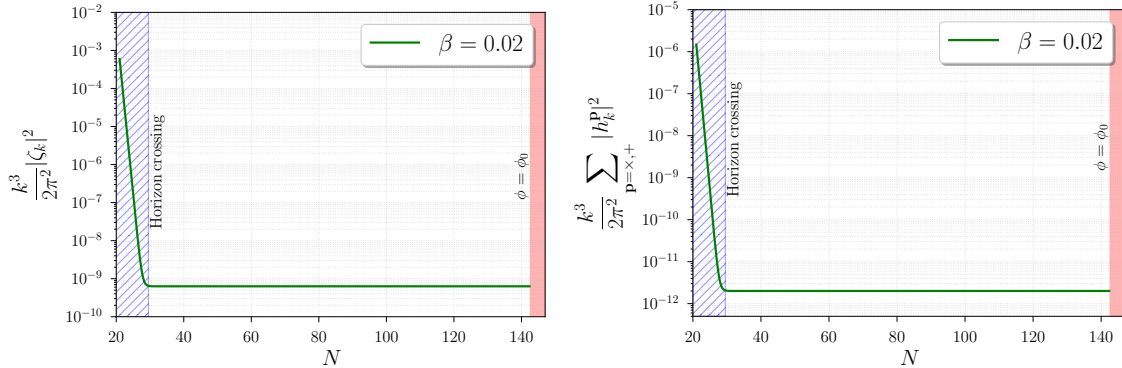


Figure 2.2: Left panel: Example of the evolution of the curvature fluctuations for  $\beta = 0.02$ ,  $N_* = 0$  and  $M^2 = 10^{-11}M_{\text{Pl}}^2$ . Right panel: Evolution of the corresponding sum of the two tensor polarizations for the same model parameters.  $N$  is the number of e-folds from the start of numerical evolution of the background. We show extremely long wavelength modes emerging deep from the sub-horizon scales to demonstrate that there is absolutely no evolution on super-horizon scales in all cases. For this purpose, we picked modes propagating through  $N \sim 100$  e-folds. Such a quantity should not be confused with  $N_*$ , which represents the number of e-folds before the potential becomes zero.

order of the standard background equation of motion

$$\ddot{\phi} + 3H\dot{\phi} + V'(\phi) = 0 \quad (2.2)$$

by the constant-roll ansatz  $\ddot{\phi} = \beta H \dot{\phi}$ .  $H \equiv d \ln a / dt$  is the Hubble scale. The role of  $\beta$  is to parametrize the magnitude of the second time derivative and thus, the deviations from the slow-roll approximation. Using the two Friedmann equations

$$\begin{aligned} 3M_{\text{Pl}}^2 H^2 &= \frac{\dot{\phi}^2}{2} + V(\phi), \\ -2M_{\text{Pl}}^2 \dot{H} &= \dot{\phi}^2, \end{aligned} \quad (2.3)$$

it is possible to find a particular solution for the background evolution and reconstruct the constant-roll inflation potential  $V(\phi)$ , which turns out to be

$$V(\phi) = 3M_{\text{Pl}}^2 M^2 \left[ 1 - \frac{3 + \beta}{6} \left\{ 1 - \cos \left( \frac{\sqrt{2\beta}\phi}{M_{\text{Pl}}} \right) \right\} \right]. \quad (2.4)$$

The shape of the potential is illustrated in the left panel of Figure 2.1 and evaluated at different values of  $\beta$ . The mass  $M$  determines both the energy scale at which inflation occurs and the amplitude of the primordial fluctuations. The potential (2.4) can become negative, and must be cut off somewhere before that to exit the inflation gracefully.



In the absence of an inherent point on the potential where inflation ends, it is important to explicitly specify the field range where we will evaluate the curvature and tensor fluctuations. The background field evolution proceeds from arbitrarily small values to some upper bound  $\phi_0$  where potential is modified and inflation ends. The model presents two practical issues (a) the limit for slow-roll parameter  $\epsilon \rightarrow 1$  cannot be used as a flag to parametrize the end of inflation, and (b) the end of inflation is not well-determined. Therefore, we need evaluate the end of inflationary phase to be  $N_*$  e-folds before reaching the critical point where  $V = 0$  in the unmodified potential (2.4), and evaluate  $N_*$  as an extra parameter. This range depends on the model parameters and is illustrated in the left panel of Figure 2.1, where  $\phi_0$  can be calculated as

$$\phi_0 = \sqrt{\frac{2}{\beta}} \arcsin \left[ e^{-N_*\beta} \sin \left\{ \frac{1}{2} \arccos \left( \frac{\beta - 3}{\beta + 3} \right) \right\} \right]. \quad (2.5)$$

We note that  $\phi_0$  is independent of  $M$ . Thus, the model has three parameters, namely  $M$ ,  $\beta$  and  $N_*$ . It is clear that  $N_*$  and  $M$  are degenerate since amplitude of scalar fluctuations can be changed by either a shift in the energy scale of the potential, or by moving the endpoint  $\phi_0$  closer or further from  $\phi = 0$  where potential is flat, up to the value where  $V = 0$ .

Using the equations of motion for the field (2.2) and the Hubble scale (2.3), we scan the phase space in order to find the number of e-folds for every choice of initial conditions inside the interval  $\phi/M_{\text{Pl}} \in [-3; 3]$  and  $\dot{\phi}/M_{\text{Pl}}^2 \in [-3; 3]$ . Our results are shown in the right panel of Figure 2.1 for  $M^2 = 2.0 \times 10^{-9} M_{\text{Pl}}^2$ ,  $N_* = 55$  and  $\beta = 0.02$ , where  $\phi_0 = 3.38$  corresponds to our choice for  $\beta$ . A few phase space trajectories are also plotted in the same figure. A choice of initial conditions close to the attractor (with  $\dot{\phi}$  small in this case) generates more expansion before reaching  $\pm\phi_0$  due to a slow convergence to the attractor of the trajectories starting away from this attractor. We take  $\dot{\phi} = 0$  as a suitable initial condition for the background field velocity that always reaches the attractor, and start numerical evolution of the background sufficiently far in the past for the trajectory to settle to the attractor before considering fluctuations.

## 2.2 Perturbations

In this section, we recount the standard treatment of scalar and tensor perturbations required to obtain the power spectra of primordial fluctuations, and describe an extremely effective way to do so numerically. Let us first recall the expansion of the action (2.1) up to second order in perturbations

$$S_2 = \int a^2 d\eta d^3x \left\{ \frac{M_{\text{Pl}}^2}{8} \left[ h'_{ij} h'^{ij} - (\nabla_k h_{ij})(\nabla^k h^{ij}) \right] + \frac{\phi'^2}{2H^2} \left[ \zeta'^2 - (\nabla_i \zeta)(\nabla^i \zeta) \right] \right\}, \quad (2.6)$$

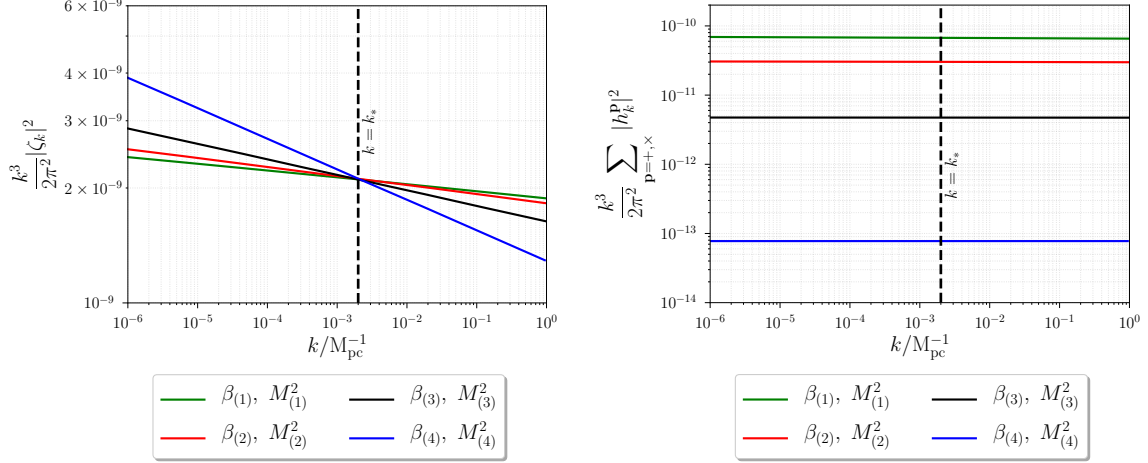


Figure 2.3: Left panel: Power spectrum of primordial curvature fluctuations using  $k_* = 2 \times 10^{-3} M_{\text{pc}}^{-1}$  as a pivot scale at  $N_* = 0$ . We considered the model parameters  $\beta_{(1)} = 0.005$ ,  $M_{(1)}^2 = 4.77 \times 10^{-11} M_{\text{Pl}}^2$ ,  $\beta_{(2)} = 0.01$ ,  $M_{(2)}^2 = 1.63 \times 10^{-10} M_{\text{Pl}}^2$ ,  $\beta_{(3)} = 0.02$ ,  $M_{(3)}^2 = 2.35 \times 10^{-11} M_{\text{Pl}}^2$ ,  $\beta_{(4)} = 0.04$  and  $M_{(4)}^2 = 3.82 \times 10^{-13} M_{\text{Pl}}^2$ . Right panel: Power spectrum of tensor perturbations for the same model parameters. None of the spectra show any features, such as changes in the slope or oscillations.

which is written in the gauge  $\delta\phi = 0$  and in conformal time  $\eta$ . Latin indices are raised and lowered by the Kronecker delta. In terms of the polarization modes  $h_{ij} \equiv \sum_{\mathbf{p}=+,\times} h^{\mathbf{p}} \sigma_{ij}^{\mathbf{p}}$ , and the scalar curvature fluctuations  $\zeta^2$ , the last expression is equivalent to

$$S_2 = \int a^2 d\eta d^3x \left\{ \frac{M_{\text{Pl}}^2}{8} \sum_{\mathbf{p}=+,\times} \left[ (h^{\mathbf{p}'})^2 - (\nabla_k h^{\mathbf{p}})(\nabla^k h^{\mathbf{p}}) \right] + \frac{\phi'^2}{2H^2} \left[ \zeta'^2 - (\nabla_i \zeta)(\nabla^i \zeta) \right] \right\}, \quad (2.7)$$

where we used the fact that  $\text{tr}(\sigma^+)^2 = \text{tr}(\sigma^\times)^2 = 1$  and  $\text{tr}(\sigma^+ \sigma^\times) = 0$ . Now, we introduce the Mukhanov-Sasaki variables  $v \equiv \phi'/H \zeta$  and  $v^{\mathbf{p}} \equiv a M_{\text{Pl}} h^{\mathbf{p}}/2$  [184, 218, 183] to rewrite the action as

$$S_2 = \frac{1}{2} \sum_{\mathbf{p}=+,\times} \int d\eta d^3x \left[ (v^{\mathbf{p}'})^2 - (\nabla_k v^{\mathbf{p}})(\nabla^k v^{\mathbf{p}}) + \frac{a''}{a} (v^{\mathbf{p}})^2 \right] + \frac{1}{2} \int d\eta d^3x \left[ v'^2 - (\nabla_i v)(\nabla^i v) + \frac{z''}{z} v^2 \right],$$

${}^2 h_{ij}$  is the spatial part of  $g_{\mu\nu}$  and  $\zeta$  is the three-dimensional Ricci scalar  $R^{(3)}$ , built from  $h_{ij}$ .

where  $z \equiv \phi'/\sqrt{2}M_{\text{Pl}}H$ . Hence, the action for perturbations is now canonically normalized. In Fourier space, the equations of motion for fluctuations are given by

$$v_k'' + \left(k^2 - \frac{z''}{z}\right)v_k = 0, \quad (2.8)$$

$$(v_k^{\text{P}})'' + \left(k^2 - \frac{a''}{a}\right)v_k^{\text{P}} = 0, \quad (2.9)$$

where the Fourier transformed Mukhanov-Sasaki variables are  $v_k \equiv \phi'/H \zeta_k$  and  $v_k^{\text{P}} \equiv aM_{\text{Pl}} h_k^{\text{P}}/2$ . Both (2.8) and (2.9) have the form of an harmonic oscillator with time-dependent frequency

$$\xi_k'' + \omega_{\text{eff}}^2(\eta)\xi_k = 0. \quad (2.10)$$

where  $\xi$  plays the same role as  $v_k$  or  $v_k^{\text{P}}$ . We will now apply a trick which is effective for numerical evaluation of the perturbation spectra, which is the single-field version of the general method developed in the following chapter [116]. The fluctuation variable  $\xi_k$  can be redefined in terms of real amplitude  $L_k$  and phase  $\Theta_k$  as  $\xi_k \equiv L_k \exp(i\Theta_k)$ . Substituting this ansatz into (2.10) splits the differential equation into real and imaginary parts

$$L_k'' + [\omega_{\text{eff}}^2(\eta) - (\Theta_k')^2] L_k = 0, \quad (2.11)$$

$$\Theta_k'' + 2\frac{L_k'}{L_k} \Theta_k' = 0, \quad (2.12)$$

where the imaginary part (2.12) is separable and has a simple analytic solution  $\Theta_k'(\eta) = \Theta_k'(\eta_0)L_k^2(\eta_0)/L_k^2(\eta)$ . Once the phase is eliminated from (2.11), we obtain

$$L_k'' + \left[\omega_{\text{eff}}^2(\eta) - \omega_{\text{eff}}^2(\eta_0)\frac{L_k^4(\eta_0)}{L_k^4(\eta)}\right] L_k = 0, \quad (2.13)$$

where the Bunch-Davies vacuum deep inside the horizon at  $\eta = \eta_0$  sets  $\Theta_k'(\eta_0) = \omega_{\text{eff}}(\eta_0)$ ,  $L_k = 1/\sqrt{2\omega_{\text{eff}}}$ , and  $L_k'(\eta_0) = 0$  as initial conditions for mode evolution. The key observation is that the last term in (2.13) cancels the effective mode oscillation frequency, allowing numerical evolution to keep track of changes in amplitude only, with precision increasing deep inside the horizon where the vacuum state is more accurate. One no longer needs to resolve exponentially large physical oscillation scale ( $k/a$ ) inside horizon, and can use a time step merely a fraction of the Hubble scale to resolve the evolution of the amplitudes without compromising the precision of the evolution routine. Concretely, the time step needed to resolve (2.13) is two orders of magnitude larger than the necessary to resolve (2.8) or (2.9). The latter expression is also known as the Ermakov-Pinney equation (see [98, 195, 143] for further details). The implementation of this technique in equations (2.8) and (2.9) allowed us to calculate the evolution of the scalar curvature and the tensor fluctuations to high precision, as shown in the two panels of Figure 2.2. We can evaluate the power spectra of

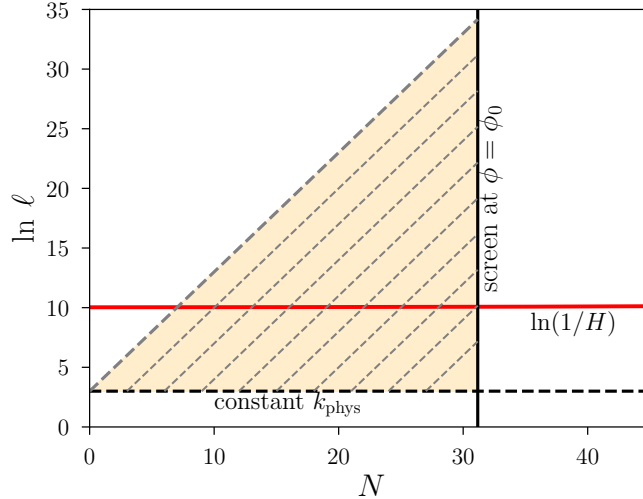


Figure 2.4: Injection scheme for the scalar and tensor modes. Evolution of the modes, along the gray lines, begins at a surface of initial conditions deep inside the horizon, with modes injected at constant physical scale  $k_{\text{phys}}$ . The evolution ends at  $\phi = \phi_0$ , denoted with a vertical black line (a screen) where the spectrum is collected.

scalar and tensor perturbations once we compute the evolution of the scalar and tensor modes for relevant wavenumbers. As an illustration, we calculated the spectra for several sets of the model parameters choosing  $k_* = 2 \times 10^{-3} M_{\text{pc}}^{-1}$  in inverse megaparsecs ( $M_{\text{pc}}^{-1}$ ) as a pivot scale in Figure 2.3. The most striking fact to observe in both panels is the absence of any features or running in the spectra including  $\beta = 0.02$ , as it was argued in [178]. This can be checked for any number of the modes used to produce each of the spectra. Thus, the estimations made in that paper about the shape of the spectrum, in analogy with the approximate treatment for natural inflation (see [107] for further details) are perfectly valid. Nevertheless, we can increase accuracy of the parameter estimation (especially away from the slow-roll regime) by calculating the power spectra directly for each of the model realizations.

To further improve the efficiency of our calculations in Figure 2.3, we use the approximate time-translational symmetry of the Bunch-Davies vacuum deep inside the horizon, and only keep track of the physical wavelengths we are interested in. Scalar and tensor modes are evolved from a constant physical length scale  $10^3$  times smaller than the horizon and then collected at moment of time when  $\phi = \phi_0$  as shown in the mode injection scheme depicted in Fig 2.4. The length scale  $1/H$  where the modes freeze out is plotted in red. Comoving modes evolve from  $\lambda_{\text{phys}} = 10^{-3}/H$  across the physical length scale  $\ell$  following the lines of constant comoving wavenumber (which have a slope of 1) until they reach the screen at  $\phi = \phi_0$ , where the mode amplitudes and the power spectra are evaluated. We can safely omit the evolution of the modes at physical scales shorter than injection point  $k_{\text{phys}}$  (below the orange triangle) as the vacuum is essentially stationary there.

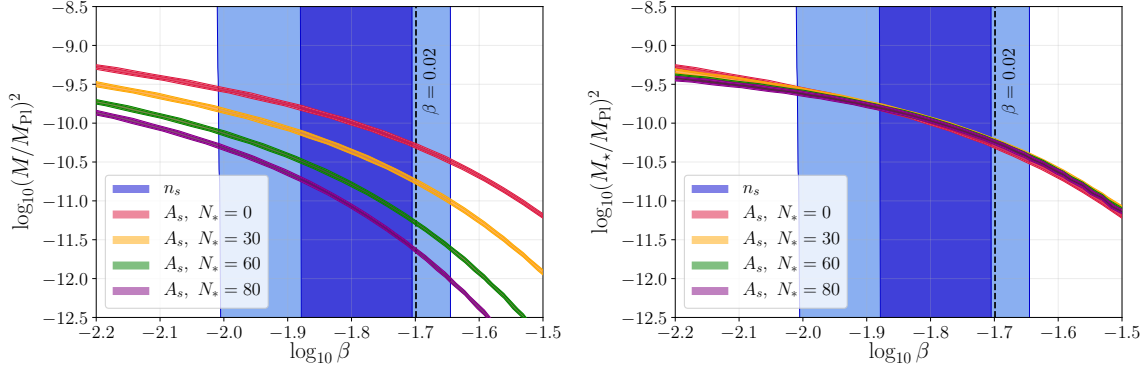


Figure 2.5: Scanning the parameters in the potential at  $N_* = 0, 30, 60, 80$ . The blue regions show the 68% C.L. (solid blue) and 95% C.L. (shaded blue) regions for the marginalized posterior probability of the scalar spectral index  $n_s$ , while the regions for the marginalized posterior of the scalar primordial amplitude  $A_s$  are plotted in different colors. On the left panel we can see the degeneracy of  $N_*$  and  $M^2$  with respect to the amplitude. The right panel shows that the degeneracy is resolved fairly well when we use  $M_*$  defined in Eq. (2.15) instead of  $M$ . The black dashed lines in both panels represent the estimate of the optimal  $\beta$  computed in [178]

### 2.3 Planck constraints

In this section we use the cosmic microwave background (CMB) anisotropy measurements from the Planck satellite [6, 9, 10] and their joint analysis with the BICEP2/Keck Array [8] to derive the constraints on the model parameters  $\beta$  and  $M^2$  for a fixed value of  $N_*$ , due to the degeneracy mentioned in Sect. 2.1. To deal with this degeneracy one can proceed in two ways. Either we fix  $N_*$  to some arbitrary value and we constrain  $M$  for that choice, or we can combine the two variables  $M$  and  $N_*$  into one that parametrizes the degeneracy. We choose the latter and to find the combination of the two parameters we work in the following way. In the exact slow roll approximation we have, for  $N_*$  adequately large,

$$A_s \propto \frac{H^2}{\epsilon} \simeq \frac{M^2 \sinh^2(\beta N_*)}{\beta} \sim \frac{M^2}{\beta} e^{2N_*\beta}, \quad (2.14)$$

where  $H^2$  is the Hubble parameter at the end of inflation evaluated analytically in [178] and the slow-roll parameter  $\epsilon$  is defined in (A.3). Thus we can constrain the combination

$$M_* \equiv M^2 \exp(2N_*\beta) \quad (2.15)$$

for which  $A_s$  is constant for a fixed  $\beta$ . We evaluate the choice of this parameter graphically in the right panel of Fig. 2.5. We can see that for different  $N_*$  values, the constrained area lies in the same range of  $M_*$ . As mentioned earlier, observational constraints on the constant-roll inflation parameters were already derived in [178] although by means of the slow roll

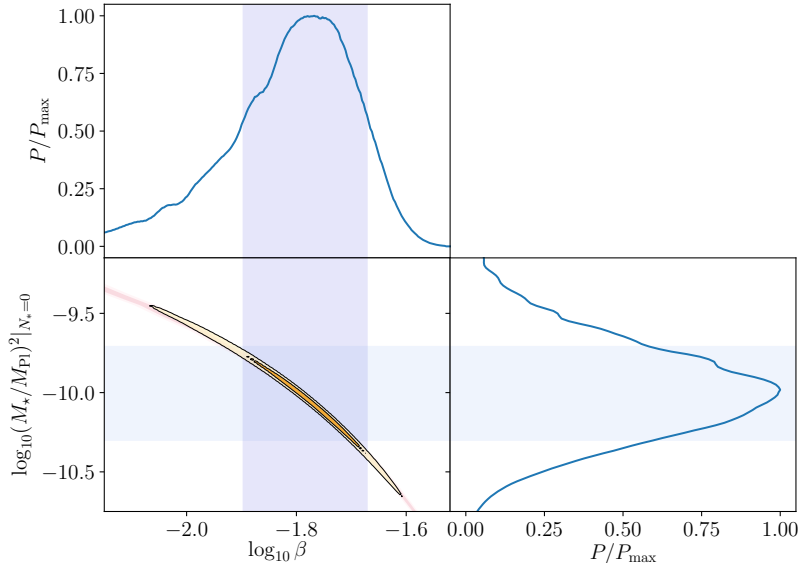


Figure 2.6: Different projections of the joint probability distribution from Planck 2015 likelihood evaluated at  $N_* = 0$ . Top panel: lateral projection of the joint distribution for  $\beta$ . Right panel: lateral projection of the joint distribution for  $M_*/M_{\text{Pl}}|_{N_*=0}$ . Left corner on the bottom: different regions of the joint posterior distribution are shown within the red stripe (containing the posterior) in orange at the 68% C.L. (solid orange) and 95% C.L. (shaded orange). The blue shaded regions correspond to the  $1\sigma$  marginalized regions for the two parameters  $\beta$  and  $M_*$ .

approximation. Here we improve on those earlier results as we are able to very accurately compute the power spectra of the scalar and tensor fluctuations using the evolution scheme presented in Sect. 2.2. Also, as discussed in Appendix A, deviations from the slow roll conditions might be noticeable even in the best fit range of  $\beta$  given the precision of the present-day observational data.

In a Bayesian framework the posterior probability for the model parameters is usually sampled through Markov Chain Monte Carlo (MCMC) engines such as CosmoMC [163] or MontePython [27] coupled to a Boltzmann solver such as CAMB [164] or CLASS [39]. The constraints on the model parameters are then derived by marginalization of the posterior probability. In this work however, we derived the constraints on constant-roll inflation by simply mapping the posterior probability on the parameters  $(n_s, A_s, r)$  to two of the constant-roll inflation parameters  $(\beta, M^2)$  at a fixed  $N_*$ . To do so, we evaluated the scalar and tensor power spectra on the logarithmic grid  $\log_{10} \beta \in [-3, -1.5]$ ,  $\log_{10}(M/M_{\text{Pl}})^2 \in [-15, -7]$  for different values of  $N_* = 0, 30, 60, 80$ , and computed the parameters  $n_s, A_s, r, n_T$  for each sample. The absence of features – i.e., changes of slope or curvature – in the power spectra, as shown in Figure 2.3, allowed us to quickly obtain the scalar and tensor spectral indexes by a simple linear regression in more than 8000 different model realizations. In Figure 2.5, we show the results obtained after marginalizing over  $A_s$

and  $n_s$ . The range for  $n_s$  at 68% C.L. and 95% C.L. is (approximately) independent of any choice of  $N_*$ . In addition to this, the joint-posterior distribution over the parameters  $\beta$  and the new parameter,  $M_*$ , was then computed according to

$$\mathcal{P} \left[ \log_{10} \beta, \log_{10} \left( \frac{M_*}{M_{\text{Pl}}} \right)^2 \right] = \mathcal{P}(n_s, \ln A_s) J, \quad (2.16)$$

where the Jacobian  $J$  was computed numerically from the results

$$n_s = n_s \left[ \log_{10} \beta, \log_{10} \left( \frac{M_*}{M_{\text{Pl}}} \right)^2 \right], \quad (2.17)$$

$$\ln A_s = \ln A_s \left[ \log_{10} \beta, \log_{10} \left( \frac{M_*}{M_{\text{Pl}}} \right)^2 \right], \quad (2.18)$$

and  $\exp(\pm N_*)$  becomes a constant multiplicative factor after  $N_*$  is fixed. The posterior joint distribution  $\mathcal{P}(n_s, \ln A)$  was generated from the MCMC chains provided by the Planck collaboration<sup>3,4</sup>. The results are shown in Figure 2.6 for  $N_* = 0$ , but apply to other values as well via the  $M_*$  scaling described above. The orange shaded regions represent the joint posterior probability  $\mathcal{P}(\log_{10} \beta, \log_{10}(M_*/M_{\text{Pl}})^2 |_{N_*=0})$ , while the red and blue shaded regions represent respectively the marginalized posteriors  $\mathcal{P}(\log A_s)$  and  $\mathcal{P}(n_s)$  projected on the parameter space  $(\log_{10} \beta, \log_{10}(M_*/M_{\text{Pl}})^2 |_{N_*=0})$ . From the definition in (2.15), the constraints on the constant-roll inflation parameters are obtained by marginalizing the posterior probability (2.16) and are  $\log_{10} \beta = -1.77^{+0.17}_{-0.35}$  and  $\log_{10}(M_*/M_{\text{Pl}})^2 = -9.98^{+0.7}_{-0.6}$  at 95% C.L.

In Figure 2.7, we illustrate the region of constant-roll model parameters we probed in the  $r$  versus  $n_s$  diagram overlaying the joint likelihood distribution provided by Planck 2015. The hatched region corresponds to the variation of  $N_*$  spanning values from 0 to 80, while the  $M$  and  $\beta$  range is in Figure 2.5. If one is willing to increase  $N_*$  further (corresponding to hill-top inflation) very small values of  $r$  can be achieved. Interestingly, the green region in Figure 2.7 does not overlap with any of the existing regions constrained by other models shown in [8], which makes constant-roll inflation a testable alternative for future observations.

## 2.4 Discussion

In this chapter, we provided constraints of the model parameters in constant-roll inflation, as proposed in [178, 180]. These are not the only efforts regarding models with similar

<sup>3</sup><https://pla.esac.esa.int/pla/>

<sup>4</sup>[https://wiki.cosmos.esa.int/planckpla2015/index.php/Cosmological\\_Parameters](https://wiki.cosmos.esa.int/planckpla2015/index.php/Cosmological_Parameters)

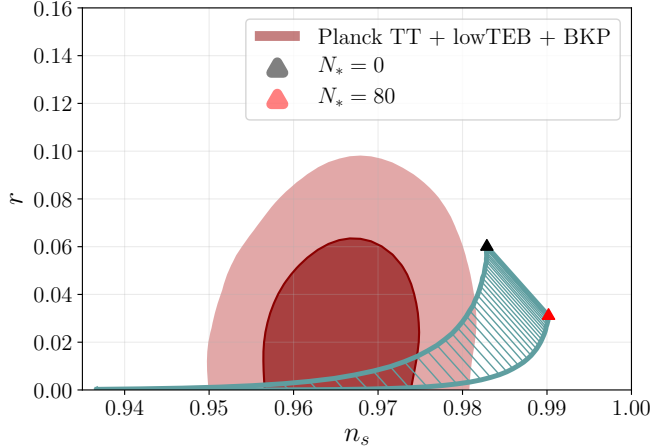


Figure 2.7: Constraints from joint Planck 2015/BKP likelihood on  $n_s$  and  $r$ . The green line shows the values of  $(n_s, r)$  from the parameter space probed in Figures 2.5 and 2.6. The 68% C.L. region is in pink, while the 95% C.L. region is in red. For higher values of  $N_*$ , the model can cover most of the lower range of  $r$ .

features, for instance see [240, 119, 20, 58, 252, 188, 179, 145, 177] for further examples. Our numerical procedure is optimized for an efficient evaluation of the scalar and tensor power spectra of primordial fluctuations, and can scan more than 8000 different choices of model parameters in a reasonable time on a personal computer with standard specifications. It does not require assuming the slow-roll approximation, as it is based on the direct computation of the cosmological parameters  $(n_s, r, A_s, n_T)$  from the featureless power spectra shown in Figure 2.3. The code passes numerous accuracy tests, and long-time integration of the mode evolution confirms that there is no spurious evolution on super-horizon scales.

In order to provide tight constraints of the model parameters, we needed to address the degeneracy between  $M$  and  $N_*$ . We found  $M_*$  defined in (2.15) to be a good auxiliary parameter that leaves the spectra almost invariant under different choices of  $N_*$  for any fixed value of  $M_*$ . After using the CMB measurements from the Planck Collaboration [6, 9, 10] and their joint likelihood with the BICEP2/Keck Array [8], we estimated  $\log_{10} \beta = -1.77^{+0.17}_{-0.35}$  and  $\log_{10}(M_*/M_{\text{Pl}})^2 = -9.98^{+0.7}_{-0.6}$  at 95% C.L. for  $N_* = 0$ , as shown in Figure 2.6. The constraints for  $\beta$  are not significantly modified by any different choice of  $N_*$ , however, due to the parameter degeneracy the same cannot be said about the constraints for  $M$ . The parameter range on  $r$  versus  $n_s$  diagram covered by constant-roll inflation in Figure 2.7 does not appear to overlap with any of the regions covered by the other inflationary models considered in [9, 10], making this model observationally interesting for the next generations of CMB experiments.



## Chapter 3

# Two-point correlators revisited: fast and slow scales in multifield models of inflation

In this chapter, we generalized the Ermakov-Pinney equation found in the previous chapter (2.13) to the case of models with more than one scalar degree of freedom. It is important to notice that these techniques can be further expanded to solve a wide variety of multifield problems with linear equations of motion (perturbative or not) beyond the inflationary regime. Direct computation of the power spectrum from equations of motion can be time consuming, especially when resolving specific features of each model in a wide range of energy scales. These problems will be aggravated for multifield models of inflation such as the proposals in [125, 239]. These models are physically motivated by the separation of two specific roles: (a) driving the accelerated expansion of the background by one of the field components and (b) the quantum-mechanical generation of primordial fluctuations.

The primordial power spectrum is valuable in finding sensible ranges of validity for the parameters of any proposed inflationary model. In the case of models with multiple fields, it encodes vital information about the power transfer between different components. The viability of a model is usually tested when the spectrum is loaded as an input in any of the existing schemes based in Boltzmann transport equations (such as CAMB in [66] or CLASS in [238]) and compared with data. Being aware of the existing difficulties to design a spectral code, we suggest an approach intended to isolate all the high-frequency terms and only use the slowly evolving quantities relevant for calculating the spectrum. These degrees of freedom remain “frozen” outside the horizon, which implies the use of large time steps in any numerical evolution scheme.

A crucial part of separating fast and slow degrees of freedom relies on focusing on the spectrum, which contains information about all the field correlations. This spectrum is generated by the symmetric product between two field multiplets, forming a correla-

tion matrix. Field dynamics reveals the approximate time-translational invariance of each multiplet component on subhorizon scales. This symmetry must be exploited to define a well-posed Cauchy problem each time vacuum correlations are defined as initial conditions. When the cases of anticorrelation are excluded, positive definite correlation matrices are suitable for Cholesky decomposition into two unique triangular factors. Anticorrelations break the uniqueness of this factorization. This decomposition has been the preferred tool of statisticians to generate correlated samples from any set of unit-variance random vectors. Amplitudes of the modes and power of the cross correlations are carried in these Cholesky factors, which act on a rotating basis of solutions, just as in the Schrodinger picture in Quantum Mechanics. The fast rotation of this basis is separated from the slow evolution of amplitudes. We implement a dynamical Cholesky decomposition motivated by the separation of wave solutions into phases and amplitudes. This separation has been explored in single-field solutions, (see [49, 32] for more details) with exact results in the case of massless perturbations.

The plan for this chapter is as follows: in section 3.1, we will review the notions of perturbation theory for inflationary models, along with the equations of motion for the background fields. In section 3.2, we describe the field decomposition technique used in order to separate the fast oscillating phases from the amplitudes. The latter are required to calculate the spectrum. In section 3.3, we discuss the background dynamics and the use of initial conditions based on asymptotic vacuum solutions. Additionally, we introduce a scheme for injecting modes in the system. To conclude, we present our results and discussions.

### 3.1 Perturbation theory: a lightning review

For the purposes of this work, we only consider Lagrangian densities with canonical kinetic terms. We will later extend our treatment in Appendix B for the case of a generic curved field space developed in [219]. The action  $S$  needed to describe a generic model of inflation with multiple coupled fields reads,

$$S = \int d^4x \sqrt{-g} \left( \frac{M_{\text{Pl}}^2}{2} R - \frac{1}{2} \partial_\mu \phi_A \partial^\mu \phi_A - V(\phi_A) \right), \quad (3.1)$$

where all the fields become coordinates of a generically non-flat field space. We pick spatially flat coordinates just as described in [219]

$$ds^2 = -(1 + 2A)dt^2 - 2a^2 \partial_i B dx^i dt + a^2 \delta_{ij} dx^i dx^j, \quad (3.2)$$

where  $A$  and  $B$  are spacetime-dependent perturbations of the FLRW metric. Now, as is usual in this perturbative approach, we decompose each component of the  $\mathcal{N}$  field multiplet

$\phi_A$  into a spatially homogeneous background field and its fluctuations

$$\phi_A(x^\mu) = \phi_A^0(t) + \tilde{\Phi}_A(x^\mu).$$

The field equations for the background field, given by (3.1) read

$$\ddot{\phi}_A^0 + 3H\dot{\phi}_A^0 + \frac{\partial V}{\partial \phi_A} = 0. \quad (3.3)$$

The expansion history is obtained from the first Friedmann equation

$$3M_{\text{Pl}}^2 H^2 = \frac{1}{2} \dot{\phi}_A^0 \dot{\phi}_A^0 + V(\phi_A^0). \quad (3.4)$$

where we define  $\dot{\phi} \equiv d\phi/dt$ . These equations describe all the quantities needed from the homogeneous limit, such as the scale factor and the masses, and hence these become a part of the overall evolution scheme.

In order to find the spectrum, quantum fluctuations are normally expressed as Fourier modes  $\Phi_A(k, t)$  evaluated on a hypersurface at constant time, where we are able to set the scale as a constant  $a$  without loss of generality. These modes are contained in a second-order expansion of (3.1)

$$S_\Phi(k) = \frac{1}{2} \int a^3 dt \left[ \dot{\Phi}_A \dot{\Phi}_A - \Phi_A \left( \frac{k^2}{a^2} \delta_{AB} + M_{AB}^2 \right) \Phi_B \right], \quad (3.5)$$

where  $M_{AB}^2 \equiv \partial^2 V / \partial \phi_A \partial \phi_B - \left( a^3 \dot{\phi}_A \dot{\phi}_B / H \right) / a^3 M_{\text{Pl}}^2$  is the well-known ‘‘mass-squared matrix’’ [97] modified by the coordinate choice made on (3.2). The term  $\left( a^3 \dot{\phi}_A \dot{\phi}_B / H \right) / a^3 M_{\text{Pl}}^2 \Phi_B$  corresponds to the metric curvature fluctuations solved in terms of the field perturbations  $\Phi_B$ . All the equations of motion just follow from the variational principle. Initial conditions will be consistent with the high-frequency behavior  $k^2/a^2 \gg M_{AB}^2$ , where the solutions for  $\Phi_A$  are treated as in Minkowski spacetime.

## 3.2 Two-point correlators revisited

It is important to compute the spectrum of linearized field perturbations at the end of inflation since it is directly related to the spectrum of primordial curvature by a gauge transformation (3.26). An interesting procedure for this calculation is described in [200], where the authors consider the evolved components of a complex ‘‘mode matrix’’, which follows the same equations of motion obtained from (3.5). More recently, the Hamiltonian evolution of the field correlators  $\langle \Phi_A, \Phi_B \rangle$  was considered in [83] with the purpose of separating fast and slow evolution scales. In this perspective, more than one time scale is still necessary to resolve the mode correlations.

Here we present a different approach: a dynamical decomposition method which suppresses the fastest oscillation scales in the equations of motion of the correlation modes regardless of the mode frequency. This is the multifield extension of the separation technique previously seen in the Ermakov-Pinney equation (2.13) in Chapter 2. Hence, the evolution of the correlation modes is more efficient, particularly for deep sub-horizon scales where integration costs scale linearly with number of e-folds in our method, as opposed to exponential scaling in other methods. To achieve that, we suggest the following extended form of the field

$$\Phi_A = L_{AB} \hat{\chi}_B, \quad (3.6)$$

as an effective way to separate a real matrix of amplitudes ( $L_{AB}$ ) from phases ( $\hat{\chi}_B$ ) on each mode. We initially assume  $\mathcal{N} \times \mathcal{N}$  independent degrees of freedom contained by  $L_{AB}$ . Field fluctuations in de Sitter spacetime before crossing the horizon only add “damping” to the standard massive wave solutions in empty space. For that reason, it is possible to consider the vector  $\hat{\chi}_B$  as a set of evolved phases. By inserting the ansatz (3.6) in (3.5), we get

$$S_\Phi = \frac{1}{2} \int a^3 dt \delta_{AB} \left[ L_{AC} L_{BD} \dot{\hat{\chi}}_C \dot{\hat{\chi}}_D + 2 \dot{L}_{BD} L_{AC} \hat{\chi}_D \dot{\hat{\chi}}_C + \dot{L}_{AC} \dot{L}_{BD} \hat{\chi}_C \hat{\chi}_D \right] - L_{AC} \left( \frac{k^2}{a^2} \delta_{AB} + M_{AB}^2 \right) L_{BD} \hat{\chi}_C \hat{\chi}_D, \quad (3.7)$$

and the equations of motion for  $\hat{\chi}_E$  are

$$\ddot{\hat{\chi}}_E + \left( 3H\delta_{EB} + 2(L^{-1})_{ED} \dot{L}_{DB} \right) \dot{\hat{\chi}}_B + \left[ (L^{-1})_{ED} \ddot{L}_{DB} + 3H(L^{-1})_{ED} \dot{L}_{DB} + (L^{-1})_{ED} \left[ \frac{k^2}{a^2} \delta_{DC} + M_{DC}^2 \right] L_{CB} \right] \hat{\chi}_B = 0, \quad (3.8)$$

which turn out to be minimally different from the case of Coriolis’ equation written in a rotating non-inertial frame. The last term corresponds to the effective rotation frequency. The conjugate momentum of  $\hat{\chi}_B$  from this action yields  $\hat{P}_B = a^3 \left( L_{AB} L_{AD} \dot{\hat{\chi}}_D + \dot{L}_{AD} L_{AB} \hat{\chi}_D \right)$ , hence the canonical commutators  $[\hat{\chi}_A, \hat{P}_B] = i\delta_{AB}$  now imply

$$[\hat{\chi}_A, \dot{\hat{\chi}}_B] = \frac{i}{a^3} (L^T)_{BC}^{-1} (L^{-1})_{CA}. \quad (3.9)$$

Observationally, a successful model of inflation is required to produce more than 60 e-folds of expansion; and therefore,  $a$  is enlarged by a factor of  $e^{60}$  by the end of inflation. The dependence on  $a^{-3}$  is responsible for the suppressed commutators during inflation. This is consistent with the decoherence conditions stated in [198]. Transitioning into classical states has dynamical consequences:  $\hat{\chi}_A$  can be treated as Gaussian random variables, as suggested in [32]. In such a case, the central limit theorem is fully applicable and the definition of complex phases is convenient but not mandatory since it is possible to evolve two copies of

the same field under different initial conditions. As a result of this, complexification is no longer a requirement. In addition to this, our prescription in (3.6) allows us to rewrite the two-point correlators as

$$\langle \Phi_A, \Phi_B \rangle = L_{AC} L_{DB}^T \langle \hat{\chi}_C, \hat{\chi}_D \rangle. \quad (3.10)$$

A similar separation is performed in [224]. It is inspired by geometrical optics and considers the evolution of the correlators by describing the elements – i.e. rotations, expansions and shears – of the unitary evolution operator acting on each mode. However, our approach is more concerned on the dynamical constraints required to hold a specific gauge choice after the separation in (3.6).

We can make a gauge choice that requires independence between different phases (i.e. a normalized covariance matrix) at all times. This is analog to using “cosine” or “sine” waves as an orthonormal basis for a simple harmonic oscillator with the purpose of maximizing *amplitude* and *velocity* as initial conditions for the oscillating system. This independence condition is our gauge choice

$$\langle \hat{\chi}_C, \hat{\chi}_D \rangle = \delta_{CD}, \quad (3.11)$$

and it must be held at all times. The expression for the correlator in (3.10) reduces to

$$\langle \Phi_A, \Phi_B \rangle = L_{AC} L_{CB}^T. \quad (3.12)$$

Because phases are fast oscillating degrees of freedom and can cancel out, these are not required to calculate two-point correlators. All information of the correlations is carried by  $L_{BC}$ , the slowly varying “square root” of the correlation matrix. We look for an effective set of equations of motion which mainly depend on amplitudes instead of phases. Therefore, we must consider that the evolution of  $\hat{\chi}_A$  follows the second-order differential equations in (3.8). Hence, time translational invariance requires two derivatives of (3.11) as additional constraints for the system at an arbitrary time slice

$$\text{Sym}_{AB}^{CD} \langle \dot{\hat{\chi}}_C, \hat{\chi}_D \rangle = 0, \quad (3.13)$$

$$\text{Sym}_{AB}^{CD} \left[ \langle \ddot{\hat{\chi}}_C, \hat{\chi}_D \rangle + \langle \dot{\hat{\chi}}_C, \dot{\hat{\chi}}_D \rangle \right] = 0, \quad (3.14)$$

where we define (Anti)Sym $_{AB}^{CD} \equiv \delta_A^C \delta_B^D \mp \delta_B^C \delta_A^D$  and its antisymmetric counterpart analog as (anti-)symmetrizing multilinear operators. Equations (3.11) and (3.13) are just constrained by initial conditions. With (3.8), we can rewrite (3.14) as

$$\begin{aligned} \text{Sym}_{AB}^{CD} \left[ (L^{-1})_{CE} \ddot{L}_{ED} + 3H (L^{-1})_{CE} \dot{L}_{ED} + (L^{-1})_{CE} \left[ \frac{k^2}{a^2} \delta_{EF} + M_{EF}^2 \right] L_{FD} - \langle \dot{\hat{\chi}}_C, \dot{\hat{\chi}}_D \rangle \right. \\ \left. + (L^{-1})_{CE} \dot{L}_{EF} \langle \dot{\hat{\chi}}_F, \hat{\chi}_D \rangle \right] = 0. \end{aligned} \quad (3.15)$$

$$\begin{aligned}
& \text{Sym} \left[ \begin{array}{c} \overbrace{\left[ \begin{array}{c} \ddots \\ \cdot \\ \cdot \\ \cdot \end{array} \right]}^{(L^{-1})_{CE}\dot{L}_{ED}} + 3\text{H} \left[ \begin{array}{c} \cdot \\ \cdot \\ \cdot \end{array} \right] + \left[ \begin{array}{c} \cdot \\ \cdot \\ \cdot \end{array} \right] + \left[ \begin{array}{c} \cdot \\ \cdot \\ \cdot \end{array} \right] + \left[ \begin{array}{c} \cdot \\ \cdot \\ \cdot \end{array} \right] \end{array} \right] = 0 \\
& \mathcal{A} = - \left[ \begin{array}{c} \cdot \\ \cdot \\ \cdot \end{array} \right] - \left[ \begin{array}{c} \cdot \\ \cdot \\ \cdot \end{array} \right] - \left[ \begin{array}{c} \cdot \\ \cdot \\ \cdot \end{array} \right] \text{ Antisymmetric parts}; \text{Sym}\mathcal{A}=0 \\
& \longrightarrow \left[ \begin{array}{c} \ddots \\ \cdot \\ \cdot \\ \cdot \end{array} \right] + 3\text{H} \left[ \begin{array}{c} \cdot \\ \cdot \\ \cdot \end{array} \right] + \left[ \begin{array}{c} \cdot \\ \cdot \\ \cdot \end{array} \right] + \left[ \begin{array}{c} \cdot \\ \cdot \\ \cdot \end{array} \right] + \left[ \begin{array}{c} \cdot \\ \cdot \\ \cdot \end{array} \right] + \mathcal{A} = \left[ \begin{array}{c} \cdot \\ \cdot \\ \cdot \end{array} \right]
\end{aligned}$$

Figure 3.1: Schematic representation of (3.15). Fixing the shape of Cholesky amplitudes by adding the antisymmetric matrix  $\mathcal{A}_{CD}$ . This matrix is an antisymmetrized collection of all components outside of the lower triangular form. After rearranging terms in the final sum, the expression in (3.17) keeps its Cholesky shape at all times.

In all the terms, symmetrization in both free indices indicates the existence of  $\mathcal{N}(\mathcal{N}-1)/2$  repeated degrees of freedom in the system. When anticorrelations are discarded, we can use the positive-definiteness of the correlation matrix to eliminate the redundancy in (3.15) by picking  $L_{AB}$  to be a unique Cholesky matrix. These do not have more than  $\mathcal{N}(\mathcal{N}+1)/2$  non-zero real elements in the lower triangular corner of the matrix. Our choice of Cholesky matrices is convenient for a variety of reasons, especially since matrix inversions, linear filters and other matrix operations are computationally inexpensive and easily scalable for the case of models with a large number of fields.

Moreover, the whole expression inside the square brackets of equation (3.15) has a gauge symmetry due to the overall symmetrization acting on it. Such a gauge freedom can be exploited to fix the shape of the Cholesky representation at all times. Only the first two terms in this expression preserve the shape of a Cholesky matrix. As the system evolves, all the other terms will migrate degrees of freedom out of the lower triangular form of  $L$ . Consequently, we need to add an antisymmetric matrix  $\mathcal{A}_{CD}$ , which will be canceled out when symmetrized. In Figure 3.1, we represent the way in which the Cholesky representation is preserved.

The gauge fixing condition emerges by suppressing the upper diagonal terms ( $D > C$ )

$$\mathcal{A}_{CD} = - \left( L^{-1} \right)_{CE} M_{EF}^2 L_{FD} - (L^{-1})_{CE} \dot{L}_{EF} \langle \dot{\chi}_F, \dot{\chi}_D \rangle + \langle \dot{\chi}_C, \dot{\chi}_D \rangle. \quad (3.16)$$

Thus, Cholesky matrices evolve in agreement with

$$\ddot{L}_{AB} + 3\text{H}\dot{L}_{AB} + \left[ \frac{k^2}{a^2} \delta_{AC} + M_{AC}^2 \right] L_{CB} + L_{AC} \mathcal{A}_{CB} + \dot{L}_{AC} \langle \dot{\chi}_C, \dot{\chi}_B \rangle - L_{AC} \langle \dot{\chi}_C, \dot{\chi}_B \rangle = 0. \quad (3.17)$$

To find appropriate expressions for the expected phase correlators  $\langle \dot{\hat{\chi}}_A \dot{\hat{\chi}}_B \rangle$  and  $\langle \dot{\hat{\chi}}_A \hat{\chi}_B \rangle$ , we will write the derivatives for each one of the unknown correlators

$$\begin{aligned}\frac{d}{dt} \langle \dot{\hat{\chi}}_A, \dot{\hat{\chi}}_B \rangle &= \text{Sym}_{AB}^{CD} \langle \ddot{\hat{\chi}}_C, \dot{\hat{\chi}}_D \rangle, \\ \frac{d}{dt} \langle \dot{\hat{\chi}}_A, \hat{\chi}_B \rangle &= \langle \ddot{\hat{\chi}}_A, \hat{\chi}_B \rangle + \langle \dot{\hat{\chi}}_A, \dot{\hat{\chi}}_B \rangle.\end{aligned}\tag{3.18}$$

The last expression is equivalent to

$$\begin{aligned}\frac{d}{dt} \langle \dot{\hat{\chi}}_A, \hat{\chi}_B \rangle &= \frac{1}{2} \text{Sym}_{AB}^{CD} \left[ \langle \ddot{\hat{\chi}}_C, \hat{\chi}_D \rangle + \langle \dot{\hat{\chi}}_C, \dot{\hat{\chi}}_D \rangle \right] + \frac{1}{2} \text{Antisym}_{AB}^{CD} \left[ \langle \ddot{\hat{\chi}}_C, \hat{\chi}_D \rangle + \langle \dot{\hat{\chi}}_C, \dot{\hat{\chi}}_D \rangle \right] \\ &= \frac{1}{2} \text{Antisym}_{AB}^{CD} \langle \ddot{\hat{\chi}}_C, \hat{\chi}_D \rangle\end{aligned}\tag{3.19}$$

Equation (3.19) conserves the antisymmetric properties of  $\langle \dot{\hat{\chi}}_A, \hat{\chi}_B \rangle$  found in (3.13), whose behavior seems to match the rotation generators in a real vector space. Using (3.8) and (3.17), we can write equations of motion for the missing two-point correlators

$$\begin{aligned}\frac{d}{dt} \langle \dot{\hat{\chi}}_A, \dot{\hat{\chi}}_B \rangle &= \text{Sym}_{AB}^{CD} \left[ -3H \langle \dot{\hat{\chi}}_C, \dot{\hat{\chi}}_D \rangle - 2(L^{-1})_{CE} \dot{L}_{EF} \langle \dot{\hat{\chi}}_F, \dot{\hat{\chi}}_D \rangle - \mathcal{A}_{CE} \langle \dot{\hat{\chi}}_E, \dot{\hat{\chi}}_D \rangle \right. \\ &\quad \left. + (L^{-1})_{CE} \dot{L}_{EF} \langle \dot{\hat{\chi}}_F, \hat{\chi}_G \rangle \langle \hat{\chi}_G, \dot{\hat{\chi}}_D \rangle + \langle \dot{\hat{\chi}}_C, \dot{\hat{\chi}}_F \rangle \langle \dot{\hat{\chi}}_F, \dot{\hat{\chi}}_D \rangle \right],\end{aligned}\tag{3.20}$$

and also

$$\frac{d}{dt} \langle \dot{\hat{\chi}}_A, \hat{\chi}_B \rangle = \mathcal{A}_{AB} - 3H \langle \dot{\hat{\chi}}_A, \hat{\chi}_B \rangle - \frac{1}{2} \text{Antisym}_{AB}^{CD} \left[ (L^{-1})_{CE} \dot{L}_{EF} \langle \dot{\hat{\chi}}_F, \hat{\chi}_D \rangle \right].\tag{3.21}$$

At first glance, the symmetrizer doubles the first coefficients in (3.20). After comparing (3.20) with (3.21) we notice that  $\langle \dot{\hat{\chi}}_A, \dot{\hat{\chi}}_B \rangle \sim \langle \dot{\hat{\chi}}_A, \hat{\chi}_B \rangle^2$ , which is consistent with our analogy with the rotation generators in a real vector space. However, a careful review of all the terms in both expressions shows that this is not a strict equality. Henceforth, both correlators are considered as separate elements in the evolving system. The expressions found in (3.17), (3.20) and (3.21) constitute the system of differential equations required to evolve the ‘‘square root’’ of the two-point correlators.

### 3.3 Initial conditions and spectral evolution scheme

It is reasonable to ask about the proper set of values required to initialize the equations of motion as described in (3.3) and (3.17). To do so, we first consider the evolution of the background fields.

It is important to mention that the application of alternative time scales does not affect the overall performance of any evolution scheme. Throughout the rest of the chapter, we choose

$$V(\phi, \sigma) = \frac{\lambda}{4} \phi^4 + \frac{g}{2} \phi^2 \sigma^2,\tag{3.22}$$

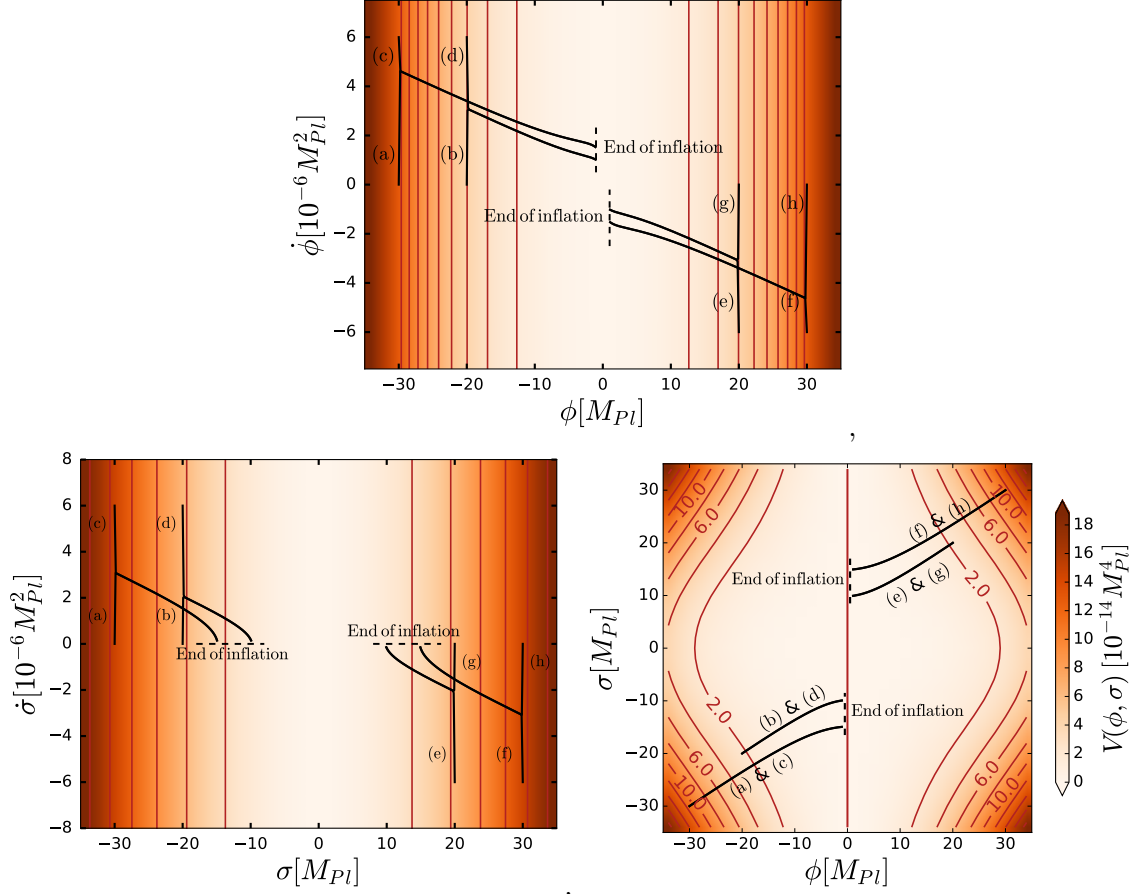


Figure 3.2: Evolution of eight different background trajectories labeled from (a) to (h) and represented in three transversal sections of the phase space:  $(\dot{\phi}, \phi)$  in the first figure,  $(\dot{\sigma}, \sigma)$  in the second and  $(\phi, \sigma)$  in the third. The projection  $(\phi, \sigma)$  is embedded on the field potential. Here we observe the overlap of trajectories with the same initial values of  $\phi(t_0)$  and  $\sigma(t_0)$ . Equipotential curves of (3.22) are plotted in the three projections as a reference for the energy scale at different field configurations.



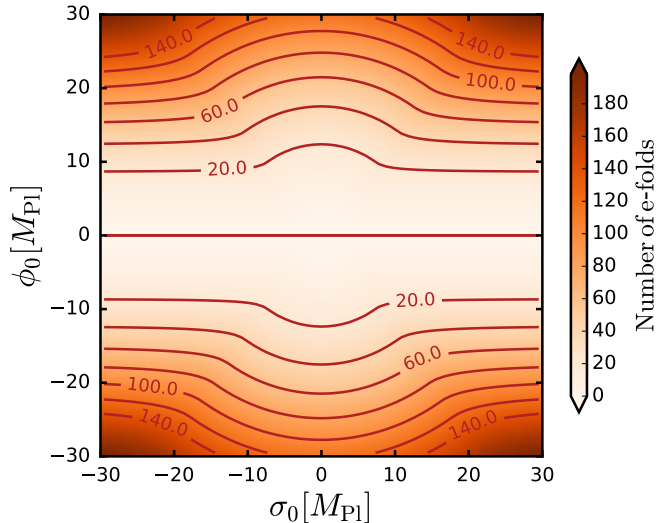


Figure 3.3: Projected surface of initial conditions. The contours plotted highlight the regions (similar to equipotential curves) which would generate 20, 60, 100 and 140 e-folds of inflation.

as an example of a multifield non-linear potential. Having a system of highly coupled second-order differential equations, we must investigate the behaviour of first and second derivatives for both fields since those provide initial conditions for the background. Thus, we can observe in Figure 3.2 three phase space projections of the background field trajectories, where  $\lambda = g/2 = 10^{-14}$  is the numerical value assigned to the coupling constant. From Figure 3.2, we notice that  $\dot{\phi}(t_0) \approx \dot{\sigma}(t_0) \approx 0.0$  are suitable choices for the derivatives of the slowly rolling background field. Other values will not modify the convergence time substantially. The lapse of time the system takes to fall into the inflationary attractor is very small. However, we always have the option of getting closer to the attractor in order to reduce the convergence time of the complete system of equations, which includes fluctuations. Hence, we are left with two numbers we have to fix in order to achieve enough expansion in the model.

In Figure 3.3, we generated a “map” of initial values for  $\phi$  and  $\sigma$ , including the number of expanded e-folds. Once we choose a set of initial field coordinates, we can ensure the conditions necessary to produce an inflating homogeneous background state considering the potential in (3.22). In this case, following the data from the map in Figure 3.3, initial conditions were chosen to produce sufficient expansion, we arbitrarily choose 88 (approx.) e-folds of inflation, with  $\phi_0 = \sigma_0 = 20 M_{\text{Pl}}$ . The horizon and all the physical wavenumbers ( $k_{\text{phys}}$ ) associated with each perturbation mode evolve according to the curves in Figure 3.4.

To describe the evolution of the correlations between perturbations of the different scalar degrees of freedom, we rely on our knowledge of the correlators  $\langle \Phi_A, \Phi_B \rangle$ ,  $\langle \dot{\Phi}_A, \Phi_B \rangle$  and  $\langle \dot{\Phi}_A, \dot{\Phi}_B \rangle$  to provide suitable (approximate) initial conditions at  $(t = t_0)$ .

Asymptotic consistency with the field amplitudes in Minkowski vacuum with a non-diagonal mass matrix is sufficient to determine these correlation matrices. Diagonalization of the mass matrix in the initial time surface provides estimated values of the correlations in  $\langle \Phi_A, \Phi_B \rangle_{t_0}$ :

$$\begin{aligned} D_{AB} &\equiv U_{AC} U_{DB}^T M_{CD}^2, \\ \langle \Phi_A, \Phi_B \rangle_{t_0} &= U_{AC}^T U_{DB} \left( \frac{a^{-3}}{2\hat{\omega}_{CD}} \right), \end{aligned} \quad (3.23)$$

where  $\hat{\omega}_{CD} \equiv \sqrt{(k^2/a^2)\delta_{CD} + D_{CD}}$ ,  $D_{AB}$  is the diagonal version of  $M_{AB}^2$  and  $U_{AB}$  is the orthonormal transformation matrix responsible for the diagonalization.

The classicality arguments stated in section 3.2 allow us to consider independent initial conditions for each component of the multiplet and its derivatives:

$$\begin{aligned} \langle \Phi_A, \Phi_B \rangle_{t_0} &= L_{AC} L_{CB}^T, \\ \langle \dot{\Phi}_A, \Phi_B \rangle_{t_0} &= \dot{L}_{AC} L_{CB}^T + L_{AC} L_{DB}^T \langle \dot{\chi}_C, \hat{\chi}_D \rangle_{t_0} = 0, \\ \langle \dot{\Phi}_A, \dot{\Phi}_B \rangle_{t_0} &= \dot{L}_{AC} \dot{L}_{CB}^T + L_{AC} L_{DB}^T \langle \dot{\chi}_C, \dot{\chi}_D \rangle_{t_0} + \left( \dot{L}_{AC} L_{DB}^T - L_{AC} \dot{L}_{DB}^T \right) \langle \dot{\chi}_C, \hat{\chi}_D \rangle_{t_0}. \end{aligned} \quad (3.24)$$

Initial conditions for  $\dot{L}_{AB}$  must be compatible with both the classicality  $\langle \dot{\Phi}_A, \Phi_B \rangle_{t_0} = 0$  and the antisymmetry of  $\langle \dot{\chi}_A, \hat{\chi}_B \rangle_{t_0}$ , which leads us to  $\dot{L}_{AB} = \langle \dot{\chi}_A, \hat{\chi}_B \rangle_{t_0} = 0$ . Therefore, it is possible to use (3.24) to obtain the corresponding initial state of every phase correlations. From (3.24), we observe that the dependence of  $\langle \dot{\chi}_A, \dot{\chi}_B \rangle_{t_0}$  on both  $\langle \dot{\Phi}_A, \dot{\Phi}_B \rangle_{t_0}$  and  $L_{AB}^{-2}(t_0)$  guarantees the suppression of the fastest frequency scales at the time these reached their maximum values.

The scheme of evolution is also responsible for the efficiency of any spectral code. It represents the way in which modes are injected to the system and then evolved from sub-horizon scales to a final instant of time outside the horizon. We are interested in reducing the time in which mode evolution is irrelevant to the spectrum via time translational invariance. To achieve this, we inject modes every five or ten e-folds from a constant energy scale  $k_{\text{phys}}$  as in Figure 3.4, being aware of the initial conditions for the fluctuation modes and the background discussed previously. Each mode can be traced back to a physical wave mode leaving the horizon. This simple technique saves half of the evolution time necessary to evolve all the modes from any constant-time hypersurface.

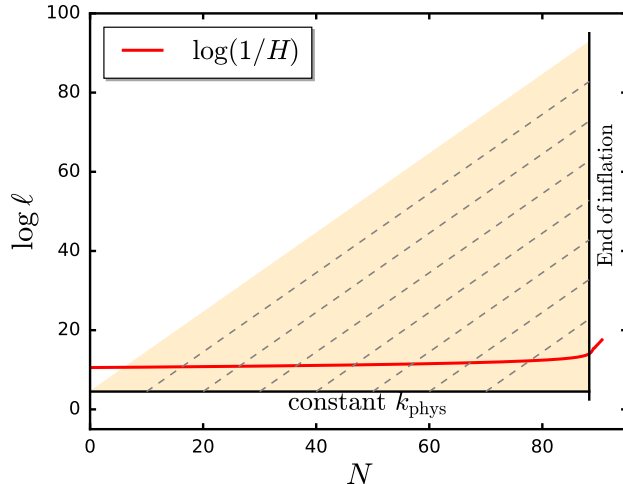


Figure 3.4: Mode injection scheme. Cholesky modes injected every 10 e-folds from a surface of constant physical wavelength and evolved until a fixed time “screen” at the end of inflation. Initial conditions allow up to 88 e-folds of inflation.  $\ell$  is the physical length scale in the system.

### 3.4 Results

In order to evaluate the validity of the statements made so far, we produced two codes: the first one generates the correlation matrix by taking correlations of a random sample. In the second one, we solve the system given by (3.17), (3.20) and (3.21). In both scenarios, we followed the same initial conditions stated in the previous section. Also, we used the same solver in both cases, a symplectic eighth-order-accurate Gauss-Legendre integrator (see [254] for more details).

In the first case, we used the Box-Muller algorithm to generate a set of four independent unit-variance random vectors ( $\hat{\chi}_A$ ) satisfying (3.11): two amplitudes and two *velocities*. By using (3.6), we reproduce a certain number of field realizations (between 100-500) consistent with all the calculable two-point correlators, i.e.  $\langle \Phi_A, \Phi_B \rangle_{t_0}$ ,  $\langle \dot{\Phi}_A, \Phi_B \rangle_{t_0}$  and  $\langle \dot{\Phi}_A, \dot{\Phi}_B \rangle_{t_0}$ , at the surface of initial conditions. Each one of these realizations evolves in agreement with the equations of motion obtained from (3.5). We are aware that this is not the most efficient way to calculate correlations; nevertheless, it is worth to compare with the “static” version of the idea we are developing in this project.

By implementing this idea, we confirm by direct calculation the gauge fixing conditions provided on (3.11), (3.13) and (3.14), which are necessary to produce the Cholesky decomposition, can be held at all times. The dynamics of the system and the separation in fast and slow parameters relies entirely on these statements. In Figure 3.5, we verified the first of these gauge choices. After solving for  $\Phi_1$  and  $\Phi_2$ , the inversion of (3.6) is used to confirm (3.11) as a valid gauge condition. The Cholesky decomposition of any positive-definite

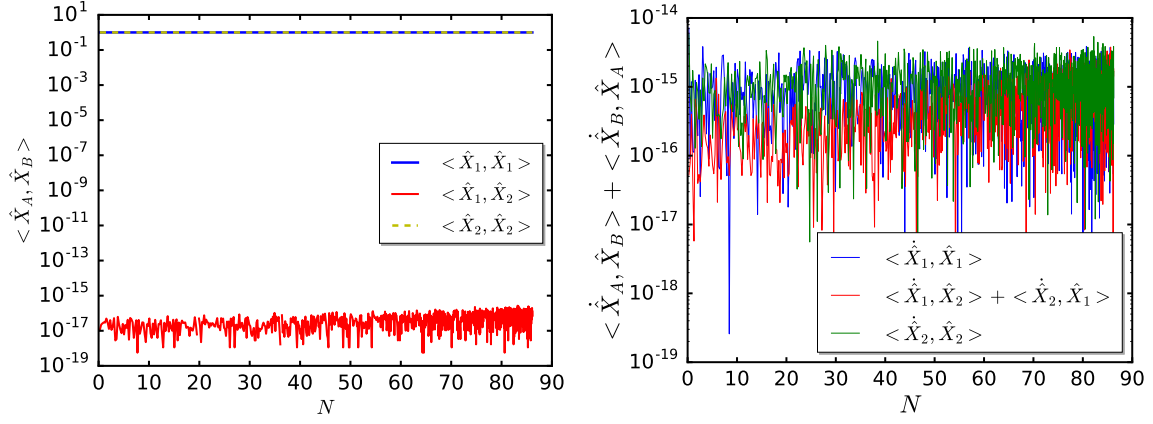


Figure 3.5: Left panel: The gauge choice  $\langle \hat{\chi}_A, \hat{\chi}_B \rangle = \delta_{AB}$  holds at all times. Off-diagonal terms are numerically zero. Right panel: We observe the antisymmetry of  $\langle \dot{\hat{\chi}}_A, \dot{\hat{\chi}}_B \rangle$  since both of the diagonal terms, and the sum of the off-diagonal elements are numerically zero (up to machine precision).

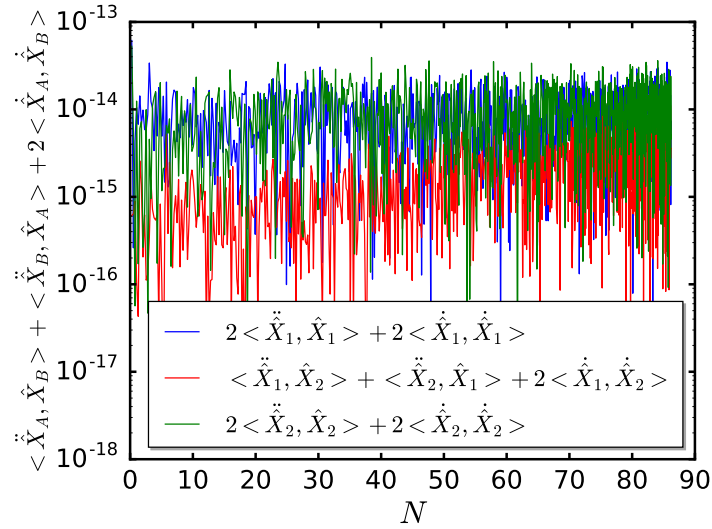


Figure 3.6: Verifying the final gauge condition in (3.14) by checking that all the matrix elements noted in the legend are numerically zero (up to machine precision).

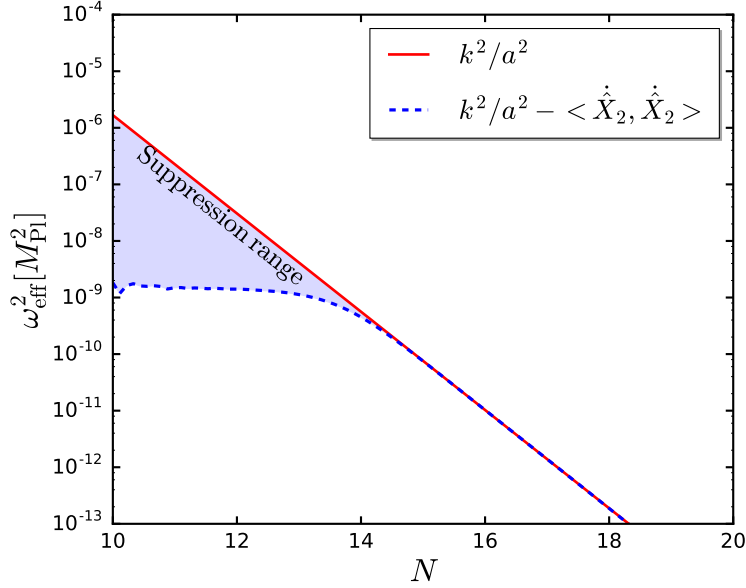


Figure 3.7: Suppressed oscillation scale in a mode injected at  $k_1 = e^{10}k_{\text{phys}}$ . The effective oscillation frequency ( $k^2/a^2$ ) is reduced by three orders of magnitude. The effect due to  $\langle \hat{\chi}_1, \hat{\chi}_1 \rangle$  is the same.

correlation matrix is independent of the instant of time in which we choose to perform it. It is mainly supported by time-translational invariance of the approximated Minkowski (or Bunch-Davies) vacuum state. In addition to this fact, we must also consider that this does not depend on the choice of any particular initial length scale.

In the right panel of Figure 3.5 we check the numerical cancellation of the symmetric part of  $\langle \hat{\chi}_A, \hat{\chi}_B \rangle$ . Phase cross-correlators  $\langle \hat{\chi}_1, \hat{\chi}_2 \rangle$  and  $\langle \hat{\chi}_2, \hat{\chi}_1 \rangle$  do not cancel separately. On the contrary, their strength is enhanced until the modes cross the horizon. It is possible to show that a Taylor expansion of  $\langle \hat{\chi}_A, \hat{\chi}_B \rangle$  in powers of time, will only depend on  $\langle \hat{\chi}_A, \hat{\chi}_B \rangle$  and  $\langle \hat{\chi}_A, \hat{\chi}_B \rangle$ . The antisymmetric behaviour is consistent, again, with the notion of these correlators as rotation generators: the rotation transfers power from one mode to another.

In Figure 3.6, we tested the last dynamical gauge constraint in (3.14). Here the combinations plotted are numerically zero up to machine precision, after using double-precision floats. The use of this condition yields the equations of motion of the “square root” factor  $L_{AB}$ .

Now we present the results of implementing the dynamical Cholesky scheme developed to get the expressions in (3.17), (3.20) and (3.21).

One of the objectives of this chapter is to separate the fast and slow degrees of freedom required to solve the spectrum of fluctuations. Such a separation is achieved by reducing the effective oscillation frequency  $\omega_{\text{eff}}^2 \sim k^2/a^2 + M_{AB}^2$  by the introduction of  $\langle \hat{\chi}_A, \hat{\chi}_B \rangle$  acting as counterterms in (3.17). In this particular case, even when the addition of the mass matrix alters the coupling between different field components, none of these magnitudes is enough

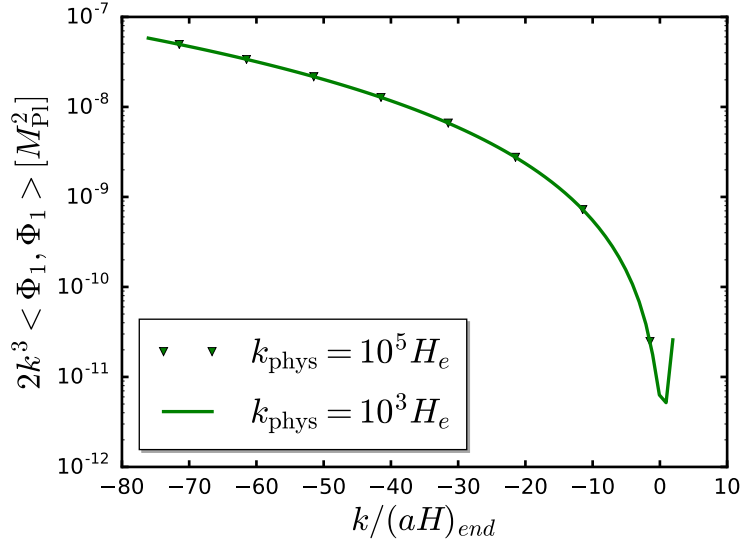


Figure 3.8:  $\langle \Phi_1, \Phi_1 \rangle$  correlator obtained after injecting modes from two different physical length scales  $k_{\text{phys}} = 10^3 H_e$  and  $k_{\text{phys}} = 10^5 H_e$ . The spectrum remains unaltered.

to contribute significantly to  $\omega_{\text{eff}}^2$ . In Figure 3.7, we can see an effective suppression of the higher frequency terms, which confirms that there has been a separation of oscillatory scales in the resolution of the equations of motion for the Cholesky amplitude matrices (3.17). The new oscillation scale is (at least) three orders of magnitude smaller than  $k^2/a^2$ . In the hypothetical case of a very large mass, the actual structure of the counterterms, provided by initial conditions (proportional to  $\langle \dot{\Phi}_A, \dot{\Phi}_B \rangle_{t_0}^2 \sim \omega_{\text{eff}}^2$ ) and equations of motion in (3.20), will affect the effective oscillating frequencies in exactly the same way. Therefore, due to this suppression, we can increase the time step required for resolving each Cholesky mode, reducing the computational time remarkably when compared with other schemes.

In order to prevent convergence issues coming from any harmless inaccuracies in defining initial conditions (from either Minkowski or Bunch-Davies vacua), we evolve the modes for a couple of e-folds using smaller time steps. After a few iterations, the time step can be significantly increased. Consequently, modes can be injected from smaller length scales to increase the precision of the initial conditions for the correlators.

In Figure 3.8, we observe that there is no reason to expect any change in the shape of the spectrum if we decide to inject the modes from a different physical wavelength surface, even when this surface is deep inside subhorizon scales.

In Figure 3.9, we observe the evolution of two of the amplitude modes which constitute the spectrum injected from  $k_{\text{phys}} = 10^3 H_e$ , where  $H_e$  is the Hubble parameter at the end of inflation. The injection scheme described in section 3.3 is applied in order to collect the correlation amplitudes on a “screen” located at  $N \approx 88.3$ . Notice the decay and the absence of oscillations before the horizon crossing.

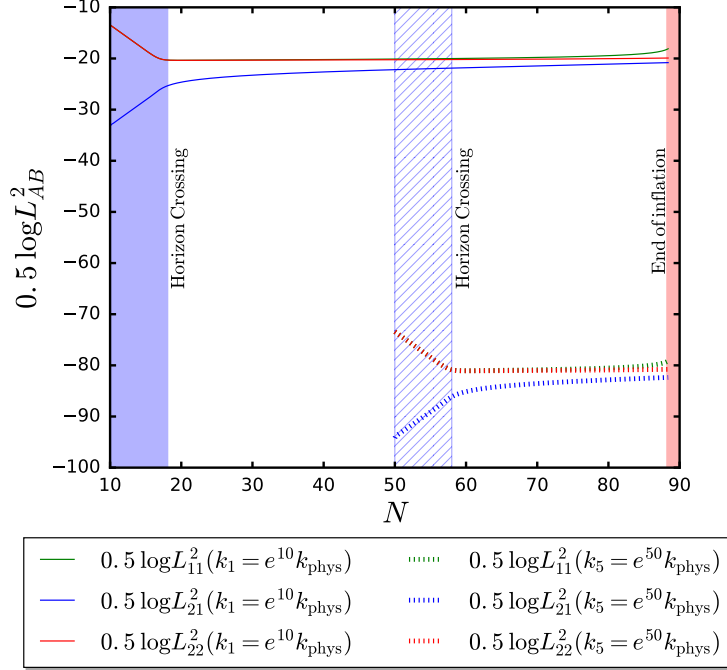


Figure 3.9: Evolution of two real Cholesky modes inserted at  $N \equiv \ln a = 10$  and  $N = 50$ . We detect the suppression of oscillations before crossing the horizon (at  $\ell = 1/H$ ).

In Appendix C we present our results for the two-point correlators as calculated by both of the approaches we used to find the spectrum. Results from the “random sampling code” are labeled as *standard* and the outcome from the direct evolution of the Cholesky factors is labeled as *gauged*. Both sets of results agree with a margin of relative uncertainty smaller than 0.1%. The speed enhancement in the *gauged* routine allows us to insert more modes with negligible computational cost.

Using our method, it is also possible to calculate the comoving curvature perturbations, which are given by

$$\zeta_{\mathbf{k}} = \frac{H}{\dot{\phi}_A \dot{\phi}_B} \left( \dot{\phi}_B \Phi_B \right), \quad (3.25)$$

in the spatially flat gauge. Therefore, we find its corresponding power spectrum:

$$\langle \zeta_{\mathbf{k}}^2 \rangle_{t > t_0} = \frac{H^2}{\left( \dot{\phi}_A \dot{\phi}_B \right)^2} \left[ \dot{\phi}_B \dot{\phi}_C \right] \langle \Phi_B, \Phi_C \rangle_{t > t_0}, \quad (3.26)$$

where  $\langle \Phi_B, \Phi_C \rangle_{t > t_0}$  is now reconstructed at all instants of time by multiplying the Cholesky factors  $L_{BD}$  as these evolve. As an additional result, we tested the production of primordial curvature fluctuations in the well-known double quadratic potential as proposed in [200,

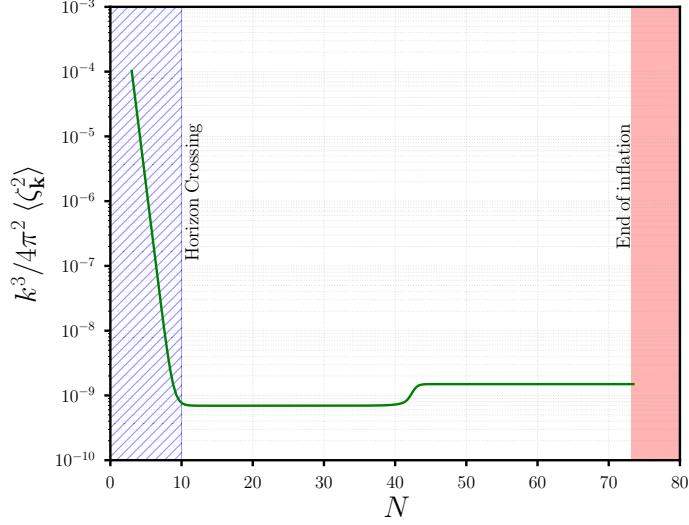


Figure 3.10: Evolution of  $\langle \zeta_{\mathbf{k}}^2 \rangle$  as a function of the time variable  $N \equiv \ln a$ . Notice the change of the spectrum in super-horizon scales, it is now possible to inject the modes from smaller length scales and observe the earlier stages of evolution.

[137, 161, 28, 105]

$$V(\phi, \chi) = \frac{m_\phi^2}{2} \phi^2 + \frac{m_\chi^2}{2} \chi^2, \quad (3.27)$$

at super-horizon scales. The shape of this potential is an elliptic paraboloid when we use the same parameters as in [137]:  $m_\phi = 1.4 \times 10^{-6} M_{\text{Pl}}$  and  $m_\chi = 7m_\phi$ . Turning field trajectories are generated by the broken azimuthal symmetry of the potential in (3.27). We pick  $\phi_0 = \chi_0 = 12M_{\text{Pl}}$  and  $\dot{\phi}_0 = \dot{\chi}_0 = 0$  as initial conditions for the background fields. In Figure 3.10 we use our decomposition method for a mode with  $k \approx 1.3 \times 10^5 H_*$ , where  $H_*$  is the Hubble parameter at the initial point of the field trajectory. We reproduce the spectrum of primordial curvature perturbations, which coincides exactly with the results obtained in [137]. It is relevant to study turning trajectories in field space since these are the source of curvature perturbations even in more complicated potentials.

### 3.5 Discussion

In this chapter, we present a new method to separate fast and slow scales in the context of multifield models of inflation. We describe a scheme based on the Cholesky factorization of any positive-definite correlation matrix.

As an outcome, we manage to find equations of motion for the “square root” of the correlation matrix in terms of slowly varying quantities. After reviewing the dynamical properties and contributions of the background fields, we specify a set of approximate initial conditions for the evolving system, and check that our results are consistent with



straightforward averaging over all the realizations of the evolved random fields. We use the new code to calculate spectra of a few well-known models, and check that the shape of the spectrum depends on the choice of background trajectories.

This perspective based on dynamical Cholesky decomposition is significantly different from previous efforts in [224, 200]. More recently, the Hamiltonian evolution of the field correlators  $\langle \Phi_A, \Phi_B \rangle$  was considered in [83], which is a transport scheme quite similar to ours in spirit. However, our method achieves significant computational gains by separating fast time scale of the sub-horizon mode evolution. Additionally, in our evolution scheme  $\langle \hat{\chi}_A, \hat{\chi}_B \rangle = \delta_{AB}$  at every instant in time, which makes it convenient to generate properly-correlated random realizations of the fields for Monte-Carlo simulations.

This approach can be easily extended to a diverse number of systems ruled by (almost) any perturbative manifestation arising from hyperbolic differential equations, which present fairly similar structures. We will leave the non-Gaussian extension of this method in application to bispectrum computations.

## Chapter 4

# Unbraiding the bounce: superluminality around the corner

In this chapter, we present a different type of EFT, where the dynamics of a theory are now generated by including higher-order derivatives in the effective action which modify the kinetic term. Nevertheless, the equations of motion for this theory remain being second-order. The production of a healthy bouncing cosmology (which contract the Hubble scale up to a minimum size, enabling thermal contact, and then re-expand) is a step forward towards a viable alternative to inflation, producing a sensible expansion history free of singularities. It is important to notice that a satisfactory non-singular bounce might not require from a complete description of the theory in the ultraviolet limit, including Quantum Gravity, while remaining coherent with the observed stages of homogeneity and isotropy seen in Cosmic Microwave Background (CMB).

Since 2010 it is well known that minimally-coupled scalar-tensor theories with *Kinetic Gravity Braiding* [79] can dynamically violate the Null Energy Condition (NEC)<sup>1</sup> and cross the phantom divide<sup>2</sup> without developing ghost and gradient instabilities<sup>3</sup>, see [79, 152, 72, 96]. For a recent review of NEC violation see e.g. [211]. These kinetically braided theories are generalizations of two families of models: (a) the k-essence models in [22, 25, 24, 114], which now includes a braiding term, and (b) the decoupling limit of DGP (Dvali-Gabadadze-Porrati) in [168, 185] or cubic Galileon [186] which are extended to also include higher nonlinear derivative interactions. The nonlinear interactions break the Galilean symmetry in the field space even in the Minkowski spacetime, but do not

<sup>1</sup>For a system with energy-momentum tensor  $T^{\mu\nu}$ , the NEC holds provided  $T_{\mu\nu}n^\mu n^\nu \geq 0$  for all null / light-like vectors  $n^\mu$ .

<sup>2</sup>This divide is physically impossible to cross [242, 135, 61, 251, 95, 77] for k-essence, and theories with minimal coupling to gravity and without higher-derivatives introducing the braiding between the derivatives of the metric and of the scalar field.

<sup>3</sup>Despite the positivity of the energy density for linear perturbations, it is important to note that any theory violating the NEC necessarily has the energy density unbounded from below [221].

change the speed of propagation for the gravitational waves. For timelike field derivatives, kinetically braided theories represent imperfect fluids with the energy transport along the spatial gradients of the chemical potential [203]. The form of the braiding term defines the dependence of the transport coefficient on the chemical potential. In the cubic Galileon the transport coefficient is given by the square of the chemical potential. In the general *Kinetic Gravity Braiding*, the transport coefficient can be an arbitrary function of the chemical potential including the most natural case of a constant.

After the rediscovery [78, 153] of the general Horndeski theories [134] in 2011, these kinetically braided models are often referred to as “first two terms of Horndeski theories” or simply generalized / “cubic” Galileons. Since 2011 it is known [204, 93] that these theories can describe spatially flat Friedmann universes evolving from contraction to expansion while being manifestly free of ghost and gradient instabilities around this cosmological bounce. Hence, these theories can realize a smooth “healthy” bounce. The possibility of the bounce in such systems was briefly mentioned in [72]. Furthermore, in [93] it was demonstrated that we can easily construct spatially flat “healthy” bouncing universes with bouncing solutions of a non-vanishing measure. This reference established that there is a continuum of such minimally coupled healthy bouncing theories. The work provided sufficient conditions in the form of inequalities on the Lagrangian free functions to ensure a “healthy” bounce. Kinetically braided bouncing models also work in the (unavoidable) presence of normal matter, such as radiation, etc [93]. In particular, they allow for a smooth transition to the radiation-dominated epoch (“Hot G-Bounce”, see Fig 1, on page 10 in [93]). In the same work, singularities in the gravitational metric and in the acoustic metric describing the cones of propagation for the scalar perturbations were discussed. These singularities can be at the beginning or at the end of the evolution, or both. Physically, these singularities correspond to (naively infinitely) strongly coupled configurations, where either the quasi-classical general relativity (GR) or quasi-classical description of the scalar field break down. Both theories are not renormalizable, have dynamical cones of influence/geometry, and require a nontrivial ultraviolet (UV) completion. Under certain assumptions, the presence of these singularities was later proven for general kinetically braided theories in [165]. This proof was extended to general Horndeski theories in [150] and to theories interacting with another scalar field in [157, 150]<sup>4</sup>. In this respect, kinetically braided theories, as well as more general Horndeski theories are not that different from regular GR, where the existence of singularities is a well established fact [128]. The only advantage is that it is possible to relocate the initial cosmological singularity in the classical dynamical equations from the expanding to the contracting stage, even in a spatially flat universe. Hence the big bang could occur not at the beginning of the cosmological expansion, but at the onset of contraction. This crucial

<sup>4</sup>It seems that we can have a healthy evolution, without any end or the beginning singularities, in theories going beyond Horndeski construction [73, 59].

difference opens up new ways of thinking about initial conditions in the early universe. This is relevant for the initial conditions of inflation, which could now be preceded by a contraction, bounce or even the Minkowski space [72, 71, 130, 131, 196, 154, 187]. There is plenty of theoretical and philosophical motivation to consider bounces and NEC violation in the early universe; for recent reviews see e.g. [46, 35, 211]. If the NEC can be violated by a physical system we can even consider such an exotic opportunity as a creation of a universe in a laboratory [210].

An interesting feature of kinetically braided theories is that the scalar perturbations around generic backgrounds propagate along an “acoustic” cone different from the light cone [7, 185, 79, 100]. This “acoustic” cone can be wider than the light cone or protrude outside of it just in some directions. In these cases the perturbations propagate faster than light [7]. Contrary to k-essence where it is possible to establish subluminality constraints on the form of the Lagrangian, in kinetically braided theories it seems that there are no such conditions. For a recent discussion on the dilatationally invariant subclass of these theories see [157]. There are examples [71, 94] of such theories where there is no superluminality for *all* cosmological configurations; for the proof see [94]. However, this only happens in an idealized universe without any external matter. An unusual property of the kinetically braided theories is that the value of the sound speed depends not only on the local state of the field, but also on the energy-momentum tensor of other matter fields present in the same point of spacetime. Even in the case of totally subluminal cosmological phase space [71, 94], an introduction of external matter sources instigates the superluminality at least for some regions of phase space [94].

The superluminality (with hyperbolic equations of motion for perturbations) per se does not necessarily cause any causal paradoxes [31, 115, 50, 23, 144, 51]. Nevertheless, it is always possible to construct nontrivial non-cosmological configurations (in these configurations, the Hubble parameter is not a real solution of Friedmann equations), where closed causal curves (CCC) can be formed at the level of classical dynamics [7, 101, 100]. Operators in quantum field theory (QFT) cannot be time-ordered along these curves, which behave as time machines propagating fluctuations to the past. However, similarly to GR where we have *the chronology protection conjecture* due to Hawking [127], QFT may protect the system from forming CCC in all such theories with dynamical cones of influence, see e.g. [31, 56, 50].

On the other hand, there are powerful arguments that EFTs with at least one configuration permitting superluminality do not allow for a standard Wilsonian UV-completion in terms of local, Lorentz-invariant and weakly coupled fields or strings [7]. In order to apply these arguments, the superluminal configurations should belong to an EFT with a viable ultraviolet limit. The latter condition is rather nontrivial, as different semiclassical states can be isolated by regions with ghosts (fields coupled to gravity with negative kinetic energy), regions with strong coupling, or other features where the EFT breaks down. In

these cases each separated region corresponds to a *different* EFT. The way out is provided by a recent conjecture concerning a possible Wilsonian UV-completion in such nonstandard theories. It was conjectured [91, 92] (see also [89]), that a theory can UV-complete itself by forming *classicalons* - extended field configurations playing the role of elementary quantum excitations, hence, the term *classicalization*. These *classicalons* appear as intermediate long-lived states and slowly decay into a large number of soft IR elementary excitations. Later, it was argued that this UV-completion by *classicalization* takes place, only provided some configurations allow for the superluminal propagation [243, 88, 90]. The extended elementary excitations may induce a non-locality of the UV completion of these theories [147].

Following this discussion, it is expected that general bouncing cosmologies can only be realized in theories equipped with superluminality around some configurations. Consequently, these theories cannot be UV-completed in the standard way. Only classicalization, or maybe some other yet unknown construction, can UV-complete such bouncing models.

In 2016, Ijjas and Steinhardt (IS) proposed in [139] an interesting “inverse” method. The method allows one to find particular realizations of the cosmological bouncing scenario in a specific subclass of kinetically braided theories. In a bouncing scenario, the Hubble scale contracts to a minimal size and then re-expands. Specifically, they found a model for a given cosmological evolution  $H(t)$ , where  $H(t)$  is the Hubble parameter. Kinetically braided theories have two free functions,  $K(\phi, \partial\phi)$  and  $G(\phi, \partial\phi)$ . Thus, there is enough freedom to choose not only  $H(t)$ , but also a time dependence for one of the two coefficients in the quadratic action for curvature perturbations. The advantage of this method is that it allows to construct a theory for a given evolution while keeping a direct control over perturbations. This procedure enables one to find  $\phi(t)$  and to specify different free functions in the Lagrangian as functions of time. Hence, this method yields an *implicit* construction of the Lagrangian of the model realizing the bounce. Using the inverse method, IS found a particular theory, which accommodates the bounce free of ghosts and gradient instabilities. For convenience we denote this realization as *IS-bounce*. The *IS-bounce* was not only claimed to be free from ghost and gradient instabilities, but also to be exempt from superluminal propagation of perturbations. The reconstructed solution also included healthy stages before and after NEC violation. In this way, the system could enter the NEC-violating bouncing stage and leave it without encountering any problem for stability or UV-completion. These findings are illustrated by explicit numerical calculations and plots corresponding to two sets of five independent free parameters.

The layout of this chapter, where we analyze the system introduced by Ijjas and Steinhardt in [139], is as follows: First, in section 4.1 we derive and discuss the main equations for the dynamics of cosmological solutions and perturbations in *braided* theories under consid-

eration. In section 4.2, we briefly discuss the notion of acoustic geometry for cosmological perturbations, convenient variables and their relations by different gauge and conformal transformations. Then, in section 4.3, we uncover the specific structure of the Lagrangian by deriving the functions  $k(\phi)$  and  $q(\phi)$  of the theory. We then use the derived action to study the *IS-bounce* for the two sets of parameters suggested in [139]. Furthermore, in section 4.4 we reveal the phase space structure in a patch surrounding the IS bouncing trajectory, as plotted in Figure 4.4. Additionally, we look for cycles and other features of this patch by spanning it with sufficient field trajectories. We also show the regions where initial conditions provide a viable expansion history (if these exist). Only in this chapter, we use the signature  $(+, -, -, -)$  and the unit convention fixing  $M_{\text{Pl}}^2 = 1$ .

## 4.1 Model and main equations

The *IS-bounce* uses a class of Kinetic Gravity Braiding theories with explicitly strongly *broken* shift-symmetry  $\phi \rightarrow \phi + c$ , where the action for the field excludes the curvature term seen in (1.11)

$$S = \frac{1}{2} \int d^4x \sqrt{-g} \left( k(\phi) (\partial\phi)^2 + \frac{1}{2} q(\phi) (\partial\phi)^4 + (\partial\phi)^2 \square\phi \right), \quad (4.1)$$

where

$$(\partial\phi)^2 \equiv g^{\mu\nu} \partial_\mu \phi \partial_\nu \phi \equiv 2X, \quad \square\phi \equiv g^{\mu\nu} \nabla_\mu \nabla_\nu \phi, \quad (4.2)$$

where  $\nabla_\mu$  is the usual Levi-Civita connection<sup>5</sup>. The scalar field is supposed to be minimally coupled to gravity. Hence, the theory is defined by two free functions  $k(\phi)$  and  $q(\phi)$ . In notation of [79] where generic theories of the type

$$S = \int d^4x \sqrt{-g} [K(X, \phi) + G(X, \phi) \square\phi], \quad (4.3)$$

were introduced, we have<sup>6</sup>

$$K(X, \phi) = k(\phi) X + q(\phi) X^2, \quad G(X, \phi) = X. \quad (4.4)$$

This identification allows us to directly use all necessary formulas derived in [79] (see also [152]) for *arbitrary*  $K(X, \phi)$  and  $G(X, \phi)$  for the background dynamics and perturbations

<sup>5</sup>Further we use: the standard notation  $\sqrt{-g} \equiv \sqrt{-\det g_{\mu\nu}}$  where  $g_{\mu\nu}$  is the metric, the signature convention  $(+, -, -, -)$  (contrary to [139]), and the units  $c = \hbar = 1$ ,  $M_{\text{Pl}} = (8\pi G_{\text{N}})^{-1/2} = 1$ .

<sup>6</sup>At the beginning the authors of [139] also used  $G(X, \phi) = b(\phi) X$ , however this additional free function  $b(\phi)$  can be eliminated by the simple field-redefinition:  $d\bar{\phi} = b^{-1/3}(\phi) d\phi$ .

in the spatially flat Friedmann universe

$$ds^2 = dt^2 - a^2(t) d\mathbf{x}^2. \quad (4.5)$$

Below, instead of rederiving formulas for the particular case (4.4), as it was done by IS, we use general results from [79]. In particular, the pressure is

$$\mathcal{P}(\phi, X, \ddot{\phi}) = K - 2XG_{,\phi} - 2XG_{,X}\ddot{\phi} = kX + qX^2 - 2X\ddot{\phi}, \quad (4.6)$$

and the broken Noether charge density corresponding to the shift  $\phi \rightarrow \phi + c$  yields

$$J = \dot{\phi} \left( K_{,X} - 2G_{,\phi} + 3\dot{\phi}HG_{,X} \right) = \dot{\phi} \left( k + 2qX + 3\dot{\phi}H \right), \quad (4.7)$$

where  $H = \dot{a}/a$  is the Hubble parameter. The variation of the action (4.3) with respect to the field  $\phi$  gives an equation of motion, which in terms of the charge density takes the following elegant form

$$\dot{J} + 3HJ = \mathcal{P}_{,\phi}. \quad (4.8)$$

The *kinetic braiding* with gravity reveals itself once we have found how this equation depends on  $\dot{H}$ . Moreover, the general expression for the energy density

$$\varepsilon(\phi, \dot{\phi}, H) = \dot{\phi}J - \mathcal{P} + 2XG_{,X}\ddot{\phi} = 2X \left( K_{,X} - G_{,\phi} + 3\dot{\phi}HG_{,X} \right) - K, \quad (4.9)$$

reduces for the choice (4.4) to

$$\varepsilon = kX + 3qX^2 + 6\dot{\phi}HX. \quad (4.10)$$

Further the first Friedmann equation reads

$$3H^2 = \varepsilon = kX + 3qX^2 + 6\dot{\phi}HX, \quad (4.11)$$

while for the second equation, we have

$$\dot{H} = -\frac{1}{2}(\varepsilon + \mathcal{P}) = XG_{,X}\ddot{\phi} - \frac{1}{2}\dot{\phi}J. \quad (4.12)$$

Later, in section 4.3, our inversion procedure will require that both the energy density and the first Friedmann equation contain a term linear in  $H$ . Therefore for *kinetically braided* systems the branches resulting from the first Friedmann equation do not correspond to expansion and contraction of the universe. Indeed, solving the quadratic equation we obtain

$$H_{\pm} = XG_{,X}\dot{\phi} \pm \sqrt{\left( XG_{,X}\dot{\phi} \right)^2 + \frac{1}{3}(2X(K_{,X} - G_{,\phi}) - K)}. \quad (4.13)$$

This relation implies that not all configurations  $(\phi, \dot{\phi})$  with positive energy density are allowed, but only those satisfying an additional condition

$$6X (XG_{,X})^2 + 2X (K_{,X} - G_{,\phi}) - K \geq 0. \quad (4.14)$$

Finally it is convenient to write an equation of motion for the scalar field (4.8) where  $\dot{H}$  is expressed through (4.12)

$$D\ddot{\phi} + 3J(H - \dot{\phi}XG_{,X}) + \varepsilon_{,\phi} = 0, \quad (4.15)$$

where our general expression

$$D = K_{,X} + 2XK_{,XX} - 2G_{,\phi} - 2XG_{,X\phi} + 6\dot{\phi}H(G_{,X} + XG_{,XX}) + 6X^2G_{,X}^2, \quad (4.16)$$

reduces for the choice (4.4) to

$$D = k + 6Xq + 6\dot{\phi}H + 6X^2. \quad (4.17)$$

The quantity  $D$  corresponds to the determinant of the matrix in front of the second derivatives  $(\ddot{\phi}, \ddot{a})$  in the equations (4.12) and (4.8). The sound speed is given by the formula (A.11) page 36 in [79]. Now we are prepared to write the formulas for the perturbations. We use the ‘‘unitary’’ gauge, and embed the spacelike hypersurface  $\delta\phi = 0$  into the perturbed Friedmann universe using the ADM (Arnowitt-Deser-Misner) decomposition

$$ds^2 = N^2 dt^2 - a^2 e^{2\zeta} \delta_{ik} (N^i dt + dx^i) (N^k dt + dx^k), \quad (4.18)$$

which is useful to compare with the most general line element with scalar perturbations written in conformal time  $\tau$

$$ds^2 = a^2 \left[ (1 + 2\varphi) d\tau^2 + 2B_{,i} dx^i d\tau - [(1 - 2\psi) \delta_{ik} - 2E_{,ik}] dx^i dx^k \right]. \quad (4.19)$$

As it was pointed out in [152], the variable  $\zeta$  is not a *comoving* curvature perturbation, because there is an energy flow  $T_i^t = \dot{\phi}^3 G_X \partial_i \delta N$  in the gauge (4.18). Expressing the lapse fluctuation  $\delta N$  through the longitudinal part of the momentum constraint (see (A.5) on page 36 in [79])

$$(H - \dot{\phi}XG_{,X}) \delta N = \dot{\zeta}, \quad (4.20)$$



one obtains the quadratic action for curvature perturbations  $\zeta$ <sup>7</sup> (see (A.8) on page 36 in [79])

$$S_c = \frac{1}{2} \int dt d^3x a^3 \left( A(t) \dot{\zeta}^2 - \frac{B(t)}{a^2} (\partial_i \zeta)^2 \right). \quad (4.21)$$

The formula for the normalization of the kinetic term is given by (A.9) page 36 in [79]

$$A = \frac{2XD}{\left(H - \dot{\phi}XG_{,X}\right)^2}. \quad (4.22)$$

Hence, it is the coefficient  $D$ , given by (4.16), in front of the second derivative in the reduced equation of motion (4.15). The positive value of this coefficient determines that the perturbations are free of ghosts. It is interesting to note that curves on phase space with  $D = 0$  correspond to an infinitely-strong coupling of perturbations and to pressure-like curvature singularity [79], where GR breaks down, see (4.6) and (4.15). Clearly the reduced equation of motion is singular on these curves.

$$c_s^2 = \frac{B(t)}{A(t)} = \frac{\dot{\phi}XG_{,X} \left(H - \dot{\phi}XG_{,X}\right) - \partial_t \left(H - \dot{\phi}XG_{,X}\right)}{XD}, \quad (4.23)$$

where we assumed that the field  $\phi$  is the only source of energy-momentum. We can write

$$\frac{1}{2}B(t) = \frac{\dot{\phi}XG_{,X} \left(H - \dot{\phi}XG_{,X}\right) - \partial_t \left(H - \dot{\phi}XG_{,X}\right)}{\left(H - \dot{\phi}XG_{,X}\right)^2} \quad (4.24)$$

after multiplying (4.22) by (4.23). It is natural to introduce a quantity

$$\gamma = H - \dot{\phi}XG_{,X} \quad (4.25)$$

in terms of which the expression for  $B$  reads

$$\frac{1}{2}B(t) = \frac{d}{dt}\gamma^{-1} + H\gamma^{-1} - 1 \quad (4.26)$$

The expression for  $B(t)$  was written in this elegant form in [139] for a particular choice (4.4) of functions  $K$  and  $G$ . Before that this variable (4.25) was used in [165] and [205]. The vanishing  $\gamma$  corresponds to the change of the branch in the solution of the first Friedmann equation with respect to the Hubble parameter (4.13). In that case we cannot express the perturbation of the lapse  $\delta N$  from the momentum constraint (4.20). Thus, there is no other option than using other dynamical variables to describe the dynamics around this point.

<sup>7</sup>Note that [139] does not use the canonical normalization with 1/2 in front of the action. Hence our coefficients  $A(t)$  and  $B(t)$  are twice larger than those in [139].

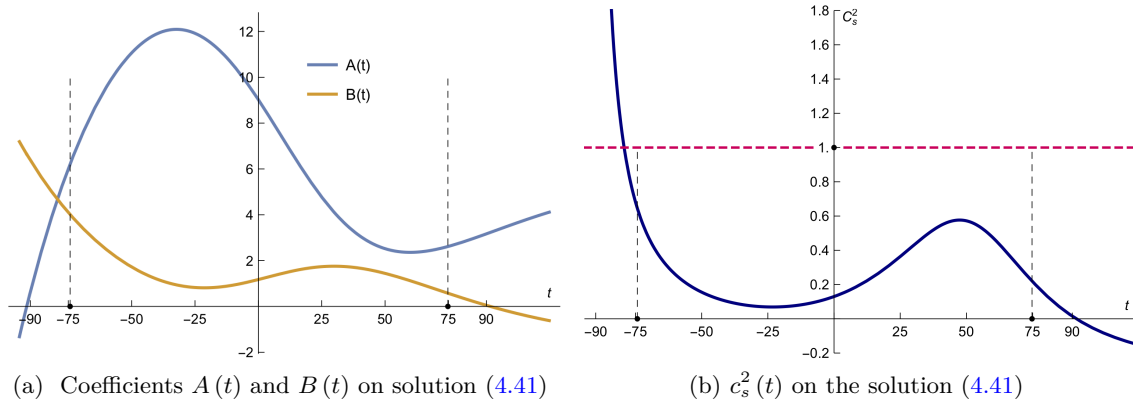


Figure 4.1: The evolution of the coefficients in the quadratic action (4.21) for the scalar perturbations is shown here for the IS solution for the choice of parameters (4.50). All quantities are in the Planck units. The dashed black vertical lines correspond to  $t_- \simeq -74$  where the stage with NEC violation starts and to  $t_+ \simeq 75$  where the NEC gets restored. Our right figure corresponds to Figure 1 from [139] just with a slightly extended time range. Clearly, less than  $10 t_{\text{Pl}}$  before the beginning of the Phantom stage the sound speed is *superluminal*. On top of that, just  $15 t_{\text{Pl}}$  after NEC is restored and the bouncing phase is finished the system enters into an elliptic regime / regime with a gradient instability: where  $B < 0$  and respectively  $c_s^2 < 0$ . When the system approaches the regime, where  $c_s^2 = 0$ , the quantum fluctuations *diverge* and the system becomes strongly coupled. In this case the semiclassical equations completely lose predictability. On the other hand, just some  $15 t_{\text{Pl}}$  before the beginning of the Phantom stage the coefficient  $A(t)$  vanishes and the sound speed blows up. In order to enter the unmodified Phantom bouncing stage and leave it without either starting or ending in these strongly-coupled regimes, we need to modify dynamics on time-scales of  $10 t_{\text{Pl}}$  which is a clear challenge for the scenario.

There is an interesting discussion [34, 205, 138] of gauge issues, choice of dynamical variables and slicing around  $\gamma = 0$ . This phenomenon is not special to *kinetically braided* theories. A spatially-flat Friedmann universe driven by a scalar field with canonical kinetic term and a negative potential can evolve from expansion to contraction, see e.g. [102]. At the turning point  $\gamma = H = 0$ , and it is not possible exclude  $\delta N$  from the action for perturbations.

For the Lagrangian given by (4.4) one obtains

$$\gamma(t) = H - \dot{\phi}X, \quad (4.27)$$

so that (4.24) (or (4.26)) yields

$$B = \frac{2X \left( k + 2qX + 4H\dot{\phi} + 2\ddot{\phi} - 2X^2 \right)}{\left( H - \dot{\phi}X \right)^2}, \quad (4.28)$$

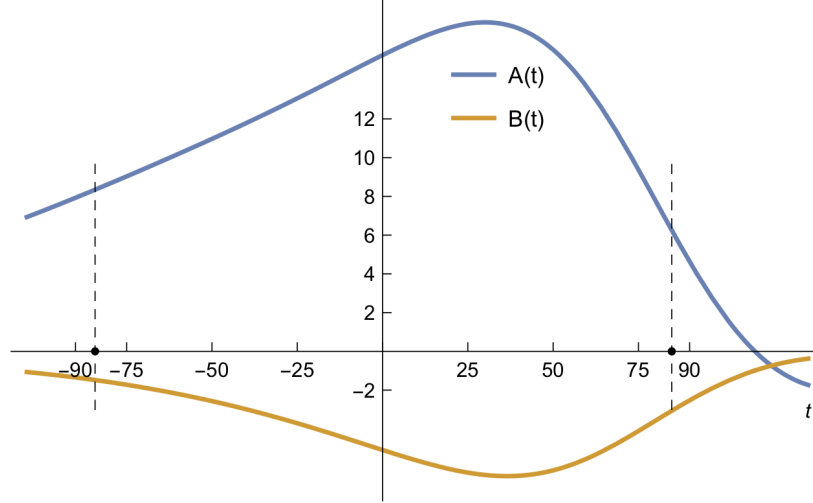


Figure 4.2: The evolution of the coefficients in the quadratic action (4.21) for the scalar perturbations for the IS solution for the second choice of parameters (4.53). All quantities are in the Planck units. The dashed black vertical lines correspond to  $t_- \simeq -84.3$  where the Phantom stage with NEC violation starts and to  $t_+ \simeq 84.8$  where the NEC gets restored.

while (4.22) reads

$$A = \frac{2X (k + 6qX + 6\dot{\phi}H + 6X^2)}{(H - \dot{\phi}X)^2}. \quad (4.29)$$

It is also useful to rewrite the action (4.21) in terms of the the canonically-normalized Mukhanov-Sasaki variable

$$v = z\zeta, \quad (4.30)$$

where we denoted

$$z = a\sqrt{A} = a\sqrt{\frac{2XD}{\gamma^2}}.$$

Then the action reads

$$S_c = \frac{1}{2} \int d\tau d^3x \left( v'^2 - c_s^2 (\partial_i v)^2 + \frac{z''}{z} v^2 \right), \quad (4.31)$$

where the prime denotes a derivative with respect to conformal time  $\tau$ , defined through  $d\tau = dt/a$ .

It is worth noting that vanishing  $D$  generically corresponds to infinities of the square of the sound speed, (4.23) and to an infinitely strong coupling between canonically normalized perturbations  $v$ .

## 4.2 Conformal transformations, gauges and acoustic geometry

As this chapter discusses superluminality, it is interesting to look at the effective (or acoustic) metric where the scalar perturbations propagate. It is possible to write the action (4.21) in an elegant way

$$S_c = \frac{1}{2} \int d^4x \sqrt{-\mathcal{G}} \mathcal{G}^{\mu\nu} \partial_\mu \zeta \partial_\nu \zeta, \quad (4.32)$$

where the *covariant acoustic* metric  $\mathcal{G}_{\mu\nu}^{-1}$  for curvature perturbations is

$$dL^2 = \mathcal{G}_{\mu\nu}^{-1} dx^\mu dx^\nu = z^2 c_s^2 (d\tau^2 - d\mathbf{x}^2), \quad (4.33)$$

the *contravariant* metric is inverse to it and is written with two raised indices consistent with the usual tensor notation. This metric  $\mathcal{G}_{\mu\nu}^{-1}$  is singular for  $\gamma = 0$ , as  $z \rightarrow \infty$ . It seems that classically this singularity is not a problem [34, 205, 138]. Though it is interesting to understand the quantum mechanical consequences of this singular behavior.

The transformation to the canonical Mukhanov-Sasaki variable can be considered as a *conformal* transformation of the acoustic metric

$$\mathcal{G}_{\mu\nu}^{-1} \rightarrow \ell_{\mu\nu}^{-1} = z^{-2} \mathcal{G}_{\mu\nu}^{-1}, \quad \zeta \rightarrow v = z\zeta.$$

The gauge part of the metric follows the propagation of the fluctuations of the field  $\delta\phi$ . In the unitary gauge this is not obvious as  $\delta\phi = 0$ . However, we can perform a gauge transformation, see e.g. page 293 [182], so that  $\widetilde{\delta\phi} = -\phi' \xi^0$  and  $\widetilde{\psi} = \psi + \xi^0 a' / a = -\zeta + \xi^0 a' / a$ . For example for  $\xi^0 = \zeta a / a'$ , the spatial metric becomes unperturbed,  $\delta g_{ik} = 0$ , and so in this “spatially flat” gauge

$$\delta\phi|_{\text{flat}} = -\frac{\dot{\phi}}{H} \zeta.$$

Using analogy between  $\gamma$  in *braided* models and  $H$  in k-essence we can introduce the “ $\gamma$ -gauge”

$$\xi^0 = \frac{\zeta}{a\gamma}, \quad (4.34)$$

which yields

$$\tilde{\varphi} = \varphi - \frac{1}{a} (a\xi^0)' = \delta N - \frac{1}{a} (a\xi^0)' = \zeta \frac{\dot{\gamma}}{\gamma^2},$$

where we used the constraint (4.20), and

$$\delta\phi|_\gamma = -\frac{\dot{\phi}}{\gamma} \zeta. \quad (4.35)$$

Using  $\delta\phi|_\gamma$  the action (4.21) reads

$$S_c = \frac{1}{2} \int d^4x \sqrt{-\mathcal{G}} \mathcal{G}^{\mu\nu} \partial_\mu \zeta \partial_\nu \zeta = \frac{1}{2} \int d^4x \sqrt{-C} C^{\mu\nu} \partial_\mu \delta\phi|_\gamma \partial_\nu \delta\phi|_\gamma + \dots, \quad (4.36)$$

where the ellipsis stands for a “mass-like” term without involving derivatives of  $\delta\phi|_\gamma$ . The change of variable  $\zeta \longleftrightarrow \delta\phi|_\gamma$  can be understood as another *conformal* transformation

$$\mathcal{G}_{\mu\nu}^{-1} \rightarrow C_{\mu\nu}^{-1} = \omega^2 \mathcal{G}_{\mu\nu}^{-1}, \quad \zeta \rightarrow \delta\phi|_\gamma = -\omega^{-1} \zeta,$$

where  $\omega = \gamma/\dot{\phi}$  so that

$$dC^2 = C_{\mu\nu}^{-1} dx^\mu dx^\nu = Dc_s a^2 (c_s^2 d\tau^2 - d\mathbf{x}^2). \quad (4.37)$$

The acoustic metric  $C_{\mu\nu}^{-1}$  differs from the metric given by the formula (3.15) [79], by the normalization  $D^2 c_s^3$ . This conformal factor is not important for the propagation of the high-frequency perturbations, and related stability studies, but is needed for a proper normalization of the action. This transformation provides a short explanation for the so-called “DPSV trick” discussed in [158]. It is instructive to compare this acoustic metric with the one obtained for k-essence and cosmological perturbations in Appendix C of [31]. There it was demonstrated that  $\delta\phi|_{\text{flat}}$  propagate in the acoustic metric (4.37) with  $D = \varepsilon_{,X} = K_{,X} + 2XK_{,XX}$ . There is a continuity in  $G_{,X}$  between “ $\gamma$ -gauge” and “flat gauge”.

The acoustic metric derived in [79] is sufficiently general and can be used to investigate the speed of propagation of fluctuations, gradient (in)stabilities and possible appearance of ghosts also around general inhomogeneous and anisotropic backgrounds. In particular, evaluating the components of the acoustic metric enables us to exclude wormholes [212, 213] and static semiclosed worlds [99]. The advantage of the acoustic metric is that it can be used for stability checks for high frequency perturbations without deriving the action for perturbations. The latter can be especially complicated in the presence of other forms of matter, apart from this imperfect fluid.

Finally it is worth mentioning that we can express perturbations through gauge-invariant variables which coincide with the conformal Newtonian gauge (notation as in [182])

$$-\zeta = \Psi + \frac{H}{\dot{\phi}} \bar{\delta\phi},$$

and respectively

$$\delta\phi|_\gamma = \frac{H}{\gamma} \bar{\delta\phi} + \frac{\dot{\phi}}{\gamma} \Psi.$$

### 4.3 Inverse method: reconstructing the theory from its solutions

The authors of IS-bounce postulated a fairly simple time-dependence of the Hubble parameter

$$H(t) = H_0 t \exp\left(-F(t - t_*)^2\right), \quad (4.38)$$

where  $H_0$ ,  $F$  and  $t_*$  are constants. They proposed an “inverse method” to find free functions  $k(\phi)$  and  $q(\phi)$  in (4.1) which can realize this cosmological evolution. The NEC is violated between  $t_-$  and  $t_+$  where

$$t_{\pm} = \frac{t_* \pm \sqrt{t_*^2 + 2F^{-1}}}{2}. \quad (4.39)$$

The bounce occurs at  $t = 0$ . For the bounce we have to start from the  $H_-$  branch of the solutions of the first Friedmann equation (4.13). The key observation of the “inverse method” proposed in [139] is that one can also independently postulate  $\gamma(t)$  in (4.26). The IS-bounce postulates

$$\gamma = \gamma_0 \exp(3\theta t) + H(t), \quad (4.40)$$

where  $\gamma_0$  and  $\theta$  are additional constants with respect to the already introduced  $H_0$ ,  $F$  and  $t_*$ . From (4.27) we obtain

$$\phi_{IS}(t) = \phi_0 + \int_{t_0}^t dt' [2(H(t') - \gamma(t'))]^{1/3},$$

where  $\phi_{IS}(t_0) = \phi_0$ . It is convenient to choose this initial value as  $\phi_0 = (-2\gamma_0/\theta)^{1/3} \exp(3t_0)$ , so that the particular solution postulated in IS-bounce is

$$\phi_{IS}(t) = \phi_{\star} \exp(\theta t), \quad (4.41)$$

where the field value at the bounce  $\phi_{\star}$  is given by

$$\phi_{\star} = \left(\frac{-2\gamma_0}{\theta^3}\right)^{1/3}.$$

Then the cosmological time  $t$  is expressed on the IS-bounce as

$$t = \frac{1}{\theta} \log(\phi_{IS}/\phi_{\star}). \quad (4.42)$$

The field values  $\phi_1$  and  $\phi_2$  corresponding to the beginning of the NEC violation and its restoration are given by

$$\phi_1 = \phi_{IS}(t_-), \quad \phi_2 = \phi_{IS}(t_+). \quad (4.43)$$

One has to rely on the viability of the reconstructed theory at least during the NEC violation, i.e. in this field range  $\phi_1 < \phi < \phi_2$ . Using the substitutions (4.38) and (4.40) one obtains the functions  $k(\phi)$  and  $q(\phi)$  as functions of time on the particular solution (4.41)

$$k(t) = -\frac{2(2\dot{H} + 3H^2 + \dot{\gamma} + 3H\gamma)}{(2(H - \gamma))^{2/3}}, \quad (4.44)$$

and

$$q(t) = \frac{4(2\dot{H} + \dot{\gamma} + 9H\gamma)}{3(2(H - \gamma))^{4/3}}. \quad (4.45)$$

It is convenient to introduce functions

$$W(\phi) = \exp\left[\frac{F}{\theta^2}\left(\log\left(\frac{\phi}{\phi_\star}\right) - \theta t_\star\right)^2\right], \quad (4.46)$$

and

$$\Omega(\phi) = W(\phi)\theta^3(\theta\phi)^3 + H_0\left[\log\left(\frac{\phi}{\phi_\star}\right)\left(4F\left[\log\left(\frac{\phi}{\phi_\star}\right) - \theta t_\star\right] + 2\theta(\theta\phi)^3\right) - 2\theta^2\right], \quad (4.47)$$

in terms of which the defining functions are

$$k(\phi) = -\frac{12H_0^2\log^2(\phi/\phi_\star) - 3W(\phi)\left[\Omega(\phi) - H_0\theta(\theta\phi)^3\log(\phi/\phi_\star)\right]}{W^2(\phi)\theta^2(\theta\phi)^2}, \quad (4.48)$$

and

$$q(\phi) = \frac{12H_0^2\log^2(\phi/\phi_\star) - 2W(\phi)\left[\Omega(\phi) + H_0\theta(\theta\phi)^3\log(\phi/\phi_\star)\right]}{W^2(\phi)\theta^2(\theta\phi)^4}. \quad (4.49)$$

These expressions defining the theory, which should be related to the very origin of the universe, neither look well-motivated nor natural from any point of view. Neither these functions can be stable with respect to the quantum corrections. This is the price for the chosen simple exact solution (4.38), (4.41). We are left with the following five free parameters  $H_0, \theta, F, \gamma_0, t_\star$  which specify the Lagrangian. The authors of [139] have chosen them below their Figure 1 as

$$H_0 = 3 \times 10^{-5}, \theta = 0.0046, F = 9 \times 10^{-5}, \gamma_0 = -0.0044, t_\star = 0.5, \quad (4.50)$$

all in reduced Planck units. The role of this tiny shift  $t_\star$  remained an open question for us. For this choice of parameters the field value at the bounce is  $\phi_\star \simeq 44.88$  and  $t_- \simeq -74.286$  while  $t_+ \simeq 74.786$ . Now we can plot the coefficients  $A(t)$  and  $B(t)$  and the sound speed  $c_s^2$  on the trajectory (4.41), see Figure 4.1a and Figure 4.1b respectively. On these plots we clearly see that less than 10  $t_{\text{Pl}}$  before the beginning of the Phantom stage the sound speed is *superluminal*. Moreover, just 15  $t_{\text{Pl}}$  after NEC is restored and the bouncing phase is

finished the system enters into elliptic regime / regime with the gradient instability. When the system approaches the regime, where  $c_s^2 = 0$  the quantum perturbations *diverge* and the system becomes strongly coupled. In that case the semiclassical equations completely lose predictability, since we cannot rely on the perturbative methods once the scalar perturbation  $\zeta$  is of  $\mathcal{O}(1)$ . On the other hand just some  $15 t_{\text{Pl}}$  before the beginning of the Phantom stage the coefficient  $A(t)$  vanishes and the sound speed becomes not only just superluminal, but simply *divergent*. Both divergent and vanishing sound speeds correspond to infinitely strongly coupled fluctuations. Indeed, in weakly coupled theories on short length scales  $\ell$ , where  $(kc_s)^2 \gg |z''/z|$ , it is possible to use the uncertainty relation [243, 95] to find

$$\delta v_\ell \cdot \delta v'_\ell \simeq \hbar \ell^{-3}. \quad (4.51)$$

Further estimating  $\delta v'_\ell \simeq \omega_\ell \delta v_\ell \simeq c_s \ell^{-1} \delta v_\ell$  we obtain

$$\delta v_\ell \simeq \ell^{-1} \sqrt{\hbar/c_s}, \quad \delta v'_\ell \simeq \ell^{-2} \sqrt{\hbar c_s}. \quad (4.52)$$

Hence larger values of  $c_s$  correspond to larger velocity fluctuation  $\delta v'_\ell$  on all short scales. Whereas vanishingly small  $c_s$  corresponds to a huge  $\delta v_\ell$ . The use of Feynman rules to calculate two-point functions in these non-canonical theories shows that both the field and the canonical momentum do enter the interaction vertices. Clearly very large (divergent) quantum fluctuations is a pathology. The only way to avoid circumvent these perturbative analysis is to assume that the theory is strongly coupled, so that the uncertainty relation is not saturated and that the fluctuation of momentum  $\delta v'_\ell$  is not related to the fluctuation of the field  $\delta v_\ell$  as it is in the quantum oscillator case. But then the theory is clearly strongly coupled in the quantum mechanical sense. In order to enter the unmodified Phantom bouncing stage and leave it without either starting or ending in these strongly-coupled regimes, where the dynamics need to be altered on time-scales of  $10 t_{\text{Pl}}$ , which is a clear challenge for the scenario.

The second example of IS was the set of parameters chosen below their Figure 3 as

$$H_0 = 3 \times 10^{-5}, \theta = 4.6 \times 10^{-6}, F = 7 \times 10^{-5}, \gamma_0 = -0.0044, t_* = 0.5. \quad (4.53)$$

For the corresponding times we have  $t_- \simeq -84.266$  while  $t_+ \simeq 84.766$ . Clearly the caption of the Figure 3 of [139] claims “all fundamental physical quantities including  $H(t)$  and  $c_s^2$  remain finite and positive” for this choice of parameters. However, we found that the sound speed is actually imaginary throughout the NEC-violating stage, see Figure 4.2 for the coefficients  $A(t)$  and  $B(t)$ . Clearly  $A(t) > 0$  whereas  $B(t) < 0$  during the whole Phantom stage. Hence the sound speed  $c_s^2 = B/A < 0$ . It seems that there is somewhere a typo in these values of parameters (4.53).



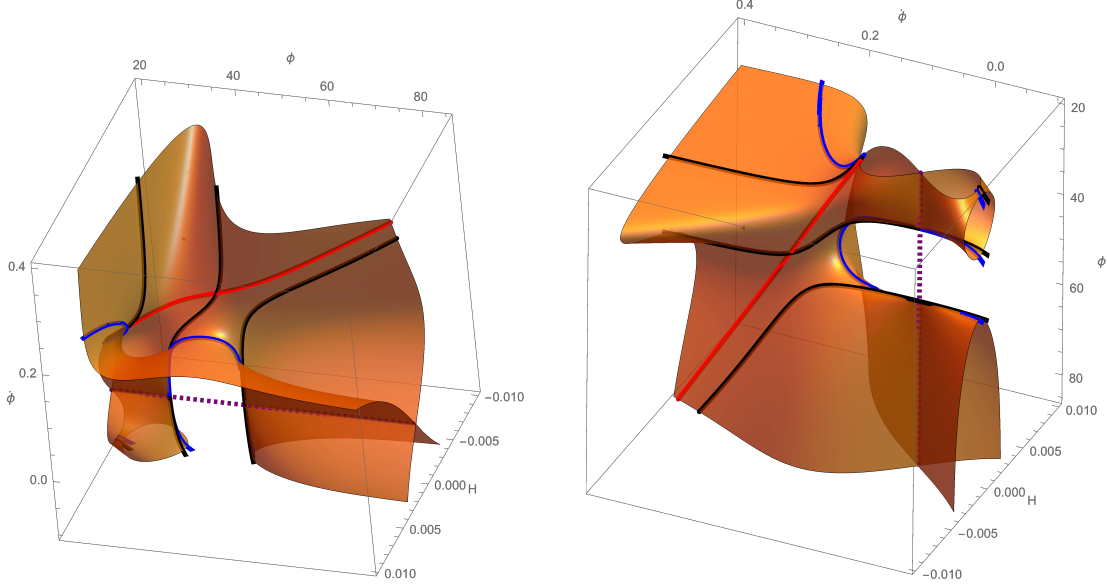


Figure 4.3: Different side views of the phase space hypersurface given by the constraint – the first Friedmann equation (4.11) for the system defined by (4.1) and (4.48), (4.49). The parameters correspond to the choice of [139] below their Figure 1, see (4.50). The red curve is the IS-bounce trajectory. The black curves correspond to  $H = 0$  while the blue curves represent  $\gamma = 0$ . The purple dashed lines represent  $\dot{\phi} = 0$ . Each point on these lines on the hypersurface of the constraint is a fixed point. Therefore the self-crossing of the hypersurface does not cause any trouble.

## 4.4 Phase space

The reconstruction of the Lagrangian through the identification of the functions (4.44) and (4.45) allows us to study the properties of other cosmological solutions in the system under consideration. A proper global analysis can follow the lines of [102]. One chooses dynamical variables  $(\phi, \dot{\phi}, H)$  whose evolution is given by the second Friedmann equation (4.12) and the equation of motion for the scalar field (4.15) written as a first-order system. These dynamical variables are moving on a hypersurface given by the constraint - first Friedmann equation (4.11), see Figure 4.3. In many cases this hypersurface cannot be uniquely projected onto the  $(\phi, \dot{\phi})$  plane, see discussion in [102] for a canonical scalar field and [93, 94] for *kinetically braided* theories. In [93, 94], it was found that sometimes it is possible to uniquely project the constraint hypersurface onto the space  $(\dot{\phi}, H)$ . To make a projection onto  $(\phi, \dot{\phi})$  plane, we have to choose the branch in the solution of the first Friedmann equation and substitute this branch  $H_{\pm}$  into the reduced field equation (4.15). In that case, it is only possible to evaluate the field dynamics in the region of the phase space where condition (4.14) holds, i.e. where

$$\dot{\phi}^4 + q(\phi)\dot{\phi}^2 + \frac{2}{3}k(\phi) \geq 0. \quad (4.54)$$

In the Figure 4.4 we plot different regions in the remaining phase space. We found other stable bouncing trajectories; see the right plot on the Figure 4.4. Note in this figure stable regions where superluminality is present. In parts of these superluminal regions the NEC holds, while in others it is violated. Moreover, there is a region of phase space where NEC is broken but the sound speed is subluminal. This shows again that the superluminality is not directly linked to stability [86]. The link is rather subtle. In particular we can find the superluminality just around the corner of the *IS-bounce*, in the neighborhood slightly below the trajectory. These superluminal stable regions are well within the field range corresponding to the NEC violation phase. Clearly a source or simple interaction can continuously deform these states into the *IS-bounce* trajectory. Hence, these states belong to the same EFT.

The origin of the trajectory is the ghostly region followed by a tiny superluminal region where NEC holds. Then it is followed by a vanishingly tiny white subluminal region where NEC holds. The *IS-bounce* trajectory leaves the ghostly region by going through the singularity of the equation of motion  $D = 0$ . This is also a pressure/curvature singularity. Thus this *IS-bounce* trajectory is clearly demonstrating the singular behavior similar to that crossing the Phantom divide in k-essence models linear in  $X$  [242]. It seems that around the point on the boundary of the central ghostly region the trajectories for a limiting cycle similarly to [95]; this is, however, an illusion, as they start and end on the singularity approaching or leaving the boundary  $D = 0$  vertically.

## 4.5 Discussion

In this chapter, we reconstructed the Lagrangian from the suggested expansion history using the inverse method in section 4.3. We found that the *IS-bounce* solution starts with a divergent sound speed around 15 Planck times before the NEC violation starts. The propagation of curvature fluctuations is still superluminal less than  $10 t_{\text{Pl}}$  before the onset of the NEC violation. Moreover, the system enters into the strongly coupled regime with vanishing sound speed and consequently loses predictive power in just  $15 t_{\text{Pl}}$  after the exit from the bouncing stage with the NEC violation. Scalar fluctuations become large and the whole perturbative treatment is not applicable anymore. From the classical perspective, the IS trajectory begins with a singularity of the acoustic metric and ends in another singularity. This evolution of the universe is evidently less appealing than that during the “Hot G-Bounce” scenario mentioned above. If the system were in a standard weakly coupled vacuum, this would imply that short-wavelength curvature perturbations evolve from a state with infinite quantum fluctuations of canonical momentum to a state with infinite quantum fluctuations of the conjugated canonical field  $\delta\mathcal{P}/\delta\dot{\phi}$ . Clearly this picture is unphysical, and this implies that the system is strongly coupled in these singular states. It is a challenge to modify the theory in such a way that preserves the required evolution,  $H(t)$ , but changes

the dynamics on these ultra-short time scales. To make a proper comparison, it is worth noting that gravity quantum strong coupling scale (and ultimate EFT cutoff) depends on the number of degrees of freedom  $N$  as  $M_{\text{Pl}}/\sqrt{N}$  [87], while already in the Standard Model there are around 100 degrees of freedom. This implies that the pathologies of the *IS-bounce* are not really separated in a distinguishable way from the desired semiclassical evolution.

Further, we plotted the phase space and the constraints for this model, see Figure 4.3 and Figure 4.4. The expansion history suggested by IS is not the only stable trajectory. Then we identified stable regions, where superluminality is present. In parts of these regions the NEC holds, while in others it is violated. Moreover, there is a region of phase space, where the NEC is broken, but the sound speed is subluminal. This shows again that the superluminality is not directly linked to stability of the Phantom stage, [86]. In particular, we found superluminality just around the corner – in the regions very close to the *IS-bounce*. These regions are well within the field range corresponding to the NEC violation phase. Clearly a source or simple interaction can continuously deform these states into the *IS-bounce* trajectory. Hence, these states belong to the same EFT. Thus it is impossible to avoid this type of superluminality by modifying functions  $k(\phi)$  and  $q(\phi)$  in the Lagrangian outside of the needed field range. In order to attempt escaping superluminality we have to modify either the desired evolution  $H(t)$  or the structure of the theory or both. Other interesting findings include the following: (a) the *IS-bounce* is a separatrix and other trajectories in its neighborhood do not seem to approach it, as can be noted in Figure 4.4. This solution goes through the singularity of the equation of motion, similarly to the singular trajectories found in [242]. (b) For the second choice of the parameters used in [139] to obtain their Figure 3, the IS claims are irreproducible. It seems that below Figure 3 from [139] there is a typo somewhere either in the set of parameters or in the form of the functions.

In Appendix D we used the same technology to calculate (i) the power spectrum of primordial scalar fluctuations and (ii) the particle production rate for scalar perturbations. We can observe that these spectra are not scale invariant at the end of the bouncing stage. Moreover, it is surprising to see that the change of the speed of sound suppresses the power of scalar fluctuations up to the point it is smaller than the power of tensors, which is far from what is expected from observational evidence.

To conclude, we think it is interesting to understand the consequences of the possible bounces in the early universe. Though, so far, this nonstandard option for the early universe seems to be inseparable from superluminality and a nonstandard UV-completion with *classicalization* as the only current candidate for the latter.

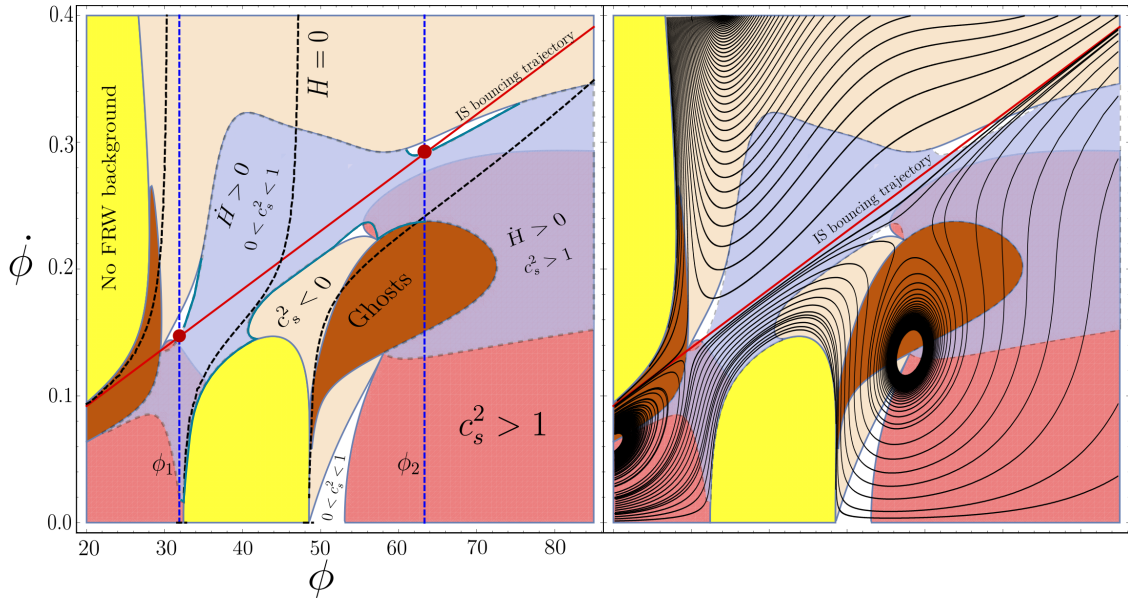


Figure 4.4: Here we plot the phase space for the system defined by (4.1) and (4.48), (4.49). We pick the  $H_-$  branch in (4.13). The parameters correspond to the choice of [139] below their Figure 1, see (4.50). This plot is a projection of the hypersurface from the Figure 4.3. The red line corresponds to the *IS-Bounce*. This bouncing trajectory is a separatrix which goes from a saddle point, as shown in the plot on the right, where the field trajectories are plotted in black. In the yellow regions, the condition (4.13) or (4.54) is not fulfilled, so that there is no spatially-flat FRW geometry there. The phase space continues to the other branch of the Friedmann equation (4.13) through the borders of these regions where  $\gamma = 0$ . In the light brown/almond regions  $c_s^2 < 0$ , and the system has a gradient instability. The borders of these regions correspond to  $c_s^2 = 0$  which causes an infinitely strong coupling of curvature perturbations. The burned orange/dark brown regions have ghosts,  $D < 0$  there, see (4.16) and (4.17). The boundaries of these regions have  $D = 0$  which implies an infinite pressure (4.6) and correspondingly an infinite curvature. These boundaries are also singularities of the background equations of motion (4.15). In the congo pink/coral regions the sound speed is superluminal  $c_s^2 > 1$ , but the NEC holds. Light blue/lavender regions correspond to the NEC violation without superluminality and free of ghosts and gradient instabilities. Purple/blue bell regions have the NEC violation and superluminality, but are free of ghosts and gradient instabilities. These superluminal regions are located only slightly below the red *IS-Bounce* trajectory. Finally, four small white regions are rather boring as they are free of ghosts, gradient instabilities, superluminality and violation of the NEC. The *IS-Bounce* crosses two of these white regions. On the red bouncing trajectory (4.41) the NEC is broken between  $\phi_1$  and  $\phi_2$ , (4.43). One has to rely on the reconstruction of the Lagrangian functions (4.48) and (4.49) *at least* between these two field values, between blue dashed lines. The black dashed curves correspond to  $H = 0$ . There are many trajectories above and below the red trajectory and on the right of the  $\phi_2$  which bounce and evolve through the black dashed curves. All trajectories start or end (or both) on a singularity or infinitely-strong coupling curves.

## Part II

# Modifying GR via variable deformations, action corrections and semiclassical effects

## Chapter 5

# Hamiltonian consistency of the gravitational constraint algebra under deformations

Einstein's theory of general relativity (GR) is considered by many to be the pinnacle of classical field theories. It provides a powerful description of strong gravitational phenomena at solar system scales and its validity has been tested in a variety of local experiments discussed in [249, 2]. Nevertheless, there are reasonable arguments to propose modifications to it, such as the failure to produce a sensible interacting picture of quantum gravity at ultraviolet scales just from promoting the classical to a quantum theory, or the intriguing nature of Dark Energy and Dark Matter, which emerge as a necessary component to explain the dynamics of the universe at cosmological scales. Regardless of the approach followed to modify Einstein's theory, the outcome should be consistent with the actual observations and must not be in conflict with the behavior of matter at scales where the standard model has accurate results, as mentioned in [54]. Some recent work on quantum gravity inspired theories and observational ties may be found in [45, 44].

On the other hand, the Hamiltonian form of all the degrees of freedom in general relativity – which in the case we study will also include matter minimally coupled to gravity – reveals its nature as a first-class constrained system. Which means that, assuming the field equations hold, each constraint commutes with all the other elements of the Hamiltonian under a Poisson bracket. In four spacetime dimensions, there are four constraints: the total scalar and three diffeomorphism constraints (and also the Gauss constraint in the case of Ashtekar variables); forming a closed “algebra”<sup>1</sup> with spacetime dependent structure constants. This is a valuable feature of any gravitational system for many reasons explored in [133, 208]; namely it fixes the surface where gauge orbits lie. This means that in order to

<sup>1</sup>As known in the literature, these constraint algebras are not true "algebras" in the strict mathematical sense.

evolve spacetime one only needs to fix the coordinates once at the surface of initial conditions. It also reveals that time and gauge evolution of each component of the Hamiltonian follows the rules of Lie transport. Moreover, once the gauge is fixed, the closure of the algebra allows dynamical classical solutions that preserve diffeomorphism invariance without imposing further conditions at each instant of time. Non-spatial diffeomorphisms generate constraint functions which are proportional to the spatial metric. Thus canonical transformations generated by these constraints do not correspond to a group action on phase space [162]. A manifestly Lorentz-covariant phase space formulation of GR has been established in [174].

Now, consider a deformed theory of gravity. Such theories are a new take on gravity, where one proposes that GR is only a low energy, albeit quite effective, theory that is bestowed on us by a more general theory. This more general theory of gravity, which could be a theory of quantum gravity or generally, any theory that extends GR, will have its own canonical variables which satisfy its own scalar, diffeomorphism and Gauss constraint algebra. The reason for this is that it, like any good theory of gravity, should have diffeomorphism symmetry within its own more general geometric formulation. From the perspective that GR is such a profoundly good theory and that any more general theory must serve the purpose of providing corrections to the local structure of GR, one can write these more general canonical variables as a function of the GR canonical variables. The map that connects GR to the more general theory is what we call a *deformation*, and shares the same motivations as the deviations shown in the toy model in Chapter 1. Specific areas where variable deformation is commonly done are, for example, in effective minisuperspace loop quantum gravity (where one applies holonomy corrections to the connection variable), as in [236, 62, 41]. In this chapter we study the deformations of such a generalized theory of gravity starting from its canonical variables, in the context of Hamiltonian systems where time evolution can be separated from gauge orbits as proposed by Dirac in [84], in order to preserve the closed form of the constraint algebra. These deformations are relevant, for example, in the growing interest in numerical simulations of astrophysical objects in the context of deformed theories of gravity, or in cases where corrections to the original theory manifest themselves as deformations of the canonical variables. In a slightly different vein, more recently a theory of gravity has been created by demanding that a general globally Lorentz invariant theory be promoted to local invariance, yielding a gravitational field theory as in [231, 232]. Deformed symmetries and general covariance in noncommutative and multifractional spacetimes has been investigated in [60, 40].

Admittedly, we do not necessarily need to deform one theory in order to get another theory, and one could simply consider some new theory from scratch. However, as mentioned above, deformations of the type studied here are common, as often one wishes for the new theory to be related in some way to the original, observed theory (GR). A good example of this technique in practice is found in [174]. In this prescription, all more general theories are



viewed from the perspective of GR, which is quite reasonable given its experimental success. It must be emphasized that if these deformations are merely canonical transformations of GR, then the deformed theory is physically equivalent to GR. What makes the discussion of deformations interesting is that in general, these deformations are not canonical transformations of GR variables. In these cases, deformed theories will introduce corrections to GR that demand extra degrees of freedom in the gravitational field, where it will be possible to describe the system using Hamiltonian mechanics in terms of an expanded set of canonical variables in the new corrected theory. Due to the presence of these extra degrees of freedom, some models of modified gravity with a closed constraint algebra will also arise from generic deformations of the canonical variables of the system, as suggested in [108, 69, 223]. In an interesting case, it has been shown that there are some special velocity dependent transformations that can lead to an equivalent theory [81, 80]. In all these cases, we will derive these quantities by keeping the original fields as configuration variables, and calculating their corresponding new conjugate momenta, which generally will not coincide with the corrected momenta, and which are constrained by the way the corrected deformed variables depend on the original ones. As mentioned, one of the motivations of these transformations is the usual modification of field variables after quantum corrections since in general the corrected fields, when replaced directly into the original action do not necessarily become new canonical variables of the system. Other field redefinitions occurring in certain theories of modified gravity have a similar effect. In a certain sense, we roughly explore the classical analog to the “inverse” transformation that integrates out degrees of freedom in order to obtain an EFT. Moreover, we provide conditions for those transformations in order to deform general relativity into another gauge theory of gravity. In this chapter, we use geometrized units ( $G = 1$ ).

The plan of this chapter is as follows: In section 5.1, we introduce the type of transformations that deform the action of a theory and their Hamiltonian analogues. To illustrate these transformations, we first provide simple examples of one-dimensional cases. In section 5.2, we briefly review the Hamiltonian formalism of general relativity as our undeformed starting point, and the derivation of the constraint algebra from the gauge algebra. We will also discuss the main properties we should preserve after deformations. In section 5.3, we apply these transformations using the standard canonical variables of the ADM formalism for the Einstein-Hilbert action. Two possible scenarios will be presented: (1) the transformation has to be canonical in agreement with Lovelock’s theorem or (2) we introduce more degrees of freedom in the theory. In section 5.4, a transformation of the Ashtekar version of GR is performed in order to obtain either one of the many different theories of general relativity or a modified theory of gravity with extra degrees of freedom. Finally, we present our discussions and conclusions.



## 5.1 Transforming the action from its canonical variables

In this section, we present two different ways to deform an action via the change of its canonical variables. To introduce these transformations several toy models are first examined as a segue to the much more complicated arena of gravitational field theory which follows. Let us consider the case of a 1-D time dependent system with an action

$$S_1 = \int \mathcal{L}(q, \dot{q}) dt, \quad (5.1)$$

where  $q$  and  $\dot{q}$  are the dynamical variables of the system. In both cases studied in the subsections below, different transformations of the action are performed via deforming its canonical variables. We find the corresponding Hamiltonian representation of the system by a Legendre transformation

$$H(p, q) = p\dot{q} - \mathcal{L}(p, q),$$

where  $p = \partial\mathcal{L}/\partial\dot{q}$  is the conjugate momentum of the canonical variable  $q$ . Other cases in which higher-order derivative terms cancel out in a manner that generates second-order equations of motion, such as seen in [78], will not be considered.

### 5.1.1 Transformations into theories with second-order equations of motion

The purpose of this section is to show transformations that lead us to describe the dynamics of the system by second-order differential equations. The canonical variables  $q$  and  $\dot{q}$  are transformed in the following way

$$q \rightarrow Q(q, \dot{q}), \quad \dot{q} \rightarrow \tilde{Q}(q, \dot{q}), \quad (5.2)$$

where both  $Q$  and  $\tilde{Q}$  do not introduce new derivatives of  $q$  in the Lagrangian. In this case, the new action reads as

$$S_2 = \int \mathcal{L}'(Q(q, \dot{q}), \tilde{Q}(q, \dot{q})) dt,$$

where the prime denotes that after the substitution, since the configuration variable is to remain as  $q$ , the resulting Lagrangian is different from the original one. If the system maintains integrability after these transformations – which is always true in the case of a canonical transformation, since in that case  $S_1 = S_2$  – it is possible to find the Hamiltonian version of both actions via invertible Legendre transformations. Each system can be mapped into the other as we describe in Figure 5.1.

As a relevant example of this type of transformations, we will consider the case of a simple harmonic oscillator:

$$S_A = \frac{1}{2} \int (\dot{q}^2 - \omega^2 q^2) dt, \quad (5.3)$$

$$\begin{array}{ccc}
\mathcal{L}(q, \dot{q}) & \xrightarrow{q \rightarrow Q(\dot{q}, q), \dot{q} \rightarrow \tilde{Q}(\dot{q}, q)} & \mathcal{L}'(\tilde{Q}, Q) \\
\begin{array}{c} \text{Leg}(\mathcal{L}) \\ \downarrow \quad \uparrow \end{array} & & \begin{array}{c} \text{Leg}(\mathcal{L}') \\ \downarrow \quad \uparrow \end{array} \\
\mathcal{H}(p, q) & \xrightarrow{p \rightarrow P(p, q), q \rightarrow Q(p, q)} & \tilde{\mathcal{H}}(P, Q)
\end{array}$$

Figure 5.1: Canonical mapping between  $S_1$  and  $S_2$  in its Lagrangian and Hamiltonian versions.

where the Hamiltonian is simply given by  $\mathcal{H}_A(p, q) = 1/2 (p^2 + \omega^2 q^2)$ . We can write the same Hamiltonian via an arbitrary similarity transformation

$$\begin{aligned}
\mathcal{H}_A &= \frac{1}{2} \begin{bmatrix} \mathcal{P} & \mathcal{Q} \end{bmatrix} \begin{bmatrix} \alpha & \beta \\ \beta & \gamma\omega^2 \end{bmatrix} \begin{bmatrix} \mathcal{P} \\ \mathcal{Q} \end{bmatrix} \\
&= \frac{1}{2} \left[ \alpha\mathcal{P}^2 + \gamma\omega^2\mathcal{Q}^2 + 2\beta\mathcal{P}\mathcal{Q} \right]
\end{aligned} \tag{5.4}$$

where  $\alpha$ ,  $\beta$  and  $\gamma$  are used as rotation parameters in phase space. In this example, it is easy to see that the similarity transformation to the auxiliary variables  $\mathcal{P}$  and  $\mathcal{Q}$  is canonical. These variables are related to the standard  $p$  and  $q$  by the characteristic orthonormal matrices of the similarity transformation. The off-diagonal term can be used to define a theory with a special class of solutions; to accomplish this one only needs to define a function  $f(t)$  such that

$$\frac{1}{f} \frac{df}{dt} = 2\beta,$$

and with the help of a new variable  $\varphi = \mathcal{Q}/\sqrt{f}$ , this off-diagonal term can be used as a generating function of canonical transformations

$$\frac{\partial G(\mathcal{P}, \varphi)}{\partial t} = \frac{1}{\sqrt{f}} \frac{df}{dt} \mathcal{P}\varphi \rightarrow G(\mathcal{P}, \varphi) = \sqrt{f}\mathcal{P}\varphi.$$

Therefore the Hamiltonian transforms via  $\mathcal{H}_A(\mathcal{P}, \varphi) = \mathcal{H}'_A(\mathcal{P}, \varphi) + \partial G(\mathcal{P}, \varphi)/\partial t$ , the conjugate momentum of  $\varphi$  is  $\pi_\varphi = \partial G(\mathcal{P}, \varphi)/\partial \varphi = \sqrt{f}\mathcal{P}$ , hence the Hamiltonian now “drains”

energy from the kinetic term and adds it to the potential term via

$$\mathcal{H}'_A(\pi_\varphi, \varphi) = \frac{1}{2} \left[ \alpha \frac{\pi_\varphi^2}{f} + f\gamma\omega^2\varphi^2 \right], \quad (5.5)$$

and its corresponding Lagrangian is

$$\mathcal{L}'(\dot{\varphi}, \varphi) = \frac{e^{2\beta t}}{2} \left[ \alpha\dot{\varphi}^2 - \gamma\omega^2\varphi^2 \right]. \quad (5.6)$$

We note the draining after replacing the analytic solution of  $f(t)$  in (5.5). This remains a one-dimensional problem while preserving the number of degrees of freedom, but it adds a time-dependent scale factor similar to the case of an oscillator in an expanding geometry. To close the maps, it is possible to transform the Lagrangian (5.3) directly into (5.6) by deforming  $\dot{q} \rightarrow \sqrt{\alpha}e^{\beta t}\dot{\varphi}$  and  $q \rightarrow \sqrt{\gamma}e^{\beta t}\varphi$ . In a similar way, we find the corresponding deformation of the Hamiltonian (5.4) into (5.5) from  $p \rightarrow \sqrt{\alpha}e^{-\beta t}\pi_\varphi$  and  $q \rightarrow \sqrt{\gamma}e^{\beta t}\varphi$ . One should note that it is only in rare circumstances that such a transformation is canonical and/or preserves the number of degrees of freedom in the system. It is convenient to write the deformations with respect to the original canonical variables in order to see the effect of the extra terms introduced in the new theory. The transformations in the Lagrangian can be written as deformations of the canonical variables

$$\dot{q} \rightarrow \dot{\varphi} + \Delta\dot{\varphi}, \quad q \rightarrow \varphi + \Delta\varphi, \quad (5.7)$$

and in an analogous way for the Hamiltonian

$$q \rightarrow \varphi + \Delta\varphi, \quad p \rightarrow \pi_\varphi + \Delta\pi_\varphi, \quad (5.8)$$

where we do not consider any specific range of magnitudes for  $\Delta\dot{\varphi}$ ,  $\Delta\varphi$  and  $\Delta\pi_\varphi$  when compared with the canonical variables, although in many cases of interest these quantities can be obtained by any perturbative expansion of the original choice for a deformation. This decomposition of the deformed variables will be used in the remaining sections of this thesis. Therefore, it is relevant to notice that the only difference between  $\varphi$  and  $q$  (including the canonical momenta  $p$  and  $\pi_\varphi$ ) is either a phase or a symmetry transformation that does not represent a significant modification of the role of the field variables.

### 5.1.2 Transformations into higher-order theories

In this section, we consider another introductory example where we will promote a system with second-order equations of motion into a higher-derivative theory by a different type of variable transformation:

$$q \rightarrow Q(q, \dot{q}), \quad \dot{q} \rightarrow \frac{d}{dt}Q(q, \dot{q}). \quad (5.9)$$

After replacing in (5.1), the new action now reads

$$S_2 = \int dt \mathcal{L}' \left( q, \dot{q}, \frac{\partial Q}{\partial \dot{q}} \ddot{q} \right), \quad (5.10)$$

which is a function of the second derivative of the field. Transformations of this type suggest that it is possible to deform an arbitrary symplectic manifold into another one. From the definition in (5.9), we can observe that it is enough to deform the field variable to promote the action since the derivative of the transformed field raises the order of the system. In analogy with the mapping proposed in the previous subsection 5.1.1, we illustrate the mapping between  $S_1$  and  $S_2$  in Figure 5.2.

$$\begin{array}{ccc}
 \mathcal{L}(q, \dot{q}) & \xrightarrow[\dot{q} \rightarrow \frac{dQ(q, \dot{q})}{dt}]{q \rightarrow Q(q, \dot{q})} & \mathcal{L}'(q, \dot{q}, \ddot{q}) \\
 \begin{array}{c} \text{Leg}(\mathcal{L}) \\ \downarrow \uparrow \end{array} & & \begin{array}{c} \downarrow \uparrow \\ \text{Leg}(\mathcal{L}') \end{array} \\
 \mathcal{H}(p, q) & \xrightarrow[p \rightarrow P(q_1, q_2, p_1, p_2)]{q \rightarrow Q} & \tilde{\mathcal{H}}(q_1, q_2, p_1, p_2)
 \end{array}$$

Figure 5.2: Mapping between  $S_1$  and  $S_2$ , which is now a higher-derivative theory, in its Lagrangian and Hamiltonian versions.

The growth in the order of the action demands the use of extra canonical variables to build the Hamiltonian version of the theory. Throughout the rest of this chapter, the Ostrogradskii formalism is applied to construct the Hamiltonian and all the associated conjugate momenta of the new higher-order theory, as seen in [190]. The corresponding Hamiltonian deformation from  $\mathcal{H}$  to  $\tilde{\mathcal{H}}$  has many peculiar features as will be discussed in the following example.

Again let us consider the case of a 1D harmonic oscillator as an example:

$$\mathcal{L}(\phi) = -\frac{1}{2} \phi^T \left( \frac{d^2}{dt^2} + \Omega^2 \right) \phi, \quad (5.11)$$

where the operator  $\hat{\mathcal{O}}\chi \equiv (d^2/dt^2 + \Omega^2)\chi$  acts on a test function  $\chi$ , which is represented by a column vector in the time domain. This operator is separable, which means it can be decomposed as  $\hat{\mathcal{O}} = \hat{\mathcal{A}}^T \hat{\mathcal{A}}$  where  $\hat{\mathcal{A}}\chi \equiv (i d/dt + \Omega)\chi$  and its transpose  $\chi^T \hat{\mathcal{A}}^T \equiv \chi^T (i d/dt + \Omega)^T = \chi^T (-i d/dt + \Omega)$ . In the last equality we considered that the time

derivative is accurately represented by a skew-symmetric matrix. Moreover, the factors of  $\hat{\mathcal{O}}$  commute,  $[\hat{\mathcal{A}}, \hat{\mathcal{A}}^T] = 0$ . A possible way to deform the action is to use the “square root” of  $\hat{\mathcal{O}}$  to change the field variable by  $\phi \rightarrow \hat{\mathcal{A}}\psi$  and its transpose by  $\phi^T \rightarrow \psi^T \hat{\mathcal{A}}^T$ . The new Lagrangian now reads

$$\mathcal{L}'(\psi) = -\frac{1}{2}\psi^T \left[ \frac{d^2}{dt^2} + \Omega^2 \right]^2 \psi, \quad (5.12)$$

which is a particular case of the widely known Pais-Uhlenbeck oscillator [19, 68]. Strictly speaking, by deforming the field variable we have also deformed  $\hat{\mathcal{O}}$  into  $\hat{\mathcal{O}}^2$ , and by inspecting the trace of the transformation law  $\text{tr}\langle \hat{\mathcal{A}}^T \hat{\mathcal{O}} \hat{\mathcal{A}} \rangle = \text{tr}\langle \hat{\mathcal{A}}^T \hat{\mathcal{A}} \hat{\mathcal{O}} \rangle = \text{tr}\langle \hat{\mathcal{O}}^2 \rangle$  we notice that a deformation of this type is not unitary, which is of special relevance when we introduce new degrees of freedom in the system. After integrating by parts in the action, the Lagrangian in (5.12) can be rewritten as

$$\mathcal{L}'(\psi, \dot{\psi}, \ddot{\psi}) = -\frac{1}{2} \left[ \ddot{\psi}^2 - 2\Omega^2 \dot{\psi}^2 + \Omega^4 \psi^2 \right]. \quad (5.13)$$

The Hamiltonian form of this theory follows from the definition of canonical momenta associated to the relabeled variables  $\psi \rightarrow \psi_1$  and  $\dot{\psi} \rightarrow \psi_2$

$$\pi_{\psi_1} = \frac{\partial \mathcal{L}'}{\partial \dot{\psi}_1} - \frac{d}{dt} \left( \frac{\partial \mathcal{L}'}{\partial \ddot{\psi}_1} \right) = 2\Omega^2 \dot{\psi}_1 + \Omega^4 \ddot{\psi}_1, \quad (5.14a)$$

$$\pi_{\psi_2} = \frac{\partial \mathcal{L}'}{\partial \dot{\psi}_2} = -\ddot{\psi}_1, \quad (5.14b)$$

hence the Hamiltonian is given by

$$\mathcal{H}'(\psi_1, \psi_2, \pi_{\psi_1}, \pi_{\psi_2}) = \pi_{\psi_1} \psi_2 - \frac{1}{2} \pi_{\psi_2}^2 - \Omega^2 \psi_2^2 + \frac{\Omega^4}{2} \psi_1^2. \quad (5.15)$$

Stability issues and field solutions with negative kinetic energy, dubbed as ghosts, will arise immediately: the linear dependence of this expression on  $\pi_{\psi_1}$  and its complex conjugate (apart from the negative signs in some of the terms) bring infinitely negative values of energy and unbounded trajectories in phase space. In [68], unstable solutions are controlled by constraining the number of canonical variables via extra algebraic constraints which reduce the order of the system. Such an effect can be achieved in both of the limits of the oscillation frequency  $\Omega^2$ :  $\Omega^2 \ll 1$  (i.e. suppressing the last term in (5.13)) and  $\Omega^2 \gg 1$  (i.e. when the first term in (5.13) is very small compared with the other two). In both scenarios, there is not much room for an effective reduction of the number of canonical pairs, but this does not have to be the case for dynamical systems with more degrees of freedom. This argument is in agreement with the discussions in [225] where the stable solutions can always be obtained by varying the model parameters around the limit where

two possibilities manifest: (a) there is no contributions from the higher-derivative terms or (b) the information carried by the extra derivatives is redundant.

Another property of the transformations used to generate a higher-order theory can be noticed if we build  $\mathcal{L}'(\psi)$  from the original Hamiltonian:

$$\mathcal{H}(\phi, \pi_\phi) = 1/2 \left( \pi_\phi^2 + \Omega^2 \phi^2 \right)$$

of the harmonic oscillator by transforming

$$\pi_\phi \rightarrow P(\psi, \pi_\psi, \dots),$$

and

$$\phi \rightarrow Q(\psi, \pi_\psi),$$

where the decomposition  $P(\psi, \pi_\psi, \dots) = \pi_\psi + \Delta\pi_\psi$  and  $Q(\psi, \pi_\psi, \dots) = \psi + \Delta\psi$  holds in the same way as in (5.8). By following the lower right corner of Figures 5.2:

$$\begin{aligned} P\dot{Q}(\psi, \pi_\psi) - \frac{1}{2} \left( P^2 + \Omega^2 Q^2 \right) &= \mathcal{L}'(\psi_1, \psi_2, \pi_{\psi_1}, \pi_{\psi_2}) \\ \rightarrow P(\psi_1, \psi_2, \pi_{\psi_1}, \pi_{\psi_2}) &= \dot{Q} \pm \sqrt{\dot{Q}^2 - 2\mathcal{L}' - \Omega^2 Q^2}, \end{aligned}$$

which means that the transformation not only brings extra canonical variables but it is also not unique. As noticed in [250] these degeneracies are typically used to by-pass Ostrogradskii instabilities (i.e., terms in the Hamiltonian with linear dependence in the conjugate momentum). Hence, deformations of this type cannot be confused with coordinate transformations.

## 5.2 Review of Hamiltonian general relativity and the gauge algebra

General relativity is a gauge theory where coordinate freedom is what enables the user to transform results from one coordinate chart to another. As in every gauge theory, it can be equivalently written in the context of a constrained system at the Hamiltonian level in order to define one gauge-fixing condition per (first-class) Hamiltonian constraint and find the generators of gauge transformations. As a first step, we will follow the standard way to find the Hamiltonian version of general relativity as discussed in [197], built from the Einstein-Hilbert action

$$S = \int d^4x \sqrt{-g} \left[ \frac{R}{8\pi} + \mathcal{L}_m(\psi, g_{\mu\nu}) \right], \quad (5.16)$$

where  $\mathcal{L}_m(\psi, g_{\mu\nu})$  is the matter Lagrangian. We will write the spacetime metric using the 3+1 decomposition

$$\begin{aligned} g_{\mu\nu} &= -(N^2 - h_{ab}N^aN^b)\delta_\mu^t\delta_\nu^t + 2h_{ab}N^b\delta_{(\mu}^t\delta_{\nu)}^a + h_{ab}\delta_\mu^a\delta_\nu^b, \\ g^{\mu\nu} &= -\frac{1}{N^2}\delta_t^\mu\delta_t^\nu + \frac{2N^a}{N^2}\delta_t^{(\mu}\delta_a^{\nu)} + (h^{ab} - N^aN^b)\delta_a^\mu\delta_b^\nu, \end{aligned}$$

where  $N$  and  $N^a$  are the lapse function and the shift vector respectively. The parenthesis “ $(ab)$ ” denote symmetrization in the pair of indices; likewise the square brackets “[ $ab$ ]” denote antisymmetrization.  $h_{ab}$  is the metric of the hypersurface fixed at a constant instant of time. The Gauss-Codazzi equations allow us to write the gravitational part of the action by using the decomposed metric [197]

$$R = R^{(3)} + K^{ab}K_{ab} - K^2 - 2\nabla_\alpha \left( n^\beta \nabla_\beta n^\alpha - n^\alpha \nabla_\beta n^\beta \right), \quad (5.17)$$

where  $R^{(3)}$  is the Ricci scalar calculated from  $h_{ab}$ ,  $n^\alpha$  are the components of the normal of the hypersurface at a fixed instant of time and  $K^{ab}$  is the extrinsic curvature of the same surface, which is defined as the change of the normal projected by a basis of vectors tangent to the surface. In (5.17) the last term between parentheses is a surface term that generally requires cancellation via the addition of the Gibbons-Hawking term [253]. The conjugate momentum to  $h_{ab}$  is determined by writing the extrinsic curvature as a function of  $\dot{h}_{ab} \equiv \mathcal{L}_t h_{ab}$

$$K_{ab} = \frac{1}{2N} \left( \dot{h}_{ab} - \nabla_b N_a - \nabla_a N_b \right), \quad (5.18)$$

where the metric is Lie transported along a timelike trajectory whose tangent vector is denoted by  $t^\alpha$ , which is not necessarily parallel to  $n^\alpha$ , the unit normal of the  $t = \text{const.}$  surfaces. As in standard field theory, the momentum  $\pi_{ab}$  is determined by

$$\begin{aligned} \pi_{ab} &= \frac{\partial}{\partial \dot{h}_{ab}} \left( \frac{\sqrt{-g}R}{8\pi} \right) = \frac{1}{8\pi} \frac{\partial K_{cd}}{\partial \dot{h}_{ab}} \frac{\partial}{\partial K_{cd}} (\sqrt{-g}R) \\ &= \frac{\sqrt{h}}{16\pi} (K_{ab} - Kh_{ab}). \end{aligned} \quad (5.19)$$

Once that the momentum is defined, we can use Legendre transformations to build the total Hamiltonian of the system

$$\begin{aligned} \mathcal{H}_T &= \int d^3x \left[ \pi^{ab}\dot{h}_{ab} + \pi_\psi\dot{\psi} - \left( \frac{\sqrt{-g}R}{8\pi} + \mathcal{L}_m(\psi, g_{\mu\nu}) \right) \right] \\ &= \int d^3x [N\mathcal{H}_0(x) + N^a\mathcal{H}_a(x)]. \end{aligned} \quad (5.20)$$

( $\psi$  representing possible minimally coupled matter contributions).

The Hamiltonian has been written with respect to  $\mathcal{H}_0$  and  $\mathcal{H}_a$ , which are known as the scalar and vector constraints respectively:

$$\begin{aligned}\mathcal{H}_0(x) &= -\frac{\sqrt{h}R^{(3)}}{16\pi} + \frac{16\pi}{\sqrt{h}} \left( \pi^{ab}\pi_{ab} - \frac{1}{2}\pi^2 \right) + \mathcal{H}_0^\psi(x) \\ \mathcal{H}_a(x) &= -32\pi\sqrt{h}\nabla^b \left( \frac{\pi_{ab}}{\sqrt{h}} \right) + \mathcal{H}_a^\psi(x).\end{aligned}\tag{5.21}$$

Here  $\mathcal{H}_0^\psi$  and  $\mathcal{H}_a^\psi$  are the scalar and vector constraints obtained from a matter field (for example, a scalar field). This procedure summarizes the so-called ADM formalism for general relativity [26]. In addition to this, the so-called smeared constraints are also important in our discussion, these are defined by

$$\mathcal{H}(N) \equiv \int d^3x N(x)\mathcal{H}_0(x),\tag{5.22a}$$

$$\mathcal{H}(N^a) \equiv \int d^3x N(x)^a\mathcal{H}_a(x).\tag{5.22b}$$

We must remark that the shift and lapse play the role of Lagrange multipliers since neither  $\dot{N}$  nor  $\dot{N}^a$  appear explicitly in the action or in the Hamiltonian. Moreover, it is important to figure out if the absence of these terms is not just a gauge artifact. To do so, we must transform both the lapse and the shift vector following the infinitesimal gauge transformation rules of  $g^{\mu\nu}$  along an arbitrary vector field  $\varepsilon$ :

$$\delta_\varepsilon g^{\mu\nu} = \frac{\partial g^{\mu\nu}}{\partial x^\alpha} \varepsilon^\alpha - g^{\mu\rho} \frac{\partial \varepsilon^\nu}{\partial x^\rho} - g^{\nu\rho} \frac{\partial \varepsilon^\mu}{\partial x^\rho}.$$

It is enough to use  $\delta_\varepsilon g^{00}$  and  $\delta_\varepsilon g^{0a}$  to determine  $\delta_\varepsilon N$  and  $\delta_\varepsilon N^a$  as in [199], which are given by

$$\delta_\varepsilon N = \frac{\partial N}{\partial x^\mu} \varepsilon^\mu + N \frac{\partial \varepsilon^0}{\partial x^0} - N N^a \frac{\partial \varepsilon^0}{\partial x^a},\tag{5.23a}$$

$$\delta_\varepsilon N^a = \frac{\partial N^a}{\partial x^\mu} \varepsilon^\mu + N^a \frac{\partial \varepsilon^0}{\partial x^0} - \left( N^2 h^{ab} + N^a N^b \right) \frac{\partial \varepsilon^0}{\partial x^b} + \frac{\partial \varepsilon^a}{\partial x^0} - N^b \frac{\partial \varepsilon^a}{\partial x^b},\tag{5.23b}$$

where  $N^\mu = N\delta_0^\mu + N^a\delta_a^\mu$  and the total Hamiltonian is  $\mathcal{H}(N^\mu)$ . We now need to find a solution for  $\varepsilon^\mu$  such that  $\partial\delta_\varepsilon N^\nu/\partial\dot{N}^\mu = 0$ , which means that we do not generate any



momenta while doing a gauge transformation, which leads us to 4 equations for  $\varepsilon^\mu$ :

$$\begin{aligned}\varepsilon^0 + N \frac{\partial \varepsilon^0}{\partial N} &= 0, \\ \frac{\partial \varepsilon^0}{\partial N^a} &= 0, \\ N^a \frac{\partial \varepsilon^0}{\partial N} + \frac{\partial \varepsilon^a}{\partial N} &= 0, \\ \varepsilon^0 \delta_b^a + \frac{\partial \varepsilon^a}{\partial N^b} &= 0.\end{aligned}$$

It is now simple to observe that none of these equations depends explicitly on  $h_{ab}$ , which will be important at the time we perform deformations of the canonical variables. The general solution for this system is  $\varepsilon^0 = \xi^0/N$  and  $\varepsilon^a = \xi^a - \xi^0 N^a/N$ , where  $\xi^\mu$  is an arbitrary spacetime-dependent vector field. We can equivalently use  $\xi^\mu$  to represent the same solutions

$$\xi^0 = N\varepsilon^0; \quad \xi^a = \varepsilon^a + N^a\varepsilon^0, \quad (5.24)$$

this inversion now makes  $\xi^\mu$  a function of  $N^\mu$  and defines a new set of coordinates attached to the constant-time hypersurface. Hence, it is safe to perform gauge transformations as long as these do not generate momenta of  $N^\mu$ . Once we identify these vector fields, gauge transformations along any of these solutions are defined just like the equations of motion, following a procedure described in detail in [208]: First, considering that the vector fields  $\xi^\mu$  and  $\varepsilon^\mu$  can be freely exchanged to describe the same gauge flow, we define the Hamiltonian in a way analogous to (5.22a) and (5.22b)

$$\mathcal{H}(\xi^\mu) = \tilde{\mathcal{H}}(\varepsilon^\mu) \equiv \int d^3y \mathcal{H}_\mu(y) \xi^\mu,$$

where the integration occurs with respect to the coordinates of the hypersurface. The shift in any arbitrary function  $I(h_{ab}, \pi_{ab}, \psi, \pi_\psi)$  of the canonical coordinates can be computed by using the brackets [26]

$$\delta_\varepsilon I = \{I, \tilde{\mathcal{H}}(\varepsilon^\mu)\}, \quad (5.25)$$

where  $\xi^\mu$  and  $\varepsilon^\mu$  are just as defined by (5.24). The gauge algebra acting on the same test function  $I$  reads

$$(\delta_\varepsilon \delta_\zeta - \delta_\zeta \delta_\varepsilon) I = \delta_{[\varepsilon, \zeta]} I. \quad (5.26)$$

Let us evaluate the first two variations on the left

$$\delta_\varepsilon \delta_\zeta I = \left( \delta_\varepsilon N^\mu \frac{\delta}{\delta N^\mu} + \delta_\varepsilon q \frac{\delta}{\delta q} \right) \left( \delta_\zeta q \frac{\delta I}{\delta q} \right),$$

where  $\delta_\zeta q(\delta I/\delta q)$  is the shorthand notation of

$$\delta_\zeta q \frac{\delta I}{\delta q} \equiv \delta_\zeta h_{ab} \frac{\delta I}{\delta h_{ab}} + \delta_\zeta \pi_{ab} \frac{\delta I}{\delta \pi_{ab}} + \delta_\zeta \psi \frac{\delta I}{\delta \psi} + \delta_\zeta \pi_\psi \frac{\delta I}{\delta \pi_\psi}. \quad (5.27)$$

which means that the variation affects all the phase space variables of the system. Using (5.26), the two variations can be written as

$$\delta_\varepsilon \delta_\zeta I = \delta_\varepsilon N^\mu \frac{\delta}{\delta N^\mu} \{I, \tilde{\mathcal{H}}(\zeta)\} + \{\{I, \tilde{\mathcal{H}}(\varepsilon)\}, \tilde{\mathcal{H}}(\zeta)\}, \quad (5.28)$$

where a substantial difference with respect to other gauge theories comes from the fact that the first term in the right hand side does not cancel. This term is now expressed in detail:

$$\begin{aligned} \delta_\varepsilon N^\mu \frac{\delta}{\delta N^\mu} \{I, \tilde{\mathcal{H}}(\zeta)\} &= \delta_\varepsilon N^\mu \frac{\delta}{\delta N^\mu} \int d^3 y z^\alpha \{I, \mathcal{H}_\alpha\} \\ &= \int d^3 y \zeta^0 \delta_\varepsilon N^\mu \delta_\mu^\alpha \{I, \mathcal{H}_\alpha\} = \{I, \tilde{\mathcal{H}}(\delta_\varepsilon N^\mu \zeta^0)\}, \end{aligned} \quad (5.29)$$

where the vector flow  $z^\mu \equiv N \zeta^0 \delta_0^\mu + (\zeta^a + N^a \zeta^0) \delta_a^\mu$  follows from the definition in (5.24). In the last line it is possible to observe that  $\partial z^\alpha / \partial N^\mu = \delta_\mu^\alpha \zeta^0$ . Therefore the initial variation is given by

$$\delta_\varepsilon \delta_\zeta I = \{\{I, \tilde{\mathcal{H}}(\varepsilon)\}, \tilde{\mathcal{H}}(\zeta)\} + \{I, \tilde{\mathcal{H}}(\delta_\varepsilon N^\mu \zeta^0)\}.$$

With this expression it is possible to rewrite (5.26) as

$$\{\{I, \tilde{\mathcal{H}}(\varepsilon)\}, \tilde{\mathcal{H}}(\zeta)\} - \{\{I, \tilde{\mathcal{H}}(\zeta)\}, \tilde{\mathcal{H}}(\varepsilon)\} + \{I, \tilde{\mathcal{H}}(\delta_\varepsilon N^\mu \zeta^0 - \delta_\zeta M^\mu \varepsilon^0)\} = \{I, \tilde{\mathcal{H}}[\varepsilon, \zeta]\}. \quad (5.30)$$

After using the Jacobi identity in the first two terms on the left hand side of (5.30), the gauge algebra now reads

$$\{\tilde{\mathcal{H}}(\varepsilon), \tilde{\mathcal{H}}(\zeta)\} = \tilde{\mathcal{H}}([\varepsilon, \zeta] - \delta_\varepsilon N^\mu \zeta^0 + \delta_\zeta M^\mu \varepsilon^0).$$

The other basis of vectors can be used equivalently

$$\{\mathcal{H}(\xi), \mathcal{H}(z)\} = \mathcal{H}([\xi, z] - \delta_\xi N^\mu z^0 + \delta_z M^\mu \xi^0). \quad (5.31)$$

In the case of  $\xi^\mu = M \delta_0^\mu$  and  $z^\mu = N \delta_0^\mu$ , the Lie bracket cancels and the first Poisson bracket is given by

$$\{\mathcal{H}(M), \mathcal{H}(N)\} = \mathcal{H}(N \nabla^a M - M \nabla^a N), \quad (5.32)$$

and in a similar way, the remaining brackets can be determined by choosing  $\xi^\mu = M^a \delta_a^\mu$ ,  $z^\mu = N^a \delta_a^\mu$  and  $\xi^\mu = M \delta_0^\mu$ ,  $z^\mu = N^a \delta_a^\mu$ :

$$\{\mathcal{H}(M^a), \mathcal{H}(N^a)\} = \mathcal{H}(\mathcal{L}_{N^a} M^a), \quad (5.33a)$$

$$\{\mathcal{H}(M), \mathcal{H}(N^a)\} = -\mathcal{H}(\mathcal{L}_{N^a} M). \quad (5.33b)$$

The expressions (5.32–5.33b) constitute the constraint algebra of general relativity, which explains the way spacetime contorts as described in [234]. Strictly speaking, this has spacetime-dependent structure constants, so it is not an algebraic structure in the rigorous meaning of the word. An important property of this algebra is its closure, which has been used as a motivation to search for a valid ultraviolet limit of the theory. Nevertheless, our perspective is more conservative and is closely related with the possibility of safely fixing its gauge degrees of freedom. To do so, any choice of gauge should satisfy

$$\frac{\delta S}{\delta N^\mu} = 0 \rightarrow \mathcal{H}_\mu(y) \approx 0,$$

which separately implies  $\mathcal{H}(N) = \mathcal{H}(N^a) \approx 0$ , where “ $\approx$ ” means that this statement holds along with the equations of motion. These are also known as on-shell conditions which represent the constrained hypersurfaces where we can find all the possible gauge selections. In order to fix the gauge properly, we must ensure that these surfaces do not evolve in time:

$$\dot{\mathcal{H}}(M) = \{\mathcal{H}(N), \mathcal{H}(M)\} + \{\mathcal{H}(N^a), \mathcal{H}(M)\} \approx 0, \quad (5.34a)$$

$$\dot{\mathcal{H}}(M^b) = \{\mathcal{H}(N), \mathcal{H}(M^b)\} + \{\mathcal{H}(N^a), \mathcal{H}(M^b)\} \approx 0, \quad (5.34b)$$

which are also known as secondary constraints. The closure of the algebra in (5.32–5.33b) ensures that each of the Poisson brackets will always be proportional to other constraints that vanish when evaluated on-shell. In Figure 5.3, we depict the evolution of the hypersurfaces that contain all the possible gauge choices, and the change of any specific choice at a fixed instant of time. Even though a fully detailed discussion on the proper way to do gauge fixing is beyond the scope of this study, it is important to remark that the gauge degrees of freedom cannot be fixed without this condition. As an additional comment, we must observe that the procedure we followed to derive the algebra is already invariant under coordinate transformations. Later, it will become apparent that one way to keep the same structure under deformations is to introduce an orthogonal generator per new degree of freedom.

We need to consider that this procedure is valid at the infinitesimal level. Consequently, as noticed in [208], one cannot apply the gauge transformations mentioned here to any phase space configuration, since in general these will combine canonical variables (and their derivatives) at different instants of time. Hence, the gauge transformations applied in here can only map a set of solutions of the equations of motion into another version of the same set of solutions. In the subsequent sections, we will translate this procedure to actions that were modified from deforming their canonical variables. It is interesting to explore what kind of transformations of the gauge trajectories in (5.24) will transform (5.26) covariantly.

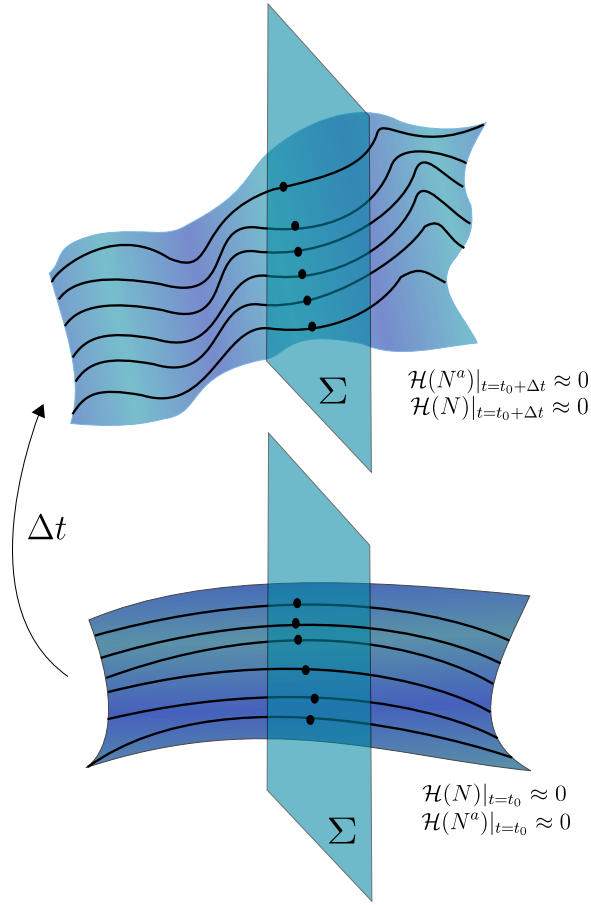


Figure 5.3: Gauge fixing by the intersection with the surface  $\Sigma$  as the scalar and vector constraint evolve. The gauge choice changes as the surface (and the orbits) deforms.

The transformed version of (5.26) reads

$$\left(\delta_{\tilde{\varepsilon}}\delta_{\tilde{\zeta}} - \delta_{\tilde{\zeta}}\delta_{\tilde{\varepsilon}}\right) I = \delta_{[\tilde{\varepsilon}, \tilde{\zeta}]} I.$$

It will be enough to write the first two variations to understand the dependencies of a generic transformation represented in a matrix form by  $\tilde{\zeta} = \left(T_{\zeta \rightarrow \tilde{\zeta}}\right) \zeta$

$$\delta_{\tilde{\varepsilon}}\delta_{\tilde{\zeta}} I = \left( (T_{\varepsilon \rightarrow \tilde{\varepsilon}}) \delta_{\varepsilon} N^{\mu} \frac{\delta}{\delta N^{\mu}} + (T_{\varepsilon \rightarrow \tilde{\varepsilon}}) \delta_{\varepsilon} q \frac{\delta}{\delta q} \right) \times \left( (T_{\zeta \rightarrow \tilde{\zeta}}) \delta_{\zeta} q \frac{\delta I}{\delta q} \right),$$

where the shorthand notation for all the canonical variables  $q$  still holds. The only way in which this expression transforms covariantly is if the transformations  $T_{\zeta \rightarrow \tilde{\zeta}}$  do not depend on any of the canonical variables (including matter) or on the lapse and shift. This complements the independence on  $h_{ab}$  was already used to determine (5.24). Therefore, the smeared constraint algebra in (5.32–5.33b) preserves its form under these conditions.

### 5.3 Deforming canonical general relativity

In this section, we deform the gravitational canonical variables  $h_{ab}$  and  $\pi_{ab}$  following the transformations described in 5.1.1 and 5.1.2 from the Einstein-Hilbert action in (5.16) written using the Gauss-Codazzi equations. An equivalent way to express this action is built from the Hamiltonian in ADM variables

$$S = \int dt \int d^3x \left[ \pi_\psi \dot{\psi} + \pi^{ab} \dot{h}_{ab} - \mathcal{H}(N) - \mathcal{H}(N^a) \right]. \quad (5.35)$$

In all the cases covered in this chapter, for simplicity, we will not perform any transformation on the canonical variables of matter. Although this could be done, the particular matter field utilized, and the form of its action, is usually motivated by physics other than gravitational field theory. The purpose of the transformations which follow is to find other theories where both diffeomorphism invariance and the gauge structure are preserved.

#### 5.3.1 Lovelock's theorem

In this section, we will show that these transformations lead us unavoidably to Lovelock's theorem, which shows that the only second-order curvature based metric gravitational theory equipped with diffeomorphism invariance is general relativity. In order to do that, we deform the canonical variables  $h_{ab}$  and  $\pi_{ab}$  in (5.16) by considering a transformation of variables analogous to what was presented in 5.1.1, which in the Hamiltonian formalism would be

$$h_{ab} \rightarrow H_{ab}(\tilde{h}_{ab}, \tilde{\pi}_{ab}) = \tilde{h}_{ab} + \Delta\tilde{h}_{ab}, \quad (5.36a)$$

$$\pi_{ab} \rightarrow P_{ab}(\tilde{h}_{ab}, \tilde{\pi}_{ab}) = \tilde{\pi}_{ab} + \Delta\tilde{\pi}_{ab}, \quad (5.36b)$$

which correspond to the transformations of the variables  $h_{ab}$  and  $\dot{h}_{ab}$  in the Lagrangian. Notice that in the right hand side of both expressions the terms were expanded in the same way as in (5.8). In its simplest version, we can consider the deviations of these variables as  $\Delta\tilde{h}_{ab} = H_{ab}(\tilde{h}_{ab}, \tilde{\pi}_{ab}) - \tilde{h}_{ab}$  and  $\Delta\tilde{\pi}_{ab} = P_{ab}(\tilde{h}_{ab}, \tilde{\pi}_{ab}) - \tilde{\pi}_{ab}$  without any further assumptions on the magnitudes of  $\Delta\tilde{h}_{ab}$  and  $\Delta\tilde{\pi}_{ab}$ . After these deformations the action in (5.35) is given by

$$S' = \int dt \int d^3x \left[ \pi_\psi \dot{\psi} + \tilde{\pi}^{ab} \dot{\tilde{h}}_{ab} - \tilde{\mathcal{H}}(N) - \tilde{\mathcal{H}}(N^a) \right] + \Delta\mathcal{L}(\tilde{h}_{ab}, \tilde{\pi}_{ab}, \Delta\tilde{h}_{ab}, \Delta\tilde{\pi}_{ab}, \psi). \quad (5.37)$$

The term  $\Delta\mathcal{L}$  contains all of the terms proportional to some power of  $\Delta\tilde{h}_{ab}$  and/or  $\Delta\tilde{\pi}_{ab}$ . We will count degrees of freedom in the same manner as in [129]:

$$2 \times \{\#\text{ of degrees of freedom}\} = \{\#\text{ of canonical variables}\} \\ - 2 \times \{\#\text{ of first-class constraints}\} - 2 \times \{\#\text{ of second-class constraints}\}. \quad (5.38)$$

GR does not have second-class constraints. If the number of canonical variables has not changed and/or if the new theory remains a metric theory, there is no reason to expect any change in the number of degrees of freedom. Also, we expect that the existing constraints commute on-shell with each other otherwise diffeomorphism invariance is broken. Since we require the presence of that symmetry, none of the constraints should be demoted to second-order. Now, the procedure suggested by Dirac in [84] allows us to decompose  $\Delta\mathcal{L}$  in (5.37) as

$$\Delta\mathcal{L} = N^\mu V_\mu, \quad (5.39)$$

meaning that it is possible find a vector – in the basis formed by the normal and the triad vectors tangential to the hypersurface – in which the extra piece of the action can be reprojected. It is possible therefore, to rewrite the action in (5.37) with respect to a new Hamiltonian

$$S' = \int dt \int d^3x \left[ \pi_\psi \dot{\psi} + \tilde{\pi}^{ab} \dot{h}_{ab} - \hat{\mathcal{H}}(N) - \hat{\mathcal{H}}(N^a) \right], \quad (5.40)$$

where the new scalar and vector constraints are given by

$$\hat{\mathcal{H}}(N) = \tilde{\mathcal{H}}(N) + NV_0, \quad \hat{\mathcal{H}}(N^a) = \tilde{\mathcal{H}}(N^a) + N^a V_a.$$

If we demand that the new Hamiltonian constraints satisfy the gauge algebra in (5.32–5.33b) and the condition in (5.39), we have 4 conditions for the four components of  $V^\mu$ . If there is not a unique solution, the system has more degrees of freedom than the ones already counted, which would be a contradiction. Therefore, we will assume that there is a unique solution for  $V^\mu$ . On the other hand, the Lie derivative of a scalar function  $F$  along the time direction  $t$  is given by

$$\mathcal{L}_t F = t^\alpha \nabla_\alpha F = (Nn^\alpha + N^a e_a^\alpha) \nabla_\alpha F \equiv N^\kappa \nabla_\kappa F, \quad (5.41)$$

where we selected a basis in which, by definition, the normal defines an orthogonal coordinate to the surface. This works in the same way as the basis that allows us to write the four indices in  $N^\mu$ . A term like this would correspond to the time derivative of the generator of canonical transformations. Such a modification would only make the new action different from general relativity by a total derivative and hence produce identical equations of motion. A comparison of (5.39) with the last expression reveals that it is not possible to generate  $V^\mu$  via the “gradient” in this basis, meaning that the vector  $V^\mu$  needs an extra “solenoidal”

current to be reconstructed. The existence of an extra current would be a clear indication of extra degrees of freedom, which contradicts the counting previously made. So the only possibility we have is that the new action is different from the one in (5.16) just by a derivative along the time direction. This means that if one wants to preserve the symmetry and the number of degrees of freedom after transforming the canonical variables, there is no other option than a canonical transformation. This is fully consistent with Lovelock’s theorem, just as stated in [69]. In [121], it was shown that it is possible to find an extended version of the same statement that does not prescribe a specific form of the constraint algebra and only requires quadratic dependence in the canonical momenta.

### 5.3.2 Deforming GR by introducing extra degrees of freedom

In this section, we perform a concrete implementation of the transformations presented in 5.1.2 for the Einstein-Hilbert action. This is arguably the most complex type of deformation and therefore will take up the bulk of the analysis.

#### Introduction

In the following, the theory of deformation of variables is introduced for gravitation in the usual degrees of freedom. Using Weinberg’s “Folk Theorem” [247, 248], we can construct the most general EFT by constructing a Lagrangian that contains all possible diffeomorphism-invariant terms, using only the degrees of freedom of the theory. Let  $\mathcal{L}_D$  be the most general diffeomorphism-invariant theory made up of the curvature. This would produce the following expansion,

$$\mathcal{L}_D = \alpha R + \left( \beta_1 R^2 + \beta_2 R_{ab} R^{ab} + \dots \right) + \mathcal{O}\left(R^3\right), \quad (5.42)$$

where the first term would correspond to GR. The objective is to explore another sector of diffeomorphism-invariant theories by means of the method of variable deformation, in which one makes a replacement of the coordinate  $h_{ab}$  by some function of the coordinates  $H_{ab}$ , such as below

$$h_{ab} \rightarrow H_{ab}(h_{cd}, \mathcal{L}_t h_{cd}), \quad (5.43)$$

where  $H_{ab}$  is a mapping that, as mentioned in the previous sections, generally is not a canonical transformation of the original ADM variables. Since we are dealing with deformations that are not canonical transformations, this will introduce new degrees of freedom in the gravitational field, and as we shall see in this section, new types of constraints not found in GR. Without loss of generality,  $H_{ab}$  will acquire its space-time dependence through the degrees of freedom ( $h_{ab}(x)$ ,  $\mathcal{L}_t h_{ab}(x)$ , etc.), but can also have its own spacetime dependence apart from this, which we address via an example in the next subsections. Due to the additional time derivatives found in terms like the intrinsic curvature  $K_{ab}$ , this will produce a theory dependent on higher-order derivatives than what is found in GR. This

feature appears in  $R^2$  gravity as well [53]. In general, this deformation can depend on even higher-order time derivatives of the 3-metric,

$$h_{ab} \rightarrow H_{ab}(h_{cd}, \mathcal{L}_t h_{cd}, \mathcal{L}_t \mathcal{L}_t h_{cd}, \dots), \quad (5.44)$$

which will provide a theory with derivatives that are higher-order in time. We chose not to deform the volume element due to geometric reasons; the measure of all parts of the action must remain the infinitesimal volume element for it to remain a proper action. These theories provide an expanded sector of diffeomorphism-invariant theories, and are depicted in Figure 5.4.

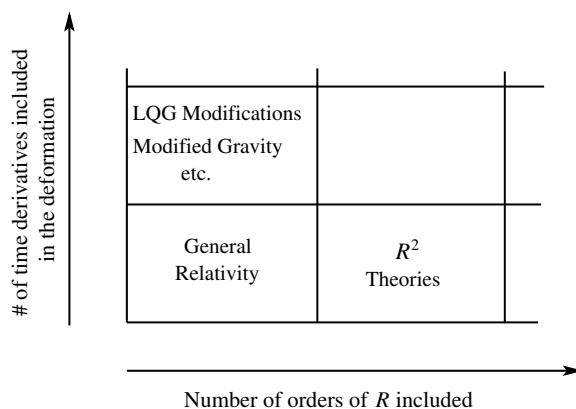


Figure 5.4: Depiction of deformation of variables. The rows determine the number of terms included from equation (5.42), while the columns determine how many variables included in the deformation  $h_{ab} \rightarrow H_{ab}(h_{cd}, \mathcal{L}_t h_{cd}, \mathcal{L}_t \mathcal{L}_t h_{cd}, \dots)$ . The focus of the rest of this section will deal with the top left sector.

To gain intuition for the effects of the deformation, this work will consider only the Einstein-Hilbert term of the expansion (5.42), with the deformation (5.43), as this is arguably the most interesting case.

### The new degrees of freedom

After deforming via a substitution like in equation (5.44), the theory will generally change. We wish to maintain the 3-metric,  $h_{ab}$ , as the configuration variable which dictates the geometric features of spacetime. It is for this reason that the volume element  $\sqrt{-g}$  will not be deformed via (5.44) or by any other means. Any other variations due to the deformation  $H_{ab}$  will serve to change the equations of motion for  $h_{ab}$ , which as stated is to be maintained as the configuration variable, through its alteration of the theory. (That is, we deform a metric theory into another metric theory.) Another point is that since  $H_{ab}$  depends on time derivatives of  $h_{ab}$ , this theory will now depend on accelerations, jerks, etc, instead of the



usual dependence on the field and its velocity field. This introduces a new degree of freedom for every step we take vertically in Figure 5.4 and must be addressed.

### Gauge Invariance and Ostrogradskii Instabilities

The essence of GR is arguably its gauge invariance, which, like any other gauge theory, generates the structure of the interactions in the theory. In gravity, the gauge transformation that must be invariant is that of the diffeomorphism, which endows the theory with the property that leaves the mechanics of gravity the same regardless of any specific location in spacetime (known as background independence). To verify this gauge invariance, one should obtain the constraints of this new theory, and what further constraints need to be satisfied. It shall be shown below, for a deformed theory, that in general there will be additional constraints generated on top of the usual scalar and vector constraints.

One further point that requires clarification is that Dirac’s “Constraint Algebra”[84] for which the scalar and vector constraints are elements, will be satisfied regardless of what their form is. This algebraic structure was shown by Rovelli to be directly derived from the diffeomorphism gauge algebra [208]. What this means is that whether one is dealing with the scalar and vector constraints for a deformed theory or a higher-order theory like the  $R^2$  variety, the “constraint algebra” should be automatically verified.

Obtaining these constraints, namely the scalar, vector and “additional” constraints, requires that the theory is phrased in Hamiltonian form, which in our case depends not only on the velocity and position field coordinates, but perhaps also that of the acceleration, jerk, etc. Typically, such theories are energetically not bound from below and thus can infinitely go into energetic debt by borrowing more and more energy to create unstable results. Ostrogradskii provided a treatment of this situation for theories without gauge ambiguities, but since gravity is a gauge theory, a modification of this treatment is required and was provided in [52, 120] and applied to  $R^2$  gravity [53]. The summary of this approach is that one can define a new canonical variable such that its time derivatives can “absorb” any higher-derivative term – and potential instabilities. This procedure can be generalized as in [120], and the unstable nature of Ostrogradskii theories will also be addressed in what follows. For the theory proposed, which is the Einstein-Hilbert action deformed via (5.43), we can decompose the deformation in the following way,

$$H_{ab}(h_{cd}, \mathcal{L}_t h_{cd}) = h_{ab} + \tilde{H}_{ab}(h_{cd}) + J_{ab}(h_{cd}, \mathcal{L}_t h_{cd}), \quad (5.45)$$

where  $\tilde{H}_{ab}(h_{cd})$  is the part of the general deformation that conformally transforms  $h_{ab}$  in a spacetime-dependent way. This can be interpreted as the gravitational analogue to the deformation that lead us to (5.12). Moreover, the deformations can also be used to represent semiclassical contributions. Later in this chapter, we will extend these procedures to the Ashtekar/Tetrad formalism in section 5.4. In the latter expression, the next term  $J_{ab}$

depends strictly on higher-order derivatives and is the natural choice for a new canonical variable, as its time derivative depends on higher-order time derivatives of  $h_{ab}$

$$\dot{J}_{ab} = \frac{\partial J_{ab}}{\partial h_{cd}} \dot{h}_{cd} + \frac{\partial J_{ab}}{\partial \dot{h}_{cd}} \ddot{h}_{cd},$$

which absorbs the higher-order time derivatives found in the new gravitation Lagrangian. It should be recalled that only  $h_{ab}$  is used to contract vectors in our spacetime, while the other terms serve to deform the theory. At this point, it is crucial to note that the relation between  $J_{ab}$  and the usual degrees of freedom, which is encoded in  $\frac{\partial J_{ab}}{\partial h_{cd}}$  and  $\frac{\partial J_{ab}}{\partial \dot{h}_{cd}}$  is determined by diffeomorphism invariance. Thus, the deformation  $H_{ab}$  must satisfy a certain functional form to be diffeomorphism-invariant. We show this fact in the next subsections.

### The form of the deformed theory

After the deformation (5.43), the Lagrangian reads:

$$\frac{16\pi}{\sqrt{-g}} \mathcal{L} = R = R^{(3)} + K^{ac} K_{ac} - K^2 - 2\nabla_\alpha \left( n^\alpha{}_{;\beta} n^\beta - n^\beta{}_{;\alpha} n^\alpha \right) + 16\pi \mathcal{L}_{\text{MG}} \left( h, \dot{h}, \ddot{h} \right),$$

which is the standard GR Lagrangian plus  $\mathcal{L}_{\text{MG}}$ , which represents the modifications due to the deformation,

$$\begin{aligned} 16\pi \mathcal{L}_{\text{MG}} \left( h, \dot{h}, \ddot{h} \right) &= R_{\tilde{H}}^{(3)} + R_J^{(3)} + V_H \left( \tilde{H}, h \right) + V_J \left( J, h \right) + \frac{KJ}{N} + \frac{J\dot{h}_{ef}}{2N^2} \left( \frac{\partial \tilde{H}}{\partial h_{ef}} \right) + \\ &\frac{1}{N} \left( K^{ab} + \frac{\partial \tilde{H}^{ab}}{\partial \frac{h_{ef}}{2N}} \dot{h}_{ef} \right) \dot{J}_{ab} + \frac{1}{4N^2} h^{ac} h^{bd} \dot{J}_{ab} \dot{J}_{cd} + \dot{h}_{cd} \left( \frac{K}{N} \frac{\partial \tilde{H}}{\partial h_{cd}} + \frac{1}{N} \frac{\partial \tilde{H}^{ab}}{\partial h_{cd}} K^{ab} \right) + \\ &\frac{1}{4N^2} \left( j^2 + \frac{\partial \tilde{H}}{\partial h_{cd}} \frac{\partial \tilde{H}}{\partial h_{ef}} + \frac{\partial \tilde{H}^{cd}}{\partial h_{gh}} \frac{\partial \tilde{H}^{cd}}{\partial h_{ef}} \right) \dot{h}_{ef} \dot{h}_{cd}, \end{aligned}$$

where the first terms come from inserting the decomposition (5.45) in the definition for  $R$ , yielding

$$\tilde{R}^{(3)} = R^{(3)} + R_{\tilde{H}}^{(3)} + R_J^{(3)} + V_H \left( \tilde{H}, h \right) + V_J \left( J, h \right),$$

In order to map the Lagrangian theory to the Hamiltonian form, we found the new corresponding conjugate momenta to  $h_{ab}$  and  $J_{ab}$  such that the Legendre transformations are defined,

$$\begin{aligned}
\pi^{ab} &= \frac{\partial(\sqrt{-g}\mathcal{L}_G)}{\partial\dot{h}_{ab}} = \pi_0^{ab} + \frac{\sqrt{h}}{16\pi} \frac{\partial\dot{J}_{cd}}{\partial\dot{h}_{ab}} (Kh^{cd} + K^{cd}) \\
&+ \frac{\sqrt{h}\dot{h}_{cd}}{32\pi N} \left( h^{ab} \frac{\partial\tilde{H}}{\partial h_{cd}} + \frac{\partial\tilde{H}^{ab}}{\partial h_{cd}} + \frac{\partial\tilde{H}}{\partial h_{cd}} \frac{\partial\tilde{H}}{\partial h_{ab}} + \frac{\partial\tilde{H}^{\tilde{c}\tilde{d}}}{\partial h_{cd}} \frac{\partial\tilde{H}_{\tilde{c}\tilde{d}}}{\partial h_{ab}} \right) \\
&+ \frac{\sqrt{h}}{32\pi N} \frac{\partial\dot{J}_{cd}}{\partial\dot{h}_{ab}} \left( h^{cd} \frac{\partial\tilde{H}}{\partial h_{ef}} \dot{h}_{ef} + \frac{\partial\tilde{H}^{cd}}{\partial h_{ef}} \dot{h}_{ef} \right) + \frac{\sqrt{h}}{16\pi} \left( K \frac{\partial\tilde{H}}{\partial h_{ab}} + K^{cd} \frac{\partial\tilde{H}_{cd}}{\partial h_{ab}} \right) \\
&+ \frac{\sqrt{h}}{32\pi N} j \left( h^{ab} + \left( \frac{\partial\tilde{H}}{\partial h_{ab}} \right) + \frac{\partial j}{\partial\dot{h}_{ab}} \right) + \frac{\sqrt{h}}{32\pi N} \left( j_{ab} \frac{\partial\tilde{H}^{cd}}{\partial h_{ab}} j_{cd} + \frac{\partial\dot{J}_{cd}}{\partial\dot{h}_{ab}} j^{cd} \right) \quad (5.46)
\end{aligned}$$

$$\begin{aligned}
\pi_J^{ab} &= \frac{\partial(\sqrt{-g}\mathcal{L}_G)}{\partial\dot{J}_{ab}} = \frac{\sqrt{h}}{32\pi N} \left( h^{ab} \frac{\partial\tilde{H}}{\partial h_{ef}} \dot{h}_{ef} + \frac{\partial\tilde{H}^{ab}}{\partial h_{ef}} \dot{h}_{ef} \right) + \frac{\sqrt{h}}{16\pi} (K^{ab} + Kh^{ab}) \\
&+ \frac{\sqrt{h}}{32\pi N} (j^{ab} + h^{ab} j), \quad (5.47)
\end{aligned}$$

where  $\pi_0^{ab} \equiv \sqrt{h}/16\pi (K^{ab} - h^{ab}K)$ . Let  $\mathcal{L}_G^0$  be the original Lagrangian for GR, then the new Hamiltonian density is,

$$\begin{aligned}
\mathcal{H}_{\text{MG}} &= \pi^{ab}\dot{h}_{ab} + \pi_J^{ab}\dot{J}_{ab} - N\sqrt{h}\mathcal{L}_G = -N\sqrt{h}\mathcal{L}_G^0 - \frac{\sqrt{h}N}{16\pi} \left( R_{\tilde{H}}^{(3)} + V_H(\tilde{H}, h) + V_J(J, h) \right) \\
&+ \frac{\sqrt{h}}{32\pi N} \left( R_J^{(3)} + \frac{1}{2}j^{ab}j_{ab} + \frac{1}{2}j^2 \right) + \frac{\sqrt{h}\dot{h}_{ab}}{16\pi} \left[ Kh^{cd} + K^{cd} + \frac{\dot{h}_{ef}}{2N} \left( h^{cd} \frac{\partial\tilde{H}}{\partial h_{ef}} + \frac{\partial\tilde{H}^{cd}}{\partial h_{ef}} \right) \right] \frac{\partial\dot{J}_{cd}}{\partial\dot{h}_{ab}} \\
&+ \frac{\sqrt{h}}{32\pi N} \left( \frac{\partial\tilde{H}^{cd}}{\partial h_{ab}} \dot{h}_{ab} j_{cd} + \frac{\partial\tilde{H}}{\partial h_{ab}} \dot{h}_{ab} j + j \frac{\partial j}{\partial\dot{h}_{ab}} \dot{h}_{ab} + \frac{\partial\dot{J}_{cd}}{\partial\dot{h}_{ab}} \dot{h}_{ab} j^{cd} \right) + \frac{\sqrt{h}}{32\pi N} (j^{ab} + h^{ab} j) \dot{h}_{ab} + \\
&+ \frac{\sqrt{h}}{32\pi N} \dot{h}_{ab} \dot{h}_{cd} \left( h^{ab} \frac{\partial\tilde{H}}{\partial h_{cd}} + \frac{\partial\tilde{H}^{ab}}{\partial h_{cd}} + \frac{1}{2} \frac{\partial\tilde{H}}{\partial h_{cd}} \frac{\partial\tilde{H}}{\partial h_{ab}} + \frac{1}{2} \frac{\partial\tilde{H}^{\tilde{c}\tilde{d}}}{\partial h_{cd}} \frac{\partial\tilde{H}_{\tilde{c}\tilde{d}}}{\partial h_{ab}} \right). \quad (5.48)
\end{aligned}$$

In the usual Hamiltonian treatment, the given theory is written strictly in terms of the canonical field variables  $\phi_\alpha$  and  $\pi^\alpha = \frac{\partial\mathcal{L}}{\partial\phi_\alpha}$  [84], which requires, at minimum, a surjective mapping from the velocities to the canonical momentum. In the general case depicted in equation (5.48), one would need both the squares of the two new momenta  $\pi_{ab}\pi^{ab}$ ,  $\pi_J^{ab}\pi_{J,ab}$  and the squares of the traces  $\pi^2$  and  $\pi_J^2$  so that one can write this as

$$\mathcal{H}_{\text{MG}} = \frac{N}{\sqrt{h}} \left( \pi_J^{ab}\pi_{J,ab} + \pi^{ab}\pi_{ab} \right) + \mathcal{H}_{\text{MG},2}(J, \dot{J}, h, \dot{h}, \pi, \pi_J),$$

where whether the mapping between these two momenta and the two velocities  $\dot{h}_{ab}$  and  $\dot{J}_{ab}$  is injective or not will determine whether one can write  $\mathcal{H}_{\text{MG},2}$  strictly in terms of the new conjugate variables. The computation for the general Hamiltonian density in terms of the

momenta but not the velocities is long and only truly required if we want the equations of motion for this theory, which we do not at this moment.

### An example

Equation (5.48) has clear kinetic energy terms for different tensorial components of  $J_{ab}$ , which is seen in the  $\left(R_J^{(3)} + \frac{1}{2}\dot{J}^{ab}J_{ab} + \frac{1}{2}\dot{J}^2\right)$  term. The form of the Hamiltonian is similar to that of a scalar field, i.e., the  $\dot{J}^2$  term, and a tensor field, through  $\dot{J}_{ab}\dot{J}^{ab}$ . These can be interpreted as different sectors of the gravitational field that come as a result of this deformation. Moreover, these deformations have less degrees of freedom than the original gravitational variables in order to circumvent the potential instabilities created by introducing higher derivatives, as discussed in [250].

Instead of acquiring the constraints in general, we follow the common practice of decomposing  $J_{ab}$  and  $\dot{J}_{ab}$  into scalar, vector and tensor components,

$$J_{ab} = Jh_{ab} + J_{ab}^V + J_{ab}^T,$$

$$\dot{J}_{ab} = \dot{J}h_{ab} + \dot{J}_{ab}^V + \dot{J}_{ab}^T,$$

and then consider the dynamics due to only a subset of these degrees of freedom. Example routes are outlined in Table (5.1).

Degs. of Freedom for $J_{ab}$	$\dot{J}^2$ Value	$\dot{J}_{ab}\dot{J}^{ab}$ Value
Only Scalar	$\dot{J}^2 \neq 0$	$\dot{J}_{ab}\dot{J}^{ab} = h\dot{J}^2$
Only Vector\Tensor	$\dot{J}^2 = 0$	$\dot{J}_{ab}\dot{J}^{ab} =$ $\left(J_{\text{tensor}}^{ab} + J_{\text{vector}}^{ab}\right)^2$
Scalar-Vector-Tensor ( <i>Special</i> )	$\dot{J}^2 \neq 0$	$\dot{J}_{ab}\dot{J}^{ab} = 0$
Scalar-Vector-Tensor ( <i>General</i> )	$\dot{J}^2 \neq 0$	$\dot{J}_{ab}\dot{J}^{ab} \neq 0$

Table 5.1: The various ways to decompose the tensorial structure of the new degree of freedom  $J_{ab}$ .

The simplest case is that where the scalar degree of freedom vanishes, i.e., the trace vanishes,  $\dot{J} = 0$ , but the tensorial structure is maintained. We assume that the natural conformal scaling due to  $\tilde{H}$  in equation (5.45) will be suppressed to zero. In this way, only the new coordinate  $J_{ab}$  deforms the theory.

In this example the conjugate momenta simplify to

$$\pi^{ab} = \frac{1}{16\pi}\sqrt{h}\left(K^{cd} - h^{cd}K\right) + \frac{\sqrt{h}}{16\pi}\frac{\partial\dot{J}_{cd}}{\partial\dot{h}_{ab}}\left[\frac{16\pi}{\sqrt{h}}\pi_J^{cd} - \frac{1}{2N}j^{cd}\right] + \frac{\sqrt{h}}{32\pi N}\left(\dot{J}_{ab} + \frac{\partial\dot{J}_{cd}}{\partial\dot{h}_{ab}}j^{cd}\right),$$

$$\pi_J^{ab} = \frac{\sqrt{h}}{16\pi}\left(K^{ab} + h^{ab}K\right) + \frac{\sqrt{h}}{32\pi N}j^{ab},$$

From these definitions one can define the extrinsic curvature in term of the new momenta,

$$K^{ab} = \underbrace{\frac{16\pi}{\sqrt{h}} \left[ \pi^{ab} - \frac{h^{ab}}{2} \text{Tr} \{ \pi^{ab} \} \right]}_{K_1^{ab}} + \frac{8\pi}{\sqrt{h}} \frac{\partial \dot{J}_{cd}}{\partial \dot{h}_{ab}} \pi_J^{cd} + \frac{1}{2N} \underbrace{\left[ j_{ab} - \frac{5}{2} \frac{\partial j^{cd}}{\partial \dot{h}_{ab}} j_{cd} \right]}_{\Delta K^{ab}} \equiv K_1^{ab} + \frac{1}{N} \Delta K^{ab},$$

Now let  $\tilde{\pi} = \text{Tr} \{ \pi^{ab} \}$  and  $\tilde{\pi}_J = h_{ab} \frac{\partial \dot{J}_{cd}}{\partial \dot{h}_{ab}} \pi_J^{cd}$ . With this, and a lengthy algebra exercise, the Hamiltonian density can be written as in (5.49). We notice that

$$\left( 16\pi/\sqrt{h} \right)^2 \left[ \pi^{ab} \pi_{ab} - \tilde{\pi}^2/2 \right] - R^{(3)},$$

contains the original scalar constraint (5.21). The quantity  $-2 \left( K_1^{ab} - K_1 h^{ab} \right)_{|b}$  is the original vector constraint. We use the notation  $A_{|b}$  to represent the intrinsic covariant derivative of  $A$ . We can also note that the surface term now depends on the new degrees of freedom through  $K^{ab}$ .

$$\begin{aligned} \mathcal{H}_G = & \frac{\sqrt{h}}{16\pi} \left[ \left( \frac{16\pi}{\sqrt{h}} \right)^2 \left[ \pi^{ab} \pi_{ab} - \frac{\tilde{\pi}^2}{2} \right] - R^{(3)} + \left( \frac{16\pi}{\sqrt{h}} \right)^2 \left[ \pi_J^{ab} \pi_{J,ab} - \frac{\tilde{\pi}_J^2}{2} \right] - R_J^{(3)} + \frac{1}{2} \left( \frac{16\pi}{\sqrt{h}} \right)^2 \tilde{\pi} \tilde{\pi}_J \right. \\ & \left. - V_J(J, h) \right] N + \frac{\sqrt{h}}{16\pi} \left[ 2K_1 K_1^{ab} \frac{\partial \dot{J}_{ab}}{\partial \dot{h}^{cd}} h^{cd} - \left[ 2 \frac{\partial \dot{J}_{cd}}{\partial \dot{h}^{ab}} + \frac{\partial \dot{J}_{ab}}{\partial \dot{h}^{ef}} \frac{\partial \dot{J}_{cd}}{\partial \dot{h}_{ef}} \right] K_1^{cd} K_1^{ab} - K_1^{ab} K_{1ab} - 5K_1^2 \right] N \\ & + \frac{\sqrt{h}}{16\pi} \left[ -2 \left( K_1^{ab} - K_1 h^{ab} \right)_{|b} \right] N_a + \underbrace{\frac{\sqrt{h}}{16\pi} \left[ 2 \left( K^{ab} - K h^{ab} \right) N_a \right]_{|b}}_{\text{surface term}} - \frac{\sqrt{h}}{16\pi} \left[ 2 \left( \Delta K^{ab} - \Delta K h^{ab} \right)_{|b} \right] \frac{N_a}{N} \\ & + \frac{\sqrt{h}}{16\pi} \left[ 2 \left( K_1 \Delta K^{ab} + \Delta K K_1^{ab} \right) \frac{\partial \dot{J}_{ab}}{\partial \dot{h}^{cd}} h^{cd} - \left[ 2 \frac{\partial \dot{J}_{cd}}{\partial \dot{h}^{ab}} + \frac{\partial \dot{J}_{ab}}{\partial \dot{h}^{ef}} \frac{\partial \dot{J}_{cd}}{\partial \dot{h}_{ef}} \right] \left( \Delta K^{cd} K_1^{ab} + \Delta K^{ab} K_1^{cd} \right) \right] \cdot 1 \\ & + \frac{\sqrt{h}}{16\pi} \left[ \left( +h_{ab} j^{cd} \frac{\partial \dot{J}_{cd}}{\partial \dot{h}^{ef}} h^{ef} - j^{cd} \frac{\partial \dot{J}_{cd}}{\partial \dot{h}^{ab}} - j^{cd} \frac{\partial \dot{J}_{ab}}{\partial \dot{h}_{cd}} + \frac{\partial \dot{J}_{ab}}{\partial \dot{h}_{cd}} \dot{h}^{cd} - j^{cd} \frac{\partial \dot{J}_{ab}}{\partial \dot{h}_{ef}} \frac{\partial \dot{J}_{cd}}{\partial \dot{h}^{ef}} - 2j^{ab} \right) K_1^{ab} \right] \cdot 1 \\ & - \frac{\sqrt{h}}{16\pi} \left[ 2K_1 \Delta K + 2 \left[ K_1^{ab} \Delta K_{ab} + 5K_1 \Delta K \right] \right] \cdot 1 - \frac{\sqrt{h}}{16\pi} \left[ 2\Delta K^2 + \left[ \Delta K^{ab} \Delta K_{ab} + 5\Delta K^2 \right] \right] \frac{1}{N} \\ & + \frac{\sqrt{h}}{16\pi} \left[ \left( h_{ab} j^{cd} \frac{\partial \dot{J}_{cd}}{\partial \dot{h}^{ef}} h^{ef} - j^{cd} \frac{\partial \dot{J}_{cd}}{\partial \dot{h}^{ab}} - j^{cd} \frac{\partial \dot{J}_{ab}}{\partial \dot{h}_{cd}} + \frac{\partial \dot{J}_{ab}}{\partial \dot{h}_{cd}} \dot{h}^{cd} - j^{cd} \frac{\partial \dot{J}_{ab}}{\partial \dot{h}_{ef}} \frac{\partial \dot{J}_{cd}}{\partial \dot{h}^{ef}} - 2j_{ab} \right) \Delta K^{ab} \right] \frac{1}{N} \\ & - \frac{\sqrt{h}}{16\pi} \left[ 2\Delta K \Delta K^{ab} \frac{\partial \dot{J}_{ab}}{\partial \dot{h}^{cd}} h^{cd} + \left[ 2 \frac{\partial \dot{J}_{cd}}{\partial \dot{h}^{ab}} + \frac{\partial \dot{J}_{ab}}{\partial \dot{h}^{ef}} \frac{\partial \dot{J}_{cd}}{\partial \dot{h}_{ef}} \right] \Delta K^{ab} \Delta K^{cd} + 2\dot{J}_{ab} \dot{h}^{ab} + 2 \frac{\partial \dot{J}_{cd}}{\partial \dot{h}_{ab}} j^{cd} \dot{h}^{ab} \right] \frac{1}{N} \\ & + \frac{\sqrt{h}}{16\pi} \left[ 2j^{ab} j^{cd} \frac{\partial \dot{J}_{cd}}{\partial \dot{h}^{ab}} - j^{cd} j^{ij} \frac{\partial \dot{J}_{ij}}{\partial \dot{h}_{ab}} \frac{\partial \dot{J}_{cd}}{\partial \dot{h}^{ab}} \right] \frac{1}{N}. \end{aligned} \quad (5.49)$$

### 5.3.3 Further constraints in the deformations

To guarantee diffeomorphism invariance, the variation of the Hamiltonian density with respect to the lapse and shift must vanish: such a variation provides the constraints. This means that the new vector and scalar constraints are,

$$C_a = -\frac{32\pi}{\sqrt{h}} \left( \pi^{ab} + \frac{1}{2} \frac{\partial \dot{J}_{cd}}{\partial \dot{h}_{ab}} \pi_J^{cd} - \frac{\tilde{\pi}_J}{2} h^{ab} \right)_{|b},$$

$$\begin{aligned} C_0 &= \left( \frac{16\pi}{\sqrt{h}} \right)^2 \left[ \pi^{ab} \pi_{ab} - \frac{\tilde{\pi}^2}{2} \right] - R^{(3)} + \left( \frac{16\pi}{\sqrt{h}} \right)^2 \left[ \pi_J^{ab} \pi_{J,ab} - \frac{\tilde{\pi}_J^2}{2} \right] - R_J^{(3)} \\ &+ \frac{1}{2} \left( \frac{16\pi}{\sqrt{h}} \right)^2 \tilde{\pi} \tilde{\pi}_J - V_J(J, h) + 2K_1 K_1^{ab} \frac{\partial \dot{J}_{ab}}{\partial \dot{h}^{cd}} h^{cd} - K_1^{ab} K_{1ab} - 5K_1^2 \\ &- \left[ 2 \frac{\partial \dot{J}_{cd}}{\partial \dot{h}^{ab}} + \frac{\partial \dot{J}_{ab}}{\partial \dot{h}^{ef}} \frac{\partial \dot{J}_{cd}}{\partial \dot{h}_{ef}} \right] K_1^{cd} K_1^{ab}. \end{aligned}$$

Furthermore, the new Hamiltonian density (5.49) contains terms proportional to  $\frac{1}{N}, \frac{N_1}{N}$  and 1. In order for Hamilton's equations to not depend on a gauge choice, these terms must individually vanish. The terms proportional to  $\frac{1}{N}, \frac{N_a}{N}$ , which will be called  $C_{-1}$  and  $C_{-1}^a$  respectively, must also vanish separately so as to not make the vector and scalar constraints depend on the gauge, a crucial feature for any gauge theory. The term proportional to unity, let us call it  $C_1$ , represents a type of *bare* Hamiltonian that must also vanish independently. If this term were to persist, then within Hamilton's equations there would exist a gauge choice of  $(N, N^a)$  such that there is no time evolution, which would allow there to be an aether-like reference frame. In both cases, if these terms do not vanish, diffeomorphism invariance will be broken and hence<sup>2</sup>,

$$\begin{aligned} C_1 &= 2 \left( K_1 \Delta K^{ab} + \Delta K K_1^{ab} \right) \frac{\partial \dot{J}_{ab}}{\partial \dot{h}^{cd}} h^{cd} - \left[ 2 \frac{\partial \dot{J}_{cd}}{\partial \dot{h}^{ab}} + \frac{\partial \dot{J}_{ab}}{\partial \dot{h}^{ef}} \frac{\partial \dot{J}_{cd}}{\partial \dot{h}_{ef}} \right] \left( \Delta K^{cd} K_1^{ab} + \Delta K^{ab} K_1^{cd} \right) \\ &+ \left( h_{ab} j^{cd} \frac{\partial \dot{J}_{cd}}{\partial \dot{h}^{ef}} h^{ef} - j^{cd} \frac{\partial \dot{J}_{cd}}{\partial \dot{h}^{ab}} - j^{cd} \frac{\partial \dot{J}_{ab}}{\partial \dot{h}^{cd}} + \frac{\partial \dot{J}_{ab}}{\partial \dot{h}^{cd}} \dot{h}^{cd} - j^{cd} \frac{\partial \dot{J}_{ab}}{\partial \dot{h}_{ef}} \frac{\partial \dot{J}_{cd}}{\partial \dot{h}^{ef}} - 2\dot{J}_{ab} \right) K_1^{ab} \\ &- 7K_1 \Delta K - 2K_1^{ab} \Delta K_{ab}, \end{aligned}$$

$$C_{-1}^a = 2 \left( \Delta K^{ab} - \Delta K h^{ab} \right)_{|b},$$

<sup>2</sup>See <https://github.com/josegalvez/HD-GR> for a generalized step-by-step explanation of all the calculations shown this subsection.

$$\begin{aligned}
C_{-1} = & -7\Delta K^2 - \left[ 2\Delta K \Delta K^{ab} \frac{\partial \dot{J}_{ab}}{\partial \dot{h}^{cd}} h^{cd} + \left( 2 \frac{\partial \dot{J}_{cd}}{\partial \dot{h}^{ab}} + \frac{\partial \dot{J}_{ab}}{\partial \dot{h}^{ef}} \frac{\partial \dot{J}_{cd}}{\partial \dot{h}_{ef}} \right) \Delta K^{ab} \Delta K^{cd} \right] \\
& - \Delta K^{ab} \Delta K_{ab} + \left( 2\dot{J}_{ab} \dot{h}^{ab} + 2 \frac{\partial \dot{J}_{cd}}{\partial \dot{h}_{ab}} j^{cd} \dot{h}^{ab} - 2j^{ab} j^{cd} \frac{\partial \dot{J}_{cd}}{\partial \dot{h}^{ab}} - j^{cd} j^{ij} \frac{\partial \dot{J}_{ij}}{\partial \dot{h}_{ab}} \frac{\partial \dot{J}_{cd}}{\partial \dot{h}^{ab}} \right) \\
& + \left( h_{ab} j^{cd} \frac{\partial \dot{J}_{cd}}{\partial \dot{h}^{ef}} h^{ef} - j^{cd} \frac{\partial \dot{J}_{cd}}{\partial \dot{h}^{ab}} - j^{cd} \frac{\partial \dot{J}_{ab}}{\partial \dot{h}_{cd}} + \frac{\partial \dot{J}_{ab}}{\partial \dot{h}_{cd}} \dot{h}^{cd} - j^{cd} \frac{\partial \dot{J}_{ab}}{\partial \dot{h}_{ef}} \frac{\partial \dot{J}_{cd}}{\partial \dot{h}^{ef}} - 2\dot{J}_{ab} \right) \Delta K^{ab}.
\end{aligned}$$

## 5.4 Deforming general relativity in tetrad theory and Ashtekar variables

There exist other representations of general relativity aside from that presented above. Here we will briefly review tetrad formalisms. In covariant form arguably the most popular version of a tetrad action is the tetrad-Palatini action [191] which may be written, without the Holst term for simplicity, as:

$$\begin{aligned}
S &= \int \mathbf{e} \wedge \mathbf{e} \wedge * \mathbf{F}(\omega) \\
&= \frac{1}{2} \int d^4x \epsilon_{IJKL} \epsilon^{\mu\nu\rho\sigma} e^I_\mu e^J_\nu F^KL_{\rho\sigma},
\end{aligned} \tag{5.50}$$

with  $e$  the tetrad and  $\omega$  a Lorentz (for our purposes) connection whose dual (on the capital indices, coupling to the  $so(3,1)$  algebra) field strength is denoted by  $*\mathbf{F}$ .  $e$  and  $\omega$  constitute the independent fields, and the variation with respect to the connection yields the torsionless condition for the connection whereas variation with respect to the tetrad yields the Einstein equations. The configuration space is spanned by the pair of components  $(e^I_\mu, \omega^{JK}_\nu)$ .

Let us now consider deformations of  $e$  and  $\omega$  in the action (5.50) while noting that the tetrad  $e$  should remain one of the variables in the new theory (analogous to keeping the metric variable in the deformed metric theory). Using slightly modified notation we write

$$\mathbf{e} \rightarrow \mathcal{E}(\tilde{\mathbf{e}}, \tilde{\omega}), \quad \tilde{\omega} \rightarrow \mathcal{W}(\tilde{\mathbf{e}}, \tilde{\omega}). \tag{5.51}$$

Note that this is equivalent to the deformation

$$\mathbf{e} \rightarrow \tilde{\mathbf{e}} + \Delta \tilde{\mathbf{e}}, \quad \omega \rightarrow \tilde{\omega} + \Delta \tilde{\omega}, \tag{5.52}$$

with

$$\Delta \tilde{\mathbf{e}} \equiv \mathcal{E}(\tilde{\mathbf{e}}, \tilde{\omega}) - \tilde{\mathbf{e}}, \quad \Delta \tilde{\omega} \equiv \mathcal{W} - \tilde{\omega}. \tag{5.53}$$

As a clarification, what we mean by this is that the components of  $\mathbf{e}$  and  $\omega$ , that is  $e^I_\mu$  and  $\tilde{\omega}^{IJ}_\mu$ , are the quantities deformed. Of course the group generator and differential form structure remain unaltered.

Using (5.52) in (5.50), and noting that  $\tilde{\mathbf{F}} = d\tilde{\omega} + \tilde{\omega} \wedge \tilde{\omega}$ , we define the quantity

$$\Delta^* \tilde{\mathbf{F}} \equiv * [d(\Delta\tilde{\omega}) + \tilde{\omega} \wedge \Delta\tilde{\omega} + \Delta\tilde{\omega} \wedge \tilde{\omega} + \Delta\tilde{\omega} \wedge \Delta\tilde{\omega}]. \quad (5.54)$$

Noting that the action implicitly involves a trace, the resulting action may be written as:

$$S' = S + \int \left\{ 2 [\tilde{\mathbf{e}} \wedge \Delta\tilde{\mathbf{e}} \wedge * \mathbf{F} + \tilde{\mathbf{e}} \wedge \Delta\tilde{\mathbf{e}} \wedge \Delta^* \mathbf{F}] + \tilde{\mathbf{e}} \wedge \tilde{\mathbf{e}} \wedge \Delta^* \mathbf{F} + \Delta\tilde{\mathbf{e}} \wedge \Delta\tilde{\mathbf{e}} \wedge * \mathbf{F} + \Delta\tilde{\mathbf{e}} \wedge \Delta\tilde{\mathbf{e}} \wedge \Delta^* \mathbf{F} \right\}. \quad (5.55)$$

Deformations of the tetrad-Palatini action (5.50) are particularly straight-forward to reproject via (5.39). In four spacetime dimensions the manifold of 4-forms is one-dimensional, and hence we may write <sup>3</sup>

$$\epsilon^{\mu\nu\rho\sigma} \propto N^{[\mu} \epsilon^{\nu\rho\sigma]}. \quad (5.56)$$

Therefore the modified action can be cast as the original action plus a term of the form

$$\Delta S \propto \int d^4x \epsilon^{\nu\rho\sigma} N^\mu \Delta \mathcal{L}'_{\mu\nu\rho\sigma}, \quad (5.57)$$

where  $\Delta \mathcal{L}'_{\mu\nu\rho\sigma}$  is the deformation of the

$$\epsilon_{IJKL} e^I_\mu e^J_\nu F^KL_{\rho\sigma}$$

part in the Lagrangian. The antisymmetric structure of the Levi-Civita, written as in (5.56) along with its contraction with the tetrads in the undeformed action (5.50) is actually sufficient to filter out terms proportional to  $N$  and  $N^a$ . However, for a generic deformation, the new action may need to be reprojected in the manner illustrated in the previous sections. Simple deformations (for example those that do not alter the linear dependence on  $N^\mu$  in the new variables) will not suffer from this.

Before proceeding we should note that  $\Delta\tilde{\omega}$  may depend on the tetrad and, as mentioned, we wish to retain the tetrad as a fundamental degree of freedom in the new theory. Therefore we can state the following points about variable deformations in the Palatini Lagrangian:

- Since  $d(\Delta\tilde{\omega}) = d\mathcal{W}(\tilde{\mathbf{e}}, \tilde{\omega}) - d\tilde{\omega}$ , in general we pick up a generalized “velocity” conjugate to the tetrad as now derivatives of the tetrad are explicitly present in the action. This is an example of acquiring new degrees of freedom via the deformation.
- One needs to identify the corresponding connection variable(s). These other variable(s) may or may not comprise  $\tilde{\omega}$ . The situation regarding the new variables tends to be

<sup>3</sup>The numerical structure of the three-index permutation symbols  $\epsilon^{\nu\rho\sigma}$  is implied by equation (5.56). It is a different quantity for each value of the index  $\mu$  in (5.56). The antisymmetrization is to preserve the algebraic structure of the four index Levi-Civita when dealing with components, as we are here.



clearer in the Hamiltonian picture, which is the main focus of this chapter, and will be discussed below when we go to the Hamiltonian formalism.

- The new connection may no longer be torsion free.
- Related to the previous point, the tetrad's covariant derivative may no longer be annihilated. This is not surprising since we now have a new connection, in a new theory whose symmetry may differ from the original symmetry. The new constraints will serve to enforce this new symmetry.

Next we wish to address the main point, which is the issue of Hamiltonian consistency of a deformed theory. As in the introduction, we shall first consider the undeformed action in its canonical guise, then identify the configuration-momentum variables, and then perform the variable deformation. Since we will be deforming the previous action, but in a different form and also a different set of variables, the deformed theory will not necessarily be the same as if one deforms the Palatini action directly as above. (This is also true due to discarding surface terms when transforming one undeformed action into another form of the same action.) The tetrad-Palatini action (with the Holst term) in canonical form leads almost directly to the Ashtekar-Barbero action. The transformations required from the tetrad-Palatini action to the Ashtekar action may be found in [209]. The Ashtekar variables traditionally comprise an  $su(2)$  valued densitized triad,  $E_i^a = \det|e|e_i^a$ , and a connection,  $A_a^i$ , where the indices  $i, j$ , etc. couple to the  $SU(2)$  generators (to use notation most often seen in loop quantum gravity). The relationships between these new variables and the ADM variables are given by

$$hh^{ab} = E_i^a E_j^b \delta^{ij}, \quad (5.58a)$$

$$A_a^i = \Gamma_a^i + \gamma K_a^i. \quad (5.58b)$$

Here  $\Gamma_a^i$  is the spin connection, annihilating an orthonormal triad via covariant differentiation,  $K_a^i$  is the densitized extrinsic curvature

$$K_a^i \equiv \frac{1}{\sqrt{E}} K_{ab} E_j^b \delta^{ij}, \quad (5.59)$$

and  $h$  is  $\det h_{ab}$ . The quantity  $\gamma$  is known as the Barbero-Immirzi parameter, which from the point of view of the bulk classical equations of motion is arbitrary, but its exact value is of importance in the quantum theory. It has been shown that the variables  $E_i^a, A_a^i$  are related to the ADM variables in the previous section via a canonical transformation [36, 235].

The Poisson algebra in these variables is given by the brackets

$$\{E_i^a(x), A_b^j(y)\} = \kappa\gamma\delta(x,y)\delta_i^j\delta_b^a, \quad (5.60a)$$

$$\{E_i^a(x), E_j^b(y)\} = \{A_a^i(x), A_b^j(y)\} = 0. \quad (5.60b)$$

In these variables the action may be written as

$$S = \frac{1}{\kappa} \int dt \int d^3x \left[ E_i^a \dot{A}_a^i - \mathcal{H}(N) - \mathcal{H}(N^a) - \mathcal{G}(\lambda^i) \right], \quad (5.61)$$

plus corresponding possible matter terms. In this case the scalar and vector constraints are given by

$$\mathcal{H}(N) = N \frac{E_i^a E_j^b}{\sqrt{E}} \left( F_{ab}^k \epsilon^{ij}_k - 2(\gamma^2 - 1) K_{[a}^i K_{b]}^j \right), \quad (5.62a)$$

$$\mathcal{H}(N^b) = N^b \left[ E_i^a F_{ab}^i - (\gamma^2 + 1) K_b^i G_i \right]. \quad (5.62b)$$

$F_{ab}^i$  is the field-strength tensor of the connection,  $F_{ab}^i \equiv \partial_a A_b^i - \partial_b A_a^i + \epsilon_{jk}^i A_a^j A_b^k$ . Note that since we are dealing with a (densitized) triad variable in lieu of a metric variable, a new constraint is introduced which fixes the internal  $SU(2)$  rotation of the triad. This is the so-called Gauss constraint,

$$G_i \lambda^i =: \mathcal{G}(\lambda^i) \equiv \left( \partial_a E_i^a + \epsilon_{ij}^k A_a^j E_k^a \right) \lambda^i, \quad (5.63)$$

with its own Lagrange multiplier,  $\lambda^i$ , which fixes the metricity condition on the densitized triad.

Since the internal spatial geometry is encoded in the densitized triad we will, in analogy to keeping the 3-metric as the configuration variable in the ADM variables, keep the densitized triad as the canonical gravitational momentum variable after deformation. In brief, as in the previous section the deformation may be written schematically as

$$E_i^a \rightarrow \tilde{E}_i^a + \Delta \tilde{E}_i^a, \quad (5.64a)$$

$$A_a^i \rightarrow \tilde{A}_a^i + \Delta \tilde{A}_a^i. \quad (5.64b)$$

Before continuing, it should be noted that in principle the quantities in the Gauss constraint are to be deformed so that the Gauss constraint becomes some complicated function of both the densitized triad and the connection. However, caution should be applied in this case since the Gauss constraint, in its original form, enforces the specific condition of metricity fixing. It may be desirable, regardless of the specific deformation, to enforce “by hand” that the Gauss constraint transform as  $\mathcal{G}(\lambda_i, E_j^a) \rightarrow \mathcal{G}(\lambda_i, \tilde{E}_j^a)$  so that after deformation triad metricity fixing is still enforced by this constraint. A comment on this follows the example below.

The general deformation of the variables (5.64a) and (5.64b) be applied to (5.61) and the resulting action re-written in Hamiltonian canonical form by identifying the new configuration-momentum pairs. In principle this may be done, but the resulting action will generally be very complicated and not very perspicuous, not least because of the fact that  $K^i_a = \gamma^{-1}[A^i_a - \Gamma^i_a]$  and the spin connection is given by the complicated expression

$$\Gamma^i_a = \frac{1}{2}\epsilon^i_j{}^k E_k^b \left[ -2\partial_{[a} E^j_{b]} + E^j_c E_a^\ell \partial_b E_\ell^c \right] + \frac{1}{4}\epsilon^i_j{}^k E_k^b \left[ 2E^j_a \partial_b \ln(E) - E^j_b \partial_a \ln(E) \right], \quad (5.65)$$

as well as the contracted triad  $E_j^a = E_k^a E_\ell^b \delta^{kl} E_b^i \delta_{ij}$ . Therefore we illustrate the scheme on an example relevant to some studies of loop quantum gravity. A specific example of such deformations in these variables is provided by the often used holonomy correction inspired by loop quantum gravity. In such scenarios the connection variable is deformed in order to represent loop quantum corrections of the connection as a holonomy; namely, in the language of (5.36a) and (5.36b):

$$A^i_a \rightarrow H^i_a \left( \tilde{A}^i_a, \tilde{E}_j^b \right) = \frac{\sin \left[ \tilde{A}^i_a \delta(\tilde{E}_j^b) \right]}{\delta(\tilde{E}_j^b)}, \quad (5.66a)$$

$$E_i^a \rightarrow P_i^a \left( \tilde{A}^i_a, \tilde{E}_j^b \right) = \tilde{E}_i^a, \quad (5.66b)$$

$$\Delta \tilde{A}^i_a = \frac{\sin \left[ \tilde{A}^i_a \delta(\tilde{E}_j^b) \right]}{\delta(\tilde{E}_j^b)} - \tilde{A}^i_a, \quad \Delta \tilde{E}_i^a = 0. \quad (5.66c)$$

The quantity  $\delta(\tilde{E}_j^b)$  is related to the proper-length along the path which the holonomy is taken, and hence depends on  $\tilde{E}_j^b$  but not the connection [65] (although sometimes  $\delta$  is taken to be constant for simplicity). Note that here the deformation is performed at the level of the Hamiltonian variables, compatible with the analysis of this thesis. This is due to the fact that the holonomy correction is inspired by the operator representation of the algebra of the commutator of loop quantum gravity, and therefore these modifications are often applied via direct substitution of (5.66a) and (5.66b) into the action (5.61). The issue now remains as to what to do with the canonical term in (5.61),  $E_i^a \dot{A}^i_a$ . One method is to simply insert the time derivative of (5.64b) in lieu of  $\dot{A}^i_a$ . If one proceeds in this manner the resulting action is

$$\begin{aligned} S' &= \frac{1}{\kappa} \int dt \int d^3x \left[ P_i^a \dot{H}^i_a - \tilde{\mathcal{H}}(N) - \tilde{\mathcal{H}}(N^b) - \tilde{\mathcal{G}}(\lambda^i) \right] \\ &= \frac{1}{\kappa} \int dt \int d^3x \left\{ \tilde{E}_i^a \left[ \cos(\tilde{A}^i_a \delta) \dot{\tilde{A}}^i_a + \left( \cos(\tilde{A}^i_a \delta) \frac{\partial \delta}{\partial \tilde{E}_j^b} \delta^{-1} - \sin(\tilde{A}^i_a \delta) \frac{\partial \delta}{\partial \tilde{E}_j^b} \delta^{-2} \right) \dot{\tilde{E}}_j^b \right] \right. \\ &\quad \left. - \hat{\mathcal{H}}(N) - \hat{H}(N^b) - \hat{G}(\lambda^i) \right\}. \end{aligned} \quad (5.67)$$

(Due to the nonlinear nature of the deformation, the index structure is awkward in (5.67). In each term repeated indices are summed, even if they appear more than twice.) The natural interpretation of the above is that the resulting theory has more degrees of freedom than general relativity; the Hamiltonian degrees of freedom being:

$$\tilde{A}_{,a}^i, {}_A\tilde{\pi}_i^a \equiv \tilde{E}_i^a \cos(\tilde{A}_a^i \delta) \quad (\text{no sum}) \quad \&, \quad (5.68a)$$

$$\tilde{E}_i^a, {}_E\tilde{\pi}_b^j \equiv \tilde{E}_i^a \left( \cos(\tilde{A}_a^i \delta) \frac{\partial \delta}{\partial \tilde{E}_j^b} \delta^{-1} - \sin(\tilde{A}_a^i \delta) \frac{\partial \delta}{\partial \tilde{E}_j^b} \delta^{-2} \right). \quad (5.68b)$$

It is noted that in this particular scenario the system retains second-order equations of motion, and therefore the Ostrogradskii stability issues presented in the previous section are avoided. However, if one a priori assumes some relationship between  $\tilde{A}_a^i$  and  $\tilde{E}_i^a$  (such as in, for example, electromagnetism where the electric field is related to the time derivative of the potential), then one could induce a higher-order theory via the  $\dot{\tilde{E}}_j^b$  term in (5.67). We do not assume this since the canonical degrees of freedom are independent here. The Poisson brackets are now defined with respect to the canonical variables from the new degree of freedom. That is

$$\{X, Y\} = \frac{\partial X}{\partial \tilde{A}_a^i} \frac{\partial Y}{\partial ({}_A\tilde{\pi}_i^a)} - \frac{\partial X}{\partial ({}_A\tilde{\pi}_i^a)} \frac{\partial Y}{\partial \tilde{A}_a^i} + \frac{\partial X}{\partial \tilde{E}_i^a} \frac{\partial Y}{\partial ({}_E\tilde{\pi}_i^a)} - \frac{\partial X}{\partial ({}_E\tilde{\pi}_i^a)} \frac{\partial Y}{\partial \tilde{E}_i^a}. \quad (5.69)$$

The decomposition (5.39) is straightforward since the deformation of  $\tilde{\mathcal{H}}(N)$  is still only proportional to  $N$  and the deformation of  $\tilde{\mathcal{H}}(N^a)$  is still only proportional to  $N^a$ . This results in the following constraints in the new theory:

$$\hat{\mathcal{H}}(N) = N \frac{\tilde{E}_i^a \tilde{E}_j^b}{\sqrt{\tilde{E}}} \left\{ \left( \tilde{F}_{ab}^k + \Delta \tilde{F}_{ab}^k \right) \epsilon^{ij}_k - 2(\gamma^2 - 1) \left( \tilde{K}_o^i + \Delta \tilde{K}^i \right)_{[a} \left( \tilde{K}_o^j + \Delta \tilde{K}^j \right)_{b]} \right\}, \quad (5.70a)$$

$$\hat{\mathcal{H}}(N^b) = N^b \left\{ \tilde{E}_i^a \left[ \tilde{F}_{ab}^i + \Delta \tilde{F}_{ab}^i \right] - (\gamma^2 + 1) \left[ \tilde{K}_o^i \tilde{G}_i + \tilde{K}_o^i \Delta \tilde{G}_i + \Delta \tilde{K}_b^i \tilde{G}_i + \Delta \tilde{K}_b^i \Delta \tilde{G}_i \right] \right\}, \quad (5.70b)$$

$$\hat{\mathcal{G}}(\lambda^i) = \lambda^i \left[ \tilde{G}_o^i + \Delta \tilde{G}_i \right]. \quad (5.70c)$$

Here, the “ $o$ ” subscript refers to the original (before applying the deformation) quantities and the remaining quantities are as follows:

$$\Delta \tilde{F}_{ab}^i = 2\partial_{[a}(\Delta \tilde{A}_{b]}^i) + \epsilon^i{}_{jk} \left[ \tilde{A}_a^j \Delta \tilde{A}_b^k + \Delta \tilde{A}_a^j \tilde{A}_b^k + \Delta \tilde{A}_a^j \Delta \tilde{A}_b^k \right], \quad (5.71)$$

$$\Delta \tilde{K}_a^i = \frac{1}{\gamma} \Delta \tilde{A}_a^i, \quad (5.72)$$

$$\Delta \tilde{G}_i = \epsilon_{ij}{}^k \tilde{E}_k^a \Delta \tilde{A}_a^j. \quad (5.73)$$

Note specifically that the deformed Gauss constraint,  $\hat{\mathcal{G}}(\lambda^i)$ , can be satisfied either by making terms in  $\Delta G_i$  cancel terms in  $G_{o_i}$ , or else by enforcing  $G_{o_i}$  and  $\Delta G_i$  equal to zero separately. In the first case the Gauss constraint no longer enforces metricity fixing of the densitized tetrad whereas in the second case it does (since the Gauss constraint in its original form vanishes) and hence is generally preferable. In the second case there will be the enforcement of the metricity fixing condition along with another constraint demanded by the vanishing of (5.73).

The action (5.67) along with the set of constraints (5.70a), (5.70b) (supplemented with (5.70c)) yields the deformed theory whose constraints will obey the constraint algebra (5.32–5.33b). However, although this scenario was reasonably straightforward to implement, it should be noted that the variables which undergo Hamiltonian evolution in this example are not  $A_b^i$  and  $E_j^b$  but the configuration and momentum variables in (5.68a) and (5.68b). The deformed theory must be written in terms of these variables, which depends on the invertibility of the transformation equations (5.68a) and (5.68b). Moreover, this invertibility requirement must be attached to the idea of a transformation from a symplectic manifold to another symplectic manifold. One must therefore know the explicit form of  $\delta(E_j^b)$  in order to do this. In other words, the equation (5.27), utilized in order to derive the algebra among the constraints, picks up the extra degrees of freedom:

$$\delta_\zeta q \frac{\delta I}{\delta q} = \delta_\zeta \tilde{A}_a^i \frac{\delta I}{\delta \tilde{A}_a^i} + \delta_\zeta ({}_A \tilde{\pi}_i^a) \frac{\delta I}{\delta ({}_A \tilde{\pi}_i^a)} + \delta_\zeta \tilde{E}_i^a \frac{\delta I}{\delta \tilde{E}_i^a} + \delta_\zeta ({}_E \tilde{\pi}^i_a) \frac{\delta I}{\delta ({}_E \tilde{\pi}^i_a)}, \quad (5.74)$$

where here we have only considered the gravitational sector. It is important to note at this stage that it is generally a non-trivial matter to rewrite the action, and resulting equations of motion, solely in terms of the new variables. It is also possible, depending on the particular transformation, that there is no unique way of writing the deformed action in terms of the new variables. In the case of the holonomy corrections presented above, *one* way to proceed is by simply leaving the action in the form (5.67), since  $A_a^i$  and  $E_i^a$  are legitimate degrees of freedom even in the deformed theory as can be seen from (5.68a-ii). That would however lead to a theory which would only contain stationary gravity ( $\dot{\tilde{E}}_i^a = \partial \mathcal{H} / \partial {}_E \tilde{\pi}_a^i = 0$ ,  $\dot{\tilde{A}}_a^i = \partial \mathcal{H} / \partial {}_A \tilde{\pi}_i^a = 0$ ) as there is no dependence on either of the canonical momenta. In fact,

all Poisson brackets between the constraints would also trivially vanish. (Convexity would also be lost therefore introducing ambiguity in transforming to the Lagrangian formulation.)

There is also another form of the canonical form of the action, which essentially reverses the roles of  $A$  and  $E$  as configuration and momentum [209]. In this guise the gravitational action has the canonical form

$$S = \frac{1}{\kappa} \int dt \int d^3x \left[ A_a^i \dot{E}_i^a + \mathcal{H}(N) + \mathcal{H}(N^a) + \mathcal{G}(\lambda^i) \right]. \quad (5.75)$$

In order to employ a straightforward holonomy correction to this form of the action one must utilize the momentum representation of the quantum operators [209]. Here the holonomy correction for the momentum representation takes the form

$$A_a^i \rightarrow P_a^i \left( \tilde{A}_a^i, \tilde{E}_j^b \right) = - \frac{\sin \left[ \tilde{A}_a^i \delta(\tilde{E}_j^b) \right]}{\delta(\tilde{E}_j^b)}, \quad (5.76a)$$

$$E_i^a \rightarrow H_i^a \left( \tilde{A}_a^i, \tilde{E}_j^b \right) = \tilde{E}_i^a, \quad (5.76b)$$

which result in the corresponding modified action

$$S' = \frac{1}{\kappa} \int dt \int d^3x \left[ - \frac{\sin \left( \tilde{A}_a^i \delta(\tilde{E}_j^b) \right)}{\delta(\tilde{E}_j^b)} \dot{\tilde{E}}_i^a + \hat{\mathcal{H}}(N) + \hat{\mathcal{H}}(N^a) + \hat{\mathcal{G}}(\lambda^i) \right]. \quad (5.77)$$

Note that here, on the other hand, the corrected theory retains the same number of degrees of freedom as the original, though they are not the same ones as in the original theory:

$$\tilde{E}_i^a, \quad {}_E \tilde{\pi}_a^i \equiv - \frac{\sin \left( \tilde{A}_a^i \delta(\tilde{E}_j^b) \right)}{\delta(\tilde{E}_j^b)}. \quad (5.78)$$

In this case the resulting action can certainly be written in terms of the new canonical variables only. We will not explicitly calculate the constraints in this case as they are more straightforward here than in the previous scenario. It is again important to note that the same base theory, written in different guises, gives rise to completely different theories under variable deformations. It might seem that in this second case we have not gained a new theory, since the new phase-space variables,  $\tilde{E}_i^a$  and  ${}_E \tilde{\pi}_a^i$ , evolve in exactly the same way as the old ones,  $E_i^a$  and  $A_a^i$ , under Hamiltonian evolution. However, information about the geometry is encoded in the metric (or  $E_i^a$ ) and the extrinsic curvature (related to  $A_a^i$  via (5.58b)). Therefore, even though the new variables evolve in the same way as the old, the *geometry* will not evolve in the same way as in the undeformed theory.

We end this example with a comment that the above deformation method is not the usual way that holonomy corrections are implemented. This is because in the usual scheme one

wishes to demand that the connection and densitized tetrad remain canonically conjugate variables of the theory as in (5.60a,b). However, it has been shown that in certain cases that may lead to inconsistencies in the Poisson algebra of the constraints when matter is present [41]. The scheme presented in this thesis is specifically designed to ensure consistency of the algebra even in the presence of matter.

## 5.5 Discussion

In this chapter, we proposed a systematic treatment of theories generated by the modification of the canonical variables of general relativity both in metric variables and tetrad variables. The objective of this approach is to explore under which conditions the constraint algebra retains its first-class structure (which supports stable gauge fixing) and its diffeomorphic symmetries. The deformed fields and momenta were re-introduced in the original theory in order to observe the effects of the transformed variables. We covered two possible cases (I) deformations that do not introduce new higher-derivatives terms in the action and (II) non-unitary modifications that will create new degrees of freedom. Furthermore, we evaluated the transformed gravitational variables in two well-known incarnations of the gravitational action: the Einstein-Hilbert action and in the tetrad formalism of the Palatini action and in the Ashtekar variables. We must remark, however, that it is viable to deform the canonical variables of other actions following the same procedure we described in this chapter.

In the case of the variable deformations in the Einstein-Hilbert action, the preservation of the original number of degrees of freedom in case (I) unavoidably leads us into Lovelock's theorem, which restricts these deformations to be canonical transformations. In case (II), the deformations of the canonical variables induce higher-derivative terms that increase the number of degrees of freedom. The latter case must be studied carefully since it is possible to alter the theory in a way that does not produce a healthy Hamiltonian representation. We presented an example where the modifications of the metric are traceless and symmetric, which in some sense mimics potential graviton corrections. In this example, we found that the new Hamiltonian in (5.49) demands further constraints on the deformations, which are required in order to hold gauge independent scalar and vector constraints. The evaluation of these constraints can only have two possible outcomes: the deformations can either remove the extra degrees of freedom from the generators of the diffeomorphism group, or break some of them by reinterpreting the extra fields as Goldstone modes. In the circumstance of the first case, the dynamics of the additional field has been explored in a more realistic environment [111] and it can be benign.

Similarly, we extended this scheme for the tetrad-Palatini and the Ashtekar-Barbero actions. In this case, we suggested the so-called holonomy corrections as a specific form of the deformation (although there is no reason to limit the deformations to just this type).

The scenario presented is similar in the sense of the possible introduction of extra degrees of freedom in the system. Nonetheless, if the extra terms appearing in the deformed action (which might or might not include extra fields) are projected into the additional Gauss constraint, the system can be forced to a different metric realization. In the existing literature [159], it is possible to find that Lovelock's theorem is bypassed since there is not a unique way to write the theory in these variables. Such a case was not covered in this thesis. We derived the new constraints and the effects of the deformations in the tetrad variables in the cases when extra degrees of freedom appear (or not) in the system. If the deformations do not alter the shift and lapse gauge orbits, there is no reason to expect a different realization of the constraint algebra, which now will also require closure with the Gauss constraint, and the deformations can be constrained to produce stable gauge fixing.



## Chapter 6

# Unscreening scalarons with a black hole

Einstein's theory of general relativity (GR) is one of the greatest achievements of modern science, due to its ability to describe many of the gravitational phenomena with impressive level of detail. Nevertheless, there are many motivations to look for alternative theories: the observation of cosmic acceleration, the unknown nature of dark matter and dark energy and the lack of an ultraviolet completion of general relativity related with the unavoidable presence of spacetime singularities in this theory. Any successful modification of Einstein's theory should solve some of these conundrums, while remaining consistent with the local tests of general relativity and do no harm to the standard behaviour of matter as discussed in [249, 54].

For example,  $f(R)$  gravity was postulated in [230] as an attempt to produce a renormalisable theory of quantum gravity. It introduces a ghost-free functional of curvature, analogous to the notion of free energy in thermodynamics. Since its first incarnation, however, different forms of  $f(R)$  have been used to solve issues at cosmological scales (see [228, 136, 229]). Notwithstanding, either considering a functional source of gravitational interaction different from the Ricci scalar, or simply adding extra gauge degrees of freedom in the gravitational sector has consequences at all energy scales. Gravity is not only defined by the metric, but also by other fields as we learned in Chapter 5. If gravitational interaction is not only defined by the spacetime geometry, the force exerted by any extra degree of freedom violates the stringent solar scale constraints, which are consistent with general relativity. Screening mechanisms such as theories in [149, 194, 241] are designed to circumvent this issue by diluting the sources of this force.

In the case of an astrophysical black hole, one naively expects that every extra force will be screened by large environmental energy densities. In the particular case of a force sourced by a scalar, screening is expected to be a consequence of the no-hair theorem, as stated in [37], applicable in the case of a source with positive energy density. Nonetheless, as noticed in [75], the presence of a non-trivial distribution of accreting matter and the way

this is coupled to the scalar field allows scalar hair – i.e., an attribute different than mass, angular momentum or charge, which modifies the black hole solution – outside the event horizon.

In this chapter, we simulate the accretion of the additional scalar degree of freedom in the  $f(R)$  models presented in [136, 229], the symmetron model in [132] and the Ratra-Peebles chameleon in [206] in a dense environment. We assume that in such a region we can form a stable Schwarzschild black hole via gravitational collapse. This spherically symmetric black hole interacts with the screened extra real scalar field in a non-trivial matter distribution and accretes around the event horizon. The accreting matter density profile proposed here is a slight generalization to that suggested in [75]. Even when the accretion in astrophysical black holes takes place in rotating spacetime solutions, it is interesting to explore the test case of a spherically symmetric system. The objective of this study is to visualize the process of accretion of the scalar field for various choices of model parameters, and discuss the time scales involved in the convergence to a non-trivial static profile. We designed a compact and efficient spectral code, flexible to modification and capable of producing time-dependent solutions of a scalar field in a Schwarzschild-like background. It is available for further application to other models at <https://github.com/andrei-v-frolov/accretion>.

The layout of this chapter is as follows. In section 6.1, we define the matter environment and the spacetime geometry in which the extra scalars propagate. In section 6.2, we review the equations of motion and particular features of the scalar degrees of freedom in the chosen  $f(R)$  models and study how these fields accrete. In section 6.3, we modify these models by adding terms proportional to  $R^2$  and show the dynamical resolution of the curvature singularities in the Hu-Sawicki and the Starobinsky model. We extend our treatment for the symmetron model and the Ratra-Peebles chameleon in sections 6.4 and 6.5, respectively. Finally, we present summary of our results and conclusions in section 7.4. Numerical implementation is discussed in detail in Appendix E.

## 6.1 Matter distribution for spherically symmetric black holes

These are legitimate reasons to believe that astrophysical black holes are different from solutions of Einstein’s field equations since a typical theoretical solution is (i) a spherically symmetric solution modelled in a vacuum environment and (ii) has (at least) one singular point. Although astrophysical black holes are rotating systems, spherically symmetric solutions remain interesting when exploring some of the dynamical subtleties of the extra scalars in modified gravity. From [222, 109], we learn that the fate of a collapsing spherically symmetric system in standard scalar-tensor theories is to become a Schwarzschild black hole.

It is then sensible to ask whether the Schwarzschild solution remains a valid description of spacetime even in the presence of accreting matter. To answer this question, we briefly

review the dynamics of a steady flow of matter to estimate the accretion rate of the black hole. We calculate the luminosity ( $L$ ) assuming the power lost by a generic inflow of particles traveling from infinity to the innermost stable circular orbit (ISCO) at  $r_{\text{ISCO}} = 6GM$

$$L = \left(1 - \sqrt{\frac{8}{9}}\right) \dot{M} \sim 0.06 \dot{M}. \quad (6.1)$$

Using the table of luminosities of active galactic nuclei included in [148], we note that the accretion rate of a supermassive black hole with  $M_{\text{BH}} = 10^9 M_{\odot}$  is  $\dot{M} \lesssim 1 M_{\odot}/\text{yr}$ . The accretion rate in a rotating black hole of similar luminosity could be even smaller, since  $L \sim 0.42 \dot{M}$  for near-extremal rotation<sup>1</sup>. This implies that it would take  $\sim 10^7$  years to change the mass of the black hole by 1%. Therefore, the time scales we are interested in are defined by the intervals in which the geometry of the accreting system is nearly static.

At this point of the discussion, it is necessary to provide an approximate expression of the matter density distribution outside the black hole’s horizon. This is not by any means a full discussion of the radial structure equations for accretion disks. However, we provide sufficient arguments to justify our choice of a matter distribution. It must remain nearly static within the time scale estimated previously. For that purpose, we consider that radial matter density at a given radius  $r$  is proportional to some positive power of the time that particles spend in orbits passing through that  $r$ . Stable orbits are possible only when  $r \geq r_{\text{ISCO}} = 6GM$ . Therefore, the dynamics of a test particle moving in Schwarzschild spacetime only provides two scenarios in which matter can be found at  $r < r_{\text{ISCO}}$ : (I) these are on “no-return” trajectories towards the horizon or (II) eccentric trajectories with a minimal radius smaller than  $r_{\text{ISCO}}$ . The latter case is highly unlikely as viscous forces diffuse anisotropies all along the accretion disk. In [104], one can find a simplified linear model explaining that the cause of viscosity is the radial propagation of angular momentum from one orbit to another in the disk of matter. In this case, a final state of radial homogeneity is reached very rapidly. In a more realistic scenario, diffusion is driven by non-linear viscous forces studied in magnetohydrodynamical (MHD) simulations of rotating (and slightly magnetized) systems, as explained in [5]. In any case, the probability of finding matter on orbits within the innermost stable circular orbit (ISCO) is greatly reduced, and in consequence, so is the matter density in those regions. For black holes with low accretion rates, this density drop could be sufficient to unscreen the extra scalar degrees of freedom, dubbed as scalarons, within immediate vicinity of the black hole, as we will show in the following sections.

Using the arguments aforementioned, we define the density contrast parameter ( $\sigma$ ) as the ratio between the densities outside and inside  $r_{\text{ISCO}}$ . Such a ratio is in the range  $\sigma \in [0, 1)$

<sup>1</sup>A black hole in the near-extremal regime has the minimal possible mass for a stable rotating system.

and it is sufficient to complete our rough prescription for the pressureless matter distribution

$$\rho = \begin{cases} \sigma\rho_0; & r_g < r < r_{\text{ISCO}}, \\ \rho_0; & r \geq r_{\text{ISCO}}, \end{cases} \quad (6.2)$$

where  $r_g = 2GM$  is gravitational radius where black hole horizon is located. This coincides with the distribution suggested in [75] when  $\sigma = 0$ . For numerical reasons, the use of a smooth matter profile approximated by a hyperbolic tangent is more convenient

$$\rho = (1 - \sigma)\rho_0 \frac{1 + \tanh a_0(r - r_{\text{ISCO}})}{2} + \sigma\rho_0, \quad (6.3)$$

where  $a_0 \gg 1$  and  $\rho_0 > 0$ . The shape of this matter distribution is a crude approximation of the results presented in [5] when  $\sigma < 10^{-4}$ . As a consequence, we will setup all the wave equations for the scalar field using the Schwarzschild geometry

$$ds^2 = - \left(1 - \frac{r_g}{r}\right) dt^2 + \frac{dr^2}{1 - \frac{r_g}{r}} + r^2 d\Omega^2. \quad (6.4)$$

where  $r_g = 2M$ , and the matter density profile suggested in (6.3). However, it is convenient to change from Schwarzschild to tortoise coordinates  $dr = (1 - r_g/r) dx$

$$ds^2 = \left(1 - \frac{r_g}{r(x)}\right) \left[-dt^2 + dx^2\right] + r^2(x) d\Omega^2. \quad (6.5)$$

The coordinate change from  $r$  to  $x$  and its inversion is discussed in detail in Appendix E.6. We neglect back-reaction of the scalaron dynamics on the background geometry for all the scalar-tensor theories explored in this chapter, and treat the metric as static in the scalaron equations of motion. Using (6.5), we can write the equation of motion of the scalar field  $\square\phi = V'_{\text{eff}}(\phi)$  which appears in (6.10) and (6.25) as a spatially damped wave equation in 1+1 dimensions

$$\left[-\frac{\partial^2}{\partial t^2} + \frac{\partial^2}{\partial x^2} + \frac{2}{r(x)} \left(1 - \frac{r_g}{r(x)}\right) \frac{\partial}{\partial x}\right] \phi(t, x) - \left(1 - \frac{r_g}{r(x)}\right) V'_{\text{eff}}(\phi) = 0. \quad (6.6)$$

This choice of coordinates is sufficient for our purposes since the scalar solutions we seek do not need to cover the black hole's interior ( $r < r_g$ ). For simplicity of the implementation, we use units of  $r_g = 1$  in the code, but other choices can also be considered without difficulty.

## 6.2 Scalar accretion in $f(R)$ theories

In this section we describe the two examples of  $f(R)$  theories considered in this work: the Starobinsky and Hu-Sawicki models, where the Ricci scalar  $R$  in the Einstein-Hilbert action is replaced by a function of  $R$ . We will consider equations of motion derived in the

metric formalism. Alternative formalisms like the Palatini or the metric-affine mentioned in [226, 189, 227, 38] can change the number and/or the nature of the degrees of freedom that emerge. In particular, in [226], we see that the Palatini formulation of  $f(R)$  is equivalent to a  $\omega_0 = -3/2$  Brans-Dicke theory [47], and no new dynamical degrees of freedom appear. In all cases, one needs to ensure that the model remains ghost-free in the gravity sector and that there are no tachyonic modes for it to be viable. A recent discussion on ghosts in various formulations appeared in [155].

### 6.2.1 Chameleons in Starobinsky and Hu-Sawicki model

We first consider  $f(R)$  theories described, in the Jordan frame, by the action

$$S = \int \frac{f(R)}{16\pi G} \sqrt{-g} d^4x + S_m[g_{\mu\nu}, \psi], \quad (6.7)$$

where  $g_{\mu\nu}$  is the Jordan frame metric and  $\psi$  are the matter fields. Varying the action with respect to the metric  $g_{\mu\nu}$  we obtain equations of motion which replace Einstein's equation in the  $f(R)$  models; they are

$$f_R R_{\mu\nu} - \frac{1}{2} f g_{\mu\nu} = 8\pi G T_{\mu\nu} + \nabla_\mu \nabla_\nu f_R - g_{\mu\nu} \square f_R, \quad (6.8)$$

where  $f_R \equiv \partial f / \partial R$ . The two terms in the second line of the equation (6.8) contain fourth-order derivatives of the metric, a signal that a new degree of freedom emerges in the theory. This can be seen explicitly by taking the trace of the equation above

$$\square f_R = \frac{1}{3} (2f - f_R R) + \frac{8\pi G}{3} T, \quad (6.9)$$

which yields a second order equation of motion for the real field  $f_R$  with a canonical kinetic term under the influence of an effective potential  $V' \equiv (2f - f_R R)/3$  and an external force term  $\mathcal{F} \equiv -8\pi G T/3$  with  $T \equiv T^\mu_\mu$ . By defining  $\phi \equiv f_R - 1$  we can rewrite equation (6.9) simply as

$$\square \phi = V'(\phi) - \mathcal{F}, \quad (6.10)$$

where prime denotes derivative with respect to  $\phi$ . Alternatively, one can explicitly see the emergence of the extra degree of freedom, usually dubbed “scalaron”, by mapping the action (6.7) into the Einstein frame, as described in [169, 76]. Solving the equation (6.10) requires the knowledge of the potential  $V(\phi)$  which is defined in a parametric form via

$$\frac{dV}{dR} = \frac{dV}{d\phi} \frac{d\phi}{dR} = \frac{1}{3} (2f - f_R R) f_{RR}, \quad (6.11)$$

or, integrating with a choice  $V|_{R=0} = 0$  for a constant,

$$\phi(R) = f_R - 1, \quad (6.12)$$

$$V(R) = \frac{1}{3} \int_0^R d\tilde{R} \left( 2f(\tilde{R}) - f'(\tilde{R})\tilde{R} \right) f''(\tilde{R}). \quad (6.13)$$

When plotting the scalar potentials in Figure 6.1, we observe that they are generally multi-valued, with turning points at field values where  $f''(R) = 0$ . One must be aware of the branch choice when determining the curvature value  $R$  and the effective force  $V'(\phi)$  for the field  $\phi$  in the wave equation (6.10). The branch we are interested in is the one connected to the large curvature  $R \rightarrow +\infty$  where Einstein gravity is recovered by screening. The particular models we study are defined by specific forms of  $f(R)$

$$f_S = R + \lambda \left[ \frac{1}{(1 + (R/R_0)^2)^n} - 1 \right] R_0, \quad (6.14)$$

$$f_{HS} = R - \frac{\alpha(R/R_0)^n R_0}{1 + \beta(R/R_0)^n}, \quad (6.15)$$

which correspond to the Starobinsky[229] and Hu-Sawicki [136] – models respectively. Hence, the potentials are completely determined as functions of  $\phi$  after replacing the solution of (6.13) in  $f_S$  or  $f_{HS}$  for every physical choice of parameters. A particular feature of (6.15) is that it has an apparent extra parameter compared to (6.14). However, it is entirely free, and we can reduce the number of parameters by considering the transformation  $\alpha \rightarrow \lambda^a \alpha$ ,  $\beta \rightarrow \lambda^b \beta$  and  $R_0 \rightarrow \lambda^c R_0$ .  $f_{HS}$  is invariant under this transformation if

$$a - (n - 1)c = 0, \quad (6.16)$$

$$b - nc = 0,$$

for a given value of  $n$ . It is therefore possible to map any solution for one set of parameters to an equivalent one for a different set following (6.16), hence we fixed the parameter  $\beta$  to be 1 throughout the rest of the chapter and one can convert to other choices via these transformations. Our choices of  $\beta$  and the crossover curvature scale  $R_0$  are useful to compare these results with the solutions from the Starobinsky model. As summarized in [226],  $f(R)$  models of gravity in metric formalism must have  $f'(R) > 0$  and  $f''(R) > 0$  to avoid ghost-like gravitons and tachyonic scalarons, respectively.

From equation (6.10), we can define an environmentally dependent effective potential  $V_{\text{eff}}(\phi)$  that provides the same equations of motion in the regions of constant force  $\mathcal{F}$  by

$$V_{\text{eff}}(\phi) = V(\phi) - \mathcal{F}\phi. \quad (6.17)$$

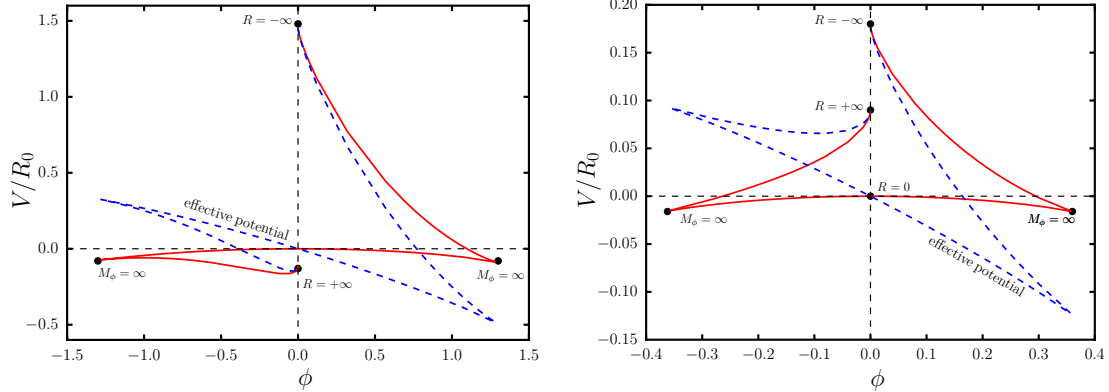


Figure 6.1: Left panel: bare and effective potential for  $\lambda = 2.0$  and  $n = 1$  in the Starobinsky model. Matter defines an effective minimum and a mass for the field. Right panel: bare and effective potential for  $\alpha = 0.8$  and  $n = 2$  in the Hu-Sawicki model. Increasing densities of surrounding matter also define a steady-state solution. Both effective potentials are concave up around the equilibrium position, which means that the scalarons are not tachyonic. Strictly speaking, the effective mass of the field defined as  $M_\phi^2 \equiv \partial V_{\text{eff}}/\partial\phi^2$  is not defined at the points labeled as  $M_\phi = \infty$ .

One peculiar feature of the effective potential is that the extra term coming from the interaction with matter provides an external source term. As a result of this, the no-hair theorem in its usual form is in general not applicable. In this chapter, the presence of matter with  $T_\mu^\mu \neq 0$  (which excludes electromagnetic radiation) is not neglected.

One must consider any particular choice of model parameters for  $f_{\text{HS}}$  and  $f_{\text{S}}$  that could emerge from their corresponding renormalization group flows. Therefore, it is prudent to study the flow lines in parameter space by exploring the stability of the scalar wave equation for different choices of model parameters, even when we consider cases where the model does not match with current observations. The field solutions are screened in the same way as we described in section 6.5, henceforth  $f_{\text{S}}$  and  $f_{\text{HS}}$  scalarons can also be dubbed as “chameleons”.

### 6.2.2 Accreting chameleons in Hu-Sawicki and Starobinsky models

Now we present our results after evaluating the scalar equations of motion in (6.10). In order to proceed, we must first find the effective potentials corresponding to (6.14) with arbitrary densities of matter. In the left panel of Figure 6.1 we observe that the features of this potential correspond to what is usually called a chameleon field. Just as described in [48], the steepness and depth of the potential grows with the surrounding matter density in which the field propagates. The effective potential of the Hu-Sawicki model is plotted in the right panel of Figure 6.1.

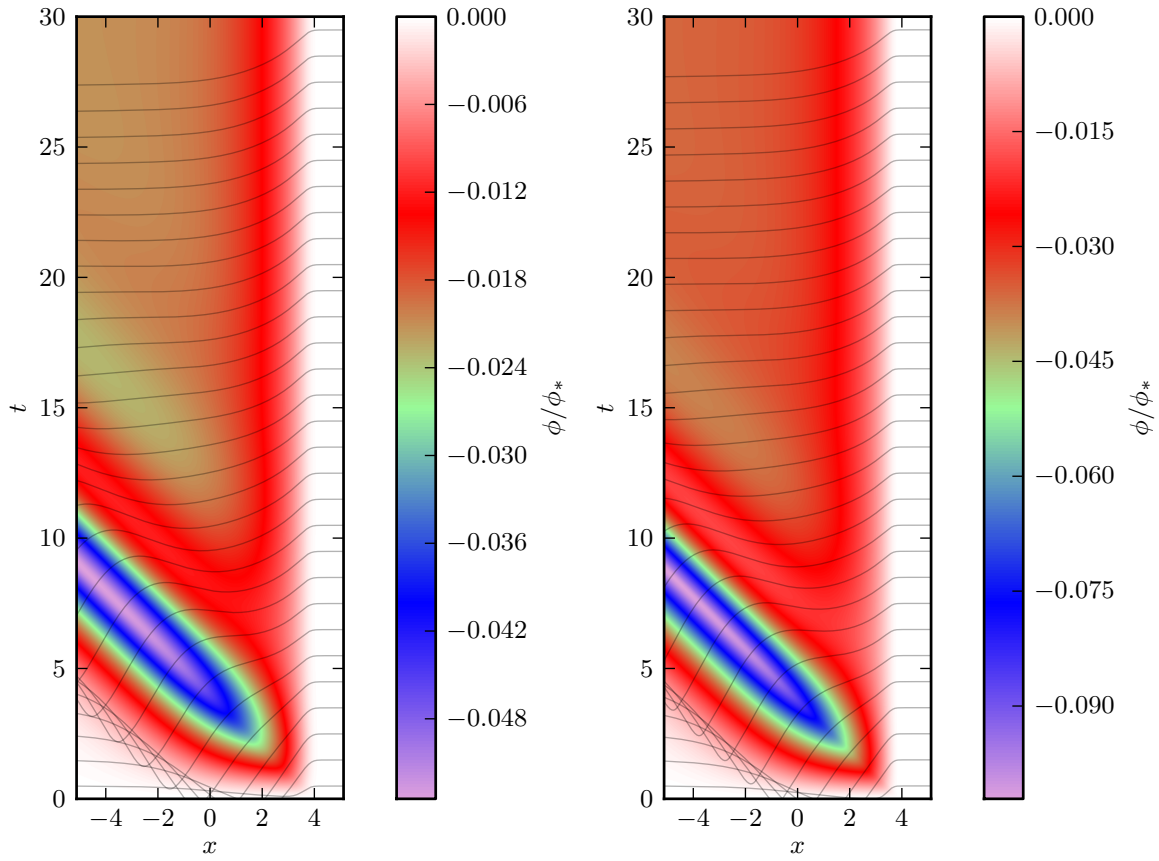


Figure 6.2: Accretion of the field in the Starobinsky (left panel) and Hu-Sawicki (right panel) models in tortoise coordinates. Field profiles are plotted on top of the intensity map: each line represents the amplitude of the field at a particular time. The values of the field are consistent with the condition  $f'(R) > 0$ .



In both cases, we observe that the formation of curvature singularities do not require infinite energies to be achieved. In addition to that, we notice the existence of an equilibrium configuration for the field, the corresponding minimum in the effective potential  $V'_{\text{eff}}(\phi) = 0$  is defined by

$$V'(\phi) = \mathcal{F}. \quad (6.18)$$

In the presence of accreting matter outside  $r_{\text{ISCO}} = 3r_g$  the field is screened, which implies a very small value of it in this region. Inside  $r_{\text{ISCO}}$ , we can set the matter density in (6.3) to zero for now. Naively, one should not expect significant differences in our results calculated in the Jordan frame when compared with what is expected in the Einstein frame after conformal transformations: inside  $r_{\text{ISCO}}$ , the matter density is zero regardless of any value of the field; outside, the screening sets the conformal coupling to one. It is typically argued that there are changes in the metric and equations of motion of a test particle when these entities are rephrased in this frame: the derivatives of the conformal coupling might modify these entities in a non-negligible way. This is true in general, however these changes do not represent a significant contribution to the solutions we present since these modifications are always proportional to the first and second radial derivatives of the field, which is a smooth function outside the event horizon.

In order to find the screening value of  $\rho_0$  in (6.3), we evaluate the equilibrium condition in (6.18) at the screened value of the field  $\phi_0$  far away from  $r_{\text{ISCO}}$  (which is very close to zero). Numerically, this is more convenient than (but still equivalent to) finding the equilibrium value of  $\phi$  for a given value of  $\rho_0$  from (6.18) since the dependence of  $V'(\phi)$  on the field is implicit.

The evolution of the system requires initial conditions. In what follows, we set the units of the field  $\phi$  in terms of a reference value  $\phi_*$ , which for  $f(R)$  models is dimensionless and is chosen to be simply  $\phi_* = 1$ . We consider a completely screened initial configuration of the field  $\phi(r, t_0) = -10^{-4}\phi_*$  which is originally spatially homogeneous, and assume  $\dot{\phi}(r, t_0) = 0$  for the initial field velocity. Our choice of initial conditions is the same in our treatment of both  $f(R)$  models we present here. In the left panel of Figure 6.2, we see the accretion of the Starobinsky chameleon until it approaches to its static solution, choosing  $n = 1$ ,  $\lambda = 2.0$  and  $R_0 = 10^{-2}/r_g^2$  as the model parameters to run the simulation. The chameleon accretes around the horizon, then it converges smoothly to the static solution, which is visible in both panels of Figure 6.2 in the black lines after  $t > 20$ . Gradients do not cancel outside the horizon for  $r \leq r_{\text{ISCO}}$ , which make the “hair” profile non-trivial. In addition to this, the screening outside  $r_{\text{ISCO}}$  is not lost during accretion. Which shows that the equilibrium condition in (6.18) holds.

Field evolution of the Hu-Sawicki chameleon is plotted in the right panel of Figure 6.2, where we used the the same initial conditions.  $n = 1$ ,  $\alpha = 2.0$  and  $R_0 = 10^{-2}/r_g^2$  were the model parameters chosen for the numerical evolution. Hu-Sawicki chameleon also accretes

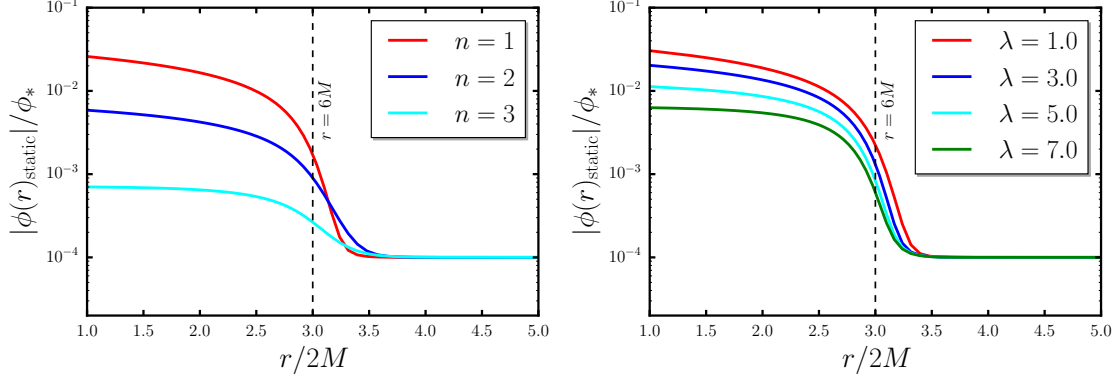


Figure 6.3: Left panel: Static profiles of the scalar field for the model parameters in (6.14). For the Starobinsky model for  $\lambda = 1.0$  and varying  $n$ . Right panel: Static profiles of the scalar field in the Starobinsky model for  $n = 1$  and varying  $\lambda$ . The figures plotted in the same color on each panel are not equivalent.

around the event horizon resulting in a non-trivial hair solution. We study the negative field branches of the potentials in Figure 6.1 that roughly scale as  $\phi^{1/\kappa}$  with  $\kappa > 2$ , therefore the field becomes less massive in the regions where its amplitude deviates from the screened value.

The convergence into a hair solution as well as its shape are sensitive to choice of model parameters. Static solutions are found using the relaxation method described in Appendix E.5, where we also discuss all the details related to the numerical evolution. In the left panel of Figure 6.3, we evaluate the solutions of (6.6) in the static limit for different parameters of the Starobinsky model. We find the solutions for different values of  $n$ , while keeping  $\lambda = 1.0$  as a constant. Likewise, in the right panel of the same figure, we evaluate the change of the static field profile when  $\lambda$  varies and  $n = 1$  is kept as a constant. In the same way, we represent static solutions for different values of the density contrast parameter  $\sigma$ , as defined in (6.2).

Different values of  $\lambda$  and  $R_0$  define how effective is the modification of gravity with respect to GR. In particular,  $\lambda$  controls the depth and vertical extension of the effective potential, and in consequence, it affects the existence and stability of the field solutions, while  $R_0$  sets the crossover curvature scale. In particular, we chose  $R_0 = 10^{-2}/r_g^2$  to have the same value throughout this chapter.

As expected, in Figure 6.4, we notice the reduction of the field amplitude in  $r \in (r_g, r_{\text{ISCO}}]$  for larger values of  $\sigma$ . However, it is not required to impose  $\sigma = 0$  to obtain a hairy solution. Furthermore, we calculate the static solutions corresponding to different choices parameters of the Hu-Sawicki model. The shape of the static solution for different values of  $n$  can be found in Figure 6.5. Additionally, static solutions for different values of  $\alpha$  and  $\sigma$  are represented in Figure 6.6. In all of these cases, the rest of the parameters were

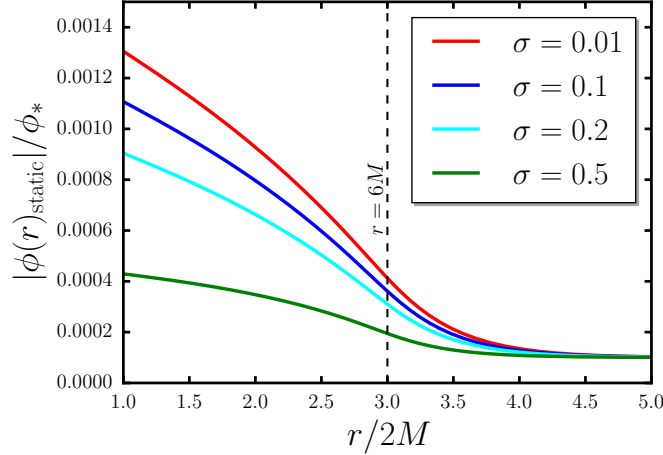


Figure 6.4: Static profiles of the scalar field in the Starobinsky model for  $n = 1$  and varying density contrast  $\sigma$ .

kept as constants. The dynamical results in Figure 6.2 expose the accretion of the chameleon solutions and prove the existence of non-trivial stable solutions (plotted in separate panels) of the static version of (6.6) outside  $r = r_g$  for the parameters we chose. The radial scalar flux  $\mathcal{J} \equiv 4\pi r^2 T[\phi]_0^r = 4\pi r^2 \phi_{,x}\phi_{,t}$  is represented in Figure 6.7, showing no propagation outside  $r_{\text{ISCO}}$ .

We show an additional way to test that the static profiles in Figure 6.3, both are suitable representations of field configurations around the minimum of the effective potentials in Figure 6.1. In the large-curvature limit, one can notice that  $V'(\phi) \simeq R/3$ , and so the equilibrium condition in (6.18) implies  $R \simeq -8\pi GT$  just as it is in GR. As a consistency check, in Figure 6.8 we tested the validity of the general relativistic limit in the case of a non-trivial value of the density contrast in the Hu-Sawicki model for a configuration that remains fully screened. This result remains valid for different values of the density contrast and further extends to the Starobinsky model.

So far, we discussed a few cases where we notice a smooth evolution into a non-trivial static solution. Nonetheless, the existence of static hair solutions is not enough to ensure smooth convergence to them. In Figure 6.1, we find the field values where infinite curvature is reached are close to the minima of the potential for different choices of model parameters, which is consistent with the results in [110, 21]. Small field excursions from the minimum are sufficient to form curvature singularities outside the event horizon, and it can happen dynamically.

Equilibrium solutions for the field are defined by locating the “valleys” of  $V_{\text{eff}}(\phi)$ , which in these cases are not far from reaching the infinite curvature limit. Further modifications of the functional form of  $f(R)$ , for example the addition of a term proportional to  $R^2$ , can

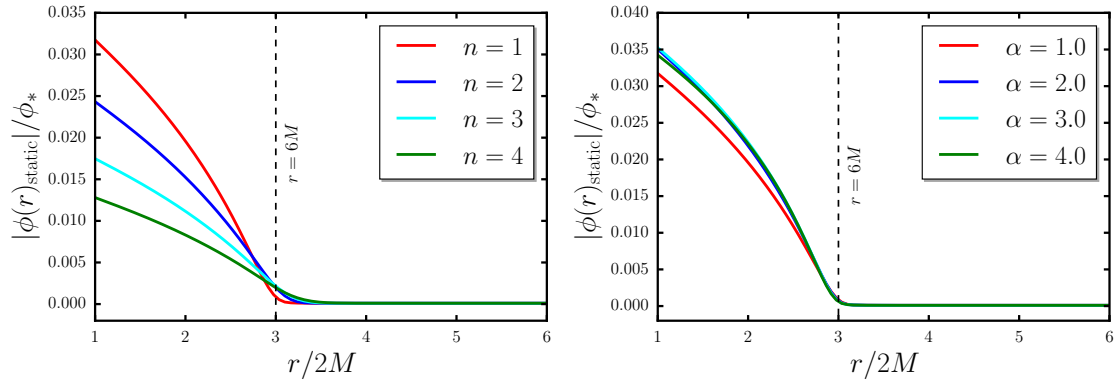


Figure 6.5: Left panel: Static profiles of the scalar field in the Hu-Sawicki model for  $\alpha = 1.0$  and varying  $n$ . Right panel: Static profiles of the scalar field in the Hu-Sawicki model for  $n = 1$  and varying  $\alpha$ .

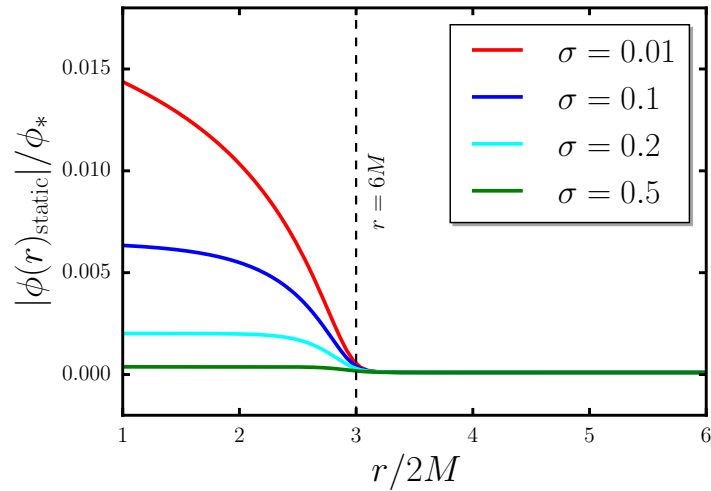


Figure 6.6: Static profiles of the scalar field in the Hu-Sawicki model for  $n = 1$  and varying density contrast  $\sigma$ .

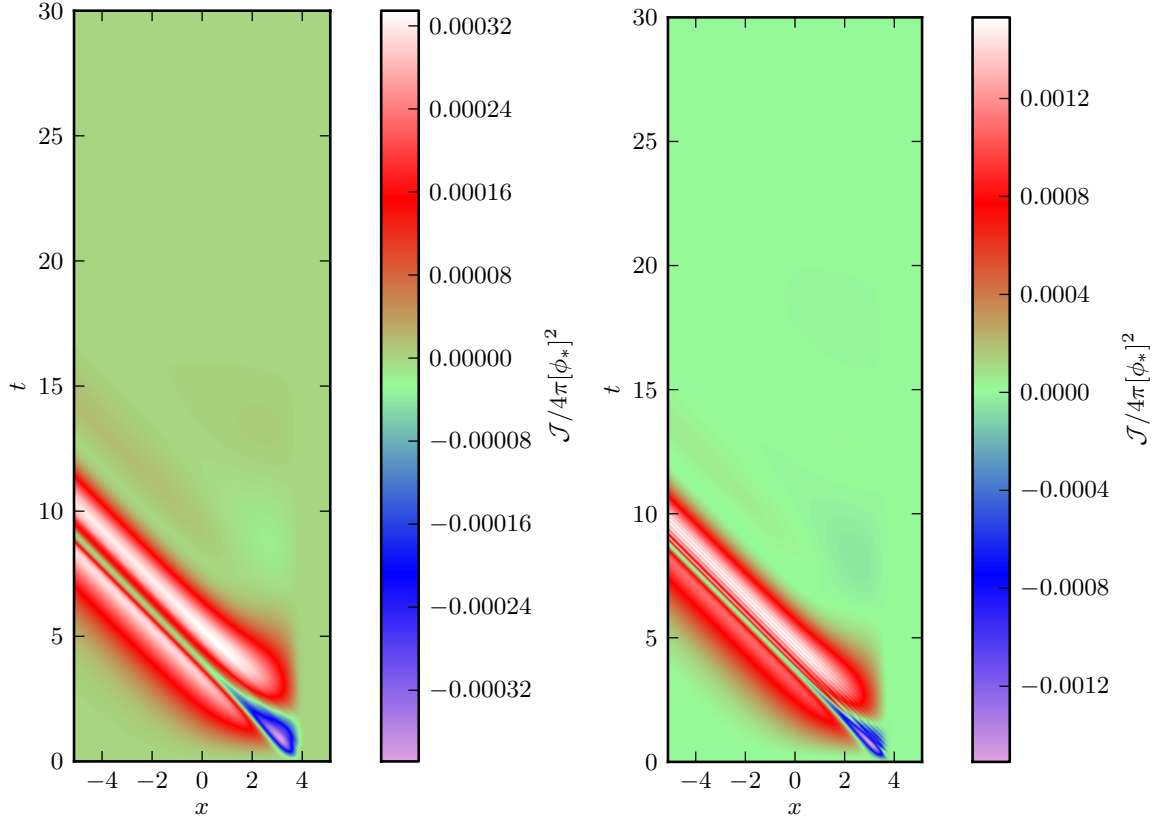


Figure 6.7: Scalar field flux accreting towards horizon in the Starobinsky model (left panel) and in the Hu-Sawicki model (right panel).

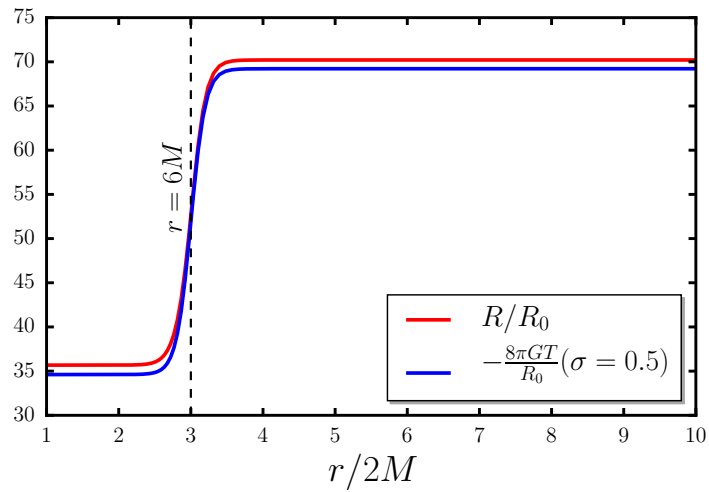


Figure 6.8: Consistency check for local scalaron equilibrium in fully screened configuration with  $\sigma = 0.5$  in the Hu-Sawicki model. This result is very similar in the case of the Starobinsky model.

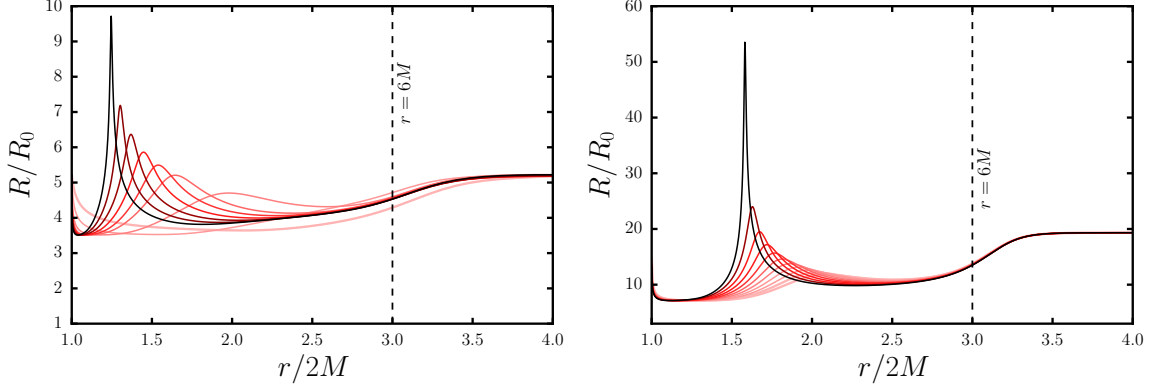


Figure 6.9: Left panel: Formation of a naked singularity for  $n = 3$  and  $\lambda = 2.1$  in the Starobinsky model. Right panel: Formation of a naked singularity for  $n = 3$  and  $\alpha = 4.31$  in the Hu-Sawicki model. In both panels, early stages of formation are plotted in pail red and the curvature profiles before divergence are plotted in black.

create a potential wall which will shield the field from reaching singularity. We will explore this alternative in the next section.

In the left panel of Figure 6.9, we show the dynamical formation of a curvature singularity outside the black hole’s event horizon. We chose  $n = 3$  and  $\lambda = 2.1$  as parameters for the Starobinsky model. Similarly, in the right panel of the same figure, we plot the formation of a naked singularity after picking  $n = 3$  and  $\alpha = 4.31$  as model parameters in the Hu-Sawicki model. The profiles of field  $\phi$  themselves do not diverge or show irregular behaviour while the singularities are formed, but the curvature  $R$  goes singular when evaluating  $R(\phi)|_{\phi=0}$ . The singularity is rather weak, and most likely of integrable type, but it is nonetheless a naked singularity formed in evolution of the regular data, which shows cosmic censorship conjecture [192] is violated in these models.

### 6.3 Resolving curvature singularities in $f(R)$ theories

In Figure 6.9, we observed the formation of integrable curvature peaks in the Starobinsky and Hu-Sawicki models. In both cases, these were located in  $r \in (r_g; r_{\text{ISCO}}]$  and appeared as a consequence of small field excursions from the potential minima reaching the field value corresponding to infinite curvature. In this section, we briefly discuss that the addition of an extra “mass” term in the functional form of  $f(R)$ , as suggested in [151, 21].

$$\tilde{f}_S = R + \lambda \left[ \frac{1}{(1 + (R/R_0)^2)^n} - 1 \right] R_0 + \frac{\mu}{R_0} R^2, \quad (6.19)$$

$$\tilde{f}_{\text{HS}} = R - \frac{\alpha(R/R_0)^n R_0}{1 + \beta(R/R_0)^n} + \frac{\mu}{R_0} R^2, \quad (6.20)$$

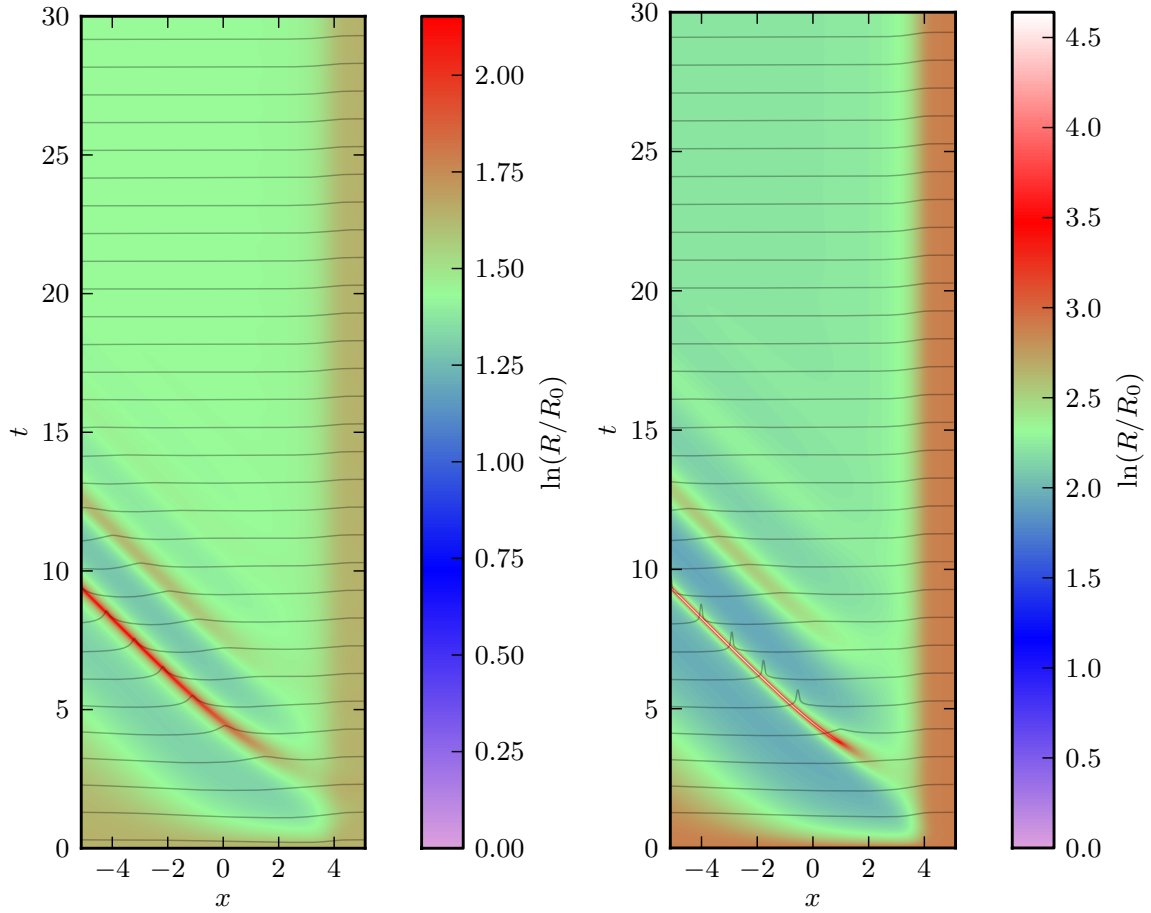


Figure 6.10: Dynamical resolution of the curvature singularities plotted in Figure 6.9 after the definitions in (6.19) and (6.20). Left panel: evolution of the curvature cusp for  $n = 3$  and  $\lambda = 2.1$  in the Starobinsky model. Right panel: evolution of curvature peak for  $n = 3$  and  $\alpha = 4.31$  in the Hu-Sawicki model. In both cases, the formation and absorption of the curvature peaks does not interfere with the stable evolution of the curvature profile.

is enough to remediate the divergences appearing in both models for the same choices of model parameters chosen in the previous section. Here the singular point is avoided by adding an infinite barrier that regularizes the potential and its derivatives. In the same references, it is possible to find constraints of the value of  $\mu$  mostly related with the expected decay time of the scalarons in cosmological scales. Here we chose  $\mu = 10^{-6}$  to leave the low-curvature features of the model unaffected, while putting a cap at moderate curvature values to avoid numerical dynamical range issues which might cloud the discussion. Note that the extra mass term does not appear in the definition of  $V'(\phi)$  described in (6.9), regardless of any choice of  $\mu$ . In Figure 6.10, we evaluated the dynamics of the scalar curvature in tortoise coordinates considering  $n = 3$  and  $\lambda = 2.1$  as parameters for the Starobinsky model and  $n = 3$ ,  $\alpha = 4.31$  for the Hu-Sawicki model. These choices produced unstable evolution truncated in the large-curvature regime when using  $f_S$  and  $f_{HS}$ . After adding the corrections in (6.19) and (6.20), the curvature peaks are limited and absorbed without reaching infinite values, with evolution towards an equilibrium configuration continuing without further inconveniences. However, even when the evolution of the curvature peaks is more benign these are still formed outside the event horizon. Thus, if there is no observational evidence of such cusps, their existence in the model will pose constraints not only for specific choices of initial conditions or parameters, but for the entire subspace of the model parameters connected to the troublesome region by the renormalization flow. For the Hu-Sawicki model, the parameter scaling (6.16) that leaves action invariant will involve  $\mu$ , nonetheless, it is still possible to find a family of parameters with similar curvature features starting from only one solution.

## 6.4 Scalar accretion for the symmetron model

### 6.4.1 Action and equations of motion

We now turn to the symmetron model described by a scalar-tensor action of the form

$$S = \int \sqrt{-g} d^4x \left[ \frac{R}{16\pi G} - \frac{1}{2}(\nabla\phi)^2 - V(\phi) \right] + S_m[A^2(\phi)g_{\mu\nu}, \psi], \quad (6.21)$$

where  $g_{\mu\nu}$  is now in the Einstein frame metric and  $\psi$  are the matter fields minimally coupled to the Jordan metric  $A^2(\phi)g_{\mu\nu}$ . For simplicity, we will describe the dynamics of the scalar  $\phi$  in the Einstein frame as in [75]. The symmetron is then modelled with a potential

$$V(\phi) = V_0 - \frac{\mu}{2}\phi^2 + \frac{\lambda}{4}\phi^4, \quad (6.22)$$

and a coupling function

$$A(\phi) = 1 + \frac{\hbar}{2} \frac{\phi^2}{m_S^2}, \quad (6.23)$$



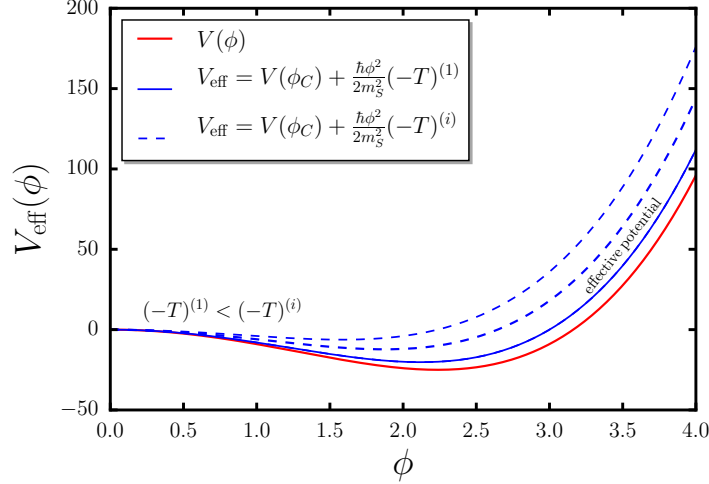


Figure 6.11: Effective potential of the symmetron model.  $\phi_*$  goes to zero as the matter density grows. The red curve shows the original potential  $V(\phi_C)$  without the influence of matter. The dashed blue curves show how the stable minima disappear as  $-T^{(i)} = \rho$  increases.

where  $\lambda$  and  $\mu$  are positive coupling constants and  $m_S^2$  is a high mass scale that suppresses any contributions higher or equal to  $\mathcal{O}(\phi^4/m_S^4)$ . The equations of motion for the Einstein frame metric are

$$R_{\mu\nu} - \frac{1}{2}Rg_{\mu\nu} = 8\pi G \left( T_{\mu\nu}^{[\phi]} + T_{\mu\nu}^{[m]} \right), \quad (6.24)$$

while for the real scalar  $\phi$  the equation of motion reads

$$\square\phi = V'_{\text{eff}}(\phi). \quad (6.25)$$

The effective potential  $V_{\text{eff}}(\phi) \equiv V(\phi) - TA(\phi)$  is defined as

$$V_{\text{eff}}(\phi) = \tilde{V}_0 + \frac{1}{2} \left( -\frac{\hbar T}{m_S^2} - \mu \right) \phi^2 + \frac{\lambda}{4} \phi^4, \quad (6.26)$$

and, as in the case of  $f(R)$  theories, it is dependent on the environment through the trace of stress-energy tensor  $T \equiv T^\mu_\mu$ . The coefficient of  $\phi^2$  in equation (6.26) changes sign depending on the magnitude of  $T$ , and determines the shape of the symmetron effective potential. In case of an environment made solely of dust<sup>2</sup> ( $T = -\rho$ ), we can define  $\rho_{\text{crit}} = \mu m_S^2/\hbar$  such that for energy densities  $\rho < \rho_{\text{crit}}$  the effective potential becomes shaped like a mexican hat. For vanishing density, the two minima are at  $\phi = \pm\phi_*$  with  $\phi_* \equiv \sqrt{\mu/\lambda}$ . In regions of high density,  $\rho > \rho_{\text{crit}}$ , there is one single minimum at  $\phi = 0$ . Hence  $A(\phi) = 1$  for high

<sup>2</sup>Pressureless matter without self-interactions, unable to propagate any excitations.

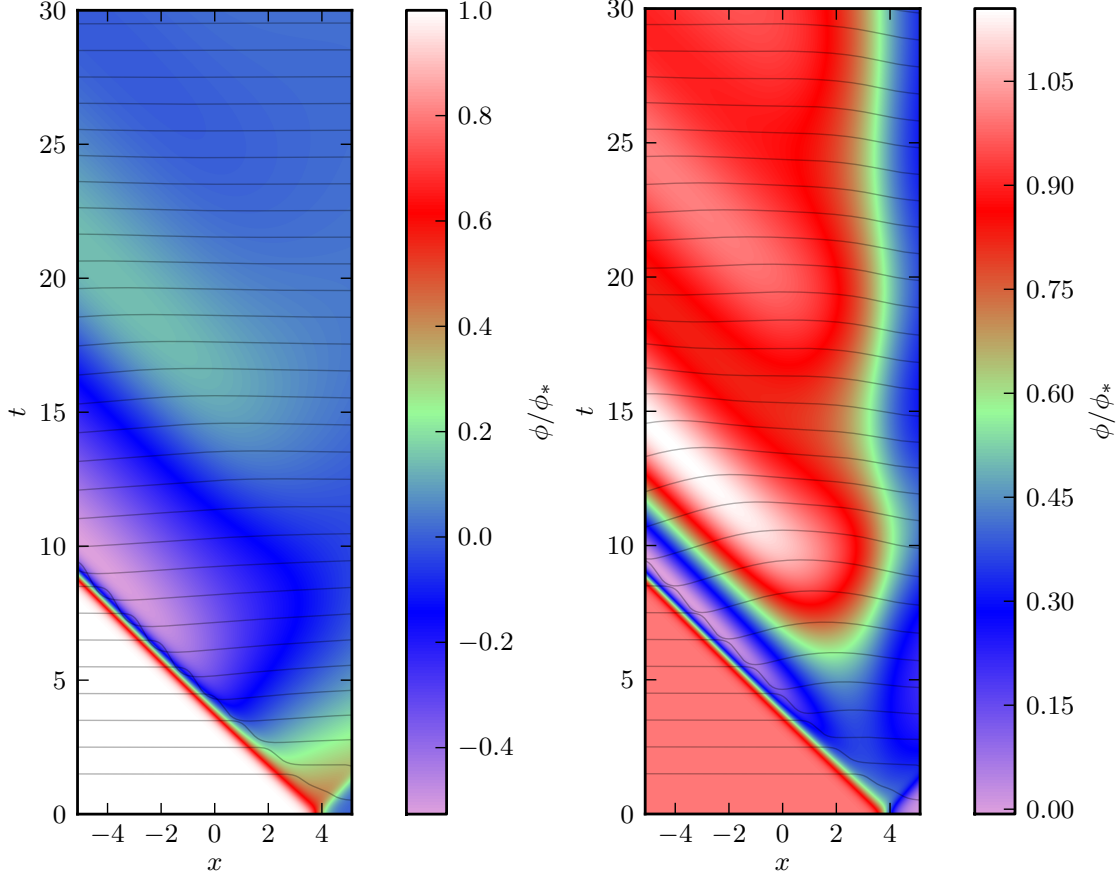


Figure 6.12: Evolution of the symmetron field for two sets of model parameters in tortoise coordinates. Left panel: Convergence towards a trivial field profile for  $\lambda = 10^{-2}/\hbar$ ,  $\mu = 8 \times 10^{-4}/r_g^2$  and  $m_S^2 = 10^{-3}\hbar^2/r_g^2$ . Right panel: Non-trivial hair solution for  $\lambda = 10^2/\hbar$ ,  $\mu = 8 \times 10^{-1}/r_g^2$  and  $m_S^2 = \hbar^2/r_g^2$ .

densities, and the field decouples from matter since  $S_m$  does not depend on  $\phi$  anymore. This mechanism allows the symmetron model, with the proper parameters, to pass the solar system tests of GR. In the case of this model, the difference between the field dynamics in high-density regions described in the Jordan and in the Einstein frame is not substantial because of the quadratic dependence of the conformal factor on  $\phi/m_S$ .

#### 6.4.2 Accreting symmetrons

In this section we evaluate the dynamics of the accreting symmetrons. Previously, in subsection 6.4.1, we discussed a simplified model equipped with spontaneously broken  $\mathbb{Z}_2$  symmetry and an environmentally dependent mass. The shape of the potential and the effects of the coupling with matter are shown in Figure 6.11. Following the potential in (6.26), we observe that in regions of high matter densities, the only stable field configuration is  $\phi = 0$ ; however, as we discussed in the previous section, the field takes a non-zero vacuum

expectation value in zones of lower matter density. In consequence, considering the mass distribution in (6.3), the initial radial profile used is

$$\phi(r, t = t_0) = \begin{cases} \phi_*, & r < r_{\text{ISCO}} \\ 0, & r \geq r_{\text{ISCO}}, \end{cases} \quad (6.27)$$

which can be smoothed by using an hyperbolic tangent in the same manner as in the matter profile. An equivalent but more physically motivated way to choose the initial field configuration is to place it in equilibrium  $V'_{\text{eff}}(\phi) = 0$  for a given matter distribution. Once again we will assume  $\dot{\phi}(r, t = t_0) = 0$  for initial field velocity. With these initial conditions and choosing  $\sigma = 0$ , we compute the evolution of the field profile for two different sets of model parameters: (a)  $\lambda = 10^{-2}/\hbar$ ,  $\mu = 8 \times 10^{-4}/r_g^2$ ,  $m_S^2 = 10^{-3}\hbar^2/r_g^2$  and (b)  $\lambda = 10^2/\hbar$ ,  $\mu = 8 \times 10^{-1}/r_g^2$ ,  $m_S^2 = \hbar^2/r_g^2$ . Depending on parameters chosen, symmetrons do not always form non-trivial static hair solutions. The flux of the symmetron field  $\mathcal{J} \equiv 4\pi r^2 \phi_{,x} \phi_{,t}$  is shown in Figure 6.13. All the ingoing scalar fluxes calculated here settle to zero smoothly after initial transient.

In the first choice of parameters there is not a clear difference between the bare and effective potentials – i.e., even when  $\phi_*$  is different than zero, the curvature of the effective potential is almost the same as in the bare potential –. Nonetheless, the bare and effective potential are distinct in every aspect for the second choice of parameter models. In Figure 6.12, we calculated the evolution of the field towards equilibrium for both choices. The difference in evolution lies in the contribution of the matter source to the effective potential: in the left panel of Figure 6.13, we suppressed the effects of the “external force” driven by the static matter density. Therefore this limit case is consistent with the standard no-hair theorem. However, that is not the case for the model depicted in the right panel, where the mass of the black hole is the same as the coupling parameter  $m_S$ . In accordance with our description in the previous subsection, we will explore the cases in which we can find non-trivial static solutions. From Figure 6.11, we can recognize at least one equilibrium field configuration corresponding to the different vacua for a given shape of the deformed “Mexican hat” potential. In Figures 6.14 and 6.15, we compute the static solutions for different values of the model parameters.

## 6.5 Accretion of the Ratra-Peebles chameleons

### 6.5.1 Equations of motion and setup

We now study the prototypical example of the chameleon screening, defined in the Einstein frame by the same scalar-tensor action as in (6.21), with the Ratra-Peebles potential

$$V(\phi) = V_0 + \frac{\gamma^{n+4}}{\phi^n} \quad (6.28)$$

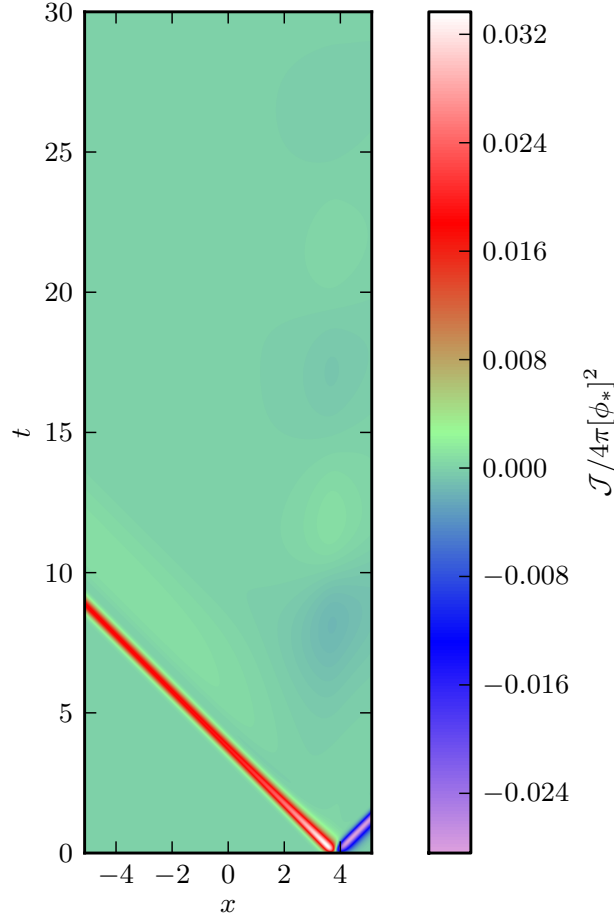


Figure 6.13: Scalar field flux in the symmetron field evolution. Initial transient splits into ingoing and outgoing waves, which are transported to horizon and spatial infinity (in the purple curve) without attenuation. Overall flux settles to zero soon after initial transient.

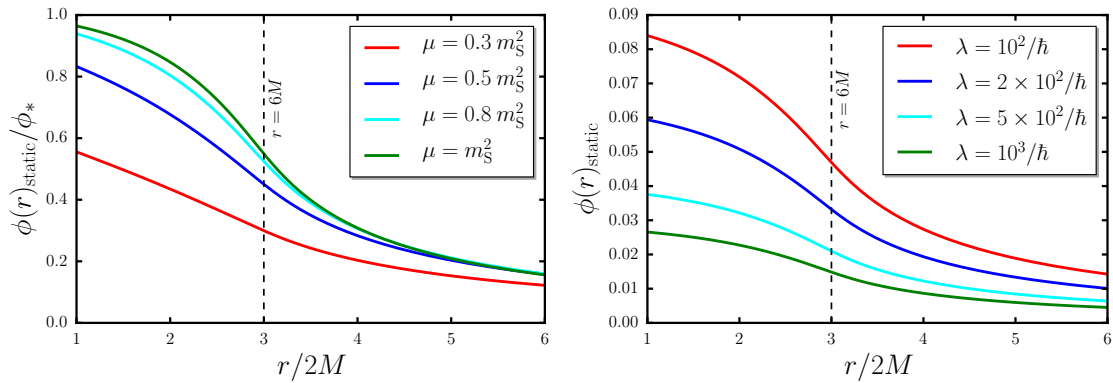


Figure 6.14: Left panel: Static solutions of the symmetron field for different values of  $\mu$ , with constant  $\sigma = 0$ . Right panel: Static solutions of the symmetron field for different values of  $\lambda$ , with constant  $\mu = 0.8m_S^2$ .  $\lambda$  acts as an overall normalization constant for the solution.

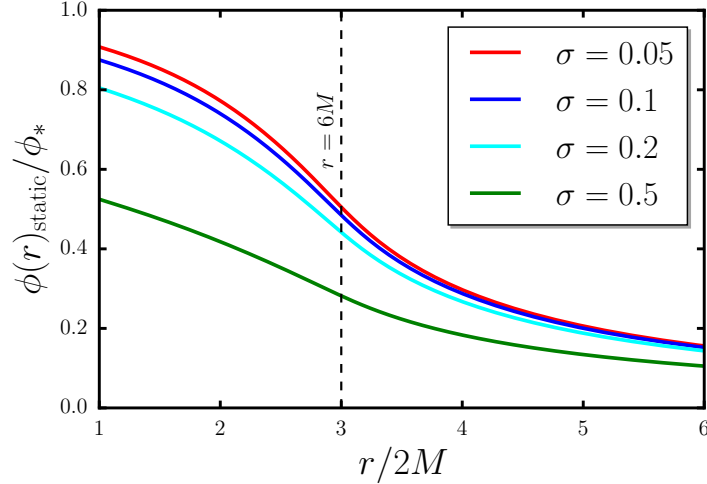


Figure 6.15: Static solutions for different values of  $\sigma$  in the symmetron model,  $\mu = 0.8m_{\text{S}}^2$  and  $\lambda = 10^2$  were held as constants.

and an approximate coupling function

$$A(\phi) \approx 1 + \frac{\varepsilon\phi}{m_{\text{C}}}, \quad (6.29)$$

where the model parameter  $\gamma$  represents the strength of the potential and the ratio  $\varepsilon/m_{\text{C}}$  determines the strength of the field coupling to matter.  $m_{\text{C}}$  plays the role of a high mass scale where the screening is effective. Potentials of this form are usually called “runaway potentials” due to their dependence on negative powers of  $\phi$ . Here we also choose to work in the Einstein frame being consistent with the procedures followed in [75]. The equations of motion for both the metric and the scalar field are the same as in (6.24) and (6.25), but now the effective potential is given by

$$V_{\text{eff}}(\phi) = V_0 + \frac{\gamma^{n+4}}{\phi^n} + \frac{\varepsilon\phi}{m_{\text{C}}}(-T). \quad (6.30)$$

where  $-T = \rho$  for dust-like matter. This is another case of an effective potential dependent on the environment. Due to the term proportional to  $T$ , it is possible to find an equilibrium configuration for the field from  $V'_{\text{eff}}(\phi) = 0$

$$\bar{\phi}_{\text{C}} = \left( n\gamma^{n+4} \frac{m_{\text{C}}}{-\varepsilon T} \right)^{\frac{1}{n+1}}, \quad (6.31)$$

in the case of pressureless matter ( $T = -\rho$ ), we see that the field is suppressed in dense regions (with energies larger than  $m_{\text{C}}$ ) and unscreened in regions with lower densities. The

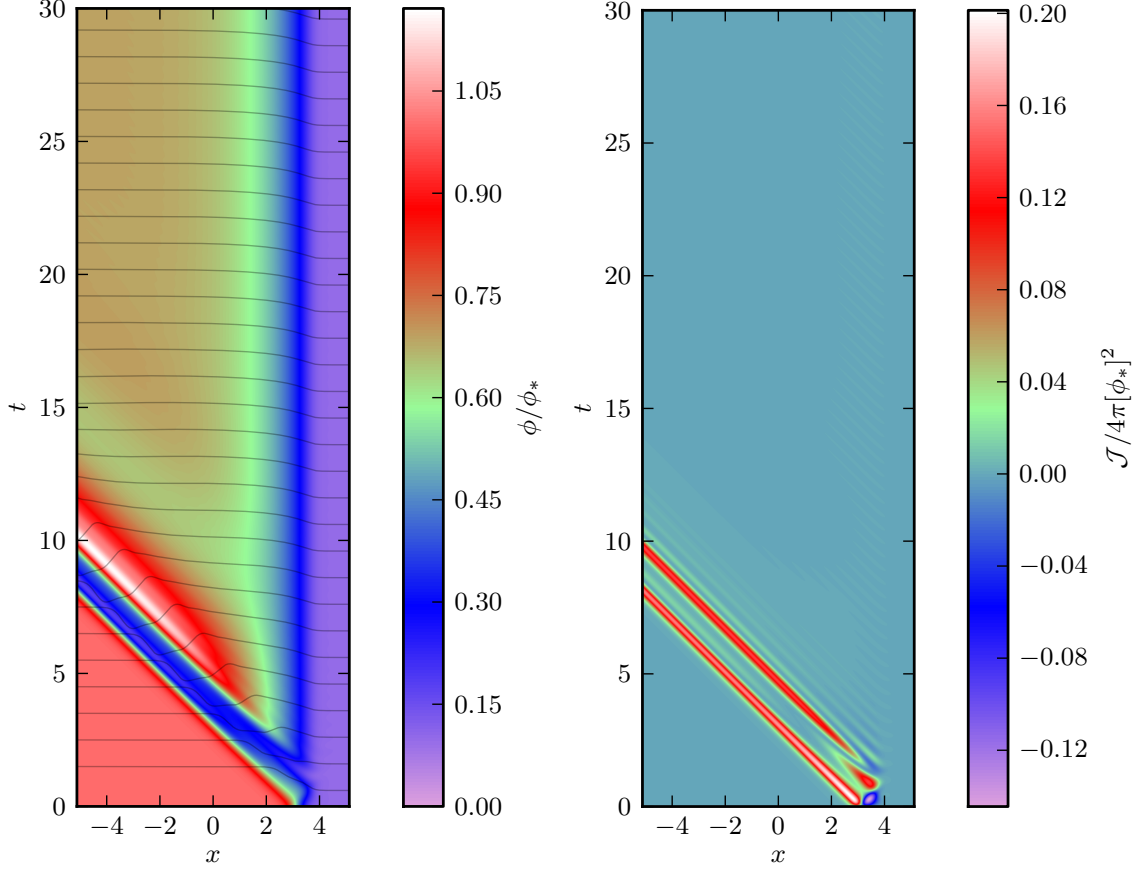


Figure 6.16: Left panel: Evolution of the Ratra-Peebles chameleon for  $n = 1$ . The field smoothly evolves into a static hair solution after initial transient. Right panel: Scalar field flux of the same evolution. The scalar flux represents how the field gets absorbed into the black hole’s event horizon.

effective mass of the field is given by

$$V_{\text{eff}}''(\bar{\phi}_C) = (n + 1) n^{-\frac{1}{n+1}} \gamma^{-\frac{n+4}{n+1}} \left( \frac{-\varepsilon T}{m_C} \right)^{\frac{n+2}{n+1}}, \quad (6.32)$$

which becomes larger in dense environments. Therefore, chameleon and symmetron fields have different forms of screening: in the case of the symmetron, it is a consequence of the reduction of the field correlation length due to a larger effective mass of the field. In a low-density environment, the minimum can be found at  $\phi = \phi_*$  with  $\phi_* \equiv (n\gamma^{n+4} m_C / (\varepsilon\sigma\rho_0))^{\frac{1}{n+1}}$ , where  $\sigma\rho_0$  is the density at  $r < r_{\text{ISCO}}$ .

### 6.5.2 Accreting chameleons

Here we evaluate the accretion of the Ratra-Peebles chameleons in the background described in section 6.1. In Figure 6.17 we observe the shape of the potential as a function of the field

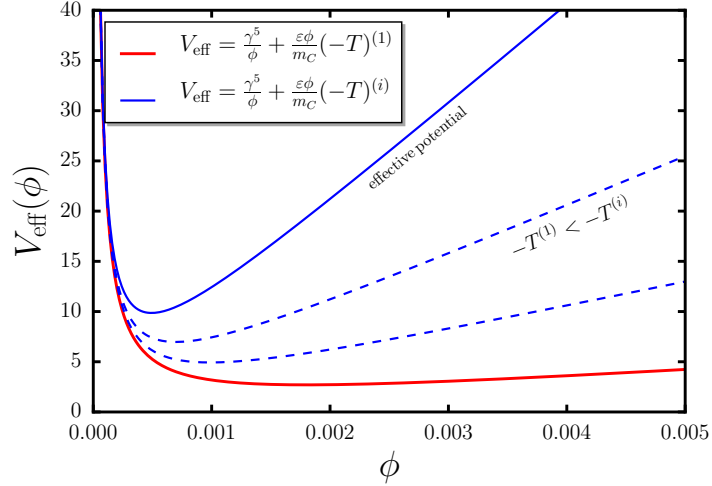


Figure 6.17: Effective potential for the Ratra-Peebles chameleon considering arbitrary spatially constant matter densities and positive model parameters for  $n = 1$ .

$\phi$ , and the effects of the coupling with matter. The effective mass – i.e. the concavity of the effective potential – increases with the environmental matter density of dust.

We derive initial conditions compatible with (6.18) by replacing the matter distribution proposed in (6.3) with (6.31), avoiding the value of  $\sigma = 0$  to not have any divergences in the initial field profile at  $r < r_{\text{ISCO}}$ . The constitution of the Ratra-Peebles model offers the possibility of finding the corresponding initial field configuration as a function of the surrounding matter density, the reverse process can also be coded without inconveniences. Assuming static initial conditions and  $\sigma = 0.01$ ,  $\varepsilon = 10^2$ ,  $\gamma = 0.3m_C$  and a surrounding dust density of  $-T = \rho_0 = 3 \times 10^{-2}m_C/r_g^3$ , we find the evolution of the field from initial conditions towards a static solution in the left panel of Figure 6.16. From this figure, we can notice that the evolution of the field is not significantly different from our results for the Starobinsky and the Hu-Sawicki models in Figure 6.2, which is consistent with the effects of the chameleon screening in these models. Additionally, the ingoing field flux is depicted in the right panel of the same figure. Here the flux is regular and converges to the limit where there is no other source apart from the static matter distribution. Ingoing flux lines are represented around  $x(r_{\text{ISCO}}) \approx 3.89$ . We also present static solutions for different choices of the model parameters. In Figures 6.18 - 6.19, we show the changes in shape of the hair profiles for different parameter choices. In this case, the tuning of the parameter in the runaway potential is sensitive to changes in the orders of magnitude: it is simple to accidentally suppress the whole contribution of this part of the potential, due to the  $(n + 4)$  power of  $\gamma$ .

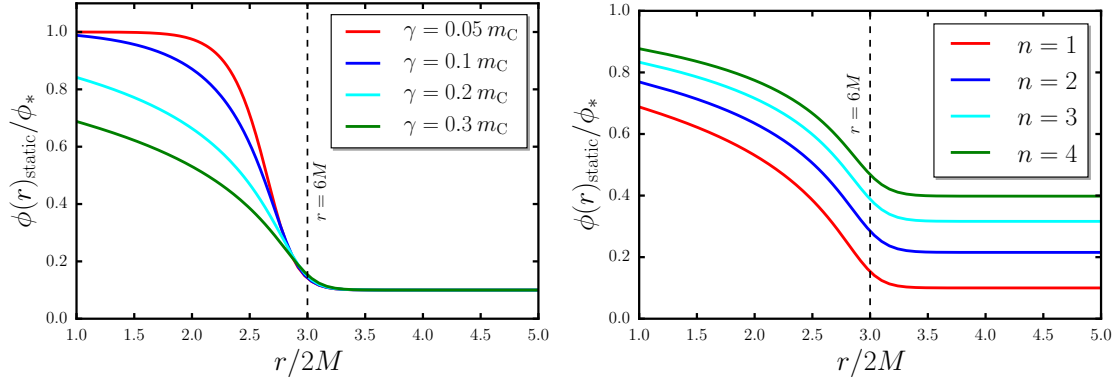


Figure 6.18: Left panel: Static solutions of the chameleon field for different values of  $\gamma$ , with constant  $n = 1$  and  $\sigma = 0.01$ . Right panel: Ratra-Peebles chameleons for different values of  $n$ . The parameter  $n$  also shifts the initial equilibrium configuration for  $\phi$ .

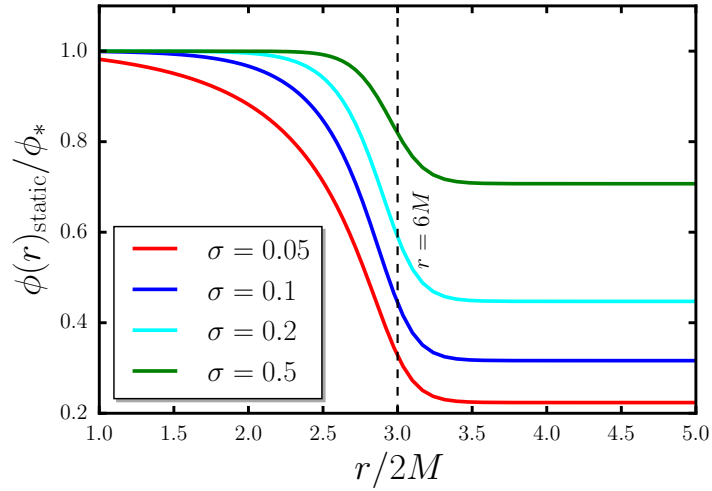


Figure 6.19: Field profiles for different values of  $\sigma$  in the chameleon model. Notice the screening at  $r < r_{\text{ISCO}} = 6M$  of the hair solution for larger values of  $\sigma$ .



## 6.6 Discussion

In this chapter, we describe the dynamics of scalar accretion onto a Schwarzschild black hole in the presence of a static matter distribution modelled by (6.3). In particular, we studied the accretion of the extra scalar degrees of freedom appearing in two models of  $f(R)$  gravity, the Starobinsky and Hu-Sawicki model, as well as in the symmetron model. Stable convergence to static scalar hair profiles results from varying parameters for each specific model. In the cases of the Starobinsky and Hu-Sawicki model, we can obtain dynamical chameleon solutions with singular curvature outside horizon without requiring an infinite energy budget. In the case of accreting symmetrons, it is not always possible to form a non-trivial static solution since it depends on the strength of the coupling with matter. More concretely, it depends on how large is the energy scale  $m_S$  compared to the mass of the black hole. Our results for the field fluxes are included for all the cases we studied, along with the static solutions for different model parameters.

Even when the simulations of astrophysical rotating black holes suggest a large density contrast, we noticed that the formation of non-trivial static solutions does not require an absolute vacuum environment close to the black hole’s event horizon, where  $r \in (r_g, r_{\text{ISCO}}]$ . We did not consider the effects of backreaction of the field in the spacetime solutions since these are small even during the formation of integrable naked singularities.

We acknowledge the progress made in [75, 74], wherein approximate analytic expressions for scalar hair solutions in the case of rotating black holes were found. Additionally, this chapter discusses the possibility of a non-negligible ratio between the radiated power from extra scalar sources and the quadrupole gravitational radiation in GR, which might be testable by the future generation of gravitational-wave detectors. In our approach, apart from calculating static solutions in different circumstances, we evaluated the scalar accretion dynamically in such a way that it is possible to converge to a hairy or a “bald” solution, depending on the model and its parameters. These results also motivate further explorations on the effect of scalar forces confined by screening, surrounded by a non-trivial matter profile for merging binary systems.

The existence of non-trivial field profiles has also been studied for scalars with non-canonical kinetic terms, such as in the Galileons studied in [29, 30]. Those solutions are described in vacuum environments and do not accrete into the black hole’s horizon. The form of the equations of motion of Galileon is not semi-linear, and is harder to study numerically, as Galileons propagate with speeds that vary at different locations. Numerical implementation of a dynamical code designed to compute evolution of such scalar fields will be covered in a future project. We are also considering to extend the techniques developed here to full 3D scalar-field scattering by a black hole.

## Chapter 7

# Echoes from the scattering of wavepackets on wormholes

The era of gravitational wave (GW) astronomy [2, 1] has begun. GW spectroscopy, in analogy to its atomic counterpart, allows us to investigate strong gravitational interactions in their radiative regime. In this new range of frequencies, it is now possible to explore the role of dynamical gravitational degrees of freedom in a wide range of astrophysical [111, 63] and cosmological [160, 11] phenomena.

The prolonged absence of observational evidence confirming the dynamical properties of spacetime has motivated a plethora of conjectures about the behaviour of gravity within and beyond [69, 233, 141] classical General Relativity (GR). The potential existence of exotic compact objects (ECOs) generated by quantum effects on gravity [176, 17, 173] (such as wormholes, firewalls and gravastars) has captured the attention of many recent efforts [156, 237, 103, 64, 4, 172, 245, 70, 246, 3]. The primary claim is that the detection of a train of “echoes” isolated from the main transient of a GW event and with generically large amplitudes would be clear evidence of ECOs. Following the effective field theory approach argued since Chapter 1, it is possible to show that the reflectivity of any potential barrier depends on the energy scale involved in the merger [55]. It is, therefore, necessary to understand (i) the mechanisms behind the production of echoes and (ii) the intensity and spectrum of the outgoing wavelets compared to the GW transient in the most straightforward possible setup. In this chapter, we explore the generation of echoes by colliding wavepackets of scalar and tensor radiation against a traversable spherically symmetric wormhole [244]. We find that such a wormhole behaves just like a Fabry-Perot cavity and shares common properties with the potential cavities made by other ECOs, like gravastars and firewalls. Additionally, considering that the main features of the outgoing pulses are similar to the ringdown signals expected from the coalescence of ECOs, our results show that the amplitude of the echoes is not generically large.

Here we consider a simplified wormhole configuration made by the junction of two Schwarzschild geometries of equal masses at  $r_0 > 2M$ , widely known as the Morris-Thorne

wormhole [64, 175]. In this case, the symmetry of the centrifugal barriers at  $r = 3M$  on each side of the throat allows us to find the reflection and transmission coefficients of the cavity. Hence, it is possible to reconstruct the spectral shape of the outgoing pulse using the geometrical optics approximation. Nevertheless, this approximation predicts an exponential decay of the subsequent higher-order reflections, which appears instead as a power-law in the full solution of the scattering problem. Thus, the excitation of quasinormal modes (QNMs) is the only cause for the presence of echoes in the time evolving profile. These modes are sourced by a sequence of internal reflections inside the potential cavity and then propagate throughout the surface of the maximal potential energy spheres (i.e., the “spikes” of the potential barriers in radial coordinates, corresponding to two-dimensional spheres in real space), while radiating energy to the exterior. QNMs of the Schwarzschild solution have been studied in detail and reproduced in various analytic and numerical simulations [67, 18]; thus it is easy to identify their characteristic frequencies in the spectrum of outgoing pulses. We also present the full scattering solution both inside and outside the wormhole cavity, along with the energy fluxes and the asymptotic solutions for the principal spherical modes of a scalar (and tensor) wavepacket. In addition to this, we find the width and frequency intervals contained in the incident wavepackets for which the outgoing wavelets have maximal amplitudes. Our computer code is optimized to solve both scalar accretion and scattering problems and is publicly available at <https://github.com/andrei-v-frolov/accretion/tree/wormhole>.

The layout for this chapter is as follows: in section 7.1, we review the scattering problem of scalar waves starting by a quick overview of the dispersion of a Gaussian pulse by a Schwarzschild black hole. The main point of this section is to calculate the transmission and reflection coefficients of each of the centrifugal barriers constituting the resonant cavity, formed in the case of a wormhole. Our results show a frequency “sweet spot” such that the incident pulse is not fully reflected nor fully transmitted by the cavity, favouring multiple internal reflections that source the QNMs. Furthermore, we solve the problem of scattering by a wormhole directly using the same ingoing Gaussian wavepacket, and then we compare the Fourier transform of this solution with the pulse reconstructed following the geometrical optics approximation. We find that the approximate reconstruction matches the full solution, up to the peaks due to the QNM frequencies. Likewise, we evaluate the amplitude of each of the echoes as a function of the width of the initial Gaussian waveform, finding that a single width of the incident pulse maximizes the amplitude of all the echoes. In Section 7.2, we extend the results in the previous section to a Gaussian pulse of tensor fluctuations of the metric by following the even and odd decomposition of the tensor modes introduced by Regge, Wheeler and Zerilli in [207, 255, 201, 202]. We can rewrite our results in the usual asymptotic polarization modes  $h_+$  and  $h_\times$ , known as the perturbations of a flat metric. We conclude with a discussion in Section 7.4.

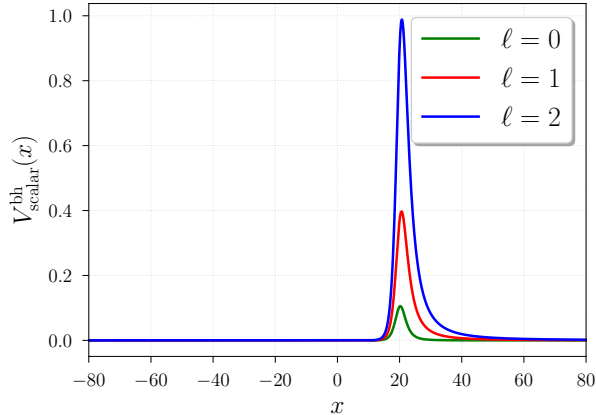


Figure 7.1: Effective potential for the spherical modes  $\mathcal{U}_{20}^{\text{bh}}(x, t)$  scattered by a Schwarzschild black hole, growing with  $\ell$ . The wall acts as a barrier transparent to certain frequencies above a transmissivity threshold and reflective for lower frequencies.

## 7.1 Scattering of scalar wavepackets

In this section, we solve the scattering of a Gaussian wavepacket by a spherically symmetric wormhole. To do so, we will first review the dispersion by the centrifugal barrier of a spherically symmetric black hole in order to find the properties of the potential cavity.

### 7.1.1 Scattering by a Schwarzschild black hole

Our primary objective is to study the dynamics of scalar and tensor wavepackets scattering from a Misner-Thorne wormhole at all points. Thus, we first review the dispersion of scalar waves by a Schwarzschild black hole, thoroughly studied in [214, 215, 216, 217], wherein the collision against each of the two potential walls (constituting the effective potential cavity formed by a wormhole) is studied in full detail. The dynamics of the scattering problem is found by solving the equation of motion for a test scalar field

$$\square\Phi = 0, \quad (7.1)$$

where  $\square \equiv g^{\alpha\beta}\nabla_\alpha\nabla_\beta$  is the standard d'Alembertian in a curved background. Here  $g_{\alpha\beta}$  is the metric tensor in a spherically symmetric Schwarzschild-like static spacetime

$$g_{\alpha\beta} = -f(r)\delta_\alpha^t\delta_\beta^t + \frac{1}{f(r)}\delta_\alpha^r\delta_\beta^r + r^2\left(\delta_\alpha^\theta\delta_\beta^\theta + \sin^2\theta\delta_\alpha^\phi\delta_\beta^\phi\right). \quad (7.2)$$

It is convenient to introduce the tortoise coordinate  $x$ :

$$x \equiv \int_{r_0}^r \frac{dr}{f(r)}, \quad (7.3)$$

In the case of the Schwarzschild metric  $f(r) = 1 - r_g/r$  the last expression yields

$$x = r - r_0 + r_g \ln \left( \frac{r - r_g}{r_0 - r_g} \right), \quad (7.4)$$

for  $r_g < r < +\infty$  and  $r_0 > r_g$ , where  $r_g = 2M$  is the usual Schwarzschild radius. By direct evaluation, we see that  $r = r_0$  corresponds to  $x = 0$ , the horizon  $r = 2M$  maps into  $x \rightarrow -\infty$  and  $r \rightarrow +\infty$  is  $x \rightarrow +\infty$ . In our numerical routine, we invert (7.4) to get  $r \equiv r(x)$  (see the appendix A, subsection 6 in [111] for more details). In tortoise coordinates, we can decompose the scalar field in spherical harmonics

$$\Phi(x, t) = \frac{1}{r(x)} \sum_{\ell, m=0} \mathcal{U}_{\ell m}^{\text{bh}}(x, t) Y_{\ell m}(\theta, \phi), \quad (7.5)$$

in that way we can rewrite (7.1) as

$$\left[ -\partial_t^2 + \partial_x^2 - V_{\text{scalar}}^{\text{bh}}(x) \right] \mathcal{U}_{\ell m}^{\text{bh}}(x, t) = 0, \quad (7.6)$$

and the effective potential  $V_{\text{scalar}}^{\text{bh}}(x)$  is given by

$$V_{\text{scalar}}^{\text{bh}}(x) = \left( 1 - \frac{r_g}{r(x)} \right) \left[ \frac{\ell(\ell+1)}{r(x)^2} + \frac{r_g}{r(x)^3} \right]. \quad (7.7)$$

After rearranging the variables, the equation of motion of the spherical modes is now written in its traditional linear waveform. In Figure 7.1, we observe the growth of the potential barrier with the angular momentum number  $\ell$ . The potential wall does not vanish for the monopole ( $\ell = 0$ ) due to the extra term proportional to  $r^{-3}$  appearing after the coordinate change, which replaces the radial damping in the original Schwarzschild coordinates  $(t, r)$ . Such a term becomes subdominant for all  $\ell \geq 1$ . Intuitively, it is reasonable to expect that the modes with frequency above a given threshold (related to the thickness of the wall) can cross the barrier, while the lower frequency modes reflect.

Now we setup the scattering problem for one of the spherical modes ( $\mathcal{U}_{20}^{\text{bh}}$ , the quadrupole) with the following initial conditions corresponding to an ingoing Gaussian wavepacket

$$\mathcal{U}_{20}^{\text{bh}}(x, 0) = \exp \left( -\frac{(x - x_0)^2}{2\sigma^2} \right), \quad \partial_t \mathcal{U}_{20}^{\text{bh}} \Big|_{t=0} = \partial_x \mathcal{U}_{20}^{\text{bh}}(x, 0), \quad (7.8)$$

After fixing the values of the width to be  $\sigma = 0.9185r_g$ , the initial position of the Gaussian at  $x_0 = 60.0r_g$ ,  $r_0 = 20.0r_g$  and the initial conditions in (7.8), we show the time-dependent solution of (7.6) in Figure 7.2, where we distinguish the incident (lines with negative slope to the right of the wall), transmitted (lines with negative slope to the left of the wall) and reflected parts (lines with positive slope to the right of the wall) of the solution. It is important to observe the absence of spurious late time reflections and interferences due

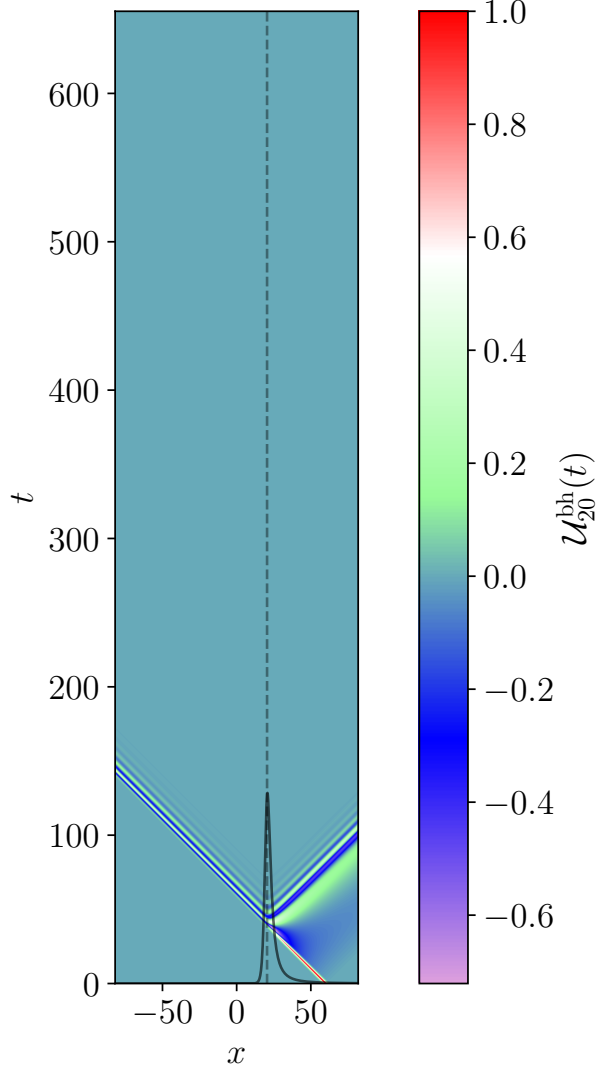


Figure 7.2: Dispersion of the incident Gaussian wavepacket  $\mathcal{U}_{20}^{\text{bh}}$  by the potential barrier (plotted in black) showing the incident, reflected and transmitted pulses, it is possible notice the ringing of the reflected solution due to the quasinormal modes.

to the implementation of perfectly matching layers (PMLs) in the outermost regions of our simulation box (see the details of our setup for PMLs in [111]). We observe the main features of the reflected signal in Figure 7.3, where the asymptotic behavior of the signal shows a sharp transient as a consequence of the collision against the potential wall, and the ringing of quasinormal modes occur right after the reflection in agreement with [193].

It is now possible to evaluate the reflection and transmission coefficients of the potential wall depicted in Figure 7.1. To do so, we compute the one-dimensional Fourier transform of the incident  $\tilde{\mathcal{U}}_{20}^{\text{inc}}(\omega) = \mathcal{F}[\mathcal{U}_{20}^{\text{bh}}(0, x)]$ , reflected  $\tilde{\mathcal{U}}_{20}^{\text{ref}}(\omega) = \mathcal{F}[\mathcal{U}_{20}^{\text{bh}}(t, +\infty)]$  and transmitted

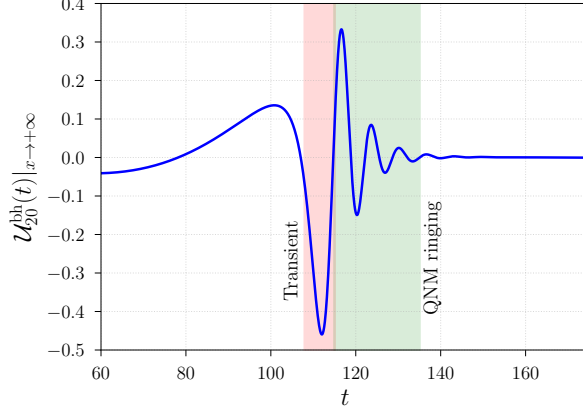


Figure 7.3: Asymptotic solution (zoomed in, for clarity) for the quadrupole mode  $\mathcal{U}_{20}^{\text{bh}}(x, t)$  by direct evaluation of the results in Figure 7.2. The reflected signal shows its maximum peak and the posterior ringing due to QNMs.

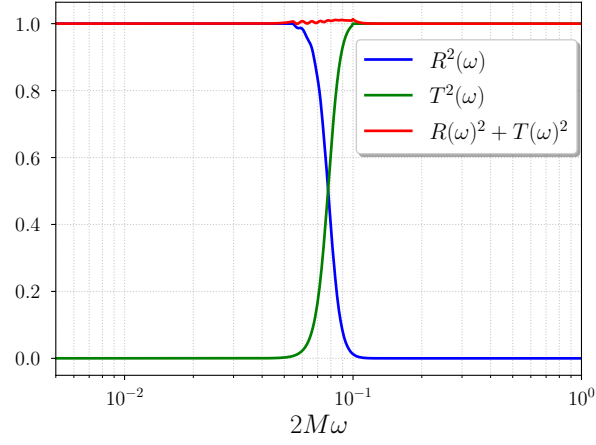


Figure 7.4: Reflection and transmission coefficients as functions of frequency ( $\omega$ ), the identity  $R^2 + T^2 = 1$  is satisfied with an error smaller than 1%.

$\tilde{\mathcal{U}}_{20}^{\text{trans}}(\omega) = \mathcal{F}[\mathcal{U}_{20}^{\text{bh}}(t, -\infty)]$  from the solved scattering modes in order to define

$$R(\omega) \equiv \frac{\|\tilde{\mathcal{U}}_{20}^{\text{ref}}(\omega)\|}{\|\tilde{\mathcal{U}}_{20}^{\text{inc}}(\omega)\|}, \quad T(\omega) \equiv \frac{\|\tilde{\mathcal{U}}_{20}^{\text{trans}}(\omega)\|}{\|\tilde{\mathcal{U}}_{20}^{\text{inc}}(\omega)\|} \quad (7.9)$$

as the transmission and reflection coefficients, respectively. In Figure 7.4, we plot the squares of these coefficients as functions of frequency observing that the identity  $R^2 + T^2 = 1$  is only approximately met because of the small contributions coming from the QNMs frequency peaks in both the transmitted and reflected solutions. The shape of both the

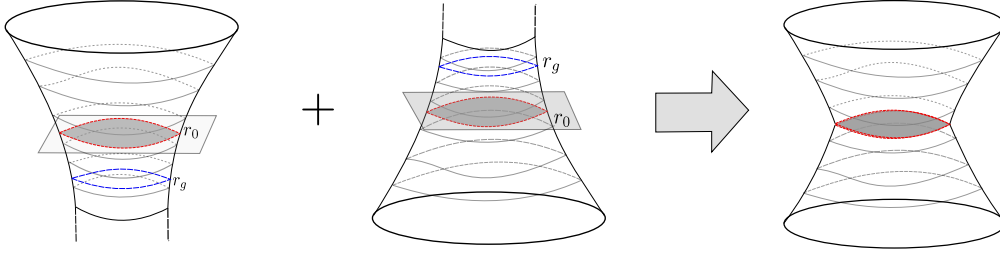


Figure 7.5: Two-dimensional schematic depiction of a Misner-Thorne wormhole made by the junction of two identical copies of the Schwarzschild geometry. This junction occurs in the red circles at  $r_0 > r_g$ , creating a discontinuity in the geometry (and in the energy-momentum tensor). Misner-Thorne geometry does not have horizons.

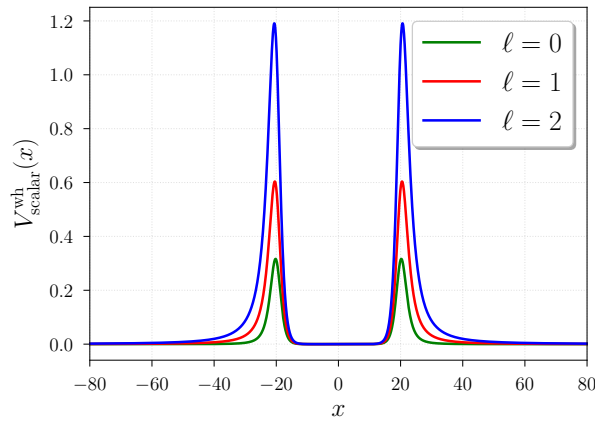


Figure 7.6: Effective potential cavity for the wormhole in (7.11), we observe the growth of the barriers with the angular momentum number  $\ell$ .

transmissivity and reflectivity curves is very similar to an hyperbolic tangent step function<sup>1</sup>, intersecting at  $R^2 = T^2 = 0.5$ , as expected. Furthermore, it is crucial to notice from the last figure that it is only in a narrow band of frequencies where the amplitudes transmitted and reflected by the potential barrier are comparable. in the case of a wormhole, such a fact will be important in our analysis.

### 7.1.2 Scattering by a traversable wormhole

In this section, we study the dispersion of Gaussian wavepackets by a traversable wormhole, formed by the junction at  $r_0 > r_g$  of two Schwarzschild geometries with equal mass, as depicted in Figure 7.5. There is a discontinuity in the Einstein tensor  $G_{\alpha\beta}$  (and thus, in the energy-momentum tensor) such that at  $r = r_0 = 20.0r_g$ , any contracting congruence of geodesics in one side of the throat starts to expand in order to reach the other side, violating

<sup>1</sup>This is not surprising after we consider the DeWitt approximation for the transmissivity [82, 112], which is precisely given by a step function.



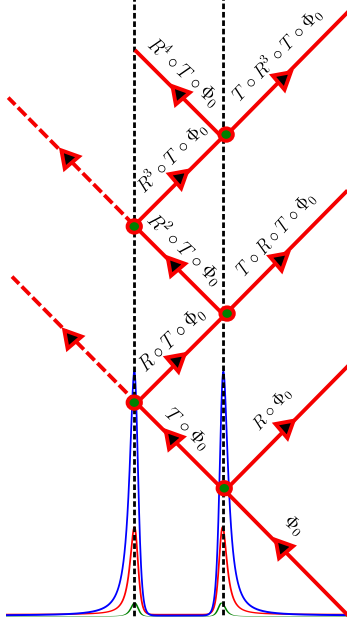


Figure 7.7: Schematic reconstruction of the outgoing solution by a sequence of reflections and transmissions inside the potential cavity. Dashed red lines propagate in the other side of the throat, hence the signals carried by them are inaccessible by any observer in the side of the emitter.

the weak energy condition. Such a configuration does not show coordinate singularities nor horizons, it is known in the literature as the Morris-Thorne traversable wormhole [175]. The dynamics of the scattering problem is still given by the solutions of (7.1) following the same decomposition in spherical modes as in (7.5). Hence, the waveform of the equation of motion for the spherical modes is given by

$$\left[-\partial_t^2 + \partial_x^2 - V_{\text{scalar}}^{\text{wh}}(x)\right] \mathcal{U}_{\ell m}(x, t) = 0, \quad (7.10)$$

and the effective potential  $V_{\text{scalar}}^{\text{wh}}(x)$  yields

$$V_{\text{scalar}}^{\text{wh}}(x) = \left(1 - \frac{r_g}{r(|x|)}\right) \left[\frac{\ell(\ell+1)}{r(|x|)^2} + \frac{r_g}{r(|x|)^3}\right]. \quad (7.11)$$

This is plotted in Figure 7.6 and coincides with the shape of the potential calculated in [64]. Strictly speaking, we refer to  $r(|x|)$  as the same inverse of the function mentioned in (7.4) now evaluated at  $|x| - r_0$ . As we can see in Figure 7.6, the new effective potential is merely a reflection of the potential barrier in Figure 7.1 about the ordinate axis; thus, it is sensible to identify this system as a potential cavity built from two potential barriers with the reflection and transmission coefficients depicted in Figure 7.4. Furthermore, let us assume that an arbitrary incident pulse  $\Phi_0$  propagates towards the cavity, it is, therefore,

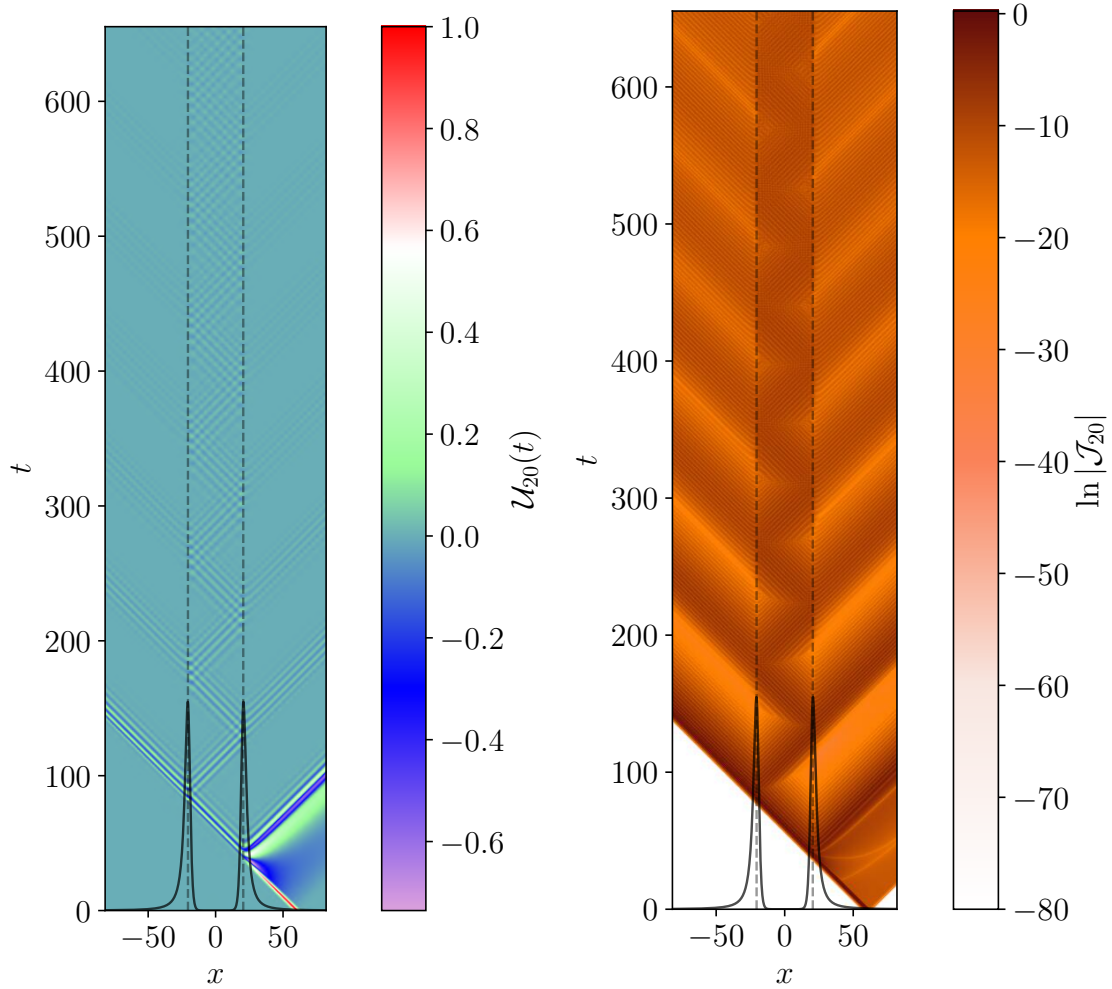


Figure 7.8: Left panel: Evolution of the clean quadrupole mode  $\mathcal{U}_{20}$  for the effective potential in Figure 7.6. We can notice the sequence of reflections and transmissions inside the cavity is very similar to the scheme depicted in Figure 7.7. Right panel: Evolution of the radial flux  $\mathcal{J}_{20} \equiv \Delta\mathcal{U}_{20,x}\Delta\mathcal{U}_{20,t}$  of the clean signal. The only incident source comes from the collision of the pulse, which dissipates very slowly to the exterior every time the internal reflections hit the walls of the potential cavity. QNM are sourced by this process.

reasonable to approximate the spectrum of the asymptotic solution by a simple geometrical series of reflections and transmissions inside the cavity acting on the incident pulse, as shown in Figure 7.7. Following this scheme, the asymptotic solution can be approximated by

$$\Phi^{\text{wh}}(\omega)|_{x \rightarrow +\infty} = \left[ R + T \circ \sum_{i=0}^{\infty} R^{2i+1} \circ T \right] \circ \Phi_0(\omega). \quad (7.12)$$

where the symbol “ $\circ$ ” represents the function composition between reflection/transmission operators. It is not difficult to see that, in the hypothetical case of a perfectly reflective wall replacing the left potential barrier in Figures 7.6 and 7.7, the reconstructed pulse is instead given by

$$\Phi^{\text{f}}(\omega)|_{x \rightarrow +\infty} = \left[ R + T \circ \sum_{i=0}^{\infty} R^i \circ T \right] \circ \Phi_0(\omega), \quad (7.13)$$

corresponding to the case of a firewall<sup>2</sup>. Nevertheless, we will not cover the features of the firewall solution in what remains of this chapter.

We now solve the scattering problem exactly for the first non-zero mode of gravitational radiation, which is the quadrupole  $\mathcal{U}_{20}(t, x)$ . Using the same initial conditions as in (7.8) for  $\sigma = 0.9185r_g$  as the standard deviation of the incident Gaussian pulse, we find the time-dependent solution of the quadrupole mode  $\mathcal{U}_{20}$  (left panel) and the radial flux  $\mathcal{J}_{20} \equiv \Delta\mathcal{U}_{20,x}\Delta\mathcal{U}_{20,t}$ , of a signal clean of backscattering effects  $\Delta\mathcal{U}_{20}|_{\text{clean}} \equiv \mathcal{U}_{20}|_{\text{original}} - \mathcal{U}_{20}^{\text{bh}}$  (right panel) in Figure 7.8. It is interesting to notice in the evolution plot (on the left) that the signal forms an interference pattern at very late times, showing that successive reflections create an interference pattern which fills the cavity. In addition to this, even when the amplitude of the modes decreases after each collision against any of the potential walls, the spherical modes propagate for longer time<sup>3</sup> throughout the spheres of maximal potential.

The scalar flux is shown in the right panel, we observe that the only source of scalar radiation comes from the first collision of the Gaussian wavepacket against the barrier in the right hand side (the ingoing flux is colored in black at the bottom of the contour plot). A sequence of reflections occurs within the potential barriers, which decay in intensity with time as the cavity leaks energy to the exterior.

Amplitudes of the outgoing signals depend on the variance of the incident Gaussian wavepacket, this is visible in Figure 7.9 where we plot the asymptotic solutions for two different ingoing wavepackets: one with  $\sigma = 0.6495r_g$  in the left panel and a second one with  $\sigma = 5.196r_g$  in the right. After subtracting the outgoing solution for a black hole, the presence of a train of wavelets, colloquially known as echoes, is very clear. For large

<sup>2</sup>A two-barrier system where the innermost wall is a perfectly reflective surface [17] located at the event horizon. It is designed to destroy all correlations between quantum fields propagating towards it.

<sup>3</sup>The inverse of the imaginary component of the quasinormal mode frequencies in [18] gives an idea of the decay timescale for each mode.

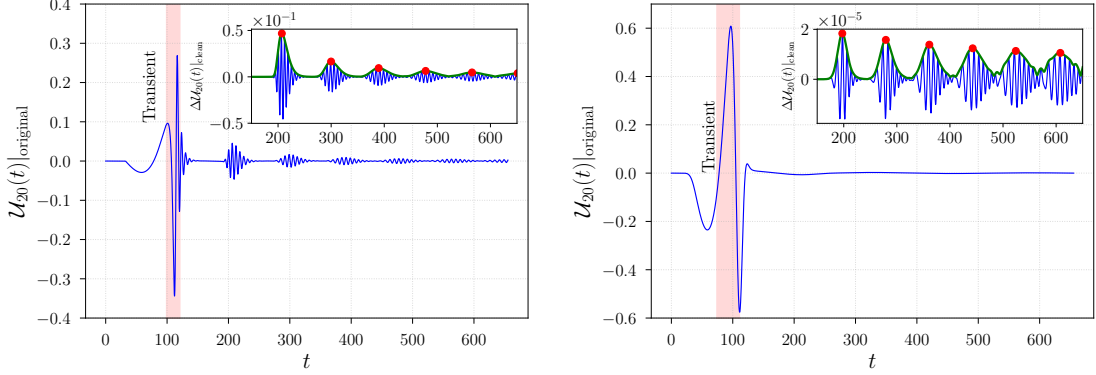


Figure 7.9: Left panel: Asymptotic (at  $x \approx 100r_g$ ) evolution of the quadrupole mode  $\mathcal{U}_{20}$  for  $\sigma = 0.6495r_g$ . Echoes are plotted in the upper corner of the plot, showing them along with their Hilbert envelope (the curves in green) and maximum amplitudes (in red). Right panel: Asymptotic evolution of the quadrupole mode  $\mathcal{U}_{20}$  for  $\sigma = 5.196r_g$ . In contrast with the left panel, echoes are four orders of magnitude smaller than the transient. The amplitude of the transient (inside the red region) in the right figure has decreased with respect to the one in the left panel.

values of  $\sigma$ , the signal is not decreasing monotonically after the transient, as we can observe in the right panel of the same figure. Therefore, subtracting the outgoing pulse (i.e., the case in which there is only one potential wall) obtained from the black hole is a convenient way to clean the signal from back reflections due to the “tails” of the potential barrier. The necessity of this procedure is more evident in the case depicted in the right panel of Figure 7.9, where the amplitudes of the echoes are four orders of magnitude smaller than the transient. In both panels, we plot the variable  $\Delta\mathcal{U}_{20}|_{\text{clean}}$  in the right upper corner of the figures to represent the echoes and their net amplitude after removing backscattering effects. Notice that, in the upper corner of both figures, the amplitude of the echoes does not decrease exponentially with time due to the successive reflections inside the cavity.

As shown in subsection 7.1.1, the curves of reflectivity and transmissivity determines which frequencies stay in the cavity: most of the power of an incident pulse with large  $\sigma$  is in the low-frequency domain, and therefore it will be reflected. The cavity is transparent to high-frequency signals, which are dominant in the pulses with small  $\sigma$ . In either of these extremal scenarios, QNMs cannot be sourced by internal reflections and thus, the amplitude of the echoes is not large in general. Furthermore, the steepness of the transition near the overlap point  $R^2(\omega) = T^2(\omega) = 0.5$  regulates the abundance of frequencies in the spectrum of outgoing signals.

As a next step, we proceed to reconstruct the asymptotic spectrum by following the geometrical optics relation in (7.12) considering the reflectivity and transmissivity operators defined in (7.9). Henceforth, the outcome should be compared with the spectral content of

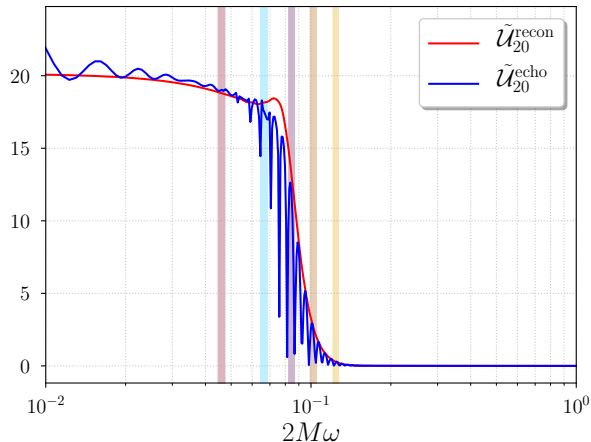


Figure 7.10: Comparing the reconstruction of the spectrum by the geometrical optics approximation in (7.12) (in red) with the Fourier transform of the full asymptotic solution  $\tilde{\mathcal{U}}_{20}^{\text{echo}}$  (in blue). The color stripes indicate a few of the first QNM frequency peaks corresponding to  $\omega_3 = 0.251M^{-1}$  in golden rod,  $\omega_4 = 0.207M^{-1}$  in peru,  $\omega_5 = 0.169M^{-1}$  in plum,  $\omega_6 = 0.133M^{-1}$  in light blue and  $\omega_7 = 0.092M^{-1}$  in rosy brown, these are the real parts of the QNM frequencies for  $n = 3, 4, 5, 6$  &  $7$  calculated in [18].

the asymptotic wave solutions of (7.10). We calculate the Fourier transforms of both the Gaussian incident pulse  $\Phi_0(\omega) = \mathcal{F}[\exp((x - x_0)^2/2\sigma^2)]$  for  $\sigma = 0.6495r_g$  and  $x_0 = 60.0r_g$ , and the asymptotic solution  $\tilde{\mathcal{U}}_{20}^{\text{echo}} \equiv \mathcal{F}[\mathcal{U}_{20}(t, +\infty)]$  including the echoes.

After applying the reconstruction expression in (7.12) up to  $i = 0$  (in red), and comparing the outcome with  $\tilde{\mathcal{U}}_{20}^{\text{echo}}$ , we show the reconstructed spectrum and  $\tilde{\mathcal{U}}_{20}^{\text{echo}}$  (in blue) in Figure 7.10. The low-frequency oscillation peaks in the blue spectrum correspond to the finite size of the simulation box. Notice that the spectrum reconstructed employing the geometrical optics approximation gives the overall shape of the spectrum with decent precision but not the QNM frequency peaks; these appear in the same frequency interval where the reflectivity and transmissivity curves intersect in Figure 7.4. It is, therefore, reasonable to talk about a “sweet spot” in the frequency domain where the cavity maximizes the amplitude of the echoes. Intuitively, after observing the results in Figure 7.9, it is possible to identify a similar “sweet spot” in the parameter space for the variances of the incident Gaussian wavepackets, considering this is a one-parameter problem. However, it is also necessary to not only compare the amplitude of each individual echo with  $\sigma$ , but also the ratio between the amplitude of the echo with the amplitude of the transient for each value of the width, which is relevant since we are finding the relative intensity of the echoes compared to the strongest outgoing signal. To do so, we proceed as follows: we setup a logarithmic 1D grid of “thicknesses” centered at  $\sigma_{\text{DW}} = \sqrt{27}r_g/2\ell$  – the width for which the transmissivity is maximum according to the DeWitt approximation [82] – and spaced by factors of  $\sqrt{2}\sigma_{\text{DW}}$ . Then, we find the amplitudes of the first four echoes for every width of the incident pulse

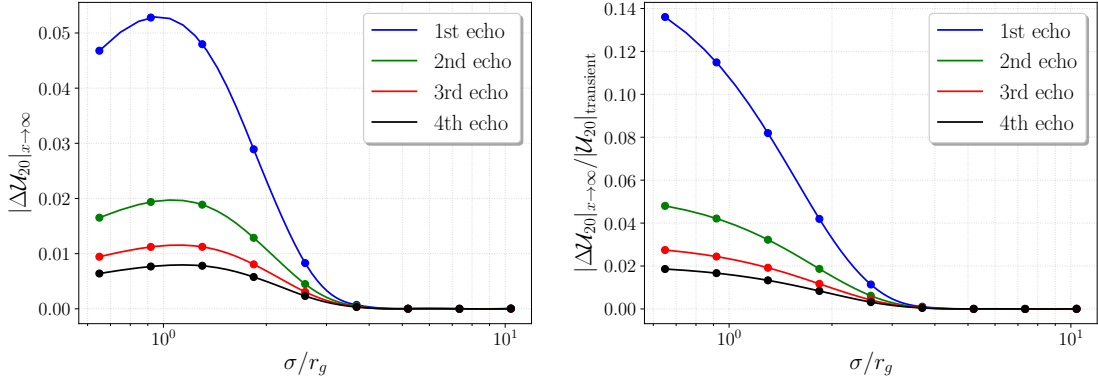


Figure 7.11: Left panel: Amplitudes of the first four echoes as a function of  $\sigma$  for  $\ell = 2$ , we observe the presence of a maximum amplitude of all the echoes at roughly  $\sigma \approx r_g$ , which is not incompatible with the de DeWitt approximation. Right panel: Relative amplitude of the first four echoes compared to the amplitude of the transient. The points represent the simulated wormhole/black hole pairs used in our analysis.

without changing the cavity. In order to determine the amplitudes of the echoes, we need to subtract the reflection coming from the scattering of a single barrier (i.e., the black hole case) by using the variable  $\Delta\mathcal{U}_{20}|_{\text{clean}}$ . This procedure requires a non-trivial computational effort since each scattering scenario needs to be solved twice (one for the wormhole and one for the black hole) in order to clean up the signal and obtain a clear view of the echoes. After refining the signal, we find the continuous envelope of the asymptotic solution by calculating its Hilbert transform [142], represented as the green curves in the upper corners of Figure 7.9, and therefore, the amplitudes of the echoes are the local maxima of these envelopes (the red dots in the same figure).

Our results can be found in Figure 7.11, where we notice in the left panel the presence of a well-defined maximal amplitude of the first four echoes. This is consistent with the idea of a range of frequencies/variances that maximize the amplitudes of the echoes, as shown in the analysis of the reflection and transmission coefficients: the cavity is transparent for small widths of the ingoing Gaussian (large frequencies) and is reflective for wide incident pulses. In the right panel, we observe the growth of the relative amplitude as the widths become smaller. Such a fact only means that the reduction of the transient is faster than the reduction of the echoes as the frequencies grow: as the cavity becomes more transparent the ingoing pulses get transmitted more efficiently. Consequently, this analysis is useful to get a basic understanding of the frequency/variance scales in which echoes could be observable.

## 7.2 Scattering of tensor wavepackets

Following the perspective of the even/odd parity decomposition for tensor perturbations of a spherically symmetric spacetime [207, 255, 201], we implement all the techniques used in

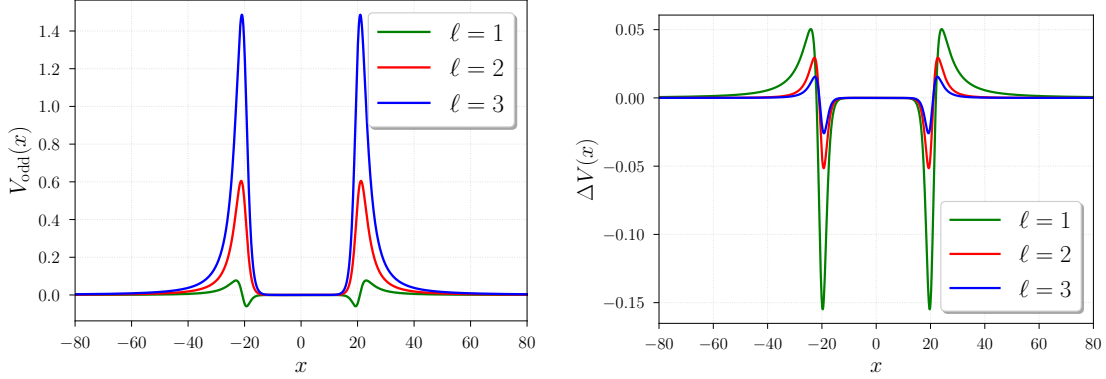


Figure 7.12: Left panel: Plot of the Regge-Wheeler potential as a function of the tortoise coordinate  $x$ . Right panel: Difference between the Regge-Wheeler and Zerilli effective potentials  $\Delta V = V_{\text{odd}} - V_{\text{even}}$ . The difference of the two potentials is below the order of 1% for ( $\ell \geq 2$ ).

section 7.1 and extend our analysis to study the scattering of a Gaussian test wavepacket of tensor perturbations. From now on, we will follow the conventions in [170], including the choice of the Regge-Wheeler gauge. The dynamics of the wave scattering problem is given by two equations of motion of the form

$$\left(\tilde{\square} - \mathcal{V}_{\text{eff}}\right) \Psi_{\ell m} = 0, \quad (7.14)$$

here  $\tilde{\square} \equiv g^{ab} \nabla_a \nabla_b$  is the 2D d'Alembertian operator in the usual  $(a, b) \rightarrow (t, r)$  Schwarzschild coordinates.  $\mathcal{V}_{\text{eff}}$  corresponds to one of two possible potentials, the Regge-Wheeler (odd) potential,  $\mathcal{V}_{\text{odd}}$

$$\mathcal{V}_{\text{odd}}(r) = \frac{\ell(\ell+1)}{r^2} - \frac{3r_g}{r^3}, \quad (7.15)$$

or the Zerilli (even) potential,  $\mathcal{V}_{\text{even}}$

$$\mathcal{V}_{\text{even}}(r) = \frac{1}{\Lambda^2} \left[ \mu^2 \left( \frac{\mu+2}{r^2} + \frac{3r_g}{r^3} \right) + \frac{9r_g^2}{r^4} \left( \mu + \frac{r_g}{r} \right) \right], \quad (7.16)$$

where  $\mu \equiv (\ell-1)(\ell+2)$  and  $\Lambda \equiv \mu + 3r_g/r$ . All the source terms proportional to the stress energy tensor and its contractions appearing in the right hand side of (7.14) in [170] are not considered for the scattering problem. The introduction of tortoise coordinates  $(t, x)$  is also very convenient and works in exactly the same way as in (7.3) and (7.4), in these coordinates the waveform of the two equations of motion – one for the odd parity modes and another for the even – is given by

$$\left[ -\partial_t^2 + \partial_x^2 - V_{\text{eff}}(x) \right] \Psi_{\ell m}(x, t) = 0, \quad (7.17)$$

where  $V_{\text{even}} \equiv [1 - r_g/r(|x|)]\mathcal{V}_{\text{even}}$  and  $V_{\text{odd}} \equiv [1 - r_g/r(|x|)]\mathcal{V}_{\text{odd}}$ . Recalling the procedure we previously followed in subsection 7.1.2; our setup already includes the effective potentials for the Morris-Thorne wormholes, obtained by reflection of the potential barriers about the ordinate axis. The effective potentials are plotted in the left panel of Figure 7.12, which is very similar to the one in the scalar scattering. In the right panel, it is possible to notice that the difference between the potentials is only substantial at  $(\ell \leq 1)$ . Both the even and odd solutions of (7.14) and (7.17) are already spherical modes used to find the two asymptotic polarizations of the tensor fluctuations propagating in a flat background, such as the term in the diagonal,  $h_+$

$$h_+ = \frac{1}{r(|x|)} \sum_{\ell,m} \left[ \Psi_{\ell m}^{\text{even}} \left( \partial_\theta^2 + \frac{1}{2}\ell(\ell+1) \right) - \Psi_{\ell m}^{\text{odd}} \frac{im}{\sin \theta} \left( \partial_\theta - \frac{\cos \theta}{\sin \theta} \right) \right] Y_{\ell m}(\theta, \phi), \quad (7.18)$$

and the off-diagonal,  $h_\times$

$$h_\times = \frac{1}{r(|x|)} \sum_{\ell,m} \left[ \Psi_{\ell m}^{\text{odd}} \left( \partial_\theta^2 + \frac{1}{2}\ell(\ell+1) \right) + \Psi_{\ell m}^{\text{even}} \frac{im}{\sin \theta} \left( \partial_\theta - \frac{\cos \theta}{\sin \theta} \right) \right] Y_{\ell m}(\theta, \phi). \quad (7.19)$$

From these expressions, it is simple to see that the the monopole ( $\ell = 0$ ) and the dipole ( $\ell = 1$ ) terms are identically zero. Thus, the first nontrivial contributions come from the quadrupole solutions  $\Psi_{20}^{\text{odd}}(x, t)$  and  $\Psi_{20}^{\text{even}}(x, t)$ , from which the differences in the odd and even potentials are small, and become even smaller for every  $\ell > 3$ , as we can see in right panel of Figure 7.12. Additionally, it is reasonable to identify  $h_+$  with the even mode and  $h_\times$  with the odd in the equatorial plane up to a constant. Hence, our analysis for the scattering dynamics and the reflected/transmitted frequencies does not require from both the even and odd solutions of (7.17) to extend the discussions from section 7.1. However, we will explain one of the consequences of the difference between the Regge-Wheeler and Zerilli potentials in section 7.3.

In analogy with the previous section, now we solve the equations of motion for the scattering process. Our setup for the initial conditions of  $\Psi_{20}^{\text{odd}}(x, 0)$  and  $\Psi_{20}^{\text{even}}(x, 0)$  and their time derivatives is not different from (7.8)

$$\begin{aligned} \Psi_{20}^{\text{odd}}(x, 0) &= \exp\left(\frac{(x-x_0)^2}{2\sigma^2}\right), \\ \partial_t \Psi_{20}^{\text{odd}}(x, t) \Big|_{t=0} &= \partial_x \Psi_{20}^{\text{odd}}(x, 0), \end{aligned} \quad (7.20)$$

and the same applies for  $\Psi_{20}^{\text{even}}$  and its initial time derivative. Using  $\sigma = 0.9185r_g$ , the same initial position of the Gaussian wavepackets – i.e.,  $x_0 = 60.0r_g$  – and the same separation between potential walls – i.e.,  $r_0 = 20.0r_g$  – as before. We show the evolution of  $\Psi_{20}^{\text{odd}}(x, t)$  in Figure 7.14, where the dispersion of the ingoing pulse is not significantly different from



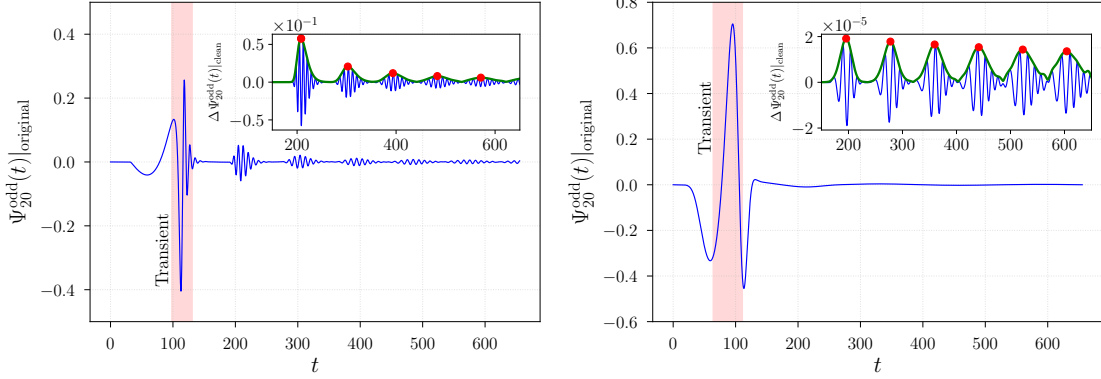


Figure 7.13: Left panel: Asymptotic solution of  $\Psi_{20}^{\text{odd}}$  considering an incident wavepacket with  $\sigma = 0.9185r_g$ . Asymptotic solution for  $\sigma = 5.196r_g$ , the amplitude of the echoes is now four orders of magnitude smaller than the transient.

our results in the left panel of Figure 7.8: this is not surprising due to the similarities between the shapes of the effective potentials for scalar and tensor modes, which seem to become even more similar for higher values of  $\ell$ . At late times, the cavity is filled showing an interference pattern. Internal reflections make the QNMs propagate for longer in the spheres of maximum effective potential.

In Figure 7.13, we observe the behavior of the asymptotic solutions for  $\sigma = 0.9185r_g$  (left panel) and  $\sigma = 5.196r_g$  (right panel). The magnitude of the echoes is not large in general, since it varies depending on the spectral content of the initial pulses, which are not the same in the case of initial Gaussian wavelets with different variances. In analogy with the scalar case, we notice in the upper corner of both figures that the amplitude of the echoes does not decay exponentially in time.

Frequency dependent reflection and transmission coefficients can be calculated by studying a scattering problem with a single potential wall, as we noticed in subsection 7.1.1, this is simply achieved by doing an algebraic inversion of the tortoise coordinate definition in (7.4): here the inverted function is evaluated in  $x - r_g$  instead of  $|x| - r_g$ . The definition of the reflectivity and transmissivity coefficients remains the same as in (7.9)

$$R(\omega) \equiv \frac{\|\tilde{\Psi}_{\text{ref}}^{\text{odd}}(\omega)\|}{\|\tilde{\Psi}_{\text{inc}}^{\text{odd}}(\omega)\|}, \quad T(\omega) \equiv \frac{\|\tilde{\Psi}_{\text{trans}}^{\text{odd}}(\omega)\|}{\|\tilde{\Psi}_{\text{inc}}^{\text{odd}}(\omega)\|}, \quad (7.21)$$

where we compute the one dimensional Fourier transforms of the incident  $\tilde{\Psi}_{\text{inc}}^{\text{odd}}(\omega) = \mathcal{F}[\Psi_{\text{bh}}^{\text{odd}}(x, 0)]$ , reflected  $\tilde{\Psi}_{\text{ref}}^{\text{odd}}(\omega) = \mathcal{F}[\Psi_{\text{bh}}^{\text{odd}}(+\infty, t)]$  and transmitted  $\tilde{\Psi}_{\text{trans}}^{\text{odd}}(\omega) = \mathcal{F}[\Psi_{\text{bh}}^{\text{odd}}(-\infty, t)]$ , where the label (bh) stands for the solutions of the scattering problem of (7.17) with a single potential barrier. These single barrier solutions are not only necessary for the study of the potential cavity, but also to clean up the low frequency (high  $\sigma$ ) solutions, since in those scenarios it is not simple to determine the amplitude of the echoes. All of the aforementioned definitions are also applicable for  $\Psi^{\text{even}}$ .

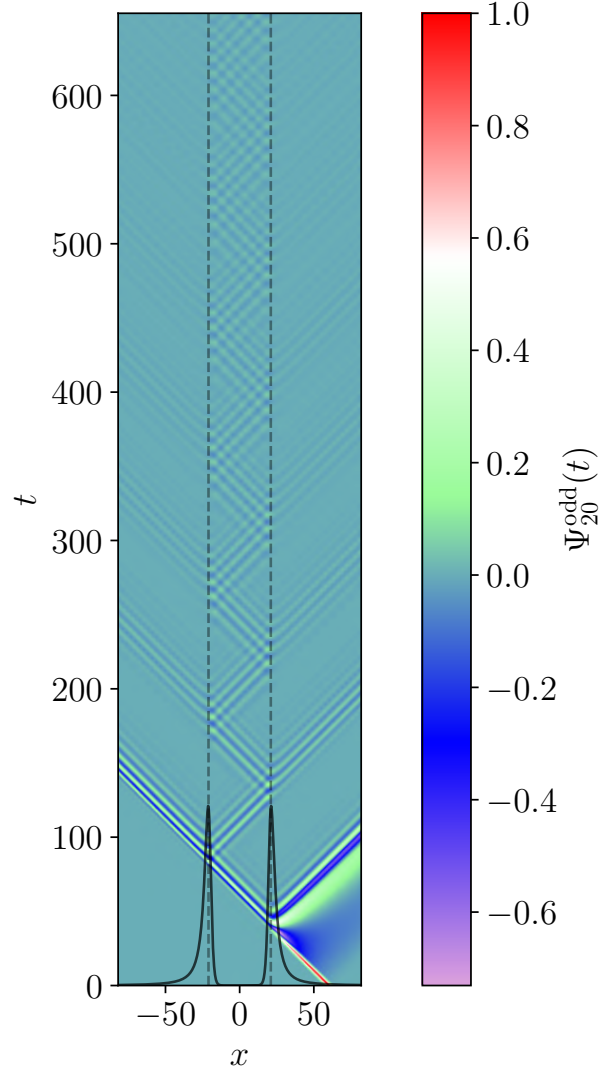


Figure 7.14: Evolution of  $\Psi^{\text{odd}}$  for an ingoing Gaussian pulse with  $\sigma = 0.9185r_g$ .

In the left panel of Figure 7.15, we show the reflection and transmission coefficients as functions of the frequency, noticing that the two curves intersect at  $R^2 = T^2 = 0.5$ , as expected. The identity  $R^2 + T^2$  is approximately satisfied. As a next step of our analysis, we reconstruct the Fourier transform of the asymptotic pulse shown in Figure 7.13. We employed the definition of the geometrical optics approximation in (7.12), applied up to  $i = 0$ , in the Fourier transform of the Gaussian incident wavepacket in order to obtain the reconstructed profile in the right panel of Figure 7.15. The signal reconstructed using the geometrical optics approximation provides a better representation of the total reflected pulse as the ingoing wavelet gets wider, and therefore, it has more power in lower frequencies.

Motivated by the drastic change in the amplitudes of the echoes seen in both panels of Figure 7.13, we now explore the dependence of the amplitude of each individual echo with the width of the incident Gaussian pulse. To do so, we follow the same procedure

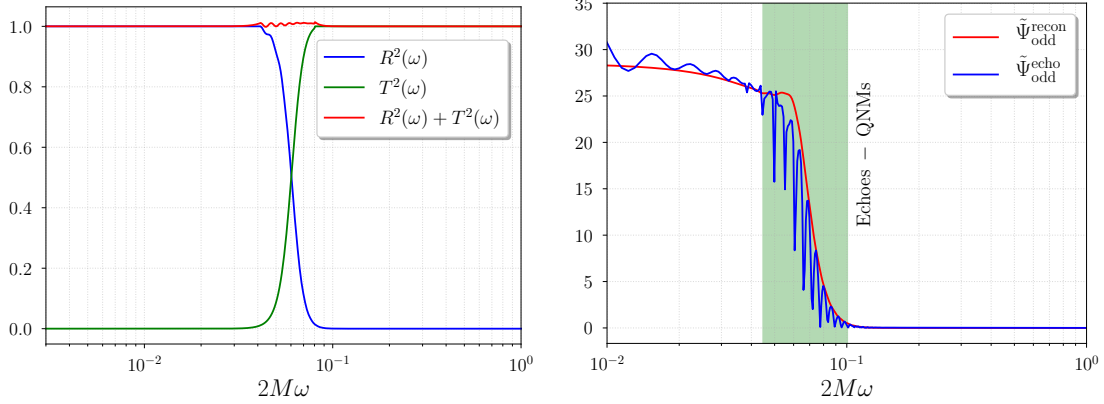


Figure 7.15: Left panel: Reflection and transmission coefficients for  $\sigma = 0.9185r_g$  and the quadrupole  $\ell, m = (2, 0)$ , the “sweet spot” in the frequency domain is located around the intersection at  $R^2 = T^2 = 0.5$ . Right panel: Geometrical optics reconstruction is plotted in red, and it is compared with the Fourier transform of the asymptotic solution shown in Figure 7.13. Ignoring the low frequency peaks (introduced by the finite size of the simulation box), we notice that the reconstructed spectrum provides a good idea of the overall shape, but it does not reproduce the power in the frequency of the QNMs. Our results are not dramatically different for the solutions of  $\Psi^{\text{even}}$ .

explained by the end of subsection 7.1.2: we construct a logarithmic grid in  $\sigma$ , centered at  $\sigma_{\text{DW}} = \sqrt{27}r_g/2\ell$  and spaced in intervals of  $\sqrt{2}\sigma_{\text{DW}}$ . In addition to this, we define the variable  $\Delta\Psi_{\text{clean}}^{\text{odd}} \equiv \Psi_{\text{original}}^{\text{odd}} - \Psi_{\text{bh}}^{\text{odd}}$  in order to clean the solutions from backscattering effects coming from the potential tails, which complicate the task of determining the amplitudes of the echoes with high  $\sigma$ /low frequency. Once the solutions are clean, the most effective way to find the maxima of each echo is by calculating the corresponding local maxima of the Hilbert envelope for the clean signal. In this case, the Hilbert envelopes are the green curves in the upper corner of the two panels in Figure 7.13, and the maxima are indicated by the red dots on top of each curve. This task is even more computationally expensive than in the scalar case, not only because we are solving the scattering problem for two systems – one with a single potential barrier and another with the potential cavity – but also we are now working with the two polarizations (i.e., the even and odd solutions). Our results of the amplitude analysis in Figure 7.16 show the existence of a value of  $\sigma$  maximizing the amplitude of the echoes. This finding is compatible with the notion of a band of widths/frequencies in which the echoes have sufficient amplitude to be measured.

It is reasonable to consider the length of the throat for a Morris-Thorne wormhole as a parameter modulating the echoes solutions. Thus, we rerun our simulation to consider the scattering of a Gaussian pulse with  $\sigma = 16 r_g$  by a wormhole with a larger throat (with a length of  $100 r_g$ , which is more than two times larger than the cavity used in the previous configuration). In the main panel of Figure 7.17, we show that the transient has a

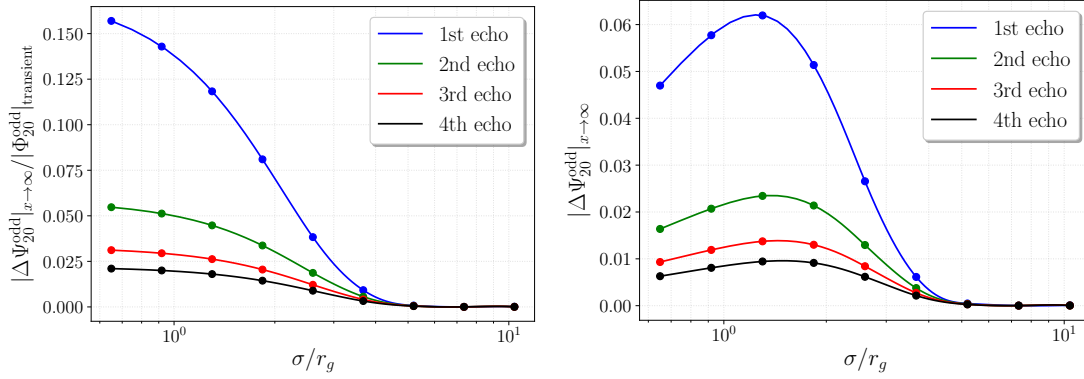


Figure 7.16: Left panel: Amplitudes of the first four echoes of  $\Psi_{20}^{\text{odd}}$  as a function of  $\sigma$  for  $\ell = 2$ . Right panel: Relative amplitude of the first four echoes compared to the amplitude of the transient. The points represent the simulated double/single wall pairs used in our analysis, as in Figure 7.11. These results are not significantly different for  $\Psi_{20}^{\text{even}}$ . At low variances, the transient decreases faster than the amplitudes of the echoes as  $\sigma$  becomes smaller.

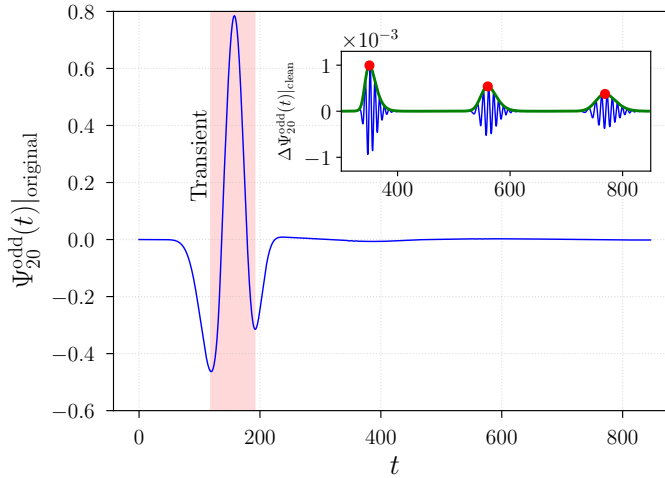


Figure 7.17: Asymptotic solution of an ingoing Gaussian pulse with  $\sigma = 16 r_g$  after its dispersion by a Morris-Thorne wormhole with a longer throat (with a length of  $100 r_g$ ). The amplitude of the transient is three orders of magnitude larger than the first echo, showing that the echoes do not have a generically large magnitude.

slightly larger magnitude: this is consistent with an increase of the wall reflectivity at lower frequencies seen in the left panel of Figure 7.15. Each of these potential barriers has the same shape of the potential barrier as in the scenario depicted in Figure 7.12, it is, therefore, still possible to find a frequency “sweet spot” for each wall. In the upper corner of Figure 7.17, we find that the amplitude of the echoes is three orders of magnitude smaller than the transient, after removing all backscattering effects from the signal. In the same figure, we

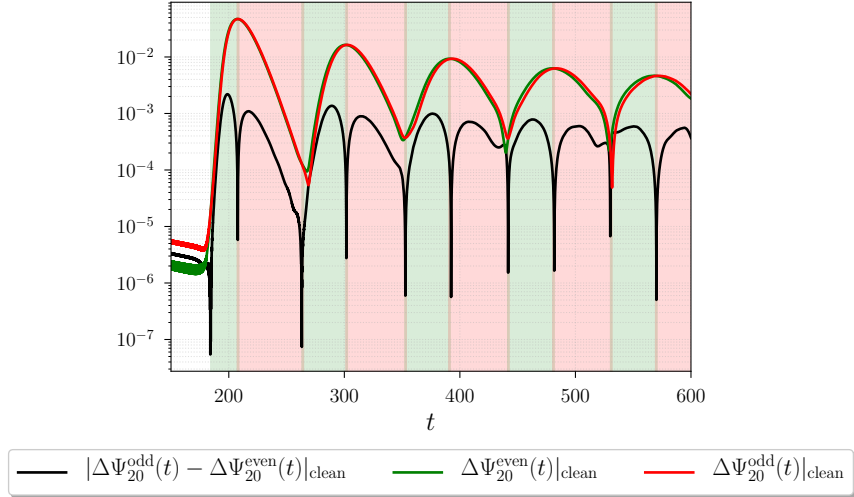


Figure 7.18: Since the phases of the asymptotic solutions are random, we compare the Hilbert envelopes of the two clean solutions for echoes. The outgoing envelopes have a small relative phase shift due to the difference in the potentials, inducing a net even ( $h_+$ ) polarization in the intervals shaded in green, and an odd ( $h_\times$ ) polarization in the intervals shaded in red. Therefore, the cavity is analog to an optically active medium changing the polarization of the ingoing Gaussian wavepacket.

notice that the time separation between echoes coincides with the time elapsed after two internal reflections, being greater than the time breach between echoes seen in Figures 7.9 and 7.13.

### 7.3 Echoes and gravitational wave polarimetry

The small difference in the Zerilli (even) and Regge-Wheeler (odd) potentials is shown in the right panel of Figure 7.12 has a particular effect in the outgoing waves. In order to illustrate it, we will just work with the even and odd quadrupole signals in the equatorial plane. In the case of a generic spherical mode with equal contributions from  $\Psi_{20}^{\text{odd}}$  and  $\Psi_{20}^{\text{even}}$ , which are the first nontrivial contributions to (7.18) and (7.19), we notice that the two polarizations are reduced to

$$h_+(x, t) = \frac{C_\theta}{r(|x|)} \Psi_{20}^{\text{even}}(x, t) \quad , \quad h_\times(x, t) = \frac{C_\theta}{r(|x|)} \Psi_{20}^{\text{odd}}(x, t), \quad (7.22)$$

where  $C_\theta$  is a constant coming from the normalized spherical harmonics evaluated at  $\theta = \pi/2$ . Considering  $\sigma = 0.6495r_g$ , the parameters of the cavity used in sections 7.1 and 7.2 and the same initial Gaussian pulses for  $\Psi_{20}^{\text{even}}(x, t)$  and  $\Psi_{20}^{\text{odd}}(x, t)$ . As can be noticed in Figure 7.18, we show that the difference between the potentials induces a relative phase between the odd and even solutions, generating an outgoing wave with a net polarization oscillating from even ( $h_+$ ) to odd ( $h_\times$ ) and only visible after the transient. It is interesting to notice

that these small effects are present even when the target is spherically symmetric. Spin-orbit coupling between the spin-2 gravitational perturbations and the angular momentum in Kerr-like solutions might enhance the polarization effects.

## 7.4 Discussion

In this chapter, we studied the scattering of a test scalar and tensor wavepacket on a Morris-Thorne wormhole, which is the purest realization of an effective potential cavity with two walls. Using a Gaussian pulse as an incident initial condition, we showed the time-dependent scattering solution of the quadrupole spherical modes of tensor and scalar radiation, both were computed inside and outside the potential cavities in Figures 7.8 and 7.14, which reflect and transmit throughout the cavity. Furthermore, after finding the transmission and reflection coefficients of the cavities in Figure 7.4 and in the left panel of Figure 7.15, we used the geometrical optics approximation to reconstruct the shape of the Fourier-transformed asymptotic solutions in Figure 7.10 and in the right panel of Figure 7.15. We find that the reconstructed shape of the spectrum is accurate, without showing, however, the QNM peaks.

We show that in general, the echoes do not have a large amplitude as we can see directly in the left panel of Figure 7.9 and in the right panel of Figure 7.13, where we also observe that the amplitude of the echoes does not decay exponentially in time. In addition to this, we found that there is a thin band of preferred frequencies (and the widths of the corresponding ingoing Gaussian signals) where the amplitude of echoes is maximum. Such a frequency band is centered around the “sweet spot” where the coefficients of transmissivity and reflectivity overlap, and it is also where the QNMs peaks are squeezed in. We extended our analysis to find the range in which the variance of the incident pulses maximize the amplitude of the first four echoes, and how large is their amplitude compared to the transient. For small widths this ratio could be as large as 15%, we should notice, however, that the amplitude of the transient gets also suppressed in this range. In Figures 7.11 and 7.16, note that for low thicknesses of the ingoing signal, as the peaks become sharper, the transient decreases faster than the amplitude of the echoes. In the study of the gravitational wave scattering by a Morris-Thorne wormhole, we find small differences between the Regge-Wheeler and the Zerilli effective potentials, as depicted in the right panel of Figure 7.12. As it is visible in Figure 7.18, such a difference modifies the polarization of every incident wave in a way analogous to the dispersion across an optically active medium, opening the possibility of studying gravitational wave polarimetry.

# Chapter 8

## Concluding remarks

In this thesis, we developed several realizations of EFTs relevant at astrophysical and cosmological scales. In part I we focused on the dynamics of scalar and tensor perturbations in the early universe. Concretely, we explored two variants of the inflationary action: an example of a single-field model dubbed as Constant-Roll Inflation as suggested in [178] in Chapter 2, in addition to double  $\lambda\phi^4$  and double quadratic inflation as examples of multi-field inflation in Chapter 3.

In Chapter 2, we developed a method to evolve scalar and tensor perturbations of Constant-Roll Inflation, based on the dynamical separation of fast and slow scales from equations of motion. Introducing the separation of scales is useful since it is known that the phases – which require from small time steps to be resolved – are not needed to find the two-point correlation functions. The outcome of this separation results in the derivation of the Ermakov-Pinney equation of motion (2.11) for the amplitudes of the scalar and tensor fluctuations. Hence, we developed an efficient numerical routine able to evolve multiple field realizations corresponding to different choices of model parameters and computes correlation functions for every point in parameter space. Constraining Constant-Roll Inflation requires from direct calculations of the scalar and tensor spectra since the purpose of this model is to parametrize deviations from the slow-roll approximation, and the analytic expressions for the tensor-to-scalar ratio  $r$  and the spectral tilt  $n_s$  [122] are only applicable within the slow-roll regime. Using the likelihood results from the joint likelihood obtained by the Planck Collaboration in [6, 10, 9], our results show that  $\log_{10} \beta = -1.76_{-0.29}^{+0.16}$  at 95% C.L., which validates the notion of small deviations from the slow-roll conditions. Furthermore, we show that the perturbative regime for curvature breaks at  $\beta \approx 0.1$ .

In Chapter 3, we generalized the separation technique of fast and slow scales in scalar and tensor perturbations implemented in Chapter 2 to also consider models with multiple scalar fields. In this case, we factorize the two-point correlation matrix into two Cholesky – i.e., lower-triangular – matrices. Furthermore, we can use the same Cholesky factors to write

the fields as a product of the amplitude matrices, with a vector of unit-variance Gaussian random variables representing the phases. Figure 3.7 shows the reduction of the effective oscillation frequency after solving the equations for the lower-triangular amplitude matrices (3.17), the phases (3.20) and the auxiliary phase correlators (3.21). Here we notice that it is possible to increase the time step needed to resolve the amplitude matrices by a factor of 30. We considered the time-translational invariance of Bunch-Davies vacuum, which provides initial conditions to inject from a constant physical length deep inside subhorizon scales. It is, therefore, feasible to use this symmetry to reduce the evaluation time of all the modes, in particular those with high- $k$ . Our results for the spectra of scalar perturbations are consistent with the results in [42, 137]. The generality of this separation was further expanded to consider the propagation of perturbations in a curved field geometry represented in Appendix B. In addition to this, this formalism can be used in a myriad of cases including linear systems of ODE's, such as the perturbative analysis of curvature and tensor modes in other early-universe scenarios.

Our discussions also extend to alternatives to the inflationary paradigm in Chapter 4, where we studied the Ijjas-Steinhardt (IS) bouncing cosmology sourced by a cubic Galileon [139]. We derived and discussed the main equations for the dynamics of the cosmological background and perturbations. In addition to this, we briefly discussed the notion of an induced acoustic geometry for cosmological perturbations, introduced convenient variables and calculated their relations by different gauge and conformal transformations. We revealed the structure of the Lagrangian for this bouncing model, by deriving the functions  $k(\phi)$  and  $q(\phi)$  of the theory in (4.46) – (4.49). Using these results, we studied the *IS-bounce* for the first set of parameters, finding that the bouncing solution in this case starts with a divergent sound speed around  $15 t_{\text{Pl}}$  before the null-energy condition (NEC) violation starts. The sound speed is still superluminal less than  $10 t_{\text{Pl}}$  before the beginning of the NEC violation phase, restricting the possibility of UV completion at tree level due to the unphysical negative cross sections [7]. The system enters into the strongly coupled regime when the sound speed vanishes, and the curvature fluctuations injected at that instant cannot be treated perturbatively. Classically, the trajectory suggested by Ijjas and Steinhardt begins with a singularity of the acoustic metric and ends in another singularity. We described the phase space structure in this model, where it is possible to notice that the IS-bouncing trajectory is a separatrix. In addition to this, in Appendix D, we use the methods developed in Chapters 2 and 3 to calculate the power spectrum of primordial scalar and tensor fluctuations and the particle production rate for scalars. We found that none of these spectra is scale invariant at the end of the bouncing stage. Moreover, we see that the change of the speed of sound suppresses the power of scalar fluctuations to the point it becomes subdominant when compared to the power of tensors, which is not consistent with



the observational evidence.

In part II, we discuss the effects of modifications in the gravitational field emerging from deformations of the canonical variables present in the gravitational action, semiclassical field equations or higher-curvature corrections to the Einstein-Hilbert action. In Chapter 5, we studied the modifications of the action generated by deforming the canonical variables and the consistency of the gravitational constraint algebra. In Chapter 6, we evaluate the scalar accretion of spherical waves in Schwarzschild black holes. Such scalars are the extra degrees of freedom appearing in theories with an action modified by higher-curvature corrections. In Chapter 7, we provide dynamical solutions of the scattering problem for scalar and gravitational radiation colliding against a Misner-Thorne wormhole, which is the most straightforward realization of a spherical system with a partially reflective cavity. The asymptotic limit of these dynamical solutions show a train of wavelets (also known as echoes) after the scattering transient.

Motivated by the deformations introduced by holonomy corrections [236, 41, 62] in the gravitational canonical variables of Loop Quantum Gravity, in Chapter 5 we studied the consistency of the constraint algebra after deforming both the Einstein-Hilbert and the tetrad-Palatini actions through their canonical variables. Our objective was to explore if the consistency of the algebra, yielding a healthy semiclassical limit, can constrain the structure of the deformations. In the case of the variable deformations in the Einstein-Hilbert action, the preservation of the original number of degrees of freedom unavoidably leads us into Lovelock’s theorem, which restricts these deformations to be canonical transformations. Otherwise, the deformations of the canonical variables will induce higher-derivative terms that increase the number of degrees of freedom. We introduced an example where the modifications of the metric are traceless and symmetric, mimicking potential graviton corrections. In this example, the new Hamiltonian in (5.49) demands further constraints on the deformations, which are necessary in order to hold both the scalar and vector constraints independent from the gauge choice. The evaluation of these constraints can only have two possible outcomes: the deformations can either remove the extra degrees of freedom from the generators of the diffeomorphism group, or break some of them by reinterpreting the extra fields as if these were “Goldstone modes”.

Similarly, we extended this scheme for the tetrad-Palatini and Ashtekar-Barbero actions. In this case, we used the holonomy corrections as sources of the deformations. The scenario presented is similar in the sense of the possible introduction of extra degrees of freedom in the system. We derived the new constraints and the effects of the deformations in the tetrad variables in the cases when extra degrees of freedom appear (or not) in the system. If the deformations do not alter the gauge orbits set by the shift and lapse functions, there is no reason to expect a different realization of the constraint algebra and the deformations can

be constrained to produce stable gauge fixing. One can intuitively summarize our results in this chapter in the language of symplectic manifolds: given a  $D$ -dimensional symplectic manifold, it is possible to construct at least one other  $(D + 2N)$ -dimensional symplectic manifold ( $2N < D$ ) such that the original manifold is a projection of the constructed one.

After learning about the addition of extra degrees of freedom in modified theories of gravity, in Chapter 6 we resolved the dynamical properties of these fields for the so-called scalar-tensor theories. The gravitational sector of the action in those cases can include higher powers of the Ricci curvature. Due to the small backreaction of the extra scalar field on the metric, it is safe to assume that the geometry does not change throughout the evolution of the additional scalar (dubbed as scalaron). In this chapter, we describe the dynamics of scalar accretion onto a Schwarzschild black hole in the presence of a static matter distribution modelled by (6.3). In particular, we studied the accretion of the scalarons appearing in two models of  $f(R)$  gravity, the Starobinsky and Hu-Sawicki model, as well as in the symmetron and Ratra-Peebles models. Stable convergence to static scalar hair profiles results from varying parameters for each specific model. In the cases of the Starobinsky and Hu-Sawicki model, we can obtain dynamical chameleon solutions with curvature singularities outside horizon without requiring an infinite energy budget. In the case of accreting symmetrons, it is not always possible to form a non-trivial static solution (known as scalar “hair”) since it depends on the strength of the coupling with matter. Even when the simulations of astrophysical rotating black holes suggest a large density contrast, we noticed that the formation of non-trivial static solutions does not require an absolute vacuum environment close to the black hole’s event horizon, where  $r \in (r_g, r_{\text{ISCO}}]$ .

We discuss the possibility of a non-negligible ratio between the radiated power from extra scalar sources and the quadrupole gravitational radiation in GR, which might be testable by the future generation of gravitational-wave detectors. In our approach, apart from calculating static solutions in various circumstances, we evaluated the scalar accretion dynamically in such a way that it is possible to converge to a hairy or a “bald” solution, depending on the model and its parameters. These results also motivate further explorations on the effect of fifth forces confined by screening, surrounded by a non-trivial matter profile for merging binary systems.

In Chapter 7, we studied the scattering of Gaussian wavepackets of scalar and tensor radiation onto a Morris-Thorne wormhole. Using a Gaussian wavelet with arbitrary variance as an incident initial condition, we showed the time-dependent scattering solution of the quadrupole spherical modes of tensor and scalar radiation; both were computed inside and outside the potential cavities as these reflect and transmit through each of the cavity walls. Moreover, after finding the transmission and reflection coefficients, we used the geometrical optics approximation to reconstruct the envelope shape of the Fourier-transformed

asymptotic solutions. We observe that the reconstructed form of the spectrum is accurate, without showing, however, the peaks from the quasinormal modes (QNMs). We show that in general, the amplitude of the isolated train of echoes is not significant.

Moreover, we also observe that the magnitude of the echoes does not decay exponentially with time: QNMs are sourced by every internal reflection while leaking energy to the exterior through the emission of echoes. We found a thin band of preferred frequencies (and the widths of the corresponding ingoing Gaussian signals) where the magnitude of echoes is maximum. Such an interval is centered around a “sweet spot” in frequency space located where the coefficients of transmissivity and reflectivity overlap, and it is also the center of the interval where QNMs peaks are confined. We extended our analysis to find the range in which the variance of the incident pulses maximizes the amplitude of the first four echoes, and how large is their magnitude compared to the transient. For small variances, this ratio could be as large as 15%. It is important to notice, however, that the transient also gets suppressed in this range.

In the specific case of the scattering by a Morris-Thorne wormhole, we find a small difference between the Regge-Wheeler and the Zerilli effective potentials. Such a difference modifies the polarization of every incident wave in a way analog to the dispersion across an optically active medium, opening the possibility of studying gravitational wave polarimetry.

We expect that the progress achieved in this thesis will be used in major cosmological surveys of the CMB [13], where it is now possible to consider multifield inflationary models. The use of more sophisticated simulation tools will also be beneficial to study semiclassical effects in gravity beyond spherical symmetry. The possibility of exploring modified theories of gravity and other semiclassical manifestations (such as wormholes, firewalls and gravastars), where we can investigate the formation of stable exotic compact solutions. The connections between gravity and thermodynamics can also be further explored by understanding the non-linear nature of equations of motion as a source of entropy [146].

# Bibliography

- [1] B. P. Abbott et al. GW151226: Observation of Gravitational Waves from a 22-Solar-Mass Binary Black Hole Coalescence. *Phys. Rev. Lett.*, 116(24):241103, 2016.
- [2] B. P. Abbott et al. Observation of Gravitational Waves from a Binary Black Hole Merger. *Phys. Rev. Lett.*, 116(6):061102, 2016.
- [3] Jahed Abedi and Niayesh Afshordi. Echoes from the Abyss: A highly spinning black hole remnant for the binary neutron star merger GW170817. 2018.
- [4] Jahed Abedi, Hannah Dykaar, and Niayesh Afshordi. Echoes from the Abyss: Tentative evidence for Planck-scale structure at black hole horizons. *Phys. Rev.*, D96(8):082004, 2017.
- [5] Marek A. Abramowicz and P. Chris Fragile. Foundations of Black Hole Accretion Disk Theory. *Living Rev. Rel.*, 16:1, 2013.
- [6] R. Adam et al. Planck 2015 results. I. Overview of products and scientific results. *Astron. Astrophys.*, 594:A1, 2016.
- [7] Allan Adams, Nima Arkani-Hamed, Sergei Dubovsky, Alberto Nicolis, and Riccardo Rattazzi. Causality, analyticity and an IR obstruction to UV completion. *JHEP*, 0610:014, 2006.
- [8] P. A. R. Ade et al. Joint Analysis of BICEP2/Keck Array and Planck Data. *Phys. Rev. Lett.*, 114:101301, 2015.
- [9] P. A. R. Ade et al. Planck 2015 results. XIII. Cosmological parameters. *Astron. Astrophys.*, 594:A13, 2016.
- [10] P. A. R. Ade et al. Planck 2015 results. XX. Constraints on inflation. *Astron. Astrophys.*, 594:A20, 2016.
- [11] P. A. R. Ade et al. BICEP2 / Keck Array X: Constraints on Primordial Gravitational Waves using Planck, WMAP, and New BICEP2/Keck Observations through the 2015 Season. *Submitted to: Phys. Rev. Lett.*, 2018.
- [12] N. Aghanim et al. Planck 2018 results. VI. Cosmological parameters. 2018.
- [13] James Aguirre et al. The Simons Observatory: Science goals and forecasts. *JCAP*, 1902:056, 2019.
- [14] Y. Akrami et al. Planck 2018 results. I. Overview and the cosmological legacy of Planck. 2018.

- [15] Y. Akrami et al. Planck 2018 results. X. Constraints on inflation. 2018.
- [16] Andreas Albrecht and Paul J. Steinhardt. Cosmology for grand unified theories with radiatively induced symmetry breaking. *Phys. Rev. Lett.*, 48:1220–1223, Apr 1982.
- [17] Ahmed Almheiri, Donald Marolf, Joseph Polchinski, and James Sully. Black Holes: Complementarity or Firewalls? *JHEP*, 02:062, 2013.
- [18] Nils Andersson and Staffan Linnæus. Quasinormal modes of a schwarzschild black hole: Improved phase-integral treatment. *Phys. Rev. D*, 46:4179–4187, Nov 1992.
- [19] K. Andrzejewski. Hamiltonian formalisms and symmetries of the Pais-Uhlenbeck oscillator. *Nucl. Phys.*, B889:333–350, 2014.
- [20] Lilia Anguelova, Peter Suranyi, and L. C. Rohana Wijewardhana. Systematics of Constant Roll Inflation. *JCAP*, 1802(02):004, 2018.
- [21] Stephen A. Appleby, Richard A. Battye, and Alexei A. Starobinsky. Curing singularities in cosmological evolution of F(R) gravity. *JCAP*, 1006:005, 2010.
- [22] C. Armendariz-Picon, T. Damour, and Viatcheslav F. Mukhanov. k-Inflation. *Phys. Lett.*, B458:209–218, 1999.
- [23] C. Armendariz-Picon and Eugene A. Lim. Haloes of k-essence. *JCAP*, 0508:007, 2005.
- [24] C. Armendariz-Picon, Viatcheslav F. Mukhanov, and Paul J. Steinhardt. A dynamical solution to the problem of a small cosmological constant and late-time cosmic acceleration. *Phys. Rev. Lett.*, 85:4438–4441, 2000.
- [25] C. Armendariz-Picon, Viatcheslav F. Mukhanov, and Paul J. Steinhardt. Essentials of k-essence. *Phys. Rev.*, D63:103510, 2001.
- [26] Richard L. Arnowitt, Stanley Deser, and Charles W. Misner. The Dynamics of general relativity. *Gen. Rel. Grav.*, 40:1997–2027, 2008.
- [27] B. Audren, J. Lesgourgues, K. Benabed, and S. Prunet. Conservative constraints on early cosmology with MONTE PYTHON. *JCAP*, 2:001, February 2013.
- [28] Anastasios Avgoustidis, Sera Cremonini, Anne-Christine Davis, Raquel H. Ribeiro, Krzysztof Turzyski, and Scott Watson. The Importance of Slow-roll Corrections During Multi-field Inflation. *JCAP*, 1202:038, 2012.
- [29] Eugeny Babichev and Christos Charmousis. Dressing a black hole with a time-dependent Galileon. *JHEP*, 08:106, 2014.
- [30] Eugeny Babichev, Christos Charmousis, Antoine Lehébel, and Tetiana Moskalaets. Black holes in a cubic Galileon universe. *JCAP*, 1609(09):011, 2016.
- [31] Eugeny Babichev, Viatcheslav Mukhanov, and Alexander Vikman. k-Essence, superluminal propagation, causality and emergent geometry. *JHEP*, 02:101, 2008.
- [32] James M. Bardeen, J. R. Bond, Nick Kaiser, and A. S. Szalay. The Statistics of Peaks of Gaussian Random Fields. *Astrophys. J.*, 304:15–61, 1986.

- [33] Neil Barnaby. On Features and Nongaussianity from Inflationary Particle Production. *Phys. Rev.*, D82:106009, 2010.
- [34] Lorenzo Battarra, Michael Koehn, Jean-Luc Lehners, and Burt A. Ovrut. Cosmological Perturbations Through a Non-Singular Ghost-Condensate/Galileon Bounce. *JCAP*, 1407:007, 2014.
- [35] D. Battefeld and Patrick Peter. A Critical Review of Classical Bouncing Cosmologies. *Phys. Rept.*, 571:1–66, 2015.
- [36] R Beig and O. Murchadha. The Poincare group as the symmetry group of canonical general relativity. *Annals Phys.*, 174:463–498, 1987.
- [37] J. D. Bekenstein. Novel “no-scalar-hair” theorem for black holes. *Phys. Rev.*, D51(12):R6608, 1995.
- [38] Jose Beltran Jimenez, Lavinia Heisenberg, Gonzalo J. Olmo, and Diego Rubiera-Garcia. Born-Infeld inspired modifications of gravity. *Phys. Rept.*, 727:1–129, 2018.
- [39] D. Blas, J. Lesgourgues, and T. Tram. The Cosmic Linear Anisotropy Solving System (CLASS). Part II: Approximation schemes. *JCAP*, 7:034, July 2011.
- [40] Martin Bojowald, Suddhasattwa Brahma, Umut Buyukcam, and Michele Ronco. Extending general covariance: Moyal-type noncommutative manifolds. *Phys. Rev.*, D98(2):026031, 2018.
- [41] Martin Bojowald, Suddhasattwa Brahma, and Juan D. Reyes. Covariance in models of loop quantum gravity: Spherical symmetry. *Phys. Rev.*, D92(4):045043, 2015.
- [42] J. Richard Bond, Andrei V. Frolov, Zhiqi Huang, and Lev Kofman. Non-Gaussian Spikes from Chaotic Billiards in Inflation Preheating. *Phys. Rev. Lett.*, 103:071301, 2009.
- [43] J. B. Boyd. Chebyshev and Fourier Spectral Methods. 2001.
- [44] Suddhasattwa Brahma and Michele Ronco. Constraining the loop quantum gravity parameter space from phenomenology. *Phys. Lett.*, B778:184–189, 2018.
- [45] Suddhasattwa Brahma, Michele Ronco, Giovanni Amelino-Camelia, and Antonino Marciano. Linking loop quantum gravity quantization ambiguities with phenomenology. *Phys. Rev.*, D95(4):044005, 2017.
- [46] Robert Brandenberger and Patrick Peter. Bouncing Cosmologies: Progress and Problems. *Found. Phys.*, 47(6):797–850, 2017.
- [47] C. Brans and R. H. Dicke. Mach’s principle and a relativistic theory of gravitation. *Phys. Rev.*, 124:925–935, Nov 1961.
- [48] Philippe Brax, Carsten van de Bruck, Anne-Christine Davis, and Douglas J. Shaw. f(R) Gravity and Chameleon Theories. *Phys. Rev.*, D78:104021, 2008.
- [49] D. J. Brooker, N. C. Tsamis, and R. P. Woodard. Precision Predictions for the Primordial Power Spectra of Scalar Potential Models of Inflation. *Phys. Rev.*, D93(4):043503, 2016.

- [50] Jean-Philippe Bruneton. On causality and superluminal behavior in classical field theories. Applications to k-essence theories and MOND-like theories of gravity. *Phys. Rev.*, D75:085013, 2007.
- [51] Jean-Philippe Bruneton and Gilles Esposito-Farese. Field-theoretical formulations of MOND-like gravity. *Phys. Rev.*, D76:124012, 2007.
- [52] I. L Buchbinder and S. L Lyakhovich. Hamiltonian formulation of theories with higher derivatives. *Sov. Phys. J*, 28(9):746, 1985.
- [53] I. L. Buchbinder and S. L. Lyakhovich. Canonical Quantization and Local Measure of  $R^{*2}$  Gravity. *Class. Quant. Grav.*, 4:1487–1501, 1987.
- [54] C. P. Burgess. The Cosmological Constant Problem: Why it’s hard to get Dark Energy from Micro-physics. In *Proceedings, 100th Les Houches Summer School: Post-Planck Cosmology: Les Houches, France, July 8 - August 2, 2013*, pages 149–197, 2015.
- [55] C. P. Burgess, Ryan Plestid, and Markus Rummel. Effective Field Theory of Black Hole Echoes. *JHEP*, 09:113, 2018.
- [56] Clare Burrage, Claudia de Rham, Lavinia Heisenberg, and Andrew J. Tolley. Chronology Protection in Galileon Models and Massive Gravity. *JCAP*, 1207:004, 2012.
- [57] J. C. Butcher. Implicit Runge-Kutta processes. *Mathematics of Computation*, 18:50–64, 1964.
- [58] Yi-Fu Cai, Xingang Chen, Mohammad Hossein Namjoo, Misao Sasaki, Dong-Gang Wang, and Ziwei Wang. Revisiting non-Gaussianity from non-attractor inflation models. *JCAP*, 1805(05):012, 2018.
- [59] Yong Cai, Youping Wan, Hai-Guang Li, Taotao Qiu, and Yun-Song Piao. The Effective Field Theory of nonsingular cosmology. *JHEP*, 01:090, 2017.
- [60] Gianluca Calcagni and Michele Ronco. Deformed symmetries in noncommutative and multifractional spacetimes. *Phys. Rev.*, D95(4):045001, 2017.
- [61] Robert R. Caldwell and Michael Doran. Dark-energy evolution across the cosmological-constant boundary. *Phys.Rev.*, D72:043527, 2005.
- [62] Miguel Campiglia, Rodolfo Gambini, Javier Olmedo, and Jorge Pullin. Quantum self-gravitating collapsing matter in a quantum geometry. *Class. Quant. Grav.*, 33(18):18LT01, 2016.
- [63] Vitor Cardoso, Edgardo Franzin, and Paolo Pani. Is the gravitational-wave ringdown a probe of the event horizon? *Phys. Rev. Lett.*, 116(17):171101, 2016. [Erratum: *Phys. Rev. Lett.* 117, no. 8, 089902 (2016)].
- [64] Vitor Cardoso, Seth Hopper, Caio F. B. Macedo, Carlos Palenzuela, and Paolo Pani. Gravitational-wave signatures of exotic compact objects and of quantum corrections at the horizon scale. *Phys. Rev.*, D94(8):084031, 2016.
- [65] W. F. Chagas-Filho. Loop Quantum Gravity in the Momentum Representation. 2017.

- [66] Anthony Challinor and Antony Lewis. Lensed CMB power spectra from all-sky correlation functions. *Phys. Rev.*, D71:103010, 2005.
- [67] S. Chandrasekhar and Steven L. Detweiler. The quasi-normal modes of the Schwarzschild black hole. *Proc. Roy. Soc. Lond.*, A344:441–452, 1975.
- [68] Tai-jun Chen, Matteo Fasiello, Eugene A. Lim, and Andrew J. Tolley. Higher derivative theories with constraints: Exorcising Ostrogradski’s Ghost. *JCAP*, 1302:042, 2013.
- [69] Timothy Clifton, Pedro G. Ferreira, Antonio Padilla, and Constantinos Skordis. Modified Gravity and Cosmology. *Phys. Rept.*, 513:1–189, 2012.
- [70] Randy S. Conklin, Bob Holdom, and Jing Ren. Gravitational wave echoes through new windows. *Phys. Rev.*, D98(4):044021, 2018.
- [71] Paolo Creminelli, Kurt Hinterbichler, Justin Khoury, Alberto Nicolis, and Enrico Trincherini. Subluminal Galilean Genesis. *JHEP*, 1302:006, 2013.
- [72] Paolo Creminelli, Alberto Nicolis, and Enrico Trincherini. Galilean Genesis: An Alternative to inflation. *JCAP*, 1011:021, 2010.
- [73] Paolo Creminelli, David Pirtskhalava, Luca Santoni, and Enrico Trincherini. Stability of Geodesically Complete Cosmologies. *JCAP*, 1611(11):047, 2016.
- [74] Anne-Christine Davis, Ruth Gregory, and Rahul Jha. Black hole accretion discs and screened scalar hair. *JCAP*, 1610(10):024, 2016.
- [75] Anne-Christine Davis, Ruth Gregory, Rahul Jha, and Jessica Muir. Astrophysical black holes in screened modified gravity. *JCAP*, 1408:033, 2014.
- [76] Antonio De Felice and Shinji Tsujikawa.  $f(R)$  theories. *Living Rev. Rel.*, 13:3, 2010.
- [77] Claudia de Rham and Scott Melville. Unitary null energy condition violation in  $P(X)$  cosmologies. *Phys. Rev.*, D95(12):123523, 2017.
- [78] C. Deffayet, Xian Gao, D.A. Steer, and G. Zahariade. From k-essence to generalised Galileons. *Phys.Rev.*, D84:064039, 2011.
- [79] Cedric Deffayet, Oriol Pujolas, Ignacy Sawicki, and Alexander Vikman. Imperfect Dark Energy from Kinetic Gravity Braiding. *JCAP*, 1010:026, 2010.
- [80] A. A. Deriglazov. Notes on Lagrangian and Hamiltonian symmetries. 1994.
- [81] A. A. Deriglazov and Z. Kuznetsova. Conversion of second class constraints by deformation of Lagrangian local symmetries. *Phys. Lett.*, B646:47–53, 2007.
- [82] Bryce S. DeWitt. Quantum Field Theory in Curved Space-Time. *Phys. Rept.*, 19:295–357, 1975.
- [83] Mafalda Dias, Jonathan Frazer, David J. Mulryne, and David Seery. Numerical evaluation of the bispectrum in multiple field inflation, the transport approach with code. *JCAP*, 1612(12):033, 2016.



- [84] P. A. M. Dirac. The Hamiltonian form of field dynamics. *Can. J. Math.*, 3:1–23, 1951.
- [85] David A. Dobre, Andrei V. Frolov, José T. Gálvez Gherzi, Sabir Ramazanov, and Alexander Vikman. Unbraiding the Bounce: Superluminality around the Corner. *JCAP*, 1803:020, 2018.
- [86] S. Dubovsky, T. Gregoire, A. Nicolis, and R. Rattazzi. Null energy condition and superluminal propagation. *JHEP*, 0603:025, 2006.
- [87] Gia Dvali. Black Holes and Large N Species Solution to the Hierarchy Problem. *Fortsch. Phys.*, 58:528–536, 2010.
- [88] Gia Dvali. Classicalize or not to Classicalize? 2011.
- [89] Gia Dvali. Strong Coupling and Classicalization. *Subnucl. Ser.*, 53:189–200, 2017.
- [90] Gia Dvali, Andre Franca, and Cesar Gomez. Road Signs for UV-Completion. 2012.
- [91] Gia Dvali, Gian F. Giudice, Cesar Gomez, and Alex Kehagias. UV-Completion by Classicalization. *JHEP*, 1108:108, 2011.
- [92] Gia Dvali and David Pirtskhalava. Dynamics of Unitarization by Classicalization. *Phys.Lett.*, B699:78–86, 2011.
- [93] Damien A. Easson, Ignacy Sawicki, and Alexander Vikman. G-Bounce. *JCAP*, 1111:021, 2011.
- [94] Damien A. Easson, Ignacy Sawicki, and Alexander Vikman. When Matter Matters. *JCAP*, 1307:014, 2013.
- [95] Damien A. Easson and Alexander Vikman. The Phantom of the New Oscillatory Cosmological Phase. 2016.
- [96] Benjamin Elder, Austin Joyce, and Justin Khoury. From Satisfying to Violating the Null Energy Condition. *Phys. Rev.*, D89(4):044027, 2014.
- [97] Joseph Elliston, David Seery, and Reza Tavakol. The inflationary bispectrum with curved field-space. *JCAP*, 1211:060, 2012.
- [98] V. P. Ermakov. Second order differential equations. Conditions of complete integrability. *Univ. Izv. Kiev*, III, 1880.
- [99] O. A. Evseev and O. I. Melichev. Instability of static semiclosed worlds in generalized Galileon theories. *Phys. Rev.*, D96(2):024030, 2017.
- [100] Jarah Evslin. Stability of Closed Timelike Curves in a Galileon Model. *JHEP*, 03:009, 2012.
- [101] Jarah Evslin and Taotao Qiu. Closed Timelike Curves in the Galileon Model. *JHEP*, 11:032, 2011.
- [102] Gary N. Felder, Andrei V. Frolov, Lev Kofman, and Andrei D. Linde. Cosmology with negative potentials. *Phys. Rev.*, D66:023507, 2002.

- [103] V. Ferrari and K. D. Kokkotas. Scattering of particles by neutron stars: Time evolutions for axial perturbations. *Phys. Rev.*, D62:107504, 2000.
- [104] J. Frank, A. King, and D. J. Raine. *Accretion Power in Astrophysics*. 2002.
- [105] Jonathan Frazer. Predictions in multifield models of inflation. *JCAP*, 1401:028, 2014.
- [106] Katherine Freese, Joshua A. Frieman, and Angela V. Olinto. Natural inflation with pseudo nambu-goldstone bosons. *Phys. Rev. Lett.*, 65:3233–3236, Dec 1990.
- [107] Katherine Freese and William H. Kinney. Natural Inflation: Consistency with Cosmic Microwave Background Observations of Planck and BICEP2. *JCAP*, 1503:044, 2015.
- [108] Laurent Freidel. Modified gravity without new degrees of freedom. 2008.
- [109] Andrei V. Frolov. Is it really naked? On cosmic censorship in string theory. *Phys. Rev.*, D70:104023, 2004.
- [110] Andrei V. Frolov. A Singularity Problem with f(R) Dark Energy. *Phys. Rev. Lett.*, 101:061103, 2008.
- [111] Andrei V. Frolov, José T. Gálvez Gherzi, and Alex Zucca. Unscreening scalarons with a black hole. *Phys. Rev.*, D95(10):104041, 2017.
- [112] V. P. Frolov and I. D. Novikov, editors. *Black hole physics: Basic concepts and new developments*, volume 96. 1998.
- [113] Jose T. Gálvez Gherzi, Alex Zucca, and Andrei V. Frolov. Observational Constraints on Constant Roll Inflation. 2018.
- [114] Jaume Garriga and Viatcheslav F. Mukhanov. Perturbations in k-inflation. *Phys. Lett.*, B458:219–225, 1999.
- [115] Robert Geroch. Faster Than Light? *AMS/IP Stud. Adv. Math.*, 49:59–70, 2011.
- [116] José T. Gálvez Gherzi and Andrei V. Frolov. Two-point correlators revisited: Fast and slow scales in multifield models of inflation. *JCAP*, 1705(05):047, 2017.
- [117] José T. Gálvez Gherzi, Andrei V. Frolov, and David A. Dobre. Echoes from the scattering of wavepackets on wormholes. 2019.
- [118] José Tomás Gálvez Gherzi, Michael J. Desrochers, Mason Protter, and Andrew DeBenedictis. Hamiltonian consistency of the gravitational constraint algebra under deformations. 2017.
- [119] Jonathan Gilbert. Power-law density fluctuations from inflation. *Phys. Rev. D*, 52:5486–5497, Nov 1995.
- [120] D. M. Gitman, S. L. Lyakhovich, and I. V. Tyutin. Hamilton formulation of a theory with high derivatives. *Rus. Phys. J*, 26(8), 1983.
- [121] Henrique Gomes and Vasudev Shyam. Extending the rigidity of general relativity. *J. Math. Phys.*, 57(11):112503, 2016.

- [122] Jinn-Ouk Gong and Ewan D. Stewart. The Density perturbation power spectrum to second order corrections in the slow roll expansion. *Phys. Lett.*, B510:1–9, 2001.
- [123] Jinn-Ouk Gong and Takahiro Tanaka. A covariant approach to general field space metric in multi-field inflation. *JCAP*, 1103:015, 2011.
- [124] Christopher Gordon, David Wands, Bruce A. Bassett, and Roy Maartens. Adiabatic and entropy perturbations from inflation. *Phys. Rev.*, D63:023506, 2001.
- [125] Patrick B. Greene, Lev Kofman, Andrei D. Linde, and Alexei A. Starobinsky. Structure of resonance in preheating after inflation. *Phys. Rev.*, D56:6175–6192, 1997.
- [126] Alan H. Guth. The Inflationary Universe: A Possible Solution to the Horizon and Flatness Problems. *Phys.Rev.*, D23:347–356, 1981.
- [127] S. W. Hawking. The Chronology protection conjecture. *Phys. Rev.*, D46:603–611, 1992.
- [128] S. W. Hawking and R. Penrose. The Singularities of gravitational collapse and cosmology. *Proc. Roy. Soc. Lond.*, A314:529–548, 1970.
- [129] M. Henneaux and C. Teitelboim. *Quantization of gauge systems*. 1992.
- [130] Kurt Hinterbichler, Austin Joyce, Justin Khoury, and Godfrey E. J. Miller. DBI Realizations of the Pseudo-Conformal Universe and Galilean Genesis Scenarios. *JCAP*, 1212:030, 2012.
- [131] Kurt Hinterbichler, Austin Joyce, Justin Khoury, and Godfrey E. J. Miller. Dirac-Born-Infeld Genesis: An Improved Violation of the Null Energy Condition. *Phys. Rev. Lett.*, 110(24):241303, 2013.
- [132] Kurt Hinterbichler and Justin Khoury. Symmetron Fields: Screening Long-Range Forces Through Local Symmetry Restoration. *Phys. Rev. Lett.*, 104:231301, 2010.
- [133] S. A. Hojman, K. Kuchar, and C. Teitelboim. Geometrodynamics Regained. *Annals Phys.*, 96:88–135, 1976.
- [134] Gregory Walter Horndeski. Second-order scalar-tensor field equations in a four-dimensional space. *Int. J. Theor. Phys.*, 10:363–384, 1974.
- [135] Wayne Hu. Crossing the phantom divide: Dark energy internal degrees of freedom. *Phys.Rev.*, D71:047301, 2005.
- [136] Wayne Hu and Ignacy Sawicki. Models of  $f(R)$  Cosmic Acceleration that Evade Solar-System Tests. *Phys. Rev.*, D76:064004, 2007.
- [137] Ian Huston and Adam J. Christopherson. Calculating Non-adiabatic Pressure Perturbations during Multi-field Inflation. *Phys. Rev.*, D85:063507, 2012.
- [138] Anna Ijjas. Space-time slicing in Horndeski theories and its implications for non-singular bouncing solutions. 2017.
- [139] Anna Ijjas and Paul J. Steinhardt. Classically stable nonsingular cosmological bounces. *Phys. Rev. Lett.*, 117(12):121304, 2016.

- [140] S. Johnson. Notes on Perfectly Matched Layers. 2010.
- [141] Austin Joyce, Bhuvnesh Jain, Justin Khoury, and Mark Trodden. Beyond the Cosmological Standard Model. *Phys. Rept.*, 568:1–98, 2015.
- [142] S. C. Kak. The discrete hilbert transform. *Proceedings of the IEEE*, 58(4):585–586, April 1970.
- [143] A Kamenshchik and Giovanni Venturi. Remarks on the method of comparison equations (generalized WKB method) and the generalized Ermakov-Pinney equation. *Russ. Phys. J.*, 52:1339–1351, 2009.
- [144] Jin U. Kang, Vitaly Vanchurin, and Sergei Winitzki. Attractor scenarios and superluminal signals in k-essence cosmology. *Phys. Rev.*, D76:083511, 2007.
- [145] Alexandros Karam, Luca Marzola, Thomas Pappas, Antonio Racioppi, and Kyriakos Tamvakis. Constant-Roll (Quasi-)Linear Inflation. *JCAP*, 1805(05):011, 2018.
- [146] Karsten Keller and Mathieu Sinn. Kolmogorov-sinai entropy from the ordinal viewpoint. *Physica D: Nonlinear Phenomena*, 239(12):997 – 1000, 2010.
- [147] Luke Keltner and Andrew J. Tolley. UV properties of Galileons: Spectral Densities. 2015.
- [148] G. A. Khorunzhev, S. Y. Sazonov, R.A. Burenin, and A. Y. Tkachenko. Masses and accretion rates of supermassive black holes in active galactic nuclei from the INTEGRAL survey. *R.A. et al. Astron. Lett.*, 38:475, 2012.
- [149] Justin Khoury and Amanda Weltman. Chameleon fields: Awaiting surprises for tests of gravity in space. *Phys. Rev. Lett.*, 93:171104, 2004.
- [150] Tsutomu Kobayashi. Generic instabilities of nonsingular cosmologies in Horndeski theory: A no-go theorem. *Phys. Rev.*, D94(4):043511, 2016.
- [151] Tsutomu Kobayashi and Kei-ichi Maeda. Can higher curvature corrections cure the singularity problem in f(R) gravity? *Phys. Rev.*, D79:024009, 2009.
- [152] Tsutomu Kobayashi, Masahide Yamaguchi, and Jun’ichi Yokoyama. G-inflation: Inflation driven by the Galileon field. *Phys.Rev.Lett.*, 105:231302, 2010.
- [153] Tsutomu Kobayashi, Masahide Yamaguchi, and Jun’ichi Yokoyama. Generalized G-inflation: Inflation with the most general second-order field equations. *Prog.Theor.Phys.*, 126:511–529, 2011.
- [154] Tsutomu Kobayashi, Masahide Yamaguchi, and Jun’ichi Yokoyama. Galilean Creation of the Inflationary Universe. *JCAP*, 1507(07):017, 2015.
- [155] Tomi S. Koivisto and Nicola Tamanini. Ghosts in pure and hybrid formalisms of gravity theories: A unified analysis. *Phys. Rev.*, D87(10):104030, 2013.
- [156] K. D. Kokkotas. Pulsating relativistic stars. In *Relativistic gravitation and gravitational radiation. Proceedings, School of Physics, Les Houches, France, September 26-October 6, 1995*, pages 89–102, 1995.

- [157] R. Kolevatov and S. Mironov. Cosmological bounces and Lorentzian wormholes in Galileon theories with an extra scalar field. *Phys. Rev.*, D94(12):123516, 2016.
- [158] R. Kolevatov, S. Mironov, V. Rubakov, N. Sukhov, and V. Volkova. Perturbations in generalized Galileon theories. *Phys. Rev.*, D96(12):125012, 2017.
- [159] Kirill Krasnov. On deformations of Ashtekar’s constraint algebra. *Phys. Rev. Lett.*, 100:081102, 2008.
- [160] Lawrence M. Krauss, Scott Dodelson, and Stephan Meyer. Primordial gravitational waves and cosmology. *Science*, 328(5981):989–992, 2010.
- [161] Z. Lalak, D. Langlois, S. Pokorski, and K. Turzynski. Curvature and isocurvature perturbations in two-field inflation. *JCAP*, 0707:014, 2007.
- [162] J. Lee and Robert M. Wald. Local symmetries and constraints. *J. Math. Phys.*, 31:725–743, 1990.
- [163] Antony Lewis and Sarah Bridle. Cosmological parameters from CMB and other data: A Monte Carlo approach. *Phys. Rev.*, D66:103511, 2002.
- [164] Antony Lewis, Anthony Challinor, and Anthony Lasenby. Efficient computation of CMB anisotropies in closed FRW models. *Astrophys. J.*, 538:473–476, 2000.
- [165] M. Libanov, S. Mironov, and V. Rubakov. Generalized Galileons: instabilities of bouncing and Genesis cosmologies and modified Genesis. *JCAP*, 1608(08):037, 2016.
- [166] Andrew R. Liddle, Paul Parsons, and John D. Barrow. Formalizing the slow roll approximation in inflation. *Phys. Rev.*, D50:7222–7232, 1994.
- [167] A. D. Linde. A new inflationary universe scenario: A possible solution of the horizon, flatness, homogeneity, isotropy and primordial monopole problems. *Phys. Lett. B*, 108:389–393, February 1982.
- [168] Markus A. Luty, Massimo Porrati, and Riccardo Rattazzi. Strong interactions and stability in the DGP model. *JHEP*, 0309:029, 2003.
- [169] Kei-ichi Maeda. Towards the Einstein-Hilbert Action via Conformal Transformation. *Phys. Rev.*, D39:3159, 1989.
- [170] Karl Martel and Eric Poisson. Gravitational perturbations of the Schwarzschild space-time: A Practical covariant and gauge-invariant formalism. *Phys. Rev.*, D71:104003, 2005.
- [171] Jerome Martin, Hayato Motohashi, and Teruaki Suyama. Ultra Slow-Roll Inflation and the non-Gaussianity Consistency Relation. *Phys. Rev.*, D87(2):023514, 2013.
- [172] Andrea Maselli, Sebastian H. Völkel, and Kostas D. Kokkotas. Parameter estimation of gravitational wave echoes from exotic compact objects. *Phys. Rev.*, D96(6):064045, 2017.
- [173] Pawel O. Mazur and Emil Mottola. Gravitational condensate stars: An alternative to black holes. 2001.

- [174] Merced Montesinos, Jorge Romero, and Mariano Celada. Manifestly Lorentz-covariant variables for the phase space of general relativity. *Phys. Rev.*, D97(2):024014, 2018.
- [175] Michael S. Morris and Kip S. Thorne. Wormholes in spacetime and their use for interstellar travel: A tool for teaching general relativity. *American Journal of Physics*, 56(5):395–412, 1988.
- [176] Michael S. Morris, Kip S. Thorne, and Ulvi Yurtsever. Wormholes, time machines, and the weak energy condition. *Phys. Rev. Lett.*, 61:1446–1449, Sep 1988.
- [177] Michael J. P. Morse and William H. Kinney. Large- $\eta$  constant-roll inflation is never an attractor. *Phys. Rev.*, D97(12):123519, 2018.
- [178] Hayato Motohashi and Alexei A. Starobinsky. Constant-roll inflation: confrontation with recent observational data. *EPL*, 117(3):39001, 2017.
- [179] Hayato Motohashi and Alexei A. Starobinsky.  $f(R)$  constant-roll inflation. *Eur. Phys. J.*, C77(8):538, 2017.
- [180] Hayato Motohashi, Alexei A. Starobinsky, and Jun'ichi Yokoyama. Inflation with a constant rate of roll. *JCAP*, 1509(09):018, 2015.
- [181] Emil Mottola. New Horizons in Gravity: The Trace Anomaly, Dark Energy and Condensate Stars. *Acta Phys. Polon.*, B41:2031–2162, 2010.
- [182] V. Mukhanov. *Physical Foundations of Cosmology*. Cambridge University Press, 2005.
- [183] V. F. Mukhanov. Quantum theory of gauge-invariant cosmological perturbations. *Zh. Eksp. Teor. Fiz.*, 94:1–11, 1988.
- [184] Viatcheslav F. Mukhanov. Gravitational Instability of the Universe Filled with a Scalar Field. *JETP Lett.*, 41:493–496, 1985. [Pisma Zh. Eksp. Teor. Fiz.41,402(1985)].
- [185] Alberto Nicolis and Riccardo Rattazzi. Classical and quantum consistency of the DGP model. *JHEP*, 0406:059, 2004.
- [186] Alberto Nicolis, Riccardo Rattazzi, and Enrico Trincherini. The galileon as a local modification of gravity. *Phys. Rev.*, D79:064036, 2009.
- [187] Sakine Nishi and Tsutomu Kobayashi. Generalized Galilean Genesis. *JCAP*, 1503(03):057, 2015.
- [188] S. Nojiri, S. D. Odintsov, and V. K. Oikonomou. Constant-roll Inflation in  $F(R)$  Gravity. *Class. Quant. Grav.*, 34(24):245012, 2017.
- [189] Gonzalo J. Olmo. Post-Newtonian constraints on  $f(R)$  cosmologies in Palatini formalism. 2005.
- [190] M. Ostrogradskii. Memoires sur les equations differentielles relatives au probleme des isoperimetres. 1850.
- [191] A. Palatini. Deduzione invariante delle equazioni gravitazionali dal principio di Hamilton. 1919.

- [192] Roger Penrose. The question of cosmic censorship. *J. Astrophys. Astron.*, 20:233–248, 1999.
- [193] L Petrich, S Shapiro, and I. Wasserman. Gravitational radiation from nonspherical infall into black holes. II - A catalog of 'exact' waveforms. *Astrop. J. Suppl. S*, 58:297–320, 1985.
- [194] Massimo Pietroni. Dark energy condensation. *Phys. Rev.*, D72:043535, 2005.
- [195] Edmund Pinney. The nonlinear differential equation  $y'' + p(x)y' + cy = 0$ . *Proceedings of the American Mathematical Society*, 1(5):681–681, 1950.
- [196] David Pirtskhalava, Luca Santoni, Enrico Trincherini, and Patipan Uttayarat. Inflation from Minkowski Space. *JHEP*, 12:151, 2014.
- [197] Eric Poisson. *A Relativist's Toolkit: The Mathematics of Black-Hole Mechanics*. Cambridge University Press, 2009.
- [198] David Polarski and Alexei A. Starobinsky. Semiclassicality and decoherence of cosmological perturbations. *Class. Quant. Grav.*, 13:377–392, 1996.
- [199] J. M. Pons, D. C. Salisbury, and L. C. Shepley. Gauge transformations in the Lagrangian and Hamiltonian formalisms of generally covariant theories. *Phys. Rev.*, D55:658–668, 1997.
- [200] Layne C. Price, Jonathan Frazer, Jiajun Xu, Hiranya V. Peiris, and Richard Easther. MultiModeCode: An efficient numerical solver for multifield inflation. *JCAP*, 1503(03):005, 2015.
- [201] Richard H. Price. Nonspherical perturbations of relativistic gravitational collapse. i. scalar and gravitational perturbations. *Phys. Rev. D*, 5:2419–2438, May 1972.
- [202] Richard H. Price. Nonspherical perturbations of relativistic gravitational collapse. ii. integer-spin, zero-rest-mass fields. *Phys. Rev. D*, 5:2439–2454, May 1972.
- [203] Oriol Pujolas, Ignacy Sawicki, and Alexander Vikman. The Imperfect Fluid behind Kinetic Gravity Braiding. *JHEP*, 1111:156, 2011.
- [204] Taotao Qiu, Jarah Evslin, Yi-Fu Cai, Mingzhe Li, and Xinmin Zhang. Bouncing Galileon Cosmologies. *JCAP*, 1110:036, 2011.
- [205] Jerome Quintin, Zeinab Sherkatghanad, Yi-Fu Cai, and Robert H. Brandenberger. Evolution of cosmological perturbations and the production of non-Gaussianities through a nonsingular bounce: Indications for a no-go theorem in single field matter bounce cosmologies. *Phys. Rev.*, D92(6):063532, 2015.
- [206] Bharat Ratra and P. J. E. Peebles. Cosmological Consequences of a Rolling Homogeneous Scalar Field. *Phys. Rev.*, D37:3406, 1988.
- [207] Tullio Regge and John A. Wheeler. Stability of a Schwarzschild singularity. *Phys. Rev.*, 108:1063–1069, 1957.

- [208] C. Rovelli. Constraint algebra in general relativity. *Il Nuovo Cimento B (1971-1996)*, 92(1):49–60, Mar 1986.
- [209] Carlo Rovelli. Ashtekar formulation of general relativity and loop space nonperturbative quantum gravity: A Report. *Class. Quant. Grav.*, 8:1613–1676, 1991.
- [210] V. A. Rubakov. Consistent NEC-violation: towards creating a universe in the laboratory. *Phys. Rev.*, D88:044015, 2013.
- [211] V. A. Rubakov. The Null Energy Condition and its violation. *Phys. Usp.*, 57:128–142, 2014. [Usp. Fiz. Nauk184,no.2,137(2014)].
- [212] V. A. Rubakov. Can Galileons support Lorentzian wormholes? *Theor. Math. Phys.*, 187(2):743–752, 2016.
- [213] V. A. Rubakov. More about wormholes in generalized Galileon theories. *Theor. Math. Phys.*, 188(2):1253–1258, 2016. [Teor. Mat. Fiz.188,no.2,337(2016)].
- [214] Norma G. Sanchez. Scattering of scalar waves from a schwarzschild black hole. *Journal of Mathematical Physics*, 17(5):688–692, 1976.
- [215] Norma G. Sanchez. The Wave Scattering Theory and the Absorption Problem for a Black Hole. *Phys. Rev.*, D16:937–945, 1977.
- [216] Norma G. Sanchez. Absorption and Emission Spectra of a Schwarzschild Black Hole. *Phys. Rev.*, D18:1030, 1978.
- [217] Norma G. Sanchez. Elastic Scattering of Waves by a Black Hole. *Phys. Rev.*, D18:1798, 1978.
- [218] Misao Sasaki. Large Scale Quantum Fluctuations in the Inflationary Universe. *Prog. Theor. Phys.*, 76:1036, 1986.
- [219] Misao Sasaki and Ewan D. Stewart. A General analytic formula for the spectral index of the density perturbations produced during inflation. *Prog. Theor. Phys.*, 95:71–78, 1996.
- [220] K. Sato. First-order phase transition of a vacuum and the expansion of the Universe. *Mon. Not. Roy. Astron. Soc.*, 195:467–479, May 1981.
- [221] Ignacy Sawicki and Alexander Vikman. Hidden Negative Energies in Strongly Accelerated Universes. *Phys.Rev.*, D87:067301, 2013.
- [222] Mark A. Scheel, Stuart L. Shapiro, and Saul A. Teukolsky. Collapse to black holes in Brans-Dicke theory. 2. Comparison with general relativity. *Phys. Rev.*, D51:4236–4249, 1995.
- [223] L. Sebastiani, S. Vagnozzi, and R. Myrzakulov. Mimetic gravity: a review of recent developments and applications to cosmology and astrophysics. *Adv. High Energy Phys.*, 2017:3156915, 2017.
- [224] David Seery, David J. Mulryne, Jonathan Frazer, and Raquel H. Ribeiro. Inflationary perturbation theory is geometrical optics in phase space. *JCAP*, 1209:010, 2012.



- [225] Jonathan Z. Simon. Higher Derivative Lagrangians, Nonlocality, Problems and Solutions. *Phys. Rev.*, D41:3720, 1990.
- [226] Thomas P. Sotiriou and Valerio Faraoni.  $f(R)$  Theories Of Gravity. *Rev. Mod. Phys.*, 82:451–497, 2010.
- [227] Thomas P. Sotiriou and Stefano Liberati. Metric-affine  $f(R)$  theories of gravity. *Annals Phys.*, 322:935–966, 2007.
- [228] Alexei A. Starobinsky. A New Type of Isotropic Cosmological Models Without Singularity. *Phys. Lett.*, B91:99–102, 1980.
- [229] Alexei A. Starobinsky. Disappearing cosmological constant in  $f(R)$  gravity. *JETP Lett.*, 86:157–163, 2007.
- [230] K. S. Stelle. Renormalization of Higher Derivative Quantum Gravity. *Phys. Rev.*, D16:953–969, 1977.
- [231] J. Struckmeier. General relativity as an extended canonical gauge theory. *Phys. Rev.*, D91(8):085030, 2015.
- [232] J. Struckmeier, J. Muench, D. Vasak, J. Kirsch, M. Hanauske, and H. Stoecker. Canonical Transformation Path to Gauge Theories of Gravity. *Phys. Rev.*, D95(12):124048, 2017.
- [233] Anastasios Taliotis. Extra dimensions, black holes and fireballs at the LHC. *JHEP*, 05:034, 2013.
- [234] Claudio Teitelboim. How commutators of constraints reflect the space-time structure. *Annals Phys.*, 79:542–557, 1973.
- [235] T. Thiemann. Generalized boundary conditions for general relativity for the asymptotically flat case in terms of Ashtekar’s variables. *Class. Quant. Grav.*, 12:181–198, 1995.
- [236] Rakesh Tibrewala. Inhomogeneities, loop quantum gravity corrections, constraint algebra and general covariance. *Class. Quant. Grav.*, 31:055010, 2014.
- [237] Kazuhiro Tominaga, Motoyuki Saijo, and Kei-ichi Maeda. Gravitational waves from a test particle scattered by a neutron star: Axial mode case. *Phys. Rev.*, D60:024004, 1999.
- [238] Thomas Tram and Julien Lesgourgues. Optimal polarisation equations in FLRW universes. *JCAP*, 1310:002, 2013.
- [239] Shinji Tsujikawa, David Parkinson, and Bruce A. Bassett. Correlation - consistency cartography of the double inflation landscape. *Phys. Rev.*, D67:083516, 2003.
- [240] Konstantinos Tzirakis and William H. Kinney. Inflation over the hill. *Phys. Rev.*, D75:123510, 2007.
- [241] A. I. Vainshtein. To the problem of nonvanishing gravitation mass. *Phys. Lett.*, B39:393–394, 1972.

- [242] Alexander Vikman. Can dark energy evolve to the phantom? *Phys. Rev.*, D71:023515, 2005.
- [243] Alexander Vikman. Suppressing Quantum Fluctuations in Classicalization. *EPL*, 101(3):34001, 2013.
- [244] Matt Visser. Traversable wormholes: Some simple examples. *Phys. Rev.*, D39:3182–3184, 1989.
- [245] Sebastian H. Volkel and Kostas D. Kokkotas. Ultra Compact Stars: Reconstructing the Perturbation Potential. *Class. Quant. Grav.*, 34(17):175015, 2017.
- [246] Sebastian H. Volkel and Kostas D. Kokkotas. Wormhole Potentials and Throats from Quasi-Normal Modes. *Class. Quant. Grav.*, 35(10):105018, 2018.
- [247] S. Weinberg. Phenomenological Lagrangians. *Physica A Statistical Mechanics and its Applications*, 96:327–340, April 1979.
- [248] Steven Weinberg. Effective field theory, past and future. *Int. J. Mod. Phys.*, A31(06):1630007, 2016.
- [249] Clifford M. Will. The Confrontation between General Relativity and Experiment. *Living Rev. Rel.*, 17:4, 2014.
- [250] Richard P. Woodard. Ostrogradsky’s theorem on Hamiltonian instability. *Scholarpedia*, 10(8):32243, 2015.
- [251] Jun-Qing Xia, Yi-Fu Cai, Tao-Tao Qiu, Gong-Bo Zhao, and Xinmin Zhang. Constraints on the Sound Speed of Dynamical Dark Energy. *Int. J. Mod. Phys.*, D17:1229–1243, 2008.
- [252] Zhu Yi and Yungui Gong. On the constant-roll inflation. *JCAP*, 1803(03):052, 2018.
- [253] James W. York. Gravitational degrees of freedom and the initial-value problem. *Phys. Rev. Lett.*, 26:1656–1658, Jun 1971.
- [254] Haruo Yoshida. Construction of higher order symplectic integrators. *Phys. Lett.*, A150:262–268, 1990.
- [255] Frank J. Zerilli. Gravitational field of a particle falling in a schwarzschild geometry analyzed in tensor harmonics. *Phys. Rev. D*, 2:2141–2160, Nov 1970.

## Appendix A

# Deviations of $n_s$ and $r$ from the slow-roll expressions

In this appendix, we compare two of the consistency relations discussed in [166, 122]

$$r = 16\epsilon, \quad (\text{A.1})$$

$$n_s = 1 - 6\epsilon + 2\eta, \quad (\text{A.2})$$

with the values of  $n_s$  and  $r$  obtained from the scalar and tensor power spectra, as shown in Figure A.1. These relations are the basis of the confrontation with Planck data made in [178]. The slow-roll parameters  $\epsilon$  and  $\eta$  appearing in (A.1) and (A.2) are calculated there to be

$$\epsilon = \frac{\beta(3 + \beta)^2 \sin^2(\sqrt{2\beta}\phi/M_{\text{Pl}})}{[-3 + \beta - (3 + \beta) \cos(\sqrt{2\beta}\phi/M_{\text{Pl}})]^2}, \quad (\text{A.3})$$

$$\eta = \frac{2\beta(3 + \beta) \cos(\sqrt{2\beta}\phi/M_{\text{Pl}})}{-3 + \beta - (3 + \beta) \cos(\sqrt{2\beta}\phi/M_{\text{Pl}})}. \quad (\text{A.4})$$

Figure A.1 shows comparison of the slow roll approximations (A.1) and (A.2) to the values inferred from the direct spectrum computation. Both slow-roll parameters are evaluated at  $\phi = \phi_0$ , which makes them independent of  $M$ . Our procedure allows us to evaluate both power spectra well beyond the slow-roll approximation, we show  $\beta \in [0.001; 0.1]$  which contains the reliability interval suggested in [178].  $M^2 = 5.64 \times 10^{-12} M_{\text{Pl}}^2$  is fixed as a constant, approximately matching its best-fit value after setting  $N_* = 60$ . From Figure A.1, it is interesting to notice that the deviations from the slow-roll definition in (A.1) are always non-negligible, especially in the range of large values of  $\beta$ . The opposite occurs with the deviations from (A.2) as we can observe in the left panel. In either of these cases, it is beneficial to avoid the approximation derived from the slow-roll approximation in order to calculate  $n_s$  and  $r$  since (i) this imposes restrictions on the valid range of  $\beta$  and (ii) as shown in Figure A.1, the calculation of both parameters from the power spectra shows noticeable deviations from the approximate expressions in (A.1) and (A.2) in both the original reliability range  $\beta \in [0.005; 0.025]$  and within the 95% C.L. range, as depicted in both panels of the last figure. One possible cause is the spurious running of  $n_s$  seen in the

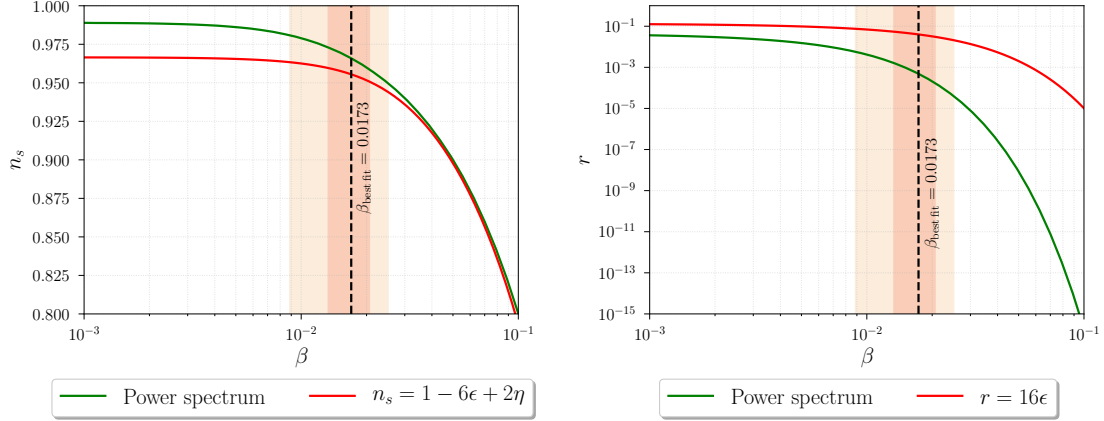


Figure A.1: Left panel: Testing the consistency relation in (A.2) as a function of  $\beta$  after fixing  $M^2 = 5.64 \times 10^{-12} M_{\text{Pl}}^2$ . Surprisingly, the tested consistency relation works well for larger values of  $\beta$ . Right panel: Testing (A.1) for the same value of  $M^2$ . Here the differences are very large (up to ten orders of magnitude) for larger values of  $\beta$ . Both consistency relations are compared with the direct calculation of  $n_s$  and  $r$  at  $N_* = 60$ , right after evaluating the power spectra scalar and tensor perturbations. The shaded regions represent the ranges of  $\beta$  within the 68% and 95% confidence levels.

slow-roll consistency relations, which makes (A.1) and (A.2) depend slightly on the exact field value they are evaluated at. If one wants high precision, it is easier to just calculate the spectra directly rather than dealing with intricacies of the slow-roll expansion [145] to get to the required expansion order.

## Appendix B

# Decomposition scheme in a curved field space

As expressed in [219], we can consider a non-canonical version of (3.1)

$$S = \int d^4x \sqrt{-g} \left( -\frac{1}{2} h_{AB} \partial_\mu \phi^A \partial^\mu \phi^B - V(\phi) \right). \quad (\text{B.1})$$

From [123, 97], we learned about the best way to consider the perturbative expansion of this action to get the equations of motion for the background

$$\begin{aligned} 3M_{\text{Pl}}^2 H^2 &= \frac{1}{2} \dot{\phi}_I \dot{\phi}^I + V(\phi) \\ \mathcal{D}_t \dot{\phi}_A + 3H \dot{\phi}_A &= \frac{\partial V}{\partial \phi_A}, \end{aligned} \quad (\text{B.2})$$

and a second order expansion of the action

$$S_\Phi(k) = \frac{1}{2} \int a^3 d^4x \left[ h^{AB} \mathcal{D}_t \Phi_A \mathcal{D}_t \Phi_B - \Phi^A \left( \frac{k^2}{a^2} h_{AB} + \mathcal{M}_{AB} \right) \Phi^B \right], \quad (\text{B.3})$$

where  $\mathcal{D}_t X^A = \dot{X}^A + \Gamma_{CD}^A X^C \dot{\phi}^D$  and  $\Gamma_{BC}^A = 1/2 h^{AD} (h_{BD,C} + h_{CD,B} - h_{BC,D})$ . Both expressions are fully covariant (and metric compatible) under translations along geodesics on the field space. The mass term  $\mathcal{M}_{AB}$  is actively affected by the field space curvature

$$\mathcal{M}_{AB} = \mathcal{D}_{AB}^2 V - R_{DABC} \dot{\phi}^D \dot{\phi}^C - \frac{1}{a^3 M_{\text{Pl}}^2} \mathcal{D}_t \left( \frac{a^3}{H} \dot{\phi}_A \dot{\phi}_B \right).$$

As we did before, we separate the field the field perturbations using  $\Phi^A = L^{AB} \hat{\chi}_B$ . Considering the case of a theory which produces equations of motion fully covariant under field space gauge transformations. Hence, the form of the action only differs from (3.7) by the use covariant derivatives instead of the total.

It is possible to promote our results (3.17), (3.20) and (3.21) after using the gauge fixing conditions for the correlators

$$\begin{aligned}\langle \hat{\chi}_C, \hat{\chi}_D \rangle &= h_{CD}, \\ \text{Sym}_{AB}^{CD} \langle \mathcal{D}_t \hat{\chi}_C, \hat{\chi}_D \rangle &= 0 \\ \text{Sym}_{AB}^{CD} [\langle \mathcal{D}_t^2 \hat{\chi}_C, \hat{\chi}_D \rangle + \langle \mathcal{D}_t \hat{\chi}_C, \mathcal{D}_t \hat{\chi}_C \rangle] &= 0\end{aligned}\tag{B.4}$$

and reshaping the form of the Cholesky amplitude matrix, for ( $B < C$ )

$$\mathcal{A}_{BC} = - \left( L^{-1} \right)_{BE} \left( h^{EG} \mathcal{M}_{GD} \right) L_C^D - \left( L^{-1} \right)_{BE} \mathcal{D}_t L^{EF} \langle \mathcal{D}_t \hat{\chi}_F, \hat{\chi}_C \rangle + \langle \mathcal{D}_t \hat{\chi}_B, \mathcal{D}_t \hat{\chi}_C \rangle.$$

We get:

$$\begin{aligned}\mathcal{D}_t^2 L_B^A + 3H \mathcal{D}_t L_B^A + \left[ \frac{k^2}{a^2} \delta_E^A + h^{AD} \mathcal{M}_{DE} \right] L_B^E + L^{AC} \mathcal{A}_{CB} + \mathcal{D}_t L^{AC} \langle \mathcal{D}_t \hat{\chi}_C \hat{\chi}_B \rangle - L^{AC} \langle \mathcal{D}_t \hat{\chi}_C \mathcal{D}_t \hat{\chi}_B \rangle &= 0, \\ \mathcal{D}_t \langle \mathcal{D}_t \hat{\chi}_A, \mathcal{D}_t \hat{\chi}_B \rangle = \text{Sym}_{AB}^{CD} \left[ -3H \langle \mathcal{D}_t \hat{\chi}_C, \mathcal{D}_t \hat{\chi}_D \rangle - 2L_{CE}^{-1} \dot{L}^{EF} \langle \mathcal{D}_t \hat{\chi}_F, \mathcal{D}_t \hat{\chi}_D \rangle - h^{EF} \mathcal{A}_{CE} \langle \mathcal{D}_t \hat{\chi}_F, \hat{\chi}_D \rangle + \right. \\ \left. L_{CE}^{-1} \mathcal{D}_t L^{EF} h^{GJ} \langle \mathcal{D}_t \hat{\chi}_F, \hat{\chi}_G \rangle \langle \hat{\chi}_J, \mathcal{D}_t \hat{\chi}_D \rangle + h^{FG} \langle \mathcal{D}_t \hat{\chi}_C, \mathcal{D}_t \hat{\chi}_F \rangle \langle \mathcal{D}_t \hat{\chi}_G, \hat{\chi}_D \rangle \right], \\ \mathcal{D}_t \langle \mathcal{D}_t \hat{\chi}_A, \hat{\chi}_B \rangle = \mathcal{A}_{AB} - 3H \langle \mathcal{D}_t \hat{\chi}_A, \hat{\chi}_B \rangle - \left( L^{-1} \right)_{AG} \mathcal{D}_t L^{GF} \langle \mathcal{D}_t \hat{\chi}_F, \hat{\chi}_B \rangle.\end{aligned}\tag{B.5}$$

Notice from (B.4) how the field metric is induced from the correlators of the fastest degrees of freedom in the system. The emergence of such a geometric structure appears as a result of averaging at each instant of time over the evolved Gaussian random variables.

## Appendix C

# Plotting two-point correlation functions

In this appendix, we show all the spectra calculated following the procedures aforementioned. In the first panel of Figure C.1, we provide the spectrum computed for the case of the specific background trajectory defined in section 3.3 using the two methods suggested.

The spectrum represented in the second panel of Figure C.1 corresponds to the case of the same initial conditions; now using a different ratio  $g/\lambda = 3$  between the coupling parameters in the potential (3.22). Here  $k/(aH)_{\text{end}}$  represents the normalization of comoving momentum with respect to the scale factor and the Hubble parameter measured at the end of inflation. In both cases, it is not possible to indicate which one of the field components dominates of the spectrum. This is due to our choice of the background field trajectories, in which the contribution of both fields is nearly the same. The only difference is the independent contribution of  $\phi$  in (3.22).

In the third panel of the same figure, we show the spectrum for the case of transversal motion along the inflaton trajectory ( $\sigma_0 = 0$ ) for  $g/\lambda = 2$ . We achieve this by setting a dominant background contribution for  $\phi$  in the same potential.

Additionally, the case of  $g/\lambda = 3$  is represented in the last panel (bottom right of the figure). All the spectra generated by these two ratios reflect the strength of the fluctuations of  $\phi$  when compared to those from  $\sigma$ . Showing a suppression of the additional field and the cross correlators. The last results are fully consistent with the input required to generate the chaotic billiards pictures produced in [42].

It has been shown in [124] that the adiabatic and isocurvature components of the spectrum can be found via a change of basis. Gram-Schmidt procedure provides an orthonormal basis of  $\mathcal{N}$  vectors made of the background field components to project into the adiabatic/isocurvature basis just as in (3.25).

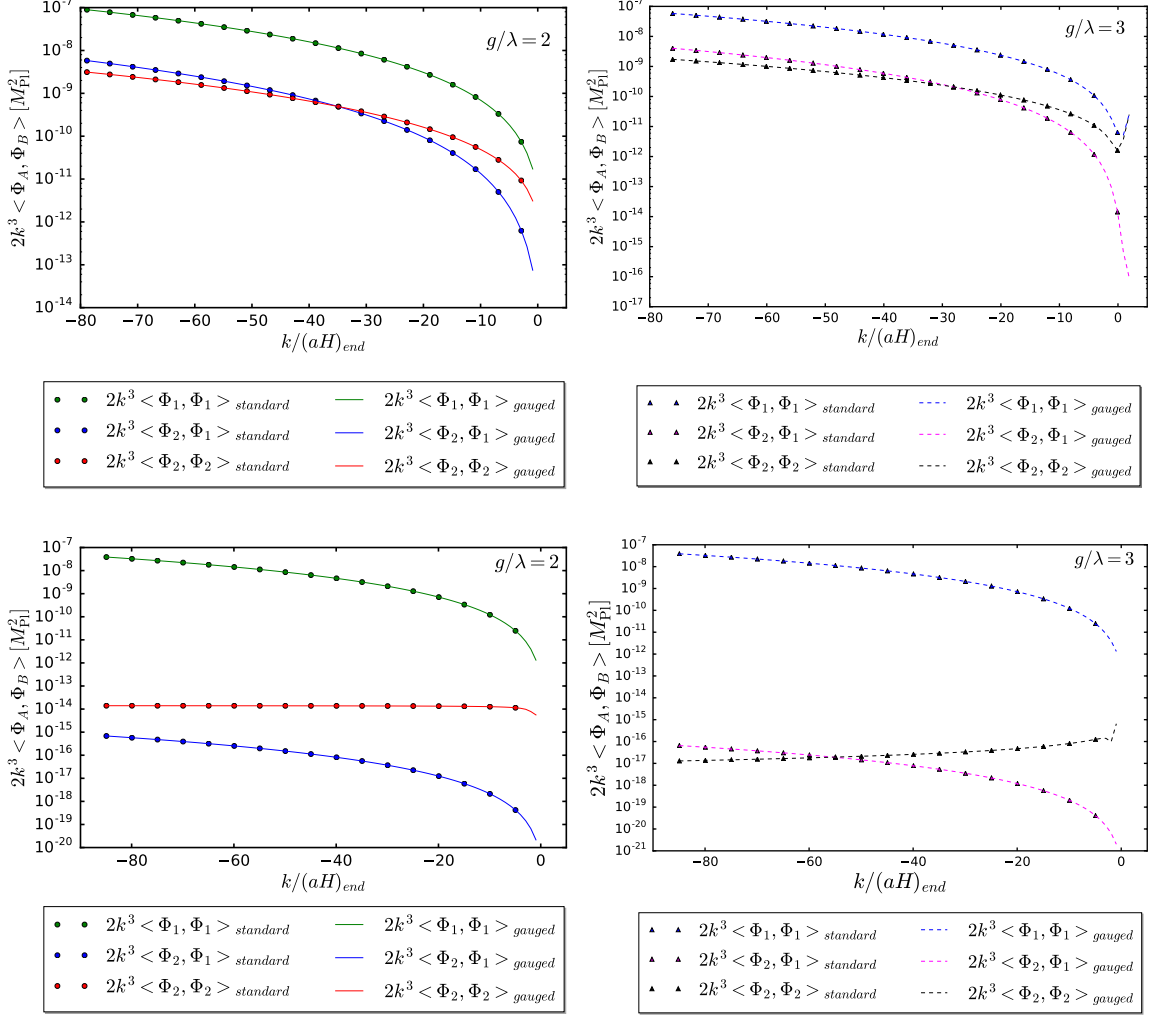


Figure C.1: Top left: Scale invariant two-point correlators for the potential in (3.22) for  $g/\lambda = 2$ : The values of the two-point correlations obtained from evolving (3.17), (3.20) and (3.21) match with our results from averaging over 100-500 evolved field realizations. Top right: Two-point correlators for the case of  $g/\lambda = 3$ . Bottom left: Two-point correlators for the case of  $g/\lambda = 2$ , in the case of a dominant contribution from  $\phi$ . Bottom right: Two-point correlators for the case of  $g/\lambda = 3$ , in the same case of dominance of  $\phi$ .



## Appendix D

# Power spectra in the Ijjas-Steinhardt bounce

In this appendix, we describe the dynamics of the scalar and tensor fluctuations by considering the IS-bouncing trajectory proposed in [139], which was described in Chapter 4. All the information needed from this trajectory is contained in the choice of  $H(t)$  in (4.38) and  $\gamma(t)$  in (4.40). For instance, we will first describe the set of equations of motion and initial conditions required for numerical evaluation.

### D.1 Setting up the equations of motion and initial conditions

The field dynamics of these fluctuations is described by the Lagrangian in (4.1) and expanded in second order of perturbations written in Fourier space,

$$\mathcal{L}_{\mathbf{k}}^{(2)} = \frac{a^3 A(t)}{2} \left( |\dot{\zeta}_{\mathbf{k}}|^2 - \frac{k^2 c_s^2}{a^2} |\zeta_{\mathbf{k}}|^2 \right) + \frac{a^3}{8} \sum_{p=+, \times} \left[ |\dot{h}_{\mathbf{k}}^p|^2 - \frac{k^2}{a^2} |h_{\mathbf{k}}^p|^2 \right]. \quad (\text{D.1})$$

Where tensor modes are also included apart from the scalar curvature and the index  $p$  is a placeholder for any of the polarization modes, conventionally dubbed by (+) and ( $\times$ ). In this case, the speed of sound follows from its previous definitions and  $A(t)$  is the same as in (4.29).

We derive the equations of motion after varying the action built from the previous expression with respect to  $\zeta_{\mathbf{k}}$  and  $h_{\mathbf{k}}^p$ ,

$$\begin{aligned} \ddot{\zeta}_{\mathbf{k}} + \frac{d \ln(a^3 A(t))}{dt} \dot{\zeta}_{\mathbf{k}} + \frac{k^2 c_s^2}{a^2} \zeta_{\mathbf{k}} &= 0, \\ \ddot{h}_{\mathbf{k}}^p + 3H \dot{h}_{\mathbf{k}}^p + \frac{k^2}{a^2} h_{\mathbf{k}}^p &= 0. \end{aligned}$$

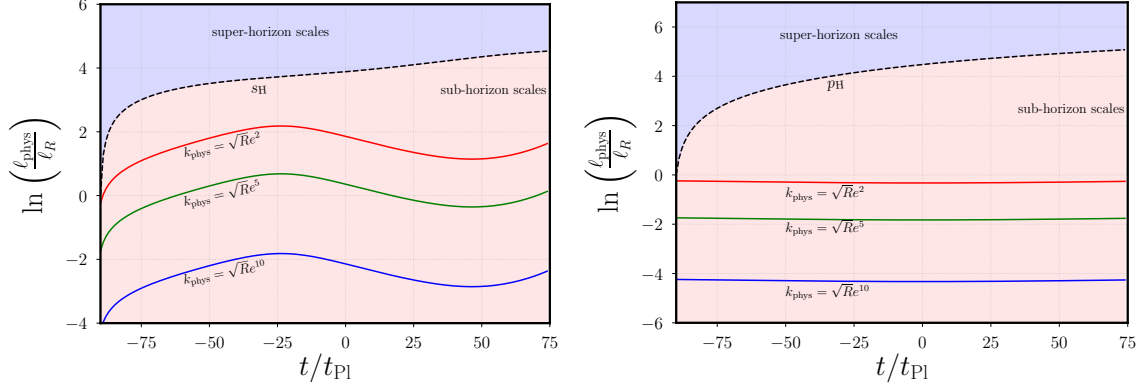


Figure D.1: Left panel: Evolution of three different scalar wavelengths  $\lambda_{\text{phys}}^{\mathcal{S}}$  and the sound horizon  $s_{\text{H}}$ . Right panel: Representing the particle horizon  $p_{\text{H}}$  and  $\lambda_{\text{phys}}^{\mathcal{T}}$ . In both cases, the initial length of the sound horizon is assumed to be  $\ell_R \approx |R(t_0)|^{-1/2}$ . Notice that none of these lengths crosses from sub-horizon (shaded in red) to super-horizon scales (shaded in blue).

With the help of the auxiliary variables  $\zeta_{\mathbf{k}} \equiv a^{-3/2}A(t)^{-1/2}\mathcal{S}_{\mathbf{k}}$  and  $h_{\mathbf{k}}^p \equiv \sqrt{2}a^{-3/2}\mathcal{T}_{\mathbf{k}}^p$  it is possible to write these equations in the form of two decoupled simple harmonic oscillators,

$$\ddot{\mathcal{S}}_{\mathbf{k}} + \omega_{\mathcal{S}}^2 \mathcal{S}_{\mathbf{k}} = 0, \quad (\text{D.2})$$

$$\ddot{\mathcal{T}}_{\mathbf{k}}^p + \omega_{\mathcal{T}}^2 \mathcal{T}_{\mathbf{k}}^p = 0, \quad (\text{D.3})$$

where the functions  $z \equiv a^{3/2}A^{1/2}$  and  $y \equiv a^{3/2}$  are useful in order to define the natural frequencies for both oscillators  $\omega_{\mathcal{S}}^2 \equiv k^2 c_s^2/a^2 - \ddot{z}/z$  and  $\omega_{\mathcal{T}}^2 \equiv k^2/a^2 - \ddot{y}/y$ . For simplicity, we will evolve these auxiliary variables instead of the original scalar and tensor modes; however it is not a problem to determine the dynamics of  $\zeta_{\mathbf{k}}$  and  $h_{\mathbf{k}}^p$  after inverting the definitions of  $\mathcal{S}_{\mathbf{k}}$  and  $\mathcal{T}_{\mathbf{k}}^p$ . Initial conditions can be determined by instantaneous energy minimization after diagonalizing the Hamiltonian of an harmonic oscillator with a time-dependent frequency in a fixed instant of time, even when it is well-known that this selection criteria is not unique. The promotion of these solutions to field operators is given by,

$$\hat{\mathcal{S}}_{\mathbf{k}} = \mathcal{S}_{\mathbf{k}} \hat{a}_{\mathbf{k}} + \mathcal{S}_{-\mathbf{k}}^* \hat{a}_{-\mathbf{k}}^\dagger; \quad \hat{\mathcal{T}}_{\mathbf{k}}^p = \mathcal{T}_{\mathbf{k}}^p \hat{b}_{\mathbf{k}} + (\mathcal{T}_{\mathbf{k}}^p)^* \hat{b}_{-\mathbf{k}}^\dagger,$$

and is consistent with the reality condition for all the fluctuation modes.  $(\hat{a}_{\mathbf{k}}, \hat{a}_{\mathbf{k}}^\dagger)$  and  $(\hat{b}_{\mathbf{k}}, \hat{b}_{\mathbf{k}}^\dagger)$  are the creation and annihilation operators for scalar and tensor perturbations. Any generic solution to (D.2) and (D.3) can be written as a function of two real modes  $\mathcal{S}_{\mathbf{k}} = \mathcal{S}_{\mathbf{k}}^{(1)} + i\mathcal{S}_{\mathbf{k}}^{(2)}$ . From the standard commutation relations for the ladder operators  $[\hat{a}_{\mathbf{k}}, \hat{a}_{\mathbf{k}'}^\dagger] = \delta(\mathbf{k} - \mathbf{k}')$  and the equal-time commutator  $[\hat{\mathcal{S}}_{\mathbf{k}}, \dot{\hat{\mathcal{S}}}_{\mathbf{k}'}] = i\delta(\mathbf{k} - \mathbf{k}')$ , we can show that the Wronskian of these real modes satisfies,

$$\mathcal{S}_{\mathbf{k}}^{(1)} \dot{\mathcal{S}}_{\mathbf{k}}^{(2)} - \mathcal{S}_{\mathbf{k}}^{(2)} \dot{\mathcal{S}}_{\mathbf{k}}^{(1)} = \frac{1}{2},$$

at every instant of time, in agreement with the canonical commutations relations. The same procedure follows to write conservation of the Wronskian for the tensor modes. Hence, it is

possible to write the canonically normalized initial conditions for all the modes involved,

$$\begin{aligned} \dot{\mathcal{S}}^{(1)}(t_0) &= 0 ; \mathcal{S}^{(1)}(t_0) = \frac{1}{\sqrt{2\omega_{\mathcal{S}}(t_0)}}, \\ \dot{\mathcal{S}}^{(2)}(t_0) &= \sqrt{\frac{\omega_{\mathcal{S}}(t_0)}{2}} ; \mathcal{S}^{(2)}(t_0) = 0, \end{aligned} \quad (\text{D.4})$$

$$\begin{aligned} (\dot{\mathcal{T}}^p)^{(1)}(t_0) &= 0 ; (\mathcal{T}^p)^{(1)}(t_0) = \frac{1}{\sqrt{2\omega_{\mathcal{T}}(t_0)}}, \\ (\dot{\mathcal{T}}^p)^{(2)}(t_0) &= \sqrt{\frac{\omega_{\mathcal{T}}(t_0)}{2}} ; (\mathcal{T}^p)^{(2)}(t_0) = 0, \end{aligned} \quad (\text{D.5})$$

in an analogous way than the standard prescription for the Bunch-Davies vacuum. Notice that even in the limit of high  $k$ , it is possible to observe that  $c_s^2(t)$  and  $a(t)$  make the scalar initial conditions not invariant under time translations. Our objective with this choice of initial conditions is the instantaneous minimization of the energy per  $k$ -mode for *only* positive values of  $\omega_{\mathcal{T}}^2$  and  $\omega_{\mathcal{S}}^2$  before the bounce. In this way, we will compare the state of the system at any posterior instant of time with the zero-point energy state at  $t = t_0$  of a time-dependent harmonic oscillator. This would be a suitable (but not unique) way to define equations of motion while setting initial conditions that minimize the energy of the system before the bounce. Notice that the evaluation of the expressions in (D.4) and (D.5) at all the posterior instants of time should never be treated as solutions to the equations of motion. Nevertheless, there is another way to rephrase the system that increases the performance of a numerical computation. For instance, let us rewrite the eikonal separation  $\mathcal{S}_{\mathbf{k}} = L_{\mathcal{S}} \exp(i\Theta_{\mathcal{S}})$ , where  $L_{\mathcal{S}}$  and  $\Theta_{\mathcal{S}}$  are real. Then we replace this expression in (D.2) obtaining two equations after separating the real and imaginary parts,

$$\begin{aligned} \ddot{L}_{\mathcal{S}} + (\omega_{\mathcal{S}}^2 - \dot{\Theta}_{\mathcal{S}}^2)L_{\mathcal{S}} &= 0 \quad (\text{Real part}), \\ \ddot{\Theta}_{\mathcal{S}} + 2\frac{\dot{L}_{\mathcal{S}}}{L_{\mathcal{S}}}\dot{\Theta}_{\mathcal{S}} &= 0 \quad (\text{Imaginary part}), \end{aligned} \quad (\text{D.6})$$

where (D.6) has a simple analytic solution given by  $\dot{\Theta}_{\mathcal{S}}(t) = L_{\mathcal{S}}^2(t_0)\dot{\Theta}_{\mathcal{S}}(t_0)/L_{\mathcal{S}}^2$ . Hence, the only equation to solve for the scalar modes is,

$$\ddot{L}_{\mathcal{S}} + \left[ \omega_{\mathcal{S}}^2 - L_{\mathcal{S}}^4(t_0) \frac{\dot{\Theta}_{\mathcal{S}}^2(t_0)}{L_{\mathcal{S}}^4} \right] L_{\mathcal{S}} = 0. \quad (\text{D.7})$$

The same idea can be straightforwardly applied for the tensor modes after replacing all the tensor components of  $\mathcal{T}_{\mathbf{k}}^p$  by  $L_{\mathcal{T}}^p \exp(i\Theta_{\mathcal{T}})$ . Assuming the same contribution from all polarizations, this will lead us to an analogous result for the phase velocity  $\dot{\Theta}_{\mathcal{T}}(t)$  and the equation of motion for the amplitudes differ from (D.7) only by considering  $\omega_{\mathcal{T}}^2$  instead of  $\omega_{\mathcal{S}}^2$ ,

$$\ddot{L}_{\mathcal{T}}^p + \left[ \omega_{\mathcal{T}}^2 - (L_{\mathcal{T}}^p)^4(t_0) \frac{\dot{\Theta}_{\mathcal{T}}^2(t_0)}{(L_{\mathcal{T}}^p)^4} \right] L_{\mathcal{T}}^p = 0. \quad (\text{D.8})$$

It is important to remember that the power spectrum only depends on the amplitudes of the original modes, which can found at all times by,

$$|\zeta_{\mathbf{k}}| = \frac{|\mathcal{S}_{\mathbf{k}}|}{a^{3/2}A^{1/2}} = \frac{L_{\mathcal{S}}}{a^{3/2}A^{1/2}}, \quad |h_{\mathbf{k}}^p| = \frac{\sqrt{2}|\mathcal{T}_{\mathbf{k}}^p|}{a^{3/2}} = \frac{\sqrt{2}L_{\mathcal{T}}^p}{a^{3/2}}. \quad (\text{D.9})$$

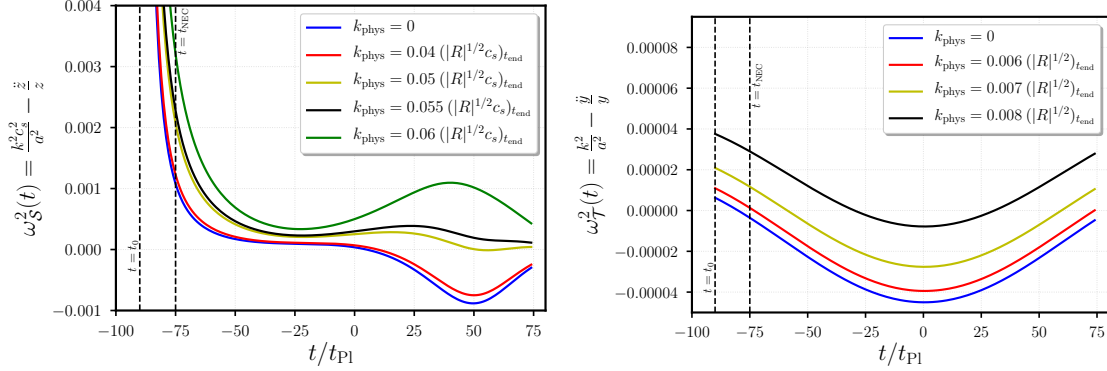


Figure D.2: Left panel: Evolution of scalar mode frequencies at different physical wavenumbers. Right panel: Corresponding frequencies of the tensor modes. We observe at which instant of time the minimal energy initial conditions are well-defined.

Initial conditions in (D.4) and (D.5) are reproduced after evaluating  $\Theta_{\mathcal{T}}(t_0) = 0$  and  $\Theta_{\mathcal{S}}(t_0) = 0$ , similarly  $\dot{L}_{\mathcal{T}}^p(t_0) = 0$  and  $\dot{L}_{\mathcal{S}}(t_0) = 0$ . The amplitudes of the modes and the phase derivatives are the only initial conditions with non-trivial values,

$$L_{\mathcal{S}}(t_0) = \frac{1}{\sqrt{2\omega_{\mathcal{S}}(t_0)}} \quad ; \quad \dot{\Theta}_{\mathcal{S}}(t_0) = \omega_{\mathcal{S}}(t_0), \quad (\text{D.10})$$

$$L_{\mathcal{T}}^p(t_0) = \frac{1}{\sqrt{2\omega_{\mathcal{T}}(t_0)}} \quad ; \quad \dot{\Theta}_{\mathcal{T}}(t_0) = \omega_{\mathcal{T}}(t_0), \quad (\text{D.11})$$

where the effective frequency of the harmonic oscillators in (D.7) and (D.8) at  $t = t_0$  is exactly zero for the scalar and tensor modes regardless of the values of  $k$ . The latter expressions are the concrete realization of (2.11) and (2.12) for our system. Hence, this procedure describes the single-field realization of the separation technique of fast and slow components shown in [116] and in Chapters 2 and 3 of this thesis. Our construction relies heavily in the positivity of  $\omega_{\mathcal{T}}^2$  and  $\omega_{\mathcal{S}}^2$  at  $t = t_0$ , for that reason the initial instant of time where the mode evolution starts needs to be chosen properly in order to avoid diverging initial conditions. Both functions are positive in the range of very high values of  $k$ , therefore we evaluated both effective frequencies in Figure D.2 in the low  $k$  limit. Henceforth, we choose  $t_0 = -90 t_{\text{Pl}}$  to be the initial instant of time where the evolution of perturbations begin. Moreover, it is also (approximately) the first moment where both  $A(t)$  and  $c_s^2$  are finite and positive, thus the system of scalar and tensor fluctuations evolves in a time domain where it is free from ghost and gradient instabilities.

## D.2 Evolution of the mode amplitudes and length scales

The definitions of the effective oscillation frequencies for the scalar curvature ( $\omega_{\mathcal{S}}^2$ ) and primordial tensor ( $\omega_{\mathcal{T}}^2$ ) modes shows that only the scalar fluctuations propagate with sound speed  $c_s$ . It is relevant, therefore, to compare the evolution of different physical length scales as these propagate from sub-horizon scales. Let us define the two physical scales with respect

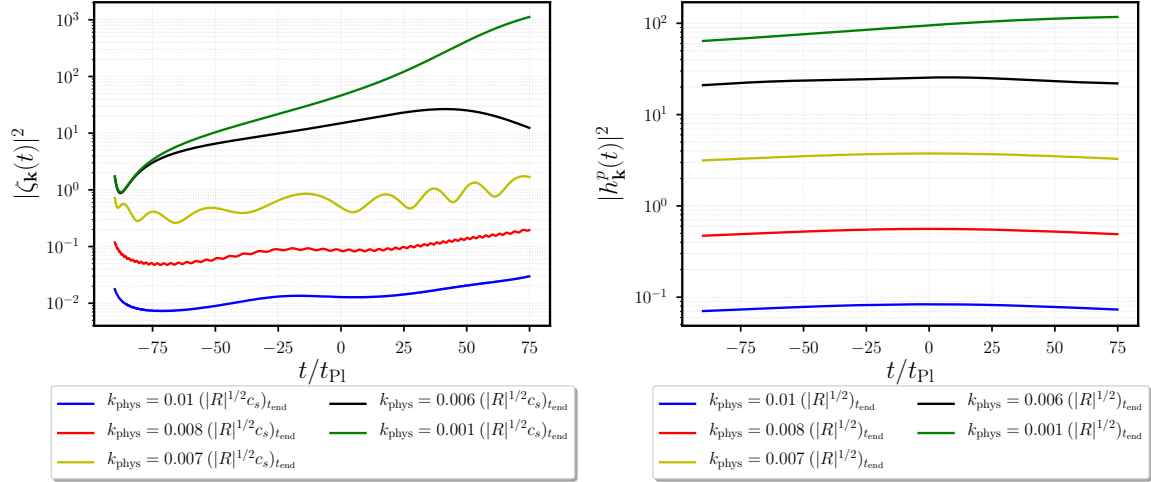


Figure D.3: Left panel: Evolution of scalar mode amplitudes  $|\zeta_{\mathbf{k}}^2(t)|$  at different physical wavenumbers. Right panel: Corresponding amplitudes of the tensor modes  $|h_{\mathbf{k}}^p(t)|^2$ .

to a given comoving wavelength  $\lambda_{\text{com}}$  by

$$\lambda_{\text{phys}}^{\mathcal{S}} = \frac{a\lambda_{\text{com}}}{c_s}, \quad (\text{D.12})$$

$$\lambda_{\text{phys}}^{\mathcal{T}} = a\lambda_{\text{com}}, \quad (\text{D.13})$$

which can be identified as the corresponding wavelength part from the definitions of  $\omega_{\mathcal{S}}^2$  and  $\omega_{\mathcal{T}}^2$ . We now evaluate the time derivative of the logarithmic versions of these two quantities, obtaining

$$\frac{d \ln \lambda_{\text{phys}}^{\mathcal{S}}}{dt} = H - \frac{1}{2} \left( \frac{\dot{B}}{B} - \frac{\dot{A}}{A} \right), \quad (\text{D.14})$$

$$\frac{d \ln \lambda_{\text{phys}}^{\mathcal{T}}}{dt} = H. \quad (\text{D.15})$$

From these expressions, we notice that none of these derivatives depends on the specific values of the evolving scalar or tensor wavelengths. From the form of  $\gamma$  and  $H$  suggested for the IS-bounce in (4.38) and (4.40) along with the construction of  $A(t)$  and  $B(t)$  described in equations (14) and (17) in [139], it is possible to compare the evolution of all the physical length scales ( $\ell_{\text{phys}}$ ) including the sound and particle horizon:

$$s_{\text{H}} = \int \frac{c_s(t)dt}{a(t)} ; p_{\text{H}} = \int \frac{dt}{a(t)},$$

through the bouncing phase. In the left panel of Figure D.1, as an example, we observe the evolution of the sound horizon and three sub-horizon physical wavelengths ( $\lambda_{\text{phys}}^{\mathcal{S}}$ ) corresponding to different comoving modes that propagate through the so-called acoustic geometry. Such scalar wavelengths never reach the sound horizon. In the same way, the evolution of the particle horizon and the corresponding tensor wavelengths ( $\lambda_{\text{phys}}^{\mathcal{T}}$ ) are depicted in the

right panel of Figure D.1, where each of these was built from the same comoving modes as in the previous case. In both scenarios, this indicates that we should not expect any transitions such as the characteristic “mode freezing” occurring during inflation, since the length stretching due to the speed of sound is not sufficient to reach super-horizon scales. In this appendix, we write the physical wavenumbers in units of the Ricci curvature  $|R|^{1/2}$ .

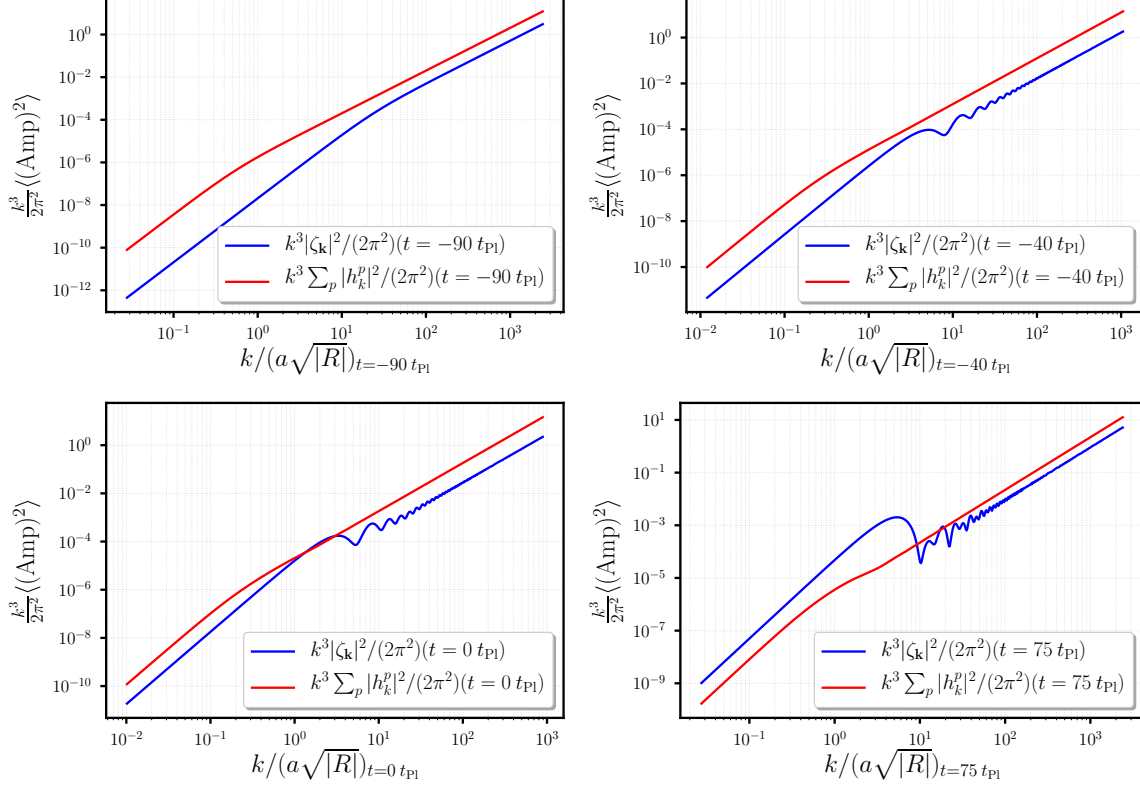


Figure D.4: Power spectrum at  $t = -90 t_{\text{Pl}}$ ,  $-40 t_{\text{Pl}}$ ,  $0 t_{\text{Pl}}$  and  $75 t_{\text{Pl}}$ , respectively. The shape of the spectra corresponds to a broken power-law, observing that there is an excess of power in the tensor modes. In all the cases, the spectra are not scale invariant.

After considering these results, we evolve the mode amplitudes for scalar and tensor fluctuations using the equations of motion in (D.7) and its tensor counterpart in (D.8) using the initial conditions shown in (D.10) and (D.11). In Figure D.3, we represent the dynamics of the amplitudes of some of the original scalar (in the left panel of Figure D.3) and tensor modes (in the right panel of Figure D.3) after using the inversion relationships in (D.9). This confirms our previous statement about the lack of a “mode freezing” phase in all the sub-horizon modes. It is possible to observe oscillations of the modes for the sub-horizon modes with the smallest values of  $k_{\text{phys}}$ . In Figure D.5, it will be possible to identify these oscillations in the scalar and tensor power spectrum and in the occupation numbers at given frequencies. In the limit where  $k$  goes to zero, the dominant scales are the negative values of  $\ddot{z}/z$  and  $\ddot{y}/y$  which behave as time-dependent effective masses.

We evaluate the scale dependence and other specific features of the power spectrum of scalar and tensor perturbations through the IS-bouncing trajectory from the choice of instantaneous minimal energy initial conditions set in (D.10) and (D.11) right before the bounce.

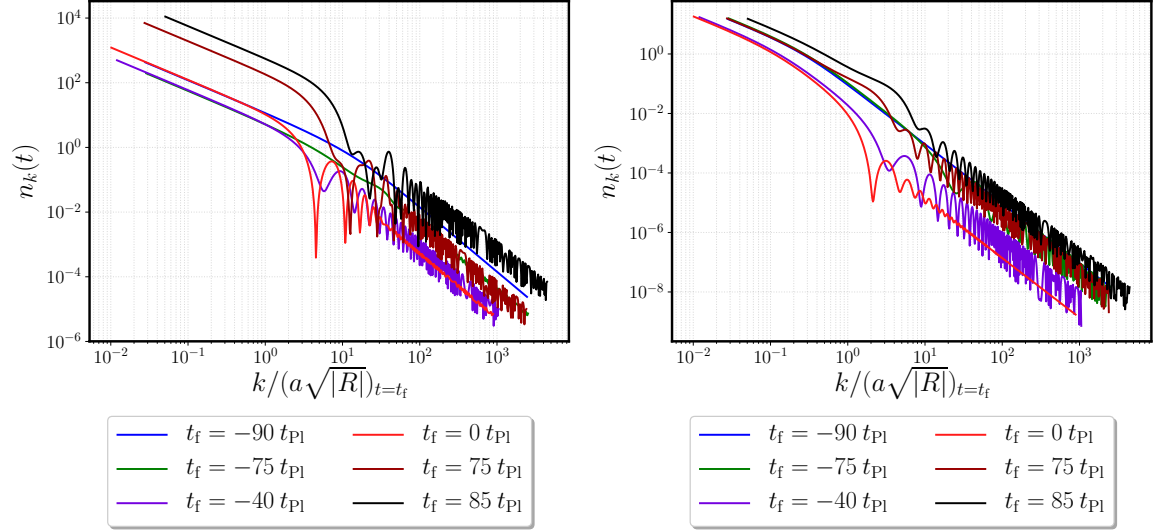


Figure D.5: Left panel: Evolution of the occupation numbers  $n_{\mathbf{k}}(t)$  of the scalar mode plotted in the same range as the power spectra. At large scales, the final occupation number can be greater than the initial by a factor of  $10^2$ . Right panel: The corresponding occupation numbers for the tensor modes. We assumed an initial state before the bounce at  $t_0 = -90t_{\text{Pl}}$ . In both figures, we can observe that particles are still being created after the violation of NEC at  $t_f = 85 t_{\text{Pl}}$ .

In addition to this, we also calculate the evolution of the occupation number of scalar and tensor fluctuations, observing that some of the features of the spectra are due to particle production. The power spectra of primordial scalar and tensor fluctuations follow from the typical definition given by,

$$P_{\zeta}(k) = \frac{k^3}{2\pi^2} |\zeta_{\mathbf{k}}(t)|^2, \quad P_h(k) = \frac{k^3}{2\pi^2} \sum_{p=+, \times} |h_{\mathbf{k}}^p(t)|^2, \quad (\text{D.16})$$

where the time evolution of the amplitudes  $|\zeta_{\mathbf{k}}(t)|^2$  and  $|h_{\mathbf{k}}^p(t)|^2$  follows from the numerical solutions for  $L_S$  and  $L_T$  described in (D.7) and (D.8) respectively. The calculations for particle production become much simpler to evaluate after we rephrase the equations of motion as in (D.2) and (D.3). We define the occupation number as,

$$\langle n_{\mathbf{k}}(t) \rangle = \frac{a^4 A(t)}{2k c_s} \left[ |\dot{\zeta}_{\mathbf{k}}|^2 + \frac{k^2 c_s^2}{a^2} |\zeta_{\mathbf{k}}|^2 \right] - \frac{1}{2}, \quad (\text{D.17})$$

where  $1/2$  corresponds to the minimum possible energy of the system for the production of scalar fluctuations. The tensor counterpart is defined in an analog way. In contrast with the definitions in [33], the last expression is not built from the time-dependent harmonic oscillators in (D.2) and (D.3) in order to not make these quantities divergent in the limit where  $\omega_S^2$  and  $\omega_T^2$  vanish. In Figure D.4, we evaluate the dependence of the amplitudes with  $k$  in four different instants of time. We evaluated the scalar and tensor power spectra in (D.16), showing that none of the spectra is scale invariant.

We must remark that the amplitude of the tensor modes dominates over the scalar amplitudes through most of the bouncing phase, as we can see in the first three panels of figures [D.4](#). This is due to the evolution of the speed of sound, where the enhancement of the scalar power at later times as shown in the last panel of the same figure coincides with the final decreasing phase of the speed of sound at  $t \sim 50t_{\text{Pl}}$ . Scalar and tensor amplitudes as depicted in these figures show a blue spectrum, consistent in the high  $k$  limit with the results presented in [\[72\]](#). The creation of particles in the scalar spectrum at later times is a visible feature of the scalar curvature spectrum, and it persists with less intensity as wavelengths become smaller. In addition to this, it is also possible to observe small low frequency oscillations in the tensor spectrum, which are evidence of particle production for these modes. We observe the evolution of the occupation number defined in [\(D.17\)](#) in [Figure D.5](#).

Here, the production of tensor fluctuations in the right panel of [Figure D.5](#) is 2-3 orders of magnitude smaller than the oscillations seen in the left panel of the same figure for the scalar case, in the same way the oscillations of the tensor amplitudes are smaller than the corresponding oscillations for the scalar power in [Figure D.4](#).



# Appendix E

## Numerical setup for scalar accretion and scattering

### E.1 Scalar field equations of motion

Equations of motion describing evolution of a scalar field  $\phi$  with a (non-linear) self-interaction potential  $V(\phi)$  and an external force term  $\mathcal{F}$  propagating on a fixed background spacetime are described by a (semi-linear) PDE

$$\square\phi = V'(\phi) - \mathcal{F}, \quad (\text{E.1})$$

where  $\square$  denotes a covariant d'Alembert operator. For a spherically symmetric black hole described by the Schwarzschild metric

$$ds^2 = -g(r) dt^2 + \frac{dr^2}{g(r)} + r^2 d\Omega^2, \quad (\text{E.2})$$

where  $d\Omega^2$  is the metric on a unit sphere, and the metric function  $g(r)$  is

$$g(r) = 1 - \frac{2M}{r}, \quad (\text{E.3})$$

the left hand side of the equation of motion is simply

$$\begin{aligned} \square\phi &= \frac{1}{\sqrt{-g}} \partial_\mu (\sqrt{-g} g^{\mu\nu} \partial_\nu \phi) \\ &= -\frac{1}{g(r)} \partial_t^2 \phi + \frac{1}{r^2} \partial_r (r^2 g(r) \partial_r \phi). \end{aligned} \quad (\text{E.4})$$

This can be reduced to a one-dimensional wave equation with constant propagation speed by introducing the tortoise coordinate  $x$  by  $\partial_x = g(r) \partial_r$ . With this re-definition, the scalar field equation of motion reads

$$-\partial_t^2 \phi + \frac{1}{r^2} \partial_x (r^2 \partial_x \phi) = g(V'(\phi) - \mathcal{F}). \quad (\text{E.5})$$

Explicit form of the tortoise coordinate  $x$  for the Schwarzschild spacetime can be obtained by integrating

$$x = \int \frac{dr}{g(r)} = r + 2M \ln \left( \frac{r}{2M} - 1 \right). \quad (\text{E.6})$$

Tortoise coordinate  $x$  is vastly preferable for numerical integration of the wave equation over areal coordinate  $r$  since the characteristic speed is constant on the sampled time slice, but the added difficulty with this choice is that accurate  $r(x)$  inversion is quite non-trivial numerically, as detailed in Appendix E.6.

The standard numerical evolution scheme would involve first-order Hamiltonian dynamical system

$$\dot{\phi} = \pi, \quad \dot{\pi} = \frac{1}{r^2} \partial_x \left( r^2 \partial_x \phi \right) - g \left( V'(\phi) - \mathcal{F} \right). \quad (\text{E.7})$$

However, as we will see in the following Section, it is easier to handle absorbing boundary conditions if we rewrite equations of motion in a flux-conservative form by introducing auxiliary variables  $u \equiv \partial_t \phi$  and  $v \equiv r^2 \partial_x \phi$ , so that equations of motion become

$$\begin{aligned} -\partial_t u + \frac{1}{r^2} \partial_x v &= g \left( V'(\phi) - \mathcal{F} \right), \\ -\partial_t v + r^2 \partial_x u &= 0. \end{aligned} \quad (\text{E.8})$$

The first equation is the identical rewrite of the wave equation (E.5), while the second is the integrability condition requiring that the partial derivatives of  $\phi$  commute.

## E.2 Absorbing boundary conditions

The scalar field degree of freedom  $\phi$  asymptotes to a free field evolution near horizon (where  $g \rightarrow 0$ ), and a massive field evolution far away from the black hole (where  $V'(\phi) \rightarrow \mathcal{F}$ ). Physically, excitations in  $\phi$  take infinite amount of time  $t$  to reach both boundaries, yet truncating or compactifying the evolution domain for numerical purposes will inevitably lead to spurious reflections unless special care is taken. The best technique to avoid spurious reflections is to introduce absorbing boundary conditions via Perfectly Matched Layers (PMLs) as described in [140], which damp the solution at the boundaries while guaranteeing identically vanishing reflection coefficient at the absorption layer. This is achieved by analytic continuation of the equations of motion into the complex domain

$$x \rightarrow x + if(x), \quad \partial_x \rightarrow \frac{\partial_x}{1 + if'(x)} \equiv \frac{\partial_x}{1 + \frac{\gamma(x)}{\partial t}}, \quad (\text{E.9})$$

which turns the oscillatory travelling waves  $e^{ikx - i\omega t}$  into exponentially decaying functions of  $x$  instead. To make attenuation length independent of  $\omega$ , frequency dependent contour deformation  $f' = \gamma(x)/\omega$  is chosen and  $i/\omega$  is transformed back into explicit integration operator in the time domain. Applying this idea to the scalar field equations of motion in

flux-conservative form (E.8) for an arbitrary damping function  $\gamma(x)$ , we obtain

$$\begin{aligned} -(\partial_t + \gamma)u + \frac{1}{r^2} \partial_x v &= \left(1 + \frac{\gamma(x)}{\partial_t}\right) \left[ g(V'(\phi) - \mathcal{F}) \right], \\ -(\partial_t + \gamma)v + r^2 \partial_x u &= 0. \end{aligned} \quad (\text{E.10})$$

To turn the inverse time evolution operator  $\partial_t^{-1}$  into a differential equation form, introduction of a third auxiliary variable  $w$  is in order. With re-definition  $u \rightarrow u + w$ , the non-reflecting PML equations of motion then become

$$\partial_t \phi = u - w, \quad (\text{E.11a})$$

$$\partial_t u = \frac{1}{r^2} \partial_x v - \gamma u, \quad (\text{E.11b})$$

$$\partial_t v = r^2 \partial_x (u - w) - \gamma v, \quad (\text{E.11c})$$

$$\partial_t w = g(V'(\phi) - \mathcal{F}). \quad (\text{E.11d})$$

The damping function  $\gamma(x)$  can be quite arbitrary, but it should have compact support near the boundaries to not affect the evolution in the interior, and have sufficient support and magnitude to absorb the impinging waves which hit the boundary during the expected evolution.

### E.3 Spectral basis

As the scalar field is usually quite stiff and does not form shocks in the course of evolution, the method of choice to evaluate derivative operators is spectral, as described in [43]. Compactifying the tortoise coordinate  $x$  on a scale  $\ell$

$$y = \frac{x}{\sqrt{x^2 + \ell^2}} \equiv \cos \theta, \quad \frac{x}{\ell} = \frac{y}{1 - y^2} = \cot \theta \quad (\text{E.12})$$

and introducing a Chebyshev basis on interval  $y \in [-1, 1]$

$$\begin{aligned} T_n &= \cos(n\theta), \\ \partial_x T_n &= \frac{n}{\ell} \sin(n\theta) \sin^2 \theta, \\ \partial_x^2 T_n &= \frac{n}{\ell^2} \left( n \cos(n\theta) + 2 \cot \theta \sin(n\theta) \right) \sin^4 \theta, \end{aligned} \quad (\text{E.13})$$

we arrive at the spectral representation of the solution

$$\phi(x) = \sum_n c_n T_n(y) \quad (\text{E.14})$$

truncated to a finite number of modes. While the Galerkin method to discretize equations of motion can be employed, the simplest method to evaluate derivative operators is pseudo-

spectral, where equations of motion are solved on a Gauss-Lobatto grid

$$\theta_i = \left(n - i + \frac{1}{2}\right) \frac{\pi}{n}, \quad x_i = \ell \cot \theta_i. \quad (\text{E.15})$$

we do not have to explicitly find coefficients  $c_n$  to evaluate the derivative operators of a function  $\phi(x)$  sampled on a collocation grid  $x_i$ . Instead, derivative operators like  $\mathcal{D}_{ij}$  and  $\mathcal{L}_{ij}$  can be found in advance by solving linear matrix equations

$$\sum_j \mathcal{D}_{ij} T_n(x_j) = \partial_x T_n(x_i), \quad (\text{E.16a})$$

$$\sum_j \mathcal{L}_{ij} T_n(x_j) = \left(\partial_x + \frac{2g}{r}\right) \partial_x T_n(x_i), \quad (\text{E.16b})$$

and so on for every basis function  $T_n$  evaluated at all nodes  $x_i$ .

## E.4 Gauss-Legendre integrator

Packing the scalar field variables  $\phi, u, v, w$  evaluated at the collocation grid points  $x_i$  into a state vector  $\vec{y} \equiv \{\phi(x_i), u(x_i), v(x_i), w(x_i)\}$ , the wave equation (E.11) reduces to an autonomous dynamical system

$$\frac{d\vec{y}}{dt} = \vec{f}(\vec{y}), \quad (\text{E.17})$$

which can be integrated by an implicit Runge-Kutta method, as presented in [57]

$$\vec{y} \rightarrow \vec{y} + \Delta t \cdot \sum_i b_i \vec{g}^{(i)}, \quad (\text{E.18})$$

where the trial directions  $\vec{g}^{(i)}$  are defined by

$$\vec{g}^{(i)} = \vec{f} \left( \vec{y} + \Delta t \cdot \sum_j a_j^i \vec{g}^{(j)} \right). \quad (\text{E.19})$$

Particularly accurate choice of coefficients for a time integrator corresponds to a Gauss-Legendre quadrature, where the trial directions are evaluated at the zeroes of the (shifted) Legendre polynomial

$$P_n(2c^{(i)} - 1) = 0, \quad (\text{E.20})$$

with coefficients  $a_j^i$  and  $b_j$  set by

$$\sum_j a_j^i [c^{(j)}]^{k-1} = \frac{1}{k} [c^{(i)}]^k \quad (\text{E.21})$$

$$\sum_j b_j [c^{(j)}]^{k-1} = \frac{1}{k}. \quad (\text{E.22})$$

The resulting time integration method is A-stable and symplectic for Hamiltonian problems, and is extremely easy to implement using a simple iterative scheme.

## E.5 Static solver

Static configurations of the field  $\phi$  have  $\partial_t\phi = 0$  and can be found by solving a (semi-linear) elliptical problem

$$\mathcal{L}\phi = g(V'(\phi) - \mathcal{F}). \quad (\text{E.23})$$

One can improve a trial solution  $\bar{\phi}$  using Newton's method by linearizing  $\phi = \bar{\phi} + \delta\phi$  and solving

$$\mathcal{L}(\bar{\phi} + \delta\phi) = g(V'(\bar{\phi} + \delta\phi) - \mathcal{F}), \quad (\text{E.24})$$

which translates the residual  $\mathcal{R} = -\mathcal{L}\bar{\phi} + g(V'(\bar{\phi}) - \mathcal{F})$  into a correction  $\delta\phi$  by solving a set of linear equations

$$(\mathcal{L} - gV''(\bar{\phi}))\delta\phi = -\mathcal{L}\bar{\phi} + g(V'(\bar{\phi}) - \mathcal{F}). \quad (\text{E.25})$$

With the basis as chosen in the last section, this scheme converges to machine precision in about 16 iterations or so for most of the potentials.

## E.6 Inverting tortoise coordinate

Accurately inverting Schwarzschild tortoise coordinate

$$x = r + 2M \ln\left(\frac{r}{2M} - 1\right) \quad (\text{E.26})$$

to yield areal coordinate  $r$  as a function of  $x$  turns out to be a rather non-trivial task, despite appearances. The problem is that asymptotic for large positive  $x$ , where  $r \simeq x - 2M \ln(x/2M - 1)$ , and for large negative  $x$ , where  $r \simeq 2M$  with exponentially suppressed metric function  $\ln g \simeq x/2M - 1$ , have vastly different derivatives with respect to  $x$  (which hampers numerical schemes like Newton's method), and no closed form algebraic inverse.

A trick that works for the entire usable range of  $x$  is to solve for an approximation variable  $q \simeq x - 2M$  instead

$$q = 2M \ln\left(\exp\left(\frac{r}{2M} - 1\right) - 1\right), \quad (\text{E.27})$$

which (unlike  $x$ ) is easily invertible to yield  $r$

$$r = 2M\left(1 + \ln\left(1 + \exp\frac{q}{2M}\right)\right), \quad (\text{E.28})$$

and can be readily found by Newton's method iterating  $q \rightarrow q + \delta q$  with

$$\delta q = -\left(r + 2M \ln\left(\frac{r}{2M} - 1\right) - x\right) \cdot \frac{dq}{dx}, \quad (\text{E.29})$$

as the derivative

$$\frac{dq}{dx} = \left(1 + \exp \frac{-q}{2M}\right) g(r) \quad (\text{E.30})$$

is of order one on the entire domain of definition of  $x$ . One still has to be careful to avoid numerical overflows in the exponents or catastrophic loss of precision when taking logarithms of one plus a small number, which can be achieved by evaluating

$$\ln(1 + e^q) = \begin{cases} q + \ln(1 + e^{-q}), & q \geq 0 \\ 2 \operatorname{atanh} \frac{e^q}{2 + e^q}, & q < 0 \end{cases} \quad (\text{E.31})$$

in different limits.